COSEISMIC AND POSTSEISMIC DEFORMATION OF THE GREAT 2004 SUMATRA-ANDAMAN EARTHQUAKE

by

KRISTIN LEIGH HELLEM HUGHES

A DISSERTATION

Submitted in partial fulfillment of the requirements
for the degree of Doctor of Philosophy
in the Department of Geological Sciences
in the Graduate School of
The University of Alabama

TUSCALOOSA, ALABAMA

2011

ABSTRACT

The 26 December 2004 M9.2 Sumatra-Andaman earthquake (SAE) induced a devastating tsunami when it ruptured over 1300 km of the boundary between the Indo-Australian plate and Burma microplate (Vigny et al., 2005; Bilek, 2007). Three months later on 28 March 2005, the M8.7 Nias earthquake (NE) ruptured over 400 km along the same trench overlapping and progressing to the south of the M9.2 rupture (Banerjee et al., 2007). The spatial and temporal proximity of these two earthquakes suggests that the SAE mechanically influenced the timing of the NE.

I analyze the coseismic and postseismic deformation, stress, and pore pressure of the 2004 SAE using 3D finite element models (FEMs) in order to determine the mechanical coupling of the SAE and NE. The motivation for using FEMs is two-fold. First, FEMs allow me to honor the geologic structure of the Sumatra-Andaman subduction zone, and second, FEMs simulate the mechanical behavior of quasi-static coseismic and postseismic deformation systems (e.g., elastic, poroelastic, and viscoelastic materials).

The results of my study include:

1) Coseismic slip distributions are incredibly sensitive to the distribution of material properties (Masterlark and Hughes, 2008),
2) Slip models derived from tsunami wave heights do not match slip models derived from GPS data (Hughes and Masterlark, 2008),

3) These FEMs predict postseismic poroelastic deformation and viscoelastic deformation simultaneously (Masterlark and Hughes, 2008),
4) Pore pressure changes induced by the SAE triggered the NE via fluid flow in the subducting oceanic crust and caused the NE to occur 7 years ahead of interseismic strain accumulation predictions (Hughes et al., 2010; Hughes et al., 2011),
5) Global Conductance Matrices provide a way to smooth an underdetermined FEM for arbitrarily irregular surfaces, and
6) FEMs are capable and desired to model subduction zone deformation built around the complexity of a subducting slab which is usually ignored in geodetic studies (Masterlark and Hughes, 2008; Hughes et al., 2010).

Rapidly advancing computational capabilities recently placed FEMs at the forefront of earthquake deformation analyses. The results and conclusions of this study will strongly influence future analyses of coseismic and postseismic deformation, stress, pore pressure, and tsunami genesis.

DEDICATION

This dissertation is dedicated to my family; Joe, Khyleigh, Don, Leigh Ann, and Nicki. Without your guidance, inspiration, and support this work would never have been completed. I thank you and love you all!

List of Abbreviations and Symbols

cm	centimeters
FEM(s)	finite element model(s)
GCM	Global Conductance matrix
GF(s)	Green's Function(s)
GPS	Global Positioning System
GRACE	Gravity Recovery and Climate Experiment
HEHS	Homogeneous elastic half-space
km	kilometers
kPa	kilo-Pascal
LEHS	Layered elastic half-space
M#	moment magnitude of #
m	meters
mm	millimeters
MPa	mega-Pascal
NE	Nias earthquake
NIE	Nicobar Islands earthquake
NSE	northern Sumatra earthquake
SAE	Sumatra-Andaman earthquake
SASZ	Sumatra-Andaman subduction zone

[,]	matrix definition (column, row)
$^{-1}$	inverse
A	constant multiple of viscosity
α	Biot-Willis coefficient
β	damping parameter
c	constant
$\boldsymbol{C}$	Global Conductance matrix
$\boldsymbol{d}$	displacement vector
Δ	change in
∂	partial derivative
$\boldsymbol{e}$	error vector
E	Young's modulus
E	error norm
ε	elastic strain
ε_{kk}	volumetric strain
$\dot{\varepsilon}$	strain rate
f	function of
f	friction
F_i	body force in i^{th} direction
G	Shear modulus
$\boldsymbol{G}$	matrix of Green's Functions
k	permeability
L	complexity

$\boldsymbol{L}$	Laplacian smoothing matrix
$\boldsymbol{m}$	slip distribution vector
$\boldsymbol{m^{est}}$	estimated slip distribution vector
μ	viscosity
n	constant characteristic of creep
η	constant characteristic of creep
υ	Poisson's ratio
P	pressure
P	pore pressure
Q	volume of fluid per bulk volume per unit time
Q_d	activation energy for dislocation creep
R	gas constant
$\boldsymbol{s}$	slip distribution vector
$\vec{s}$	slip distribution node for kinematic equation
$\boldsymbol{s}^{est}$	estimated slip distribution vector
S_ε	specific storage at constant strain
σ	stress
σ_0	deviatoric stress
σ_c	Coulomb stress
σ_d	deviatoric stress
σ_n	normal stress
σ_s	shear stress
T	transpose

t	time
T	absolute temperature
u	displacement in x direction
$\vec{u}_i$	displacement node for kinematic equation
v	displacement in y direction
V_d	activation volume for dislocation creep
w	displacement in z direction
$\boldsymbol{W}$	weighting matrix
x	Cartesian coordinate
y	Cartesian coordinate
z	Cartesian coordinate

ACKNOWLEDGEMENTS

I would like to thank all of those who helped me get to the final point of this research. I would especially like to thank my advisor, Timothy Masterlark, Ph.D., for all of his guidance and countless hours of work in helping me complete this project. I appreciate how much he has helped me learn over the past five years, and for encouraging me to take the next step. I also want to thank him for funding this project and many national and international conferences. I am grateful for the opportunity to have traveled abroad to collaborate and to share our research.

Special thanks to Andrew Goodliffe, Ph.D., Chunmiao Zheng, Ph.D., Delores Robinson, Ph.D., and Kurt Feigl, Ph.D., for their support and continuous questions. They helped me understand this material far better than I could have alone. Special thanks to the Geological Sciences department at the University of Alabama for the freedom to pursue this project.

I would like to thank Walter Mooney, Ph.D., for his guidance and understanding. He was a wonderful collaborator and colleague. Special thanks to Jeremy Pesicek, Ph.D. and Cliff Thurber, Ph.D. for all of their hard work. This project could not have been completed without their data and effort. Thanks to Haylee Dickinson, M.Sc., Sarah Needy, M.Sc., Joe Lambert, M.Sc., Philip Chapman, M.Sc., Erika Ronchin, M.Sc., Wei Tao, Ph.D., and Christodoulos Kyriakopoulos, M.Sc., for all of their support.

I am grateful to have copyright permission to include our published journal articles. Thanks especially to the Istituto Nazionale di Oceanografia e di Geofisica Sperimentale of Trieste, Italy, the American Geophysical Union in Washington, D.C., USA, the Elsevier of Amsterdam, The Netherlands, and the Geological Society of America in Boulder, Colorado, USA.

Finally, I would especially like to thank God and my family, Joe Hughes, III, Khyleigh Hughes, Don Hellem, Leigh Ann Hellem, and Nicole and Greg Estes for all of their continued and loving support. To my husband, Joe, thank you for your unending love and support. I appreciate your patience, your listening ability, and your complete understanding. To our daughter, Khyleigh, thanks for always being the bubbly and happy baby you are. To both of my parents, Don and Leigh Ann, thank you for your unconditional love and guidance, I know this has been a long road for you both. Thank you for supporting me in everything I do and encouraging me to do my best no matter how long it takes. To my sister, Nicki, and her husband, Greg, for your ability to always find the joyful side of life. Your encouragement and listening ears are deeply appreciated. I treasure in my heart what all of my family has done for me and the sacrifices they have made in getting me through this step and to the next, more than words can say.

CONTENTS

List of Tables

List of Figures

CHAPTER 1

INTRODUCTION

PROJECT BACKGROUND

The M9.2 Sumatra-Andaman earthquake (SAE) of 26 December 2004 ruptured 1300 km of the boundary separating the Indo-Australian and Burma plates (Vigny et al., 2005; Bilek, 2007). The earthquake, which lasted over 8 minutes, displaced the seafloor, inducing a devastating tsunami (Fig. 1.1) (Bilek, 2007). The tsunami affected over 12 countries and killed over 250,000 people (Rastogi and Jaiswal, 2006). Three months after the M9.2 Sumatra-Andaman earthquake, a M8.7 earthquake (28 March 2005) occurred near

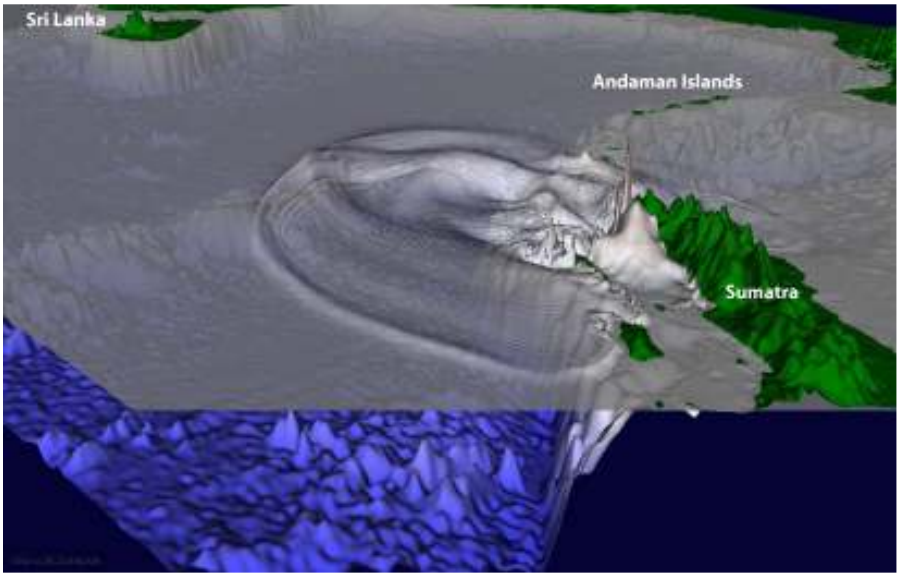

Figure 1.1. 3D image of tsunami simulation (adapted from Geist, 2005). The observed run-ups were larger in Sumatra and Thailand where the near-field slip occurred.

Nias Island and south of the 2004 rupture along the same plate boundary (Fig. 1.2) (Banerjee et al., 2007).

The SAE is the largest earthquake for which coseismic deformation is recorded by the global positioning system (GPS) thus it provides an unprecedented signal to noise ratio for earthquake deformation (Catherine et al., 2005; Jade et al., 2005; Vigny et al., 2005; Gahalaut et al., 2006). The earthquake was also recorded by seismograms all over the world, and the tsunami run-ups were measured on coastlines surrounding the Indian Ocean (Grilli et al., 2007; Stein and Okal, 2007). In addition to these data, coral head uplifts (Meltzner et al., 2006; Kayanne et al., 2007), and seafloor displacements (Moran and Tappin, 2006) were recorded, and associated tomography and Gravity Recovery and Climate Experiment (GRACE) data have been analyzed (Han et al., 2007; Pesicek

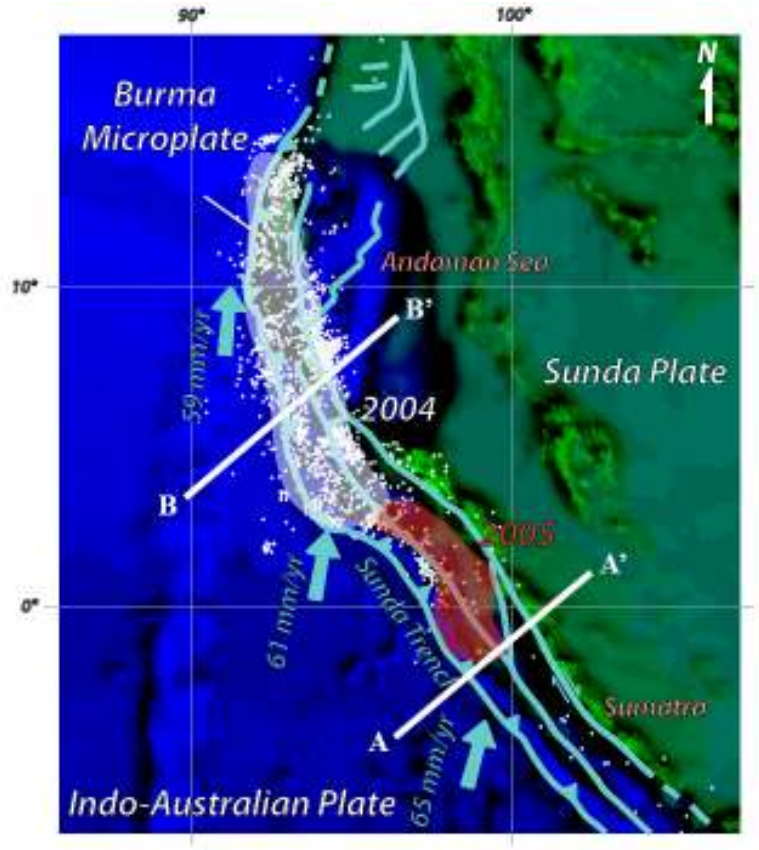

Figure 1.2. Map of rupture zones and seismicity of the Sumatra-Andaman Islands. The transparent white section represents the surface projection of the 26 December 2004 rupture, and the transparent red section represents the surface projection of the 28 March 2005 rupture. A-A' indicates the location of the southern cross-section and B-B' represents the northern cross-section used in the fully 3D model.

et al., 2008; Pesicek et al., 2010). The collection of all of these data provides unprecedented opportunities to quantify coseismic and postseismic deformation due to both great earthquakes since some of these magnitudes of cm to m data record deformation with mm uncertainty (Masterlark and Wang, 2000; Freed and Lin, 2001; Masterlark and Wang, 2002). The GPS stations on the Nicobar Islands moved about 4 m, while the Andaman Islands had the greatest displacement of about 5 m (Gahalaut et al., 2006; Subarya et al., 2006). The island of Sumatra had the least amount of displacement among the near-field GPS observations used in this study.

GEODETIC MODELING HISTORY

Analytical solutions that simulate deformation due to slip along a fault embedded in a homogeneous, elastic, half-space (HEHS) are readily available (e.g. Okada, 1992). These models are commonly implemented in deformation models of subduction zone earthquakes. In spite of their widespread use, the inherent assumptions of HEHS models are not geologically satisfying. The HEHS assumptions maintain that the model domain must be homogeneous, elastic, topographically flat, and extend to infinity in all directions (Okada, 1992). A homogeneous model domain oversimplifies the natural system of a subduction zone because it does not account for the cold, relatively stiff subducting slab which is the hallmark of a subduction zone. A topographically flat and infinitely large model domain is not a sufficient representation because it does not incorporate the actual topography or mechanical influence of other local faults. However, the HEHS model has become

the standard accepted model because it is an analytical solution that is computationally inexpensive and thus attractive for inverse methods that seek to estimate fault-slip based on geodetic data. The HEHS model is easy to conceptualize and removes design decisions which will be discussed later.

Some investigators applied alternatives (layered half-space or layered quarter-space models) to incorporate heterogeneity (e.g., Johnson and Segall, 2004; Hsu et al., 2006). These models still do not account for topography, near-field faults, and spatial heterogeneity and anisotropy which are expected to be variable in a subduction zone. In addition, the HEHS model cannot solve for viscoelastic and poroelastic behavior that is known to occur in response to megathrust earthquakes. Both of these components are an important part of postseismic deformation and stress coupling, and should not be neglected in simulations of postseismic deformation.

Finite element models (FEMs) (one type of numerical model) have been used to analyze earthquake coupling and to calculate and predict postseismic deformation at several strike-slip fault settings (e.g., Landers, Hector Mine, and Denali earthquakes) and subduction zone settings (e.g., Jalisco earthquake) (Masterlark and Wang, 2000; Freed and Lin, 2001; Masterlark and Wang, 2002; Freed et al., 2006). FEMs were utilized in some studies (Kenner and Segall, 2000; Masterlark and Wang, 2002) to incorporate the known geologic structure, evaluate the coseismic deformation, and to analyze postseismic deformation. FEMs have also been utilized for large-scale San Andreas earthquakes (Kenner and Segall, 2000;

Parsons, 2002) and other subduction zones (McCaffrey et al., 2000; Williams and McCaffrey, 2001; Wang and Ye, 2006; Schmitt et al., 2007).

FEMs are limited by computational efficiency. In the case of a subduction zone model simulating a distribution of slip, the rupture surface is divided into multiple slip patches. Greens Function (impulse response function) calculations for each patch, required for inverse analyses, can take minutes to hours for the individual analysis of each slip patch. The more patches included in the model the higher the resolution, but the increase of patches increases the computational time and solution uncertainty. Thus, increasing computational time can force the modeler to limit the resolution of the solution. The balance between the two end-members (computational time and resolution) will be discussed later in the context of trade-off curves.

GEODETIC MODELING DESIGN

The Sumatra-Andaman (SAE) and M8.7 Nias (NE) earthquakes were close in both space and time (Fig. 1.2). This observation led to my main idea; the timing of the NE was influenced by the SAE. I evaluate this idea through the quantification of coseismic and postseismic deformation of the SAE which changed the Coulomb stress regime. I address the idea using a fully 3D FEM to simulate the Sumatra-Andaman subduction zone (SASZ) as a poroelastic deformation system. More specifically, I generate two hypotheses for this study, 1) the SAE mechanically influenced the timing of the NE, and 2) an FEM can simulate the coseismic deformation of the SAE, while simultaneously accounting for the complex geometry

of the subducting slab and 3D distribution of material properties suggested by tomography, gravity, and geologic data.

The motivation for using FEMs was two-fold. First, FEMs allow me to honor the known geology and structure of the SASZ, and second, FEMs can simulate the elastic coseismic response as well as mechanisms of postseismic deformation (e.g., elastic afterslip and poroelastic and viscoelastic relaxation) and interseismic strain accumulation. The stresses caused by the SAE drive the postseismic deformation processes. Afterslip is the slip along the rupture surface after the coseismic static response to the rupture has occurred, and is usually located down-dip and up-dip from the coseismic rupture. The coseismic static response to the rupture occurs minutes after the coseismic dynamic rupture that causes the P- and S-waves. The coseismic static response to the rupture offset causes coseismic deformation which is deformation that remains following dynamic deformation of the mainshock. Afterslip has many parameters which can easily be fit to GPS data, but may not generate an accurate model due to ambiguity. This study is focused on viscoelastic and poroelastic deformation because these two components have fewer adjustable parameters than afterslip. The residual deformation not accounted for by viscoelastic and poroelastic deformation can be analyzed using afterslip.

Viscoelastic deformation occurs when stresses in the mantle relax and dissipate after an earthquake. The SAE caused large deviatoric stresses to build-up in the mantle. The surface and crust continues to deform in response to stresses relaxing via viscous flow in the mantle over the years following the coseismic displacement. Due to the magnitude of the SAE (M9.2), viscoelastic deformation

becomes important a few months after the coseismic rupture and continues for decades. The viscoelastic deformation component is a very large constituent of postseismic deformation, and is predicted to be on the order of meters over the decade following the SAE.

Poroelastic deformation occurs when fluids in the crust migrate due to pore pressure gradients induced by the static response to the rupture. The results indicate that poroelastic surface deformation due to the SAE is on the order of centimeters. These pore pressure gradients also cause triggering of later earthquakes on relatively short time scales (tens of weeks to tens of months).

Pore pressure is a component of Coulomb stress, which is the quantification of the change in tendency for slip to occur along a fault, and is defined as

$$\Delta\sigma_c = \Delta\sigma_s + f(\Delta\sigma_n + \Delta P) \qquad (1.1)$$

where σ_c is Coulomb stress, σ_s is shear stress, f is friction, σ_n is normal stress, and P is pore pressure (Wang, 2000). My results indicate that the changes in pore pressure due to the SAE are on the MPa-scale (Masterlark and Hughes, 2008; Hughes et al., 2010), which is of the same magnitude as normal stress and shear stress. Therefore, pore pressure changes are a substantial component of earthquake coupling for the SAE. The analysis of Coulomb stress and changes in pore pressure can account for shallow aftershock locations and timing after a model has been calibrated (Wang, 2000). The analysis of pore pressure changes following the SAE is an innovation of this project.

The fully 3D FEM is distinct because it simulates a 3D subduction zone by incorporating the along-strike variation of the Sunda trench. Previous FEMs of

subduction zone earthquakes were typically based on a single cross-section, and were sufficient because the geology of the problem domain did not vary substantially along strike (the regional geology did not vary on the scale of the discretization of the model). The SASZ changes substantially from north to south (Fig. 1.2). A cross-section generated to the north through the Andaman Sea should incorporate a basaltic basin due to extension, which is different when compared to a cross-section through the Sumatran Islands to the south. A suitable model domain incorporates both of these geologically varying areas. The plate motion also changes along the strike of the Sunda trench due to the curvature of the plate boundary. To the north, the Indo-Australian plate almost has a strike-slip motion with respect to the Burma microplate as opposed to the south where the Indo-Australian plate obliquely subducts under the Burma and Sunda microplates (Fig. 1.2) (Bird, 2003).

In addition to answering the question of earthquake triggering, my model can be used by tsunami modelers to better predict near-field run-ups (Fine et al., 2005; Waltham, 2005; Lovholt et al., 2006; Moore et al., 2007; Fujii and Satake, 2007; Hébert et al., 2007; Hanson et al., 2007; Geist et al., 2007; Seno and Hirata, 2007; Grilli et al., 2007), and to address further triggering with the three-earthquake sequence of 2007, the later September 2009 earthquake, and the two 2010 earthquakes with calibrated viscoelastic relaxation. The sequence ruptured a section south of Nias Island and included a M8.4, M7.9, and M7.5. The M7.0 September 2009 earthquake was much deeper (~45 km) and ruptured a projected

space between the NE and the three sequence event. Thus, this study will have broad impacts in the fields of geodesy and geophysics.

MODEL METHODS

A model is a simplification of a natural system. A good model satisfies a known purpose or goal which may be quantitative or qualitative. An accurate numerical model incorporates as much information as possible while generating the best approximation of the solution to specified governing equations. I use a formal modeling protocol (e.g., Masterlark and Hughes, 2008) to ensure the model adequately simulates the natural system (Fig. 1.3).

1. MODEL PURPOSE

The purpose of the model must be clearly defined in order to construct an accurate and viable model. Because this project examines earthquake triggering, the model evaluated coseismic and postseismic deformation. GPS data and field observations suggest 1-1.5 meters of vertical uplift and subsidence due to the SAE (Earnest et al., 2005; Anu and Rajendran, 2006; Banerjee et al., 2007; Chen et al., 2007). Models generated by other investigators (half-space and layered half-space models) calculate a maximum of 2-3 meters of

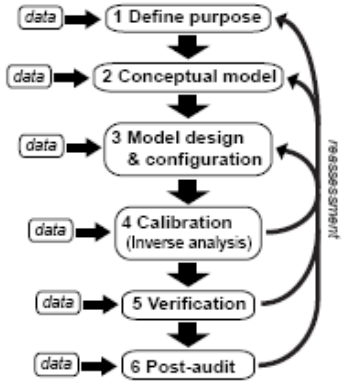

Figure 1.3. The modeling methods protocol is represented graphically (adapted from Masterlark and Hughes, 2008). Each step can be completed in order, but the graphic also indicates that one step can lead back to a previous step, if modifications are required.

vertical surface deformation (Ammon et al., 2005; Vigny et al., 2005; Subarya et al., 2006). My model differs because I incorporate the geology of both the volcanic islands of Sumatra and the back-arc spreading center in the Andaman Sea. Thus, the FEM potentially gives more accurate calculations and predictions of coseismic deformation due to a more accurate slip model. It is imperative that the slip model be accurate because the dislocation of the fault is what drives the postseismic deformation and Coulomb stress changes.

2. CONCEPTUAL MODEL

Developing an acceptable model is a central aspect to this project. An ill-designed conceptual model leads to unreliable predictions and thus introduces prediction errors to subsequent investigators for estimations of deformation, stress, and pore pressure changes. These errors propagate, in turn, into stress triggering and tsunami forecast errors. The conceptual model is a blueprint or draft of the problem domain. My conceptual model is an integration of geologic cross-sections, topography, tectonics, GRACE data, and tomography data from the published literature (Kieckhefer et al., 1980; Kopp et al., 2001; Conder et al., 2002; Kopp et al., 2002; Kopp and Kukowski, 2003; Dasgupta et al., 2003; Barber et al., 2005) including collaborators from the University of Wisconsin-Madison (Pesicek et al., 2008; Pesicek et al., 2010).

Cross-sections of the known geology and structure of the volcanic islands are well constrained (Kieckhefer et al., 1980; Kopp et al., 2001; Kopp et al., 2002; Dasgupta et al., 2003; Barber et al., 2005), and to some extent have constrained the

structure of the back-arc basin in the Andaman Sea (Dasgupta et al., 2003). Gravity measurements (Mukhopadhyay, 1988) and GRACE data (Chatterjee et al., 2007; Panet et al., 2007; Pesicek et al., 2008) and tomography data (Richards et al., 2007; Pesicek et al., 2008; Pesicek et al., 2010) are used to augment this lack of information from the Andaman Sea cross-section data and to bolster the Sumatran arc cross-section data.

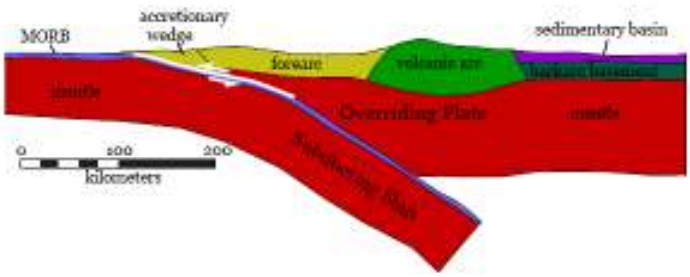

Figure 1.4. Cross-section through northern Sumatra based on geologic and structural data from Indonesia (Kieckhefer et al., 1980; Kopp et al., 2001; Conder et al., 2002; Dasgupta et al., 2003; Barber et al., 2005).

The topography, geology, and present-day tectonics are also used to create the draft of the model. The topography of the overriding plate is incorporated into the sketch (Song and Simons, 2003; Chatterjee et al., 2007). The geology data are used to determine accurate Poisson's ratio and Young's Modulus for each geologic unit (Page et al., 1979; Pal et al., 2003; Barber et al., 2005). The plate tectonics of the draft are controlled by the present-day plate boundaries and motions (Weissel, 1981; Hall, 2002; Bird, 2003; Dasgupta et al., 2003; Delescluse and Chamot-Rooke, 2007; Gahalaut and Gahalaut, 2007; Pesicek et al., 2008; Pesicek et al., 2010). The first manifestation of the model is shown in Figures 1.4 and 1.5 (Masterlark and Hughes, 2008; Hughes and Masterlark, 2008; Hughes et al., 2010). This conceptual model is based on a single cross-section through the northern part of Sumatra (Fig. 1.2, A-A'). The single cross-section was swept along the strike of the Sumatra-Andaman subduction zone to create a three-dimensional model (Fig. 1.5) (Hughes

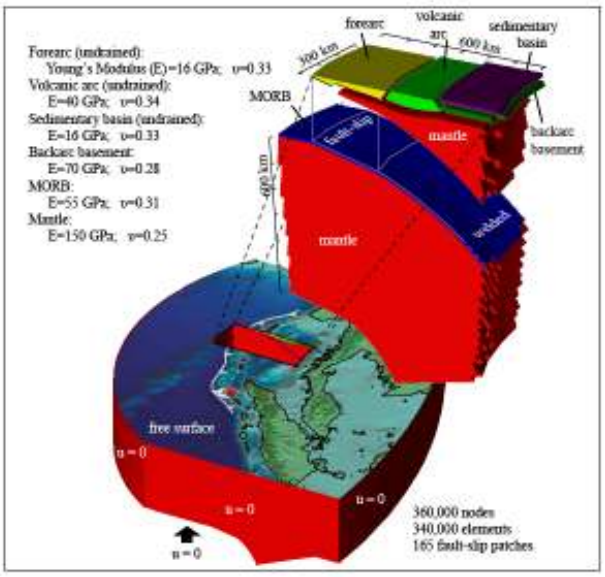

Figure 1.5. The northern Sumatra cross-section is swept along strike (adapted from Masterlark and Hughes, 2008). This creates the finite element model domain. The exploded view shows the cross-section and fault-slip detail.

and Masterlark, 2008; Masterlark and Hughes, 2008; Hughes et al., 2010). The second iteration of the model incorporates a second cross-section through the Andaman Sea (Fig. 1.2, B-B') and accounts for along-strike geologic complexity (Fig. 1.6). This fully 3D FEM is the first to simulate the SAE, and can be used by other investigators to generate a simulated tsunami. The northern cross-section (Fig. 1.2, B-B') contains a basaltic basin behind the forearc. The southern cross-section (Fig. 1.2, A-A') contains an island arc complex and typical forearc and backarc basins. The two cross-sections are not used exclusively to build the model, but are the basis to begin the model design that accounts for the known structural configuration of the SASZ.

3. Model Design

I design and construct a model to simulate the configuration and processes of the

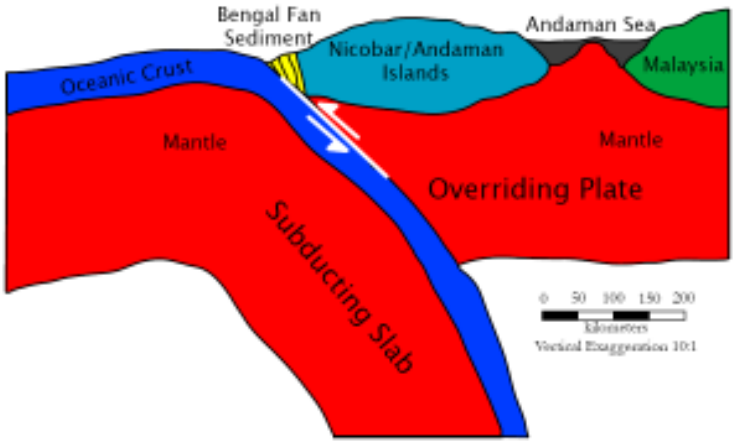

Figure 1.6. Cross-section through the Andaman Sea based on geological and structural data from Indonesia (Hutchison, 1989; Dasgupta et al., 2003; Pesicek et al., 2008).

conceptual model. The purpose of the model is to quantify the coseismic and postseismic deformation due to the SAE. The governing equations used to quantify displacement in a static elastic medium are expressed as

$$G\nabla^2 u + \frac{G}{1-2\upsilon}\left[\frac{\partial^2 u}{\partial x^2} + \frac{\partial^2 v}{\partial x \partial y} + \frac{\partial^2 w}{\partial x \partial z}\right] = -F_x$$

$$G\nabla^2 v + \frac{G}{1-2\upsilon}\left[\frac{\partial^2 u}{\partial y \partial x} + \frac{\partial^2 v}{\partial y^2} + \frac{\partial^2 w}{\partial y \partial z}\right] = -F_y \qquad (1.2)$$

$$G\nabla^2 w + \frac{G}{1-2\upsilon}\left[\frac{\partial^2 u}{\partial z \partial x} + \frac{\partial^2 v}{\partial z \partial y} + \frac{\partial^2 w}{\partial z^2}\right] = -F_z$$

where G is the shear modulus, u, v, and w are displacements in the x, y, and z directions, υ is the Poisson's ratio, and F_x, F_y, and F_z are body forces per bulk volume (Wang, 2000). Elastic strain (ε) is a function of the change in displacement and stress (σ) shown by

$$\varepsilon_{xx} = \frac{\partial u}{\partial x} = c_1\sigma_{xx} + c_2\sigma_{yy} + c_3\sigma_{zz}$$

$$\varepsilon_{yy} = \frac{\partial v}{\partial y} = c_4\sigma_{xx} + c_5\sigma_{yy} + c_6\sigma_{zz}$$

$$\varepsilon_{zz} = \frac{\partial w}{\partial z} = c_7\sigma_{xx} + c_8\sigma_{yy} + c_9\sigma_{zz} \qquad (1.3)$$

$$\varepsilon_{xy} = \frac{1}{2}\left(\frac{\partial u}{\partial y} + \frac{\partial v}{\partial x}\right) = c_{10}\sigma_{xy}$$

$$\varepsilon_{xz} = \frac{1}{2}\left(\frac{\partial u}{\partial z} + \frac{\partial w}{\partial x}\right) = c_{11}\sigma_{xz}$$

$$\varepsilon_{yz} = \frac{1}{2}\left(\frac{\partial v}{\partial z} + \frac{\partial w}{\partial y}\right) = c_{12}\sigma_{yz}$$

where $c_{1\text{-}12}$ are constants.

Part of the objective of this project is to quantify coseismic and postseismic deformation mechanisms–coseismic slip, postseismic afterslip, poroelastic relaxation, viscoelastic relaxation, and interseismic strain accumulation (backslip)–while honoring the known geology including heterogeneity. For this purpose I partition the model based on rheologic structure. The upper crust is simulated as a poroelastic medium, the lower crust as a viscoelastic medium, and the mantle as a different viscoelastic medium. The governing equations used for viscoelastic deformation are similar to Eq. 1.2, but because a viscoelastic medium is allowed to flow over time in response to deviatoric stresses I apply a creep law that expresses the strain rate $(\dot{\varepsilon})$ as a function of deviatoric stress to account for the time dependent deformation,

$$\dot{\varepsilon} = \frac{\partial \varepsilon}{\partial t} = f(\sigma) \tag{1.4}$$

There are many functions of stress that satisfy this relationship. I use a linear relationship expressed as

$$\dot{\varepsilon} = \frac{1}{2\mu}\sigma_0 \tag{1.5}$$

where μ is the viscosity of the medium and σ_0 is deviatoric stress. This relationship holds for a Newtonian fluid which I assume in this analysis.

The simulated upper crustal materials, including the subducting oceanic crust are simulated as poroelastic. The governing equations used to quantify coupled displacement and pore pressures are expressed as

$$G\nabla^2 u + \frac{G}{1-2\upsilon}\left[\frac{\partial^2 u}{\partial x^2} + \frac{\partial^2 v}{\partial x \partial y} + \frac{\partial^2 w}{\partial x \partial z}\right] = \alpha \frac{\partial P}{\partial x} - F_x$$

$$G\nabla^2 v + \frac{G}{1-2\upsilon}\left[\frac{\partial^2 u}{\partial y \partial x} + \frac{\partial^2 v}{\partial y^2} + \frac{\partial^2 w}{\partial y \partial z}\right] = \alpha \frac{\partial P}{\partial y} - F_y \qquad (1.6)$$

$$G\nabla^2 w + \frac{G}{1-2\upsilon}\left[\frac{\partial^2 u}{\partial z \partial x} + \frac{\partial^2 v}{\partial z \partial y} + \frac{\partial^2 w}{\partial z^2}\right] = \alpha \frac{\partial P}{\partial z} - F_z$$

$$\alpha \frac{\partial \varepsilon_{kk}}{\partial t} + S_\varepsilon \frac{\partial P}{\partial t} = \frac{k}{\mu}\nabla^2 P + Q \quad \text{where} \quad \varepsilon_{kk} = \varepsilon_{xx} + \varepsilon_{yy} + \varepsilon_{zz} = \frac{\partial u}{\partial x} + \frac{\partial v}{\partial y} + \frac{\partial w}{\partial z} \qquad (1.7)$$

where α is the Biot-Willis coefficient, ε_{kk} is volumetric strain, S_ε is specific storage at constant strain, k is permeability, and Q is the volume of fluid per unit bulk volume per unit time (Wang, 2000). I construct an iterative numerical FEM to satisfy the governing equations and creep laws over a specified problem domain. For elastic and viscoelastic simulations, the boundary conditions of the FEM are $u = 0$ over lateral boundaries and the base of the problem domain. The top surface is stress free. The zero displacement boundaries are placed far enough away from the dislocation to decrease edge effects in the model. The initial conditions of the FEM are equilibrium. The purpose of this model is to determine coseismic and postseismic deformation. Thus, this model is only used to determine incremental displacement and changes in stress and pore pressure due to coseismic and postseismic deformation, with respect to assumed preseismic equilibrium conditions.

Abaqus (http://www.simulia.com) was utilized to construct the 3D FEMs. Abaqus is a commercially available, general purpose finite element modeling environment that can simulate the proposed coseismic and postseismic

deformation analyses, in both forward and inverse models. I started with the U.S. Geological Survey's (2010) slab model to determine the top of the slab along the SASZ. Then, I used tomography and gravity data (Pesicek et al., 2008; Pesicek et al., 2010) to determine the rheologic properties of the rocks at the subduction zone. The northern (Andaman Sea) and southern (Sumatra Islands) cross-sections (Fig. 1.2, 1.4, and 1.6) are used to verify the Abaqus configuration. The problem domain is tessellated into smaller elements in the near-field region, and the elements increase in size progressing towards the far-field and model boundaries.

4. Model Calibration

Calibration parameters used in this model include slip dislocations. Viscosity parameters and permeability parameters will be calibrated in future analyses. The slip distribution drives the coseismic and postseismic displacements, the viscosity parameters determine the nature of viscoelastic deformation in the mantle, and the permeability parameters determine how poroelastic deformation in the crust occurs. Calibration targets are based on published measurements which include, GPS data (Gahalaut et al., 2006; Subarya et al., 2006; Simons et al., 2007), coral head measurements (Natawidjaja et al., 2004; Meltzner et al., 2006; Rajendran et al., 2007; Kayanne et al., 2007), seismicity (Engdahl et al., 2007; Chlieh, et al., 2007; Bilek, 2007; Ishii et al., 2007), and gravity (Mukhopadhyay, 1988; Chatterjee et al., 2007; Panet et al., 2007; Pesicek et al., 2008).

The forward model for deformation in an elastic problem domain, due to a distribution of fault-slip is

$$\boldsymbol{G}\,\boldsymbol{m} = \boldsymbol{d} \tag{1.8}$$

where $\boldsymbol{G}$ is a matrix of Green's Functions, $\boldsymbol{m}$ is the fault-slip vector, and $\boldsymbol{d}$ is the data vector. Green's Functions are differential equations subject to initial and boundary conditions (Menke, 1989). In a forward model, each $\boldsymbol{G_{ij}}$ coefficient is applied to a known slip on fault patch $\boldsymbol{m_i}$, causing the displacement at $\boldsymbol{d_j}$. The convention for matrix configuration for this manuscript is column by row shown as [column, row]. The problem domain for this project has variable rock properties, thus a published slip dislocation cannot be used because it is based on a homogeneous or layered half-space model and would introduce unknown conversion errors (Hsu et al., 2006; Rhie et al., 2007). Thus, I invert the data to generate the slip distribution for this model. Because the slip distribution over the fault is unknown, I estimate the slip distribution using linear inverse methods. The least-squares solution for the fault-slip distribution, $\boldsymbol{m}^{\text{est}}$, is

$$\boldsymbol{m}^{est} = (\boldsymbol{G}^{\mathrm{T}}\boldsymbol{G})^{-1}\,\boldsymbol{G}^{\mathrm{T}}\boldsymbol{d} \tag{1.9}$$

where $\boldsymbol{G}^{\mathrm{T}}$ is the transpose of $\boldsymbol{G}$ and $(\,)^{-1}$ is the inverse matrix. GPS data can be fit to any well-constructed, justifiable model because there are more parameters than data. I use a Laplacian operator to damp the underdetermined portion of the problem (Menke, 1989) for the first FEM iteration because the subducting slab had a regular geometry on a planar surface (Masterlark and Hughes, 2008; Hughes et al., 2010; Hughes et al., 2011). The smoothing matrix is appended to the $\boldsymbol{G}$ matrix, and a vector of zeros is appended to the $\boldsymbol{d}$ vector. A damping parameter β controls the trade-off between fitting the data and smoothing the fault-slip distribution

$$\begin{bmatrix} \boldsymbol{G} \\ \beta \boldsymbol{L} \end{bmatrix} [\boldsymbol{m}] = \begin{bmatrix} \boldsymbol{d} \\ 0 \end{bmatrix} \tag{1.10}$$

For the second FEM iteration, I use finite element methods for Laplacian smoothing, due to the irregular shape of the subducting slab, to damp the underdetermined portion of the inverse problem. A Global Conductance matrix (GCM) is constructed and appended to the $\boldsymbol{G}$ matrix in the same way as the Laplacian operator (Wang and Anderson, 1982). The GCM ($\boldsymbol{C}$) is constructed using a triangular mesh connecting each slip patch to the surrounding slip patches (see Chapter 6). The forward model is defined in matrix form as

$$\begin{bmatrix} \boldsymbol{G} \\ \beta \boldsymbol{C} \end{bmatrix} [\boldsymbol{m}] = \begin{bmatrix} \boldsymbol{d} \\ 0 \end{bmatrix} \tag{1.11}$$

The trade-off curve represents the trade-off between solution roughness and data misfit (Fig. 1.7), and embodies the non-unique nature of inverse methods. The β-value chosen represents the most reasonable trade-off between complexity and error. The β-value for the FEM could have been chosen based on the error of the GPS measurements or the complexity (number) of slip patches for the SAE. For example, it may be justifiable to assume that the GPS measurements are accurate to within millimeters, and an appropriate β-value could be chosen to reflect this

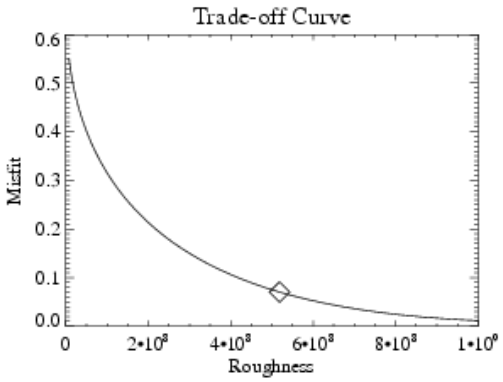

Figure 1.7. A typical trade-off curve represents the trade-off between solution roughness (complexity or large magnitude differences in slip parameters) and misfit (error). The β-value (diamond) is chosen with regards to reasonable error and complexity for the particular problem. Units are in m^2.

information. It may also be reasonable to infer that a 1300 km rupture may have multiple slip patches but not too many, and an acceptable β-value can be chosen to reflect this assumption.

5. Model Verification

Once the slip distribution is estimated from geodetic data and inverse methods, then the slip distribution is applied to load the forward FEM. The results of this forward model are compared to an independent data set which is a data set which is not used in the inversion to verify the model for both coseismic and postseismic deformation. The independent data set of zero-displacement locations is one that is instrumentally measured (not interpreted) and precise.

This project differs from previous FEMs because of the unprecedented signal-to-noise ratio of GPS measurements and because it can be further constrained by tsunami run-up (Moore et al., 2007) and coral head uplift measurements (Natawidjaja et al., 2004; Meltzner et al., 2006; Rajendran et al., 2007; Kayanne et al., 2007). The GPS data are used in the inverse model, so this data set cannot be used to verify the model (Fig. 1.8). The tsunami run-up data are driven by seafloor deformation, which was caused by the slip distribution. Tsunami run-up data could have been used to verify the slip model, but these measurements are not precise. Coral head measurements are similar to tsunami run-up data because these data are measurements, but are not precise. However, the hingeline, based on remote sensing, (line of zero displacement) is accurate and precise on the scale of verification purposes (error within the line on map, Fig. 1.9). Because the hingeline

is not used in the model inversion, it serves as an excellent data set for model verification.

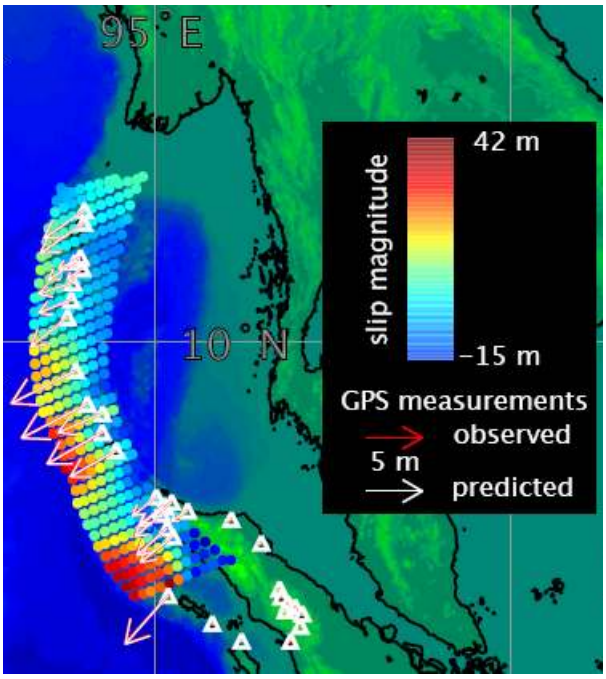

Figure 1.8. Dip-slip distribution map with GPS vectors for fully 3D FEM. The red arrows are observed GPS vectors, the white arrows are predicted GPS vectors, and the white triangles are GPS site locations.

SUMMARY OF PROJECT

The first model of this project is constructed using the southern Sumatra cross-section (Fig. 1.2, A-A') propagated along strike of the SASZ (Masterlark and Hughes, 2008). The predicted slip distribution is shown in Figure 1.10. This dislocation predicts a maximum of 5.4 m of uplift and 3.5 m of subsidence (Fig. 1.9). The predicted deformation fits the GPS measurements to within one standard deviation (Fig. 1.10). Other investigators have predicted a maximum of 2-3 m of uplift or subsidence (Chlieh et al., 2007).

Postseismic deformation results indicate that poroelastic deformation is substantial due to changes in pore pressure (MPa scale) over a large region. Changes in Coulomb stress are on the MPa scale and, because changes in pore pressure are on the same scale as the normal stress and shear stress, pore pressure changes are substantial enough to have triggered an additional earthquake (Toda et al., 1998). In addition to being substantial in Coulomb stress changes, poroelastic

deformation may better account for horizontal displacement as opposed to viscoelastic deformation or afterslip (Paul et al., 2007).

The results of this study suggest that most of the postseismic deformation is due to viscoelastic deformation. Viscoelastic surface deformation is predicted to be on the order of meters over tens of years. Some studies have attributed this surface deformation to afterslip (Chlieh et al., 2007) while other studies indicate that viscoelastic deformation can account for about 0.5-1 meter of deformation over a period of 2-3 years (Pollitz et al., 2006; Paul et al., 2007).

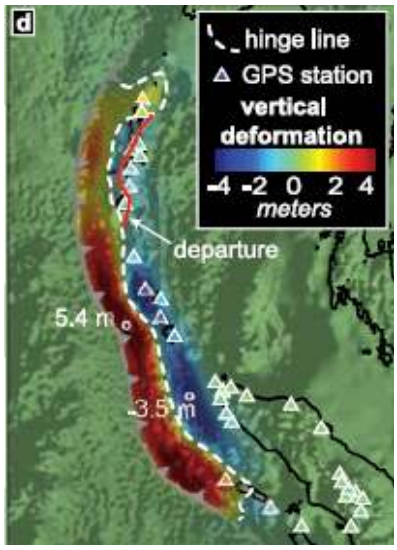

Figure 1.9. Coseismic vertical deformation map (adapted from Masterlark and Hughes, 2008) based on single cross-section model. The triangles are the locations of GPS stations. The dashed white line is the hinge line which represents zero vertical displacement. The solid red line indicates a departure of the single cross-section model compared to measured coral head displacement data. The maximum uplift predicted is 5.4 m and the maximum subsidence predicted is 3.5 m.

Although the relatively cold, stiff subducting slab is a first order feature of a subduction zone, published models simulate subduction zone deformation as a thrust fault embedded in a homogeneous (HEHS) or layered elastic half-space (LEHS) (Okada, 1992; Hsu et al., 2006). Half-space or layered half-space models do not represent geologic features accurately at the subduction zone scale. My fully 3D FEM is unique because it incorporates a 3D geologic structure.

The techniques used in this study are suitable for testing the hypothesis; the timing of the NE was mechanically influenced by the SAE, by using both forward and inverse models to examine the coseismic and postseismic deformation including

poroelastic deformation, viscoelastic deformation, and afterslip, while simultaneously accounting for the known geologic structure of the SASZ.

I invoke a modeling protocol to guide the modeling process (Masterlark and Hughes, 2008; Hughes et al., 2010). This protocol involves five steps; purpose, conceptual model, design, calibration, and verification. The modeling process is iterative, and each step leads to the next and/or reverts back to a previous step for modification (Fig. 1.3).

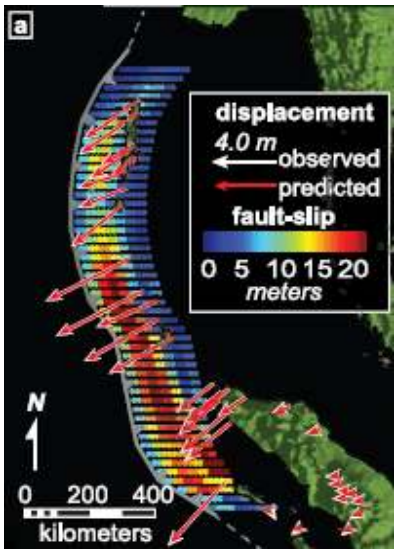

Figure 1.10. Slip distribution map with GPS vectors (adapted from Masterlark and Hughes, 2008) based on single cross-section model. The red arrows are predicted GPS vectors based on the single cross-section model. The white arrows are observed GPS vectors. The single cross-section matches the vectors better to the south where the cross-section was based.

The results of the single cross-section FEM indicate that this type of model is capable of quantitatively analyzing the 2004 and 2005 earthquakes, and the FEM predicts higher magnitude uplift and subsidence when compared to a half-space model (Fig. 1.11). Further analysis of the single cross-section FEM show that the NE was triggered by the SAE and was actually sped up by the change in pore pressures due to the SAE. The results of the fully 3D FEM show that the computed slip distribution is about 10 m higher in magnitude than our previous FEM. Additionally, the 3D FEM has two main nucleations of maximum slip within about 5 km of depth generating a larger maximum uplift (Fig. 1.12). The final results of this project have large direct implications for tsunami modelers and other

geodetic modelers of not only the SASZ, but also other subduction zones around the world where finite element modeling can be implemented.

CONNECTION BETWEEN JOURNAL ARTICLES

The results of this study have been published in several journals including, *Bollettino di Geofisica: Teorica ed Applicata* (Chapter 2) (Hughes and Masterlark, 2008), *Geophysical Research Letters* (Chapter 3) (Masterlark and Hughes, 2008), *Earth and Planetary Science Letters* (Chapter 4) (Hughes et al., 2010), and *Lithosphere* (Chapter 5) (Hughes et al., 2011) (Appendix). Each paper is included as a separate chapter starting with Chapter 2 and ending with Chapter 5. Chapter 6 will be submitted to a peer-reviewed scientific journal. The chapters show the progression through time as the project developed. Chapter 2 is the start of the project, and Chapter 6 is the completion of the project. However, further analyses and studies can be and will be built upon this work including analysis of subsequent earthquakes of the SAE on and near the rupture surface of the SAE and including tsunami models and sequences of later earthquakes in Indonesia.

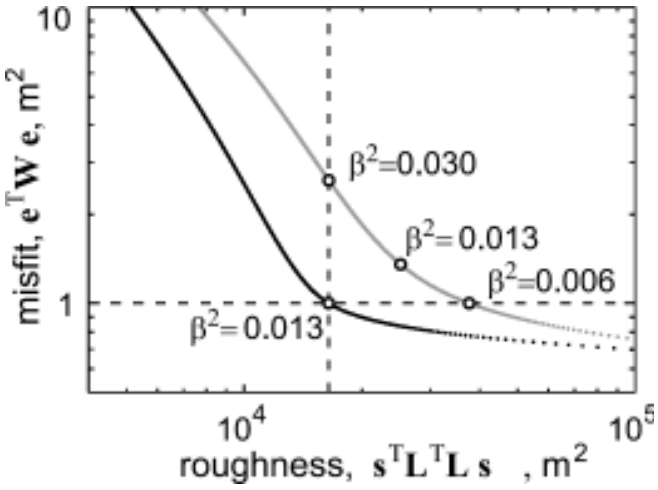

Figure 1.11. Trade-off curve for FEM and half-space models (adapted from Masterlark and Hughes, 2008). The black curve represents the FEM and the gray curve represents the half-space model. The comparison of the two curves indicates that the FEM solution has less data misfit and less complexity, thus making the FEM solution better.

Chapters 2, 3, 4, and 5

were designed and completed using the single cross-section FEM. These chapters demonstrate 1) that the SAE slip distribution depends on the data set used (e.g., near-field GPS, far-field GPS, and tsunami run-up measurements), 2) how to complete a 3D FEM using a modeling protocol, 3) how the magnitude of surface deformation differs using a single cross-section FEM instead of a HEHS or LEHS, 4) how to analyze pore pressure changes and Coulomb stress from a FEM, and 5) what can be learned from this type of analysis.

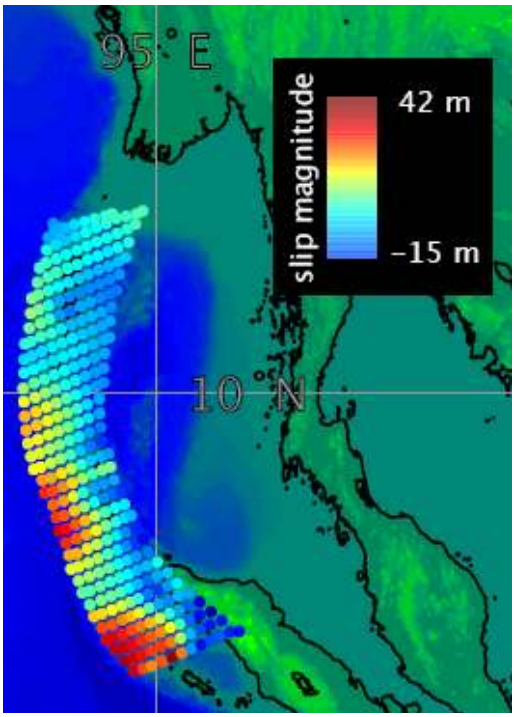

Figure 1.12. Slip distribution generated by finite element, linear inverse methods. Each dot represents a slip patch shown by diagram in Fig. 6.6 of Chapter 6. Colors represent total amount of slip. Distribution due to dip-slip motion.

Chapter 6 was achieved using the fully 3D FEM. This chapter demonstrates 1) how to complete a 3D FEM using a modeling protocol, 2) how to use finite element methods to dampen an underdetermined numerical problem, 3) the results of a model are dependent upon the parameters included and excluded in the analysis, and 4) what can be learned from this type of analysis.

The main findings of this study are that the near-field GPS data generate a more reliable slip distribution compared to far-field GPS data, both of the FEMs yield larger displacements of the seafloor than other published models which is a required result for tsunami modelers, and that pore pressure changes are on the

same order as shear stress and normal stress which has large implications for ultimately determining the change in Coulomb stress (Eq. 1.1).

REFERENCES

Ammon, C.J., Ji, C., Thio, H.K., Robinson. D., Ni, S., Hjorleifsdottir, V., Kanamori, H., Lay, T., Das, S., Helmberger, D., Ichinose, G., Polet, J., and Wald, D., 2005, Rupture process of the 2004 Sumatra-Andaman Earthquake: Science, v. 308, p. 1133–1139, doi: 10.1126/science.1112260.

Anu, R., and Rajendran, K., 2006, Co-seismic deformation along the Andaman-Nicobar arc based on GPS data and ground observations: Extended Abstract, XVIII Kerala Science Congress, p. 226-228.

Banerjee, P., Pollitz, F., Nagarajan, B., and Bürgmann, R., 2007, Coseismic slip distributions of the 26 December 2004 Sumatra-Andaman and 28 March 2005 Nias earthquakes from GPS static offsets: Bulletin of the Seismological Society of America, v. 97, p. S86-S102, doi: 10.1785/0120050609.

Barber, A. J., Crow, M.J., and Milsom, J.S., 2005, Sumatra: Geology, Resources, and Tectonic Evolution: London, Geological Society, 290 p.

Bilek, S.L., 2007, Using earthquake source durations along the Sumatra-Andaman subduction system to examine fault-zone variations: Bulletin of the Seismological Society of America, v. 97, p. S62-S70, doi: 10.1785/0120050622.

Bird, P., 2003, An updated digital model of plate boundaries: G-Cubed, v. 4, doi: 10.1029/2001GC000252.

Catherine, J.K., Gahalaut, V.K., and Sahu, V.K., 2005, Constraints on rupture of the December 26, 2004, Sumatra earthquake from far-field GPS observations: Earth and Planetary Science Letters, v. 237, p. 673-679, doi: 10.1026/j.epsl.2005.07.012.

Chatterjee, S., Bhattacharyya, R., and Majumdar, T.J., 2007, Generation and study of high-resolution satellite gravity over the Sumatran earthquake region: International Journal of Remote Sensing, v. 28, p. 2915-2925, doi: 10.1080/01431160601091829.

Chen, J.L., Wilson, C.R., Tapley, B.D., and Grand, S., 2007, GRACE detects coseismic and postseismic deformation from the Sumatra-Andaman earthquake: Geophysical Research Letters, v. 34, doi: 10.1029/2007GL030356.

Chlieh, M., Avouac, J.-P., Hjorleifsdottir, V., Song, T.-R.A., Ji, C., Sieh, K., Sladen, A., Hebert, H., Prawirodirdjo, L., Bock, Y., and Galetzka, J., 2007, Coseismic slip and afterslip of the great Mw 9.15 Sumatra-Andaman earthquake of 2004: Bulletin of the Seismological Society of America, v. 97, p. S152– S173, doi: 10.1785/0120050631.

Conder, J.A., Wiens, D.A., and Morris, J., 2002, On the decompression melting structure at volcanic arcs and back-arc spreading centers: Geophysical Research Letters, v. 29, doi: 10.1029/2002GL015390.

Dasgupta, S., Mukhopadhyay, M., Bhattacharya, A., and Jana, T.K., 2003, The geometry of the Burmese-Andaman subducting lithosphere: Journal of Seismology, v. 7, p. 155-174.

Delescluse, M., and Chamot-Rooke, N., 2007, Instantaneous deformation and kinematics of the India-Australia plate: Geophysical Journal International, v. 168, p. 818-842, doi: 10.1111/j.1365-246X.2006.03181.x.

Earnest, A., Rajendran, C.P., Rajendran, K., Anu, R., Arun, G.M., and Mohan, P.M., 2005, Near-field observations on the co-seismic deformation associated with the 26 December 2004 Andaman-Sumatra earthquake: Current Science, v. 89, p. 1237-1244.

Engdahl, E.R., Villaseñor, A., DeShon, H.R., and Thurber, C.H., 2007, Teleseismic relocation and assessment of seismicity (1918–2005) in the region of the 2004 Mw 9.0 Sumatra-Andaman and 2005 Mw 8.6 Nias Island great earthquakes: Bulletin of the Seismological Society of America, v. 97, p. S43–S61, doi: 10.1785/0120050614.

Fine, I.V., Rabinovich, A.B., and Thomson, R.E., 2005, The dual source region for the 2004 Sumatra tsunami: Geophysical Research Letters, v. 32, doi: 10.1029/GL023521.

Freed, A.M., Bürgmann, R., Calais, E., Freymueller, J., and Hreinsdóttir, S., 2006, Implications of deformation following the 2002 Denali, Alaska, earthquake for postseismic relaxation processes and lithospheric rheology: Journal of Geophysical Research, v. 111, doi: 10.1029/2005JB003894.

Freed, A.M., and Lin, J., 2001, Delayed triggering of the 1999 Hector Mine earthquake by viscoelastic stress transfer: Nature, v. 411, p. 180-183.

Fujii, Y., and Satake, K., 2007, Tsunami source of the 2004 Sumatra-Andaman earthquake inferred from tide gauge and satellite data: Bulletin of the Seismological Society of America, v. 97, p. S192-S207, doi: 10.1785/0120050613.

Gahalaut, V., and Gahalaut, K., 2007, Burma plate motion: Journal of Geophysical Research, v. 112, doi: 10.1029/JB004928.

Gahalaut, V.K., Nagarajan, B., Catherine, J.K., and Kumar, S., 2006, Constraints on 2004 Sumatra-Andaman earthquake rupture from GPS measurements in Andaman-Nicobar Islands: Earth and Planetary Science Letters, v. 242, p. 365-374, doi: 10.1016/j.epsl.200511.051.

Geist, E.L., 2005, Tsunami simulation image: The Wave that Shook the World, NOVA, http://www.pbs.org/wgbh/nova/tsunami/.

Geist, E.L., Titov, V.V., Arcas, D., Pollitz, F.F., and Bilek, S.L., 2007, Implications of the 26 December 2004 Sumatra-Andaman earthquake of tsunami forecast and assessment models for great subduction-zone earthquakes: Bulletin of the Seismological Society of America, v. 97, p. S249– S270, doi: 10.1785/0120050619.

Grilli M.ASCE, S.T., Ioualalen, M., Asavanant, J., Shi, F., Kirby M.ASCE, J.T., and Watts, P., 2007, Source constraints and model simulation of the December 26, 2004, Indian Ocean tsunami: Journal of Waterway, Port, Coastal, and Ocean Engineering, v. 133, p. 414-428, doi: 10.1061/(ASCE)0733-950X.

Hall, R., 2002, Cenozoic geological and plate tectonic evolution of SE Asia and the SW Pacific: Computer-based reconstructions, model and animations: Journal of Asian Sciences, v. 20, p. 353-431.

Han, S.-C., Ray, R.D., and Luthcke, S.B., 2007, Ocean tidal solutions in Antarctica from GRACE inter-satellite tracking data: Geophysical Research Letters, v. 34, doi: 10.1029/2007GL031540.

Hanson, J.A., Reasoner, C.L., and Bowman, J.R., 2007, High-frequency tsunami signals of the great Indonesian earthquakes of 26 December 2004 and 28 March 2005: Bulletin of the Seismological Society of America, v. 97, p. S232-S248, doi: 10.1785/0120050607.

Hébert, H., Sladen, A., and Schindelé, F., 2007, Numerical modeling of the great 2004 Indian Ocean tsunami: Focus on the Mascarene Islands: Bulletin of the Seismological Society of America, v. 97, p. S208-S222, doi: 10.1785/0120050611.

Hsu, Y.-J., Simons, M., Avouac, J.-P., Galetzka, J., Sieh, K., Chlieh, M., Natawidjaja, D., Prawirodirdjo, L., and Bock, Y., 2006, Frictional afterslip following the 2005 Nias-Simeulue earthquake, Sumatra: Science, v. 312, p. 1921-1926, doi: 10.1126/science.1126960.

Hughes, K.L.H., and Masterlark, T., 2008, Slip distribution for the 2004 Sumatra-Andaman earthquake constrained by both GPS data and tsunami run-up measurements: Bollettino di Geofisica: Teorica ed Applicata, v. 49, p. 165-169.

Hughes, K.L.H., Masterlark, T., and Mooney, W.D., 2010, Poroelastic stress-triggering of the 2005 M8.7 Nias earthquake by the 2004 M9.2 Sumatra-Andaman earthquake: Earth and Planetary Science Letters, v. 293, p. 289-299, doi: 10.1016/j.epsl.2010.02.043.

Hughes, K.L.H., Masterlark, T., and Mooney, W.D., 2011, Pore-fluid migration and the timing of the 2005 M8.7 Nias earthquake, Lithosphere, v. 3, p. 170-172, doi: 10.1130/L109.1.

Hutchison, C.S., 1989, Geological Evolution of South-East Asia: Oxford, Oxford University Press, 368 p.

Ishii, M., Shearer, P.M., Houston, H., and Vidale, J.E., 2007, Teleseismic *P* wave imaging of the 26 December 2004 Sumatra-Andaman and 28 March 2005 Sumatra earthquake ruptures using the Hi-net array: Journal of Geophysical Research, v. 112, doi: 10.1029/2006JB004700.

Jade, S., Ananda, M.B., Kumar, P.D., and Banerjee, S., 2005, Co-seismic and post-seismic displacements in Andaman and Nicobar Islands from GPS measurements: Current Science, v. 88, p. 1980-1984.

Johnson, K.M., and Segall, P., 2004, Viscoelastic earthquake cycle models with deep stress-driven creep along the San Andreas fault system: Journal of Geophysical Research, v. 109, doi: 10.1029/2004JB003096.

Kayanne, H., Ikeda, Y., Echigo, T., Shishikura, M., Kamataki, T., Satake, K., Malik, J.N., Basir, S.R., Chakrabortty, G.K., and Roy, A.K.G., 2007, Coseismic and postseismic creep in the Andaman Islands associated with the 2004 Sumatra-Andaman earthquake: Geophysical Research Letters, v. 34, doi: 10.1029/2006GL028200.

Kenner, S.J., and Segall, P., 2000, Postseismic deformation following the 1906 San Francisco earthquake: Journal of Geophysical Research, v. 105, p. 13195-13209.

Kieckhefer, R.M., Shor Jr., G.G., Curray, J.R., Sugiarta, W., and Hehuwat, F., 1980, Seismic refraction studies of the Sunda trench and forearc basin: Journal of Geophysical Research, v. 85, p. 863– 889.

Kopp, H., Flueh, E.R., Klaeschen, D., Bialas, J., and Reichert, C., 2001, Crustal structure of the central Sunda margin at the onset of oblique subduction: Geophysical Journal International, v. 147, p. 449-474.

Kopp, H., Klaeschen, D., Flueh, E.R., Bialas, J., and Reichert, C., 2002, Crustal structure of the Java margin from seismic wide-angle and multichannel reflection data: Journal of Geophysical Research, v. 107, doi: 10.1029/2000JB000095.

Kopp, H., and Kukowski, N., 2003, Backstop geometry and accretionary mechanics of the Sunda margin: Tectonics, v. 22, doi: 10.1029/2002TC001420.

Lovholt, F., Bungum, H., Harbitz, C.B., Glimsdal, S., Lindholm, C.D., and Pedersen, G., 2006, Earthquake related tsunami hazard along the western coast of Thailand: Natural Hazards and Earth System Sciences, v. 6, p. 979-997.

Masterlark, T., and Hughes, K.L.H., 2008, Next generation of deformation models for the 2004 M9 Sumatra-Andaman earthquake: Geophysical Research Letters, v. 35, doi: 10.1029/2008GL035198.

Masterlark, T., and Wang, H., 2000, Poroelastic coupling between the 1992 Landers and Big Bear earthquakes: Geophysical Research Letters, v. 27, p. 3647-3650.

Masterlark, T., and Wang, H.F., 2002, Transient stress-coupling between the 1992 Landers and 1999 Hector Mine, California, earthquakes: Bulletin of the Seismological Society of America, v. 92, p. 1470-1486.

McCaffrey, R., Zwick, P.C., Bock, Y., Prawirodirdjo, L., Genrich, J.F., Stevens, C.W., Puntodewo, S.S.O., and Subarya, C., 2000, Strain partitioning during oblique plate convergence in northern Sumatra: Geodetic and seismologic constraints and numerical modeling: Journal of Geophysical Research, v. 105, p. 28363-28376.

Meltzner, A.J., Sieh, K., Abrams, M., Agnew, D.C., Hudnut, K.W., Avouac, J.-P., and Natawidjaja, D.H., 2006, Uplift and subsidence associated with the great Aceh-Andaman earthquake of 2004: Journal of Geophysical Research, v. 111, doi: 10.1029/2005JB003891.

Menke, W., 1989, Geophysical Data Analysis: Discrete Inverse Theory: San Diego, Academic Press, 289 p.

Moore, G.F., Bangs, N.L., Taira, A., Kuramoto, S., Pangborn, E., and Tobin, H.J., 2007, Three-dimensional splay fault geometry and implications for tsunami generation: Science, v. 318, p. 1128-1131, doi: 10.1126/science.1147195.

Moran, K., and Tappin, D., 2006, SEATOS 2005 Cruise Report: Sumatra Earthquake and Tsunami Offshore Survey (SEATOS): http://ocean.oce.uri.edu/seatos.

Mukhopadhyay, M., 1988, Gravity anomalies and deep structure of the Andaman arc: Marine Geophysical Researches, v. 9, p. 197-210.

Natawidjaja, D.H., Sieh, K., Ward, S.N., Cheng, H., Edwards, R.L., Galetzka, J., and Suwargadi, W., 2004, Paleogeodetic records of seismic and aseismic subduction from central Sumatran microatolls, Indonesia: Journal of Geophysical Research, v. 109, doi: 10.1029/2003JB002398.

Okada, Y., 1992, Internal deformation due to shear and tensile faults in a half-space: Bulletin of the Seismological Society of America, v. 82, p. 1018–1040.

Page, B.G.N., Bennett, J.D., Cameron, N.R., Bridge, D.McC., Jeffery, D.H., Keats, W., and Thaib, J., 1979, A review of the main structural and magmatic features of northern Sumatra: Journal of the Geological Society of London, v. 136, p. 569-579.

Pal, T., Chakraborty, P.P., Gupta, T.D., and Singh, C.D., 2003, Geodynamic evolution of the outer-arc--forearc belt in the Andaman Islands, the central part of the Burma-Java subduction complex: Geological Magazine, v. 140, p. 289-307, doi: 10.1017/S0016756803007805.

Panet, I., Mikhailov, V., Diament, M., Pollitz, F., King, G., de Viron, O., Holschneider, M., Biancale, R., and Lemoine, J.-M., 2007, Coseismic and post-seismic signatures of the Sumatra 2004 December and 2005 March earthquakes in GRACE satellite gravity: Geophysical Journal International, v. 171, p. 177-190, doi: 10.1111/j.1365-246X.2007.03525.x.

Park, J., Song, T.-R.A., Tromp, J., Okal, E., Stein, S., Roult, G., Clevede, E., Laske, G., Kanamori, H., Davis, P., Berger, J., Braitenberg, C., Van Camp, M., Lei, X., Sun, H., Xu, H., and Rosat, S., 2005, Earth's free oscillations excited by the 26 December 2004 Sumatra-Andaman earthquake: Science, v. 308, p. 1139-1144, doi: 10.1126/science.1112305.

Parsons, T., 2002, Post-1906 stress recovery of the San Andreas fault system calculated from three-dimensional finite element analysis: Journal of Geophysical Research, v. 107, doi: 10.1029/2001JB001051.

Paul, J., Lowry, A.R., Bilham, R., Sen, S., and Smalley Jr., R., 2007, Postseismic deformation of the Andaman Islands following the 26 December, 2004 great Sumatra-Andaman earthquake: Geophysical Research Letters, v. 34, doi: 10.1029/2007GL031024.

Pesicek, J.D., Thurber, C.H., Widiyantoro, S., Engdahl, E.R., and DeShon, H.R., 2008, Complex slab subduction beneath northern Sumatra: Geophysical Research Letters, v. 35, doi: 10.1029/2008GL035262.

Pesicek, J.D., Thurber, C.H., Widiyantoro, S., Zhang, H., DeShon, H.R., and Engdahl, E.R., 2010, Sharpening the tomographic image of the subducting slab below Sumatra, the Andaman Islands and Burma: Geophysical Journal International, v. 182, p. 433-453, doi: 10.1111/j.1365-246X.2010.04630.x.

Pollitz, F.F., Bürgmann, R., and Banerjee, P., 2006, Post-seismic relaxation following the great 2004 Sumatra-Andaman earthquake on a compressible self-gravitating Earth: Geophysical Journal International, v. 167, p. 397-420, doi: 10.1111/j.1365-246X.2006.03018.x.

Rajendran, C.P., Rajendran, K., Anu, R., Earnest, A., Machado, T., Mohan, P.M., and Freymueller, J., 2007, Crustal deformation and seismic history associated with the 2004 Indian Ocean earthquake: A perspective from the Andaman-Nicobar Islands: Bulletin of the Seismological Society of America, v. 97, p. S174-S191, doi: 10.1785/0120050630.

Rastogi, B.K., and Jaiswal, R.K., 2006, A catalog of tsunamis in the Indian Ocean: Science of Tsunami Hazards, v. 25, p. 128-143.

Rhie, J., Dreger, D., Bürgmann, R., and Romanowicz, B., 2007, Slip of the 2004 Sumatra-Andaman earthquake from joint inversion of long-period global seismic waveforms and GPS static offsets: Bulletin of the Seismological Society of America, v. 97, p. S115-S127, doi: 10.1785/0120050620.

Richards, S., Lister, G., and Kennett, B., 2007, A slab in depth: Three-dimensional geometry and evolution of the Indo-Australian plate: G-Cubed, v. 8, doi: 10.1029/2007GC001657.

Schmitt, S.V., DeMets, C., Stock, J., Sánchez, O., Márquez-Azúa, B., and Reyes, G., 2007, A geodetic study of the 2003 January 22 Tecomán, Colima, Mexico earthquake: Geophysical Journal International, v. 169, p. 389–406, doi: 10.1111/j.1365-246X.2006.03322.x.

Seno, T., and Hirata, K., 2007, Did the 2004 Sumatra-Andaman earthquake involve a component of tsunami earthquakes?: Bulletin of the Seismological Society of America, v. 97, p. S296-S306, doi: 10.1785/0120050615.

Simons, W.J.F., Socquet, A., Vigny, C., Ambrosius, B.A.C., Abu, S.H., Promthong, C., Subarya, C., Sarsito, D.A., Matheussen, S., Morgan, P., and Spakman, W., 2007, A decade of GPS in southeast Asia: Resolving Sundaland motion and boundaries, Journal of Geophysical Research, v. 112, doi: 10.1029/2005JB003868.

Song, T.-R.A., and Simons, M., 2003, Large trench-parallel gravity variations predict seismogenic behavior in subduction zones: Science, v. 301, p. 630-633, doi: 10.1126/science.1085557.

Stein, S., and Okal, E.A., 2007, Ultralong period seismic study of the December 2004 Indian Ocean earthquake and implications for regional tectonics and the subduction process: Bulletin of the Seismological Society of America, v. 97, p. S279-S295, doi: 10.1785/0120050617.

Subarya, C., Chlieh, M., Prawirodirdjo, L., Avouac, J.-P., Bock, Y., Sieh, K., Meltzner, A.J., Natawidjaja, D.H., and McCaffrey, R., 2006, Plate-boundary deformation associated with the great Sumatra-Andaman earthquake: Nature, v. 440, p. 46–51, doi: 10.1038/nature04522.

Toda, S., Stein, R.S., Reasenberg, P.A., Dieterich, J.H., and Yoshida, A., 1998, Stress transferred by the 1995 M_w = 6.9 Kobe, Japan, shock: Effect on aftershocks and future earthquake probabilities: Journal of Geophysical Research, v. 103, p. 24543-24565.

U.S. Geological Survey - Earthquake Hazards Program, 2010, Slab Models for Subduction Zones, http://earthquake.usgs.gov/research/data/slab/#models, date accessed 25 April 2010, date updated 5 November 2009.

Vigny, C., Simons, W.J.F., Abu, S., Bamphenyu, R., Satirapod, C., Coosakul, N., Subarya, C., Socquet, A., Omar, K., Abidin, H.Z., Ambrosius, B.A.C., 2005, Insight into the 2004 Sumatra-Andaman earthquake from GPS measurements in Southeast Asia: Nature, v. 436, p. 201– 206, doi: 10.1028/nature03937.

Waltham, T., 2005, The Asian tsunami disaster, December 2004: Geology Today, v. 21, p. 22-26.

Wang, H.F., 2000, Theory of Linear Poroelasticity: With Applications to Geomechanics: Princeton, Princeton University Press, 287 p.

Wang, H.F., and Anderson, M.P., 1982, Introduction to Groundwater Modeling: Finite Difference and Finite Element Methods: San Diego, Academic Press, 237 p.

Wang, J., and Ye, Z.-R., 2006, Dynamic modeling for crustal deformation in the China: Comparisons between the theoretical prediction and the recent GPS data: Physics of the Earth and Planetary Interiors, v. 155, p. 201-207, doi: 10.1016/j.pepi.2005.11.003.

Weissel, J.K., 1981, Magnetic lineations in marginal basins of the western Pacific: Philosophical Transcriptions of the Royal Society of London, v. 300, p. 223-247.

Williams, C.A., and McCaffrey, R., 2001, Stress rates in the central Cascadia subduction zone inferred from an elastic plate model: Geophysical Research Letters, v. 28, p. 2125-2128.

APPENDIX

The following are the copyright release letters. These letters give me permission to include the published works in my dissertation. I also recognize this permission in the Acknowledgements section of the dissertation and at the beginning of each chapter where the work has been previously published.

Bollettino di Geofisica: Teorica ed Applicata

Letter of Permission

Dario Slejko <dslejko@ogs.trieste.it> **Wed, Apr 21, 2010 at 8:58 AM**
To: klhhughes@gmail.com

Cite as:
Hughes K.L.H. and Masterlark T.; 2008: Slip distribution for the 2004 Sumatra - Andaman earthquake constrained by both GPS data and tsunami run-up measurements. Boll. Geof. Teor. Appl., 49, n. 2 supplement, 165-170.
With this letter we give you the permission to reproduce the entire article giving reference of the journal.
Best regards.
Dario Slejko
BGTA Publishing Editor

Dario Slejko
Istituto Nazionale di Oceanografia e di Geofisica Sperimentale
Borgo Grotta Gigante, 42c
34010 Sgonico (TS)
Tel. +39 040 2140248
Fax +39 040 327307
dslejko@ogs.trieste.it

Geophysical Research Letters

Letter of Permission

Michael Connolly <MConnolly@agu.org> **Mon, Apr 19, 2010 at 12:38 PM**
To: "klhhughes@gmail.com" <klhhughes@gmail.com>

We are pleased to grant permission for the use of the material requested for inclusion in your thesis. The following non-exclusive rights are granted to AGU authors:

- All proprietary rights other than copyright (such as patent rights).
- The right to present the material orally.
- The right to reproduce figures, tables, and extracts, appropriately cited.
- The right to make hard paper copies of all or part of the paper for classroom use.
- The right to deny subsequent commercial use of the paper.

Further reproduction or distribution is not permitted beyond that stipulated. The copyright credit line should appear on the first page of the article or book chapter. The following must also be included, "Reproduced by permission of American Geophysical Union." To ensure that credit is given to the original source(s) and that authors receive full credit through appropriate citation to their papers, we recommend that the full bibliographic reference be cited in the reference list. The standard credit line for journal articles is: "Author(s), title of work, publication title, volume number, issue number, citation number (or page number(s) prior to 2002), year. Copyright [year] American Geophysical Union."

If an article was placed in the public domain, in which case the words "Not subject to U.S. copyright" appear on the bottom of the first page or screen of the article, please substitute "published" for the word "copyright" in the credit line mentioned above.

Copyright information is provided on the inside cover of our journals. For permission for any other use, please contact the AGU Publications Office at AGU, 2000 Florida Ave., N.W., Washington, DC 20009.

Michael Connolly

American Geophysical Union

2000 Florida Avenue, NW

Washington, DC 20009

202-777-7365

mconnolly@agu.org

Earth and Planetary Science Letters

Letter of Permission

ELSEVIER LICENSE
TERMS AND CONDITIONS

Jun 27, 2011

This is a License Agreement between Kristin LH Hughes ("You") and Elsevier ("Elsevier") provided by Copyright Clearance Center ("CCC"). The license consists of your order details, the terms and conditions provided by Elsevier, and the payment terms and conditions.

All payments must be made in full to CCC. For payment instructions, please see information listed at the bottom of this form.

Supplier	Elsevier Limited The Boulevard,Langford Lane Kidlington,Oxford,OX5 1GB,UK
Registered Company Number	1982084
Customer name	Kristin LH Hughes
Customer address	201 7th Ave Tuscaloosa, AL 35487
License number	2404370097754
License date	Apr 08, 2010
Licensed content publisher	Elsevier
Licensed content publication	Earth and Planetary Science Letters
Licensed content title	Poroelastic stress-triggering of the 2005 M8.7 Nias earthquake by the 2004 M9.2 Sumatra–Andaman earthquake
Licensed content author	Kristin L.H. Hughes, Timothy Masterlark, Walter D. Mooney
Licensed content date	23 March 2010
Licensed content volume number	n/a
Licensed content issue number	n/a
Number of pages	1
Start Page	
End Page	
Type of Use	Thesis / Dissertation
Requestor type	NOTSELECTED
Intended publisher of new work	NOTSELECTED
Other institution name	NOTSELECTED

Portion	Full article
Format	Both print and electronic
Are you the author of this Elsevier article?	Yes
Order reference number	
Publisher of new work	NOTSELECTED
Elsevier VAT number	GB 494 6272 12
Permissions price	0.00 USD
Value added tax 0.0%	0.00 USD / GBP
Total	0.00 USD
Terms and Conditions	

INTRODUCTION

1. The publisher for this copyrighted material is Elsevier. By clicking "accept" in connection with completing this licensing transaction, you agree that the following terms and conditions apply to this transaction (along with the Billing and Payment terms and conditions established by Copyright Clearance Center, Inc. ("CCC"), at the time that you opened your Rightslink account and that are available at any time at http://myaccount.copyright.com).

GENERAL TERMS

2. Elsevier hereby grants you permission to reproduce the aforementioned material subject to the terms and conditions indicated.

3. Acknowledgement: If any part of the material to be used (for example, figures) has appeared in our publication with credit or acknowledgement to another source, permission must also be sought from that source. If such permission is not obtained then that material may not be included in your publication/copies. Suitable acknowledgement to the source must be made, either as a footnote or in a reference list at the end of your publication, as follows:

"Reprinted from Publication title, Vol /edition number, Author(s), Title of article / title of chapter, Pages No., Copyright (Year), with permission from Elsevier [OR APPLICABLE SOCIETY COPYRIGHT OWNER]." Also Lancet special credit - "Reprinted from The Lancet, Vol. number, Author(s), Title of article, Pages No., Copyright (Year), with permission from Elsevier."

4. Reproduction of this material is confined to the purpose and/or media for which permission is hereby given.

5. Altering/Modifying Material: Not Permitted. However figures and illustrations may be altered/adapted minimally to serve your work. Any other abbreviations, additions, deletions and/or any other alterations shall be made only with prior written

authorization of Elsevier Ltd. (Please contact Elsevier at permissions@elsevier.com)

6. If the permission fee for the requested use of our material is waived in this instance, please be advised that your future requests for Elsevier materials may attract a fee.

7. Reservation of Rights: Publisher reserves all rights not specifically granted in the combination of (i) the license details provided by you and accepted in the course of this licensing transaction, (ii) these terms and conditions and (iii) CCC's Billing and Payment terms and conditions.

8. License Contingent Upon Payment: While you may exercise the rights licensed immediately upon issuance of the license at the end of the licensing process for the transaction, provided that you have disclosed complete and accurate details of your proposed use, no license is finally effective unless and until full payment is received from you (either by publisher or by CCC) as provided in CCC's Billing and Payment terms and conditions. If full payment is not received on a timely basis, then any license preliminarily granted shall be deemed automatically revoked and shall be void as if never granted. Further, in the event that you breach any of these terms and conditions or any of CCC's Billing and Payment terms and conditions, the license is automatically revoked and shall be void as if never granted. Use of materials as described in a revoked license, as well as any use of the materials beyond the scope of an unrevoked license, may constitute copyright infringement and publisher reserves the right to take any and all action to protect its copyright in the materials.

9. Warranties: Publisher makes no representations or warranties with respect to the licensed material.

10. Indemnity: You hereby indemnify and agree to hold harmless publisher and CCC, and their respective officers, directors, employees and agents, from and against any and all claims arising out of your use of the licensed material other than as specifically authorized pursuant to this license.

11. No Transfer of License: This license is personal to you and may not be sublicensed, assigned, or transferred by you to any other person without publisher's written permission.

12. No Amendment Except in Writing: This license may not be amended except in a writing signed by both parties (or, in the case of publisher, by CCC on publisher's behalf).

13. Objection to Contrary Terms: Publisher hereby objects to any terms contained in any purchase order, acknowledgment, check endorsement or other writing prepared by you, which terms are inconsistent with these terms and conditions or CCC's Billing and Payment terms and conditions. These terms and conditions, together with CCC's Billing and Payment terms and conditions (which are incorporated herein), comprise the entire agreement between you and publisher (and CCC) concerning this licensing

transaction. In the event of any conflict between your obligations established by these terms and conditions and those established by CCC's Billing and Payment terms and conditions, these terms and conditions shall control.

14. Revocation: Elsevier or Copyright Clearance Center may deny the permissions described in this License at their sole discretion, for any reason or no reason, with a full refund payable to you. Notice of such denial will be made using the contact information provided by you. Failure to receive such notice will not alter or invalidate the denial. In no event will Elsevier or Copyright Clearance Center be responsible or liable for any costs, expenses or damage incurred by you as a result of a denial of your permission request, other than a refund of the amount(s) paid by you to Elsevier and/or Copyright Clearance Center for denied permissions.

LIMITED LICENSE

The following terms and conditions apply only to specific license types:

15. **Translation**: This permission is granted for non-exclusive world **English** rights only unless your license was granted for translation rights. If you licensed translation rights you may only translate this content into the languages you requested. A professional translator must perform all translations and reproduce the content word for word preserving the integrity of the article. If this license is to re-use 1 or 2 figures then permission is granted for non-exclusive world rights in all languages.

16. **Website**: The following terms and conditions apply to electronic reserve and author websites:
Electronic reserve: If licensed material is to be posted to website, the web site is to be password-protected and made available only to bona fide students registered on a relevant course if:
This license was made in connection with a course,
This permission is granted for 1 year only. You may obtain a license for future website posting,
All content posted to the web site must maintain the copyright information line on the bottom of each image,
A hyper-text must be included to the Homepage of the journal from which you are licensing at http://www.sciencedirect.com/science/journal/xxxxx or the Elsevier homepage for books at http://www.elsevier.com , and
Central Storage: This license does not include permission for a scanned version of the material to be stored in a central repository such as that provided by Heron/XanEdu.

17. **Author website** for journals with the following additional clauses:

All content posted to the web site must maintain the copyright information line on the bottom of each image, and
he permission granted is limited to the personal version of your paper. You are not allowed to download and post the published electronic version of your article (whether

PDF or HTML, proof or final version), nor may you scan the printed edition to create an electronic version, A hyper-text must be included to the Homepage of the journal from which you are licensing at http://www.sciencedirect.com/science/journal/xxxxx , As part of our normal production process, you will receive an e-mail notice when your article appears on Elsevier's online service ScienceDirect (www.sciencedirect.com). That e-mail will include the article's Digital Object Identifier (DOI). This number provides the electronic link to the published article and should be included in the posting of your personal version. We ask that you wait until you receive this e-mail and have the DOI to do any posting.
Central Storage: This license does not include permission for a scanned version of the material to be stored in a central repository such as that provided by Heron/XanEdu.

18. **Author website** for books with the following additional clauses:
Authors are permitted to place a brief summary of their work online only.
A hyper-text must be included to the Elsevier homepage at http://www.elsevier.com

All content posted to the web site must maintain the copyright information line on the bottom of each image. You are not allowed to download and post the published electronic version of your chapter, nor may you scan the printed edition to create an electronic version.
Central Storage: This license does not include permission for a scanned version of the material to be stored in a central repository such as that provided by Heron/XanEdu.

19. **Website** (regular and for author): A hyper-text must be included to the Homepage of the journal from which you are licensing at http://www.sciencedirect.com/science/journal/xxxxx. or for books to the Elsevier homepage at http://www.elsevier.com

20. **Thesis/Dissertation**: If your license is for use in a thesis/dissertation your thesis may be submitted to your institution in either print or electronic form. Should your thesis be published commercially, please reapply for permission. These requirements include permission for the Library and Archives of Canada to supply single copies, on demand, of the complete thesis and include permission for UMI to supply single copies, on demand, of the complete thesis. Should your thesis be published commercially, please reapply for permission.

21. **Other Conditions**: None

v1.6

Gratis licenses (referencing $0 in the Total field) are free. Please retain this printable license for your reference. No payment is required.

If you would like to pay for this license now, please remit this license along with your payment made payable to "COPYRIGHT CLEARANCE CENTER" otherwise you will be invoiced within 48 hours of the license date. Payment should be in the form of a check or money order referencing your account number and this invoice number RLNK10764717. Once you receive your invoice for this order, you may pay your invoice by credit card. Please follow instructions provided at that time.

Make Payment To:
Copyright Clearance Center
Dept 001
P.O. Box 843006
Boston, MA 02284-3006

For suggestions or comments regarding this order, contact Rightslink Customer Support:
customercare@copyright.com or +1-877-622-5543 (toll free in the US) or +1-978-646-2777.

Lithosphere

Letter of Permission

Bryan Hibbard <bhibbard@geosociety.org> **Mon, Jun 27, 2011 at 8:40 AM**
To: "Kristin L.H. Hughes" <klhhughes@gmail.com>

Hi Kristin,

See http://www.geosociety.org/pubs/copyrt.htm, for our complete copyright policy. You do not need permission to use your article in a dissertation. Just be sure that you include a copyright credit line somewhere in the paper showing that this article is from our publication.

Bryan

CHAPTER 2

SLIP DISTRIBUTION FOR THE 2004 SUMATRA-ANDAMAN EARTHQUAKE CONSTRAINED BY BOTH GPS DATA AND TSUNAMI RUN-UP MEASUREMENTS

Reprinted with permission from Istituto Nazionale di Oceanografia
e di Geofisica Sperimentale and coauthor Tim Masterlark, Ph.D.

SUMMARY

The M9.3 Sumatra-Andaman earthquake (SAE) of 26 December 2004 ruptured over 1200 km of crust separating the subducting Indo-Australian plate and overriding Burma microplate. Various geodynamic models have been created to quantitatively examine the SAE. To date, no investigators have modeled onshore near-field coseismic deformation and seafloor deformation required by tsunami run-up measurements simultaneously. We identify the inconsistency between various slip distributions and provide an alternative that satisfies both onshore and offshore deformation requirements. Our results suggest (1) A forward model driven by slip distribution derived from tsunami run-ups fails to adequately predict observed near-field GPS data, although it adequately matches far-field observed GPS data, (2) GPS-based slip distribution estimations, that allow for dip-slip only, either poorly predicts near-field observed GPS data or are prohibitively rough, and (3)

More complex models that allow for both strike-slip and dip-slip dislocations are needed to adequately simulate both onshore and offshore near-field deformation.

INTRODUCTION

Over 1200 km of the Sumatra-Andaman subduction zone (SASZ) was ruptured during the 26 December 2004 M9.3 Sumatra-Andaman earthquake (SAE) (Bilek, 2007; Sørensen et al., 2007). This event induced a devastating tsunami that killed over 250,000 people in over 12 countries (Rastogi and Jaiswal, 2006). The SASZ is a large subduction zone in which the Indo-Australian Plate subducts beneath the Sunda Plate and Burma microplate (Fig. 2.1). The SAE is the largest earthquake recorded by GPS, and presents a unique opportunity to quantify the coseismic deformation. An accurate description of the fault-slip distribution for the SAE is key to any analysis of coseismic deformation, postseismic deformation, postseismic stress-coupling, and tsunami-genesis. The fault-slip of the SAE deformed the overlying seafloor, with a vertical deformation pattern that served as initial conditions for tsunami genesis models (e.g., Grilli et al., 2007). An accurate coseismic slip distribution is a prerequisite for quantitative interpretations of coseismic deformation.

Several coseismic slip distributions have been published for the SAE, based on either the near-field or far-field GPS data or both data sets (Catherine et al., 2005; Banerjee et al., 2005; Gahalaut et al., 2006; Banerjee et al., 2007). All of these slip distributions adequately fit the far-field GPS data. Alternatively, tsunami run-up measurements were recorded on many coastlines surrounding the Indian Ocean.

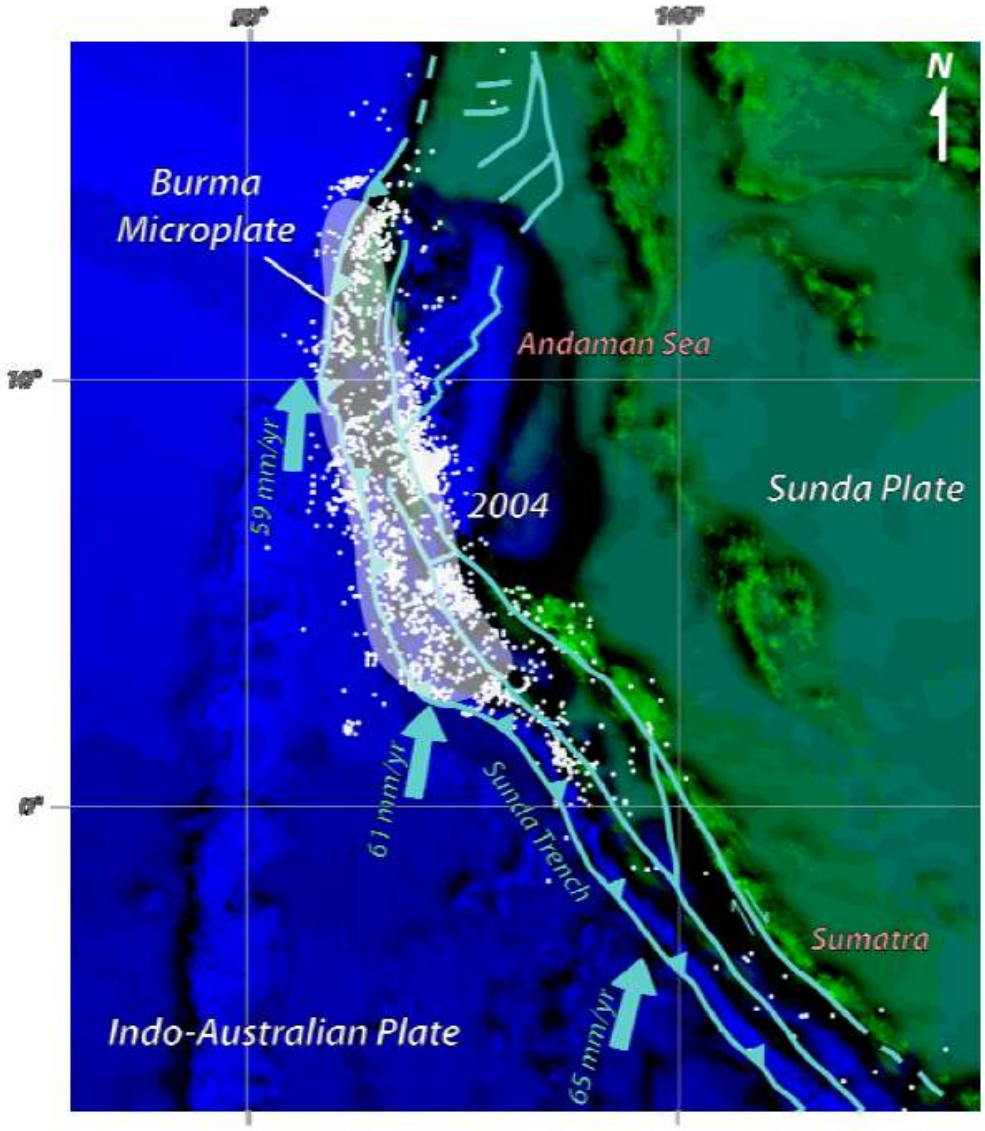

Figure 2.1. Seismotectonic setting of the SASZ. White circles represent aftershocks between 26 December 2004 and 28 March 2005. White translucent area shows projection of rupture at the land surface.

These data can also be used to quantify the coseismic seafloor deformation and thus, the slip distribution for the SAE. Several different slip distributions have been estimated based on tsunami run-up measurements (Chlieh et al., 2007; Fujii and Satake, 2007; Piatanesi and Lorito, 2007; Grilli et al., 2007).

The SAE caused a continuous coseismic deformation field, which can be measured by GPS at onshore locations. The offshore portions of the deformation

field induced instabilities in the overlying water column, for which the subsequent propagation lead to tsunami run-up measurements. Unfortunately, previously reported slip distributions estimated from either GPS or tsunami run-up measurements have been incompatible. Comparing any slip distribution solely based on GPS to any slip distribution solely based on tsunami run-up measurements reveals that neither slip distribution matches the other adequately. Both onshore and offshore deformation was generated by the SAE. A common slip distribution should satisfy both GPS and tsunami run-up data.

We propose that a more complex slip distribution is required to simultaneously account for both near-field GPS data and seafloor deformation required by tsunami run-up measurements. We examine the differences in GPS deformation predicted by forward models of slip distributions estimated from tsunami run-up measurements (e.g., Grilli et al., 2007) and differences in a corresponding slip distribution estimated from inverse models of GPS data. We then compare these homogeneous, elastic, half-space (HEHS) models to more complex heterogeneous finite element models (FEMs) to determine which model best predicts both the tsunami run-ups and GPS data.

METHODS

Models of deformation due to a dislocation embedded in an HEHS are readily available (Okada, 1992). HEHS models, and to a lesser extent layered elastic half-space models (LEHS), are commonly implemented to estimate slip distributions from tsunami run-up measurements and far-field and near-field GPS data (Chlieh et

al., 2007; Banerjee et al., 2007; Gahalaut et al., 2006). However, these data have not been used to derive a single slip distribution that simultaneously honors both onshore and offshore deformation requirements of GPS and tsunami run-up measurements.

We use a slip distribution having five fault patches, following the configuration proposed by Grilli et al. (2007) that is based on tsunami run-up measurements, to predict deformation observed at 39 near-field and far-field GPS locations (Subarya et al., 2006; Gahalaut et al., 2006). The forward model for this linear system is

$$\boldsymbol{Gm} = \boldsymbol{d} \tag{2.1}$$

where $\boldsymbol{G}$ is a matrix of Green's functions for deformation due to a dislocation, $\boldsymbol{m}$ is a vector that corresponds to a slip distribution, and $\boldsymbol{d}$ is a vector of displacement data (Menke, 1989). The data vector is constructed from all three GPS displacement components. Sensitivities of deformation to a given slip distribution can be estimated by comparing forward model predictions to observed GPS data.

In addition to comparing GPS vectors, we construct inverse models to estimate the slip distribution for the five fault patches, based on near-field GPS data. The least-squares solution for the slip distribution is

$$\boldsymbol{m}^{\text{est}} = [(\boldsymbol{WG})^{\text{T}}(\boldsymbol{WG})]^{-1}(\boldsymbol{WG})^{\text{T}}(\boldsymbol{Wd}) \tag{2.2}$$

where $\boldsymbol{m}^{est}$ is the estimated slip distribution and $\boldsymbol{W}$ is a weighting matrix constructed from GPS measurement uncertainties (Menke, 1989). The optimal slip inversion had four reverse (thrust) fault patches and one normal fault patch.

Because normal slip is not a geologically reasonable result, we invoked smoothing constraints using a Laplacian operator,

$$\begin{bmatrix} \boldsymbol{WG} \\ \beta \boldsymbol{L} \end{bmatrix} [\boldsymbol{m}] = \begin{bmatrix} \boldsymbol{Wd} \\ 0 \end{bmatrix} \tag{2.3}$$

where $\boldsymbol{L}$ is a Laplacian smoothing matrix, a null vector appends the weighted data matrix, and β is a damping parameter that controls the tradeoff of misfit versus solution complexity (Menke, 1989). All five fault patches of the resulting slip distribution are positive (thrust) and can be compared to the corresponding slip distribution estimated from tsunami run-ups.

We construct FEMs to explore sensitivities of forward and inverse model predictions to problem domain complexities beyond the restrictions of HEHS and LEHS models. We compute FEM-generated Green's Functions (Masterlark, 2003) for displacement due to a dislocation in a 3-D heterogeneous problem domain (Fig. 2.2). Although computationally expensive, FEMs allow us to honor the known geologic complexity of the SASZ. In particular, neither HEHS nor LEHS models can account for the presence of the relatively stiff subducting plate. The plate is the first order feature of a subduction zone and substantially impacts both forward and inverse models of coseismic deformation (Masterlark, 2003).

RESULTS

We forward modeled the five fault patch tsunami slip distribution for dip-slip only (Grilli et al., 2007) to determine the predicted data vectors for 39 GPS station locations. The resulting vectors poorly predict the observed GPS data (Fig. 2.3a).

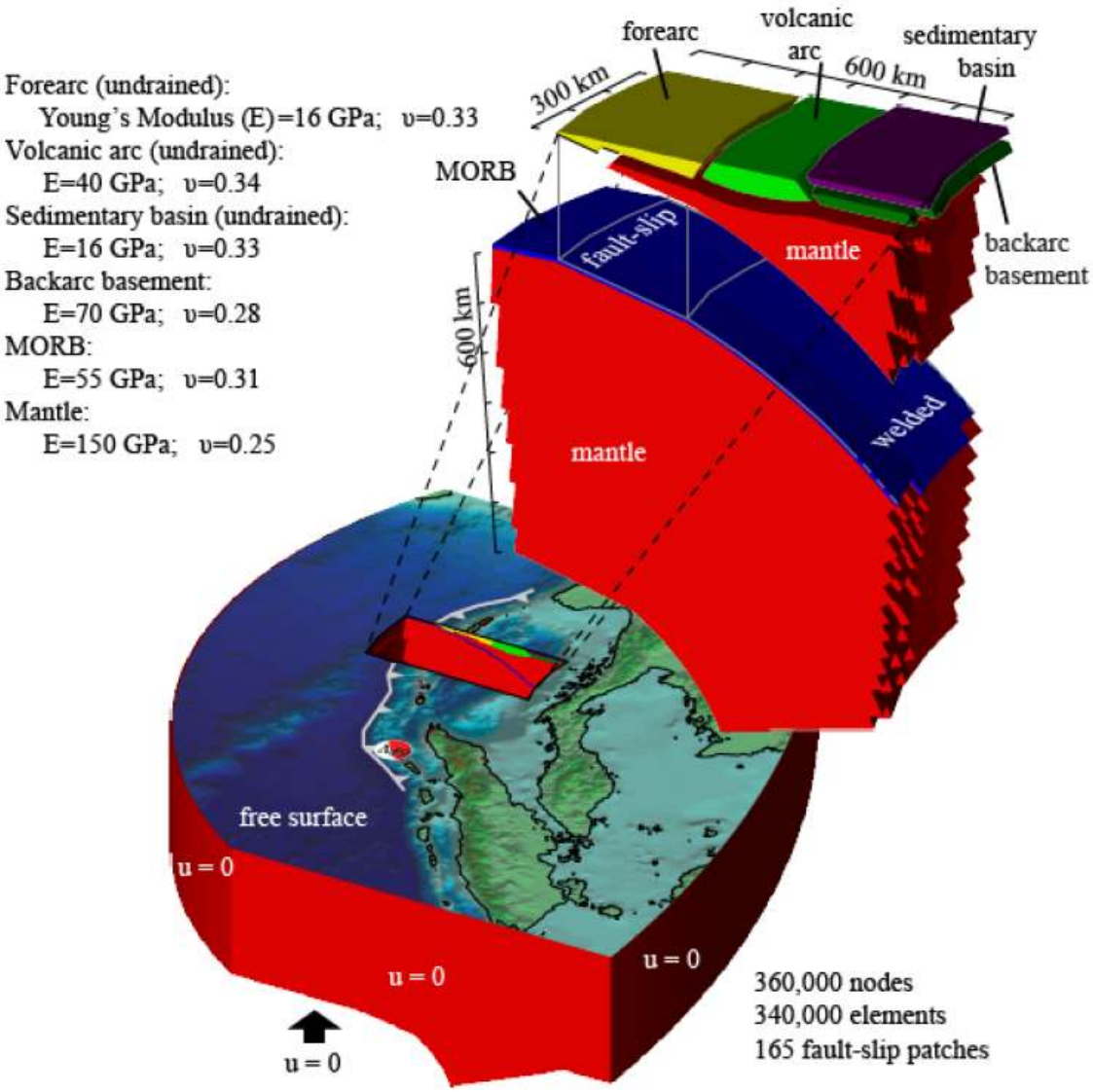

Figure 2.2. FEM problem domain. Inset shows exploded cross-section view. Cross-section was propagated along strike to create 3-D FEM.

We inverse modeled both the near-field and far-field GPS data for the five fault patches with dip-slip only. The estimated dip-slip distribution adequately matches the far-field GPS data (Fig. 2.3b), but does not match the near-field GPS data (Fig. 2.3c).

We inverse modeled the GPS data using an FEM to simulate a more refined slip distribution along the curved surface of the rupture. Increasing the number of fault patches and accounting for varying rock properties, adequately predicts the

observed GPS data based on a dip-slip only distribution (Fig. 2.4a). However, the desirable misfit comes at the expense of a very rough slip distribution. Another inverse model constructed with FEM-generated Green's Functions allows for both strike-slip and dip-slip dislocations. This latter FEM appears to better match the near-field GPS data, but still does not put large slip near the trench where it is needed for accurate tsunami models (Fig. 2.4b) (Grilli et al., 2007). A third inverse FEM allows for both dip-slip and strike-slip dislocations and includes constraints that favor shallow slip in an effort to satisfy both onshore deformation required by the GPS data and seafloor deformation required by tsunami run-up measurements (Grilli et al., 2007).

DISCUSSION

The deformation predictions from the slip distribution estimated from tsunami run-ups adequately predict the far-field GPS deformation, but poorly

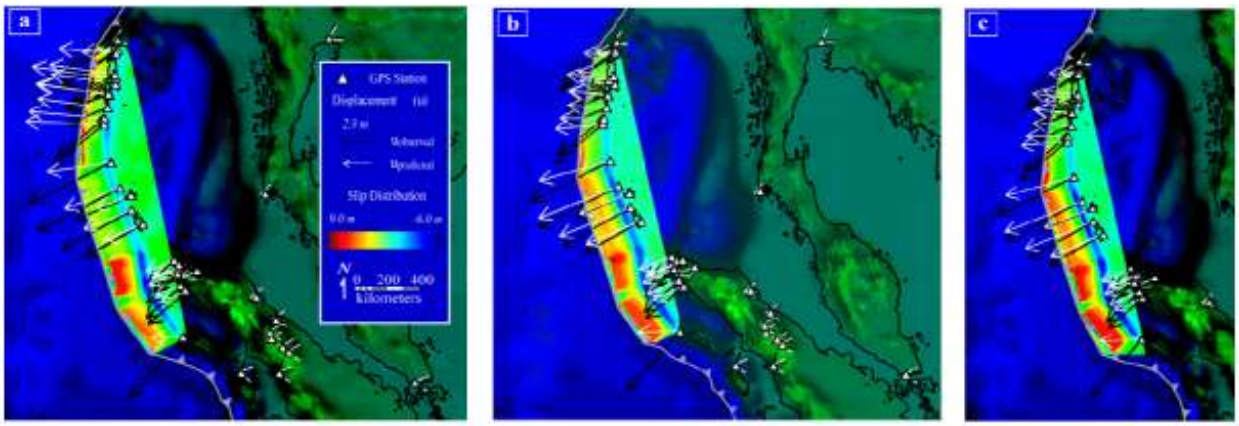

Figure 2.3. Slip distribution models using HEHS. (a) Tsunami forward model. GPS. (b) Inverse HEHS model including all 38 GPS stations with Neumann boundary conditions. (c) Inverse HEHS model including 28 near-field GPS stations with Neumann boundary conditions. Slip distributions are shown by color contours. Negative anomalies surrounded by positive deformation are an artifact of coarse grid spacing. Black arrows represent GPS, and white arrows are predicted GPS.

predict near-field GPS deformation (Fig. 2.3). This suggests that the complex deformation nearest the rupture must be resolved for quantitative tsunami-genesis analyses, in accord with seismological observations (Engdahl et al., 2007). Furthermore, the geology of the SASZ is readily accounted for by incorporating varying material properties in the FEM. These material properties significantly influence the individual elements of the ***G*** matrix and thus strongly affect estimations of slip distribution (Masterlark, 2003). Comprehensive sensitivity analyses of material properties, problem domain configurations, and associated slip-distribution estimation methods will be addressed in future analyses.

We can fit GPS data with our FEM using a distribution of dip-slip dislocations alone, but the distribution is excessively rough (Fig. 2.4). Alternatively, a smoother distribution poorly predicts the near-field GPS data. However, allowing for strike-slip dislocations, in addition to dip-slip dislocations, appears to provide reasonable

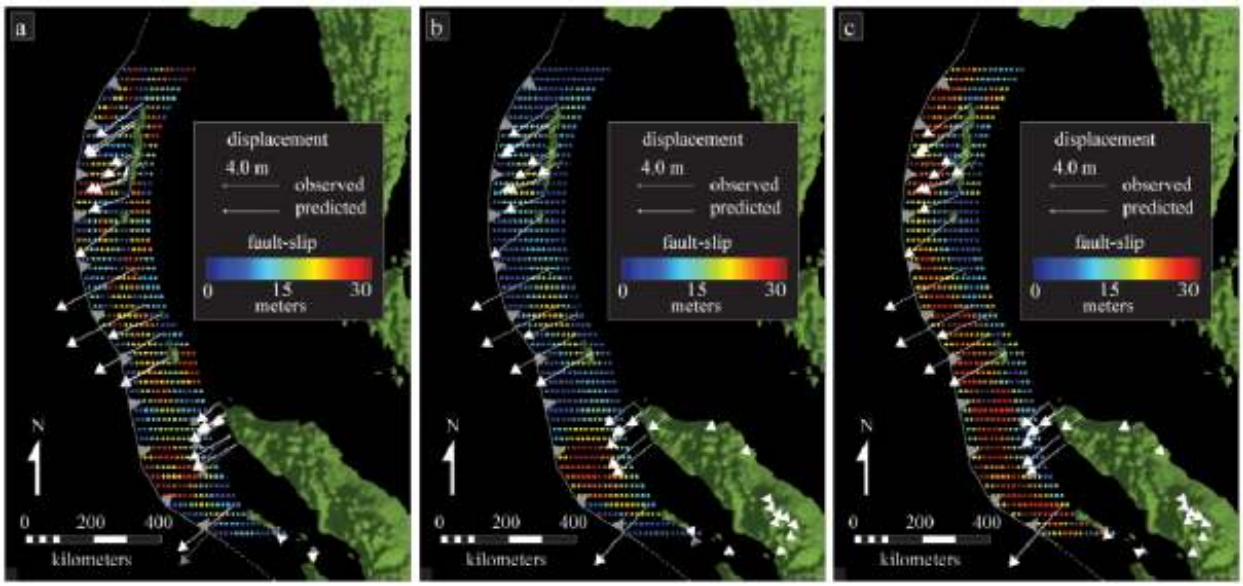

Figure 2.4. Slip distribution models using FEMs. (a) FEM inverse model for dip-slip only. (b) FEM inverse model for dip-slip and strike-slip. (c) FEM inverse model for dip-slip, strike-slip and increased shallow slip near the accretionary wedge. Slip distribution is shown by color dots. Gray arrows represent observed GPS, and white arrows represent predicted GPS.

misfit, as well as a relatively smooth slip distribution. Furthermore, additional constraints on the shallow slip result in a slip distribution having desirable misfit and smoothness, produce seafloor deformation that is consistent with tsunami-run-up measurements. Our slip distribution is consistent with that produced by using a splay fault to create large seafloor deformation (Hoechner et al., 2008).

The SASZ is an obliquely converging tectonic setting. Near the Andaman Islands the plate motions are accommodated almost completely by strike-slip motion. Aftershock activity between the M9.3 SAE and the M8.7 Nias earthquake shows a significant increase in strike-slip motion and normal faulting at the northern end of the rupture (Engdahl et al., 2007). Our results match seismicity data, suggesting that dip-slip only is not an adequate assumption for resolving GPS data in the Andaman Islands.

Our results illustrate that near-field GPS data dominate the inverse slip distribution and far-field GPS data are well fit using a five fault patch dip-slip only HEHS model (Fig. 2.3). Both forward deformation predictions and estimated slip distributions are strongly model dependent, a result that suggests model design is critical to quantitative analyses of coseismic deformation and associated processes, such as tsunami-genesis, stress-coupling, and postseismic deformation.

CONCLUSIONS

We tested the hypothesis that an estimated slip distribution can predict observed GPS data and seafloor deformation required for tsunami run-up measurements simultaneously. We determined that onshore deformation predicted

for a slip distribution, estimated based on tsunami run-up measurements (Grilli et al., 2007), does not match the observed near-field GPS data (Subarya et al., 2006; Gahalaut et al., 2006), but adequately predicts far-field GPS data. A more complex model configuration, allowing for both dip-slip and strike-slip dislocations, is required to adequately simulate the observed onshore near-field deformation while simultaneously producing elevated magnitudes of seafloor deformation required for tsunami run-up observations.

REFERENCES

Banerjee, P., Pollitz, F.F., and Bürgmann, R., 2005, The size and duration of the Sumatra-Andaman earthquake from far-field static offsets: Science, v. 308, p. 1769-1772, doi: 10.1126/science.1113746.

Banerjee, P., Pollitz, F., Nagarajan, B., and Bürgmann, R., 2007, Coseismic slip distributions of the 26 December 2004 Sumatra-Andaman and 28 March 2005 Nias earthquakes from GPS static offsets: Bulletin of the Seismological Society of America, v. 97, p. S86-S102, doi: 10.1785/0120050609.

Bilek, S.L., 2007, Using earthquake source durations along the Sumatra-Andaman subduction system to examine fault-zone variations: Bulletin of the Seismological Society of America, v. 97, p. S62-S70, doi: 10.1785/0120050622.

Catherine, J.K., Gahalaut, V.K., and Sahu, V.K., 2005, Constraints on rupture of the December 26, 2004, Sumatra earthquake from far-field GPS observations: Earth and Planetary Science Letters, v. 237, p. 673-679, doi: 10.1016/j.epsl.2005.07.012.

Chlieh, M., Avouac, J.-P., Hjorleifsdottir, V., Song, T.-R.A., Ji, C., Sieh, K., Sladen, A., Hebert, H., Prawirodirdjo, L., Bock, Y., and Galetzka, J., 2007, Coseismic slip and afterslip of the great Mw 9.15 Sumatra-Andaman earthquake of 2004: Bulletin of the Seismological Society of America, v. 97, p. S152-S173, doi: 10.1785/0120050631.

Engdahl, E.R., Villaseñor, A., DeShon, H.R., and Thurber, C.H., 2007, Teleseismic relocation and assessment of seismicity (1918-2005) in the region of the 2004 Mw 9.0 Sumatra-Andaman and 2005 Mw 8.6 Nias Island great

earthquakes: Bulletin of the Seismological Society of America, v. 97, p. S43-S61, doi: 10.1785/0120050614.

Fujii, Y., and Satake, K., 2007, Tsunami source of the 2004 Sumatra-Andaman earthquake inferred from tide gauge and satellite data: Bulletin of the Seismological Society of America, v. 97, p. S192-S207, doi: 10.1785/0120050613.

Gahalaut, V.K., Nagarajan, B., Catherine, J.K., and Kumar, S., 2006, Constraints on 2004 Sumatra-Andaman earthquake rupture from GPS measurements in Andaman-Nicobar Islands: Earth and Planetary Science Letters, v. 242, p. 365-374, doi: 10.1016/j.epsl.2005.11.051.

Grilli M.ASCE, S.T., Ioualalen, M., Asavanant, J., Shi, F., Kirby M.ASCE, J.T., and Watts, P., 2007, Source constraints and model simulation of the December 26, 2004, Indian Ocean tsunami: Journal of Waterway, Port, Coastal, and Ocean Engineering, v. 133, p. 414-428, doi: 10.1061/(ASCE)0733-950X.

Hoechner, A., Babeyko, A.Y., and Sobolev, S.V., 2008, Enhanced GPS inversion technique applied to the 2004 Sumatra earthquake and tsunami: Geological Research Letters, v. 35, doi: 10.1029/2007GL033133.

Masterlark, T., 2003, Finite element model predictions of static deformation from dislocation sources in a subduction zone: Sensitivities to homogeneous, isotropic, Poisson-solid, and half-space assumptions: Journal of Geophysical Research, v. 108, doi: 10.1029/2002JB002296.

Menke, W., 1989, Geophysical Data Analysis: Discrete Inverse Theory: San Diego, Academic Press, Inc., 289 p.

Okada, Y., 1992, Internal deformation due to shear and tensile faults in a half-space: Bulletin of the Seismological Society of America, v. 82, p. 1018-1040.

Piatanesi, A., and Lorito, S., 2007, Rupture process of the 2004 Sumatra-Andaman earthquake from tsunami waveform inversion: Bulletin of the Seismological Society of America, v. 97, p. S223-S231, doi: 10.1785/0120050627.

Rastogi, B.K., and Jaiswal, R.K., 2006, A catalog of tsunamis in the Indian Ocean: Science of Tsunami Hazards, v. 25, p. 128-143.

Sørensen, M.B., Atakan, K., and Pulido, N., 2007, Simulated strong ground motions for the great M9.3 Sumatra-Andaman earthquake of 26 December 2004: Bulletin of the Seismological Society of America, v. 97, p. S139-S151, doi: 10.1785/0120050608.

Subarya, C.M., Chlieh, M., Prawirodirdjo, L., Avouac, J.-P., Bock, Y., Sieh, K., Meltzner, A.J., Natawidjaja, D.H., and McCaffrey, R., 2006, Plate-boundary deformation associated with the great Sumatra-Andaman earthquake: Nature, v. 440, p. 46-51, doi: 10.1038/nature04522.

CHAPTER 3

NEXT GENERATION OF DEFORMATION MODELS FOR THE 2004 M9 SUMATRA-ANDAMAN EARTHQUAKE

Reprinted with permission from American Geophysical Union and coauthor Tim Masterlark, Ph.D.

ABSTRACT

The 2004 M9 Sumatra-Andaman Earthquake (SAE) ruptured the interface separating the subducting Indo-Australian plate from the overriding Burma plate. We construct finite element models (FEMs) that simulate deformation of the earthquake for a three-dimensional problem domain partitioned to account for the distribution of material properties of the subducting slab, forearc, volcanic arc, and backarc. We demonstrate a protocol-based approach for simulating coseismic deformation, in which FEMs are implemented in inverse models to estimate the fault-slip distribution of the SAE while simultaneously honoring the geologic complexity of the subduction zone. Results suggest that deformation prediction sensitivities attributed to neglecting the different material properties of the subduction zone can be more than an order of magnitude greater than reported uncertainties for near-field GPS measurements. The FEM-based techniques presented here allow for geologically satisfying deformation models that will

advance the reliability of modeling-based assessments of coseismic and postseismic deformation, stress-coupling, and tsunami genesis.

INTRODUCTION

The 2004 M9 Sumatra-Andaman Earthquake (SAE) ruptured a 1200-km-long and 200-km-wide portion of the boundary separating the subducting Indo-Australian Plate from the overriding Burma Plate (Fig. 3.1) (Ammon et al., 2005; Stein and Okal, 2005). The near-field deformation is characterized by 34 GPS sites that span the forearc and volcanic islands parallel to the Sunda trench (Appendix). The combined magnitude and spatial extent of the observed SAE deformation provides exceptional opportunities to quantitatively simulate earthquake deformation. A generally overlooked, but significant distortion of simulation predictions is tied to the validity of deformation modeling techniques.

Models provide the linkage between the observed surface deformation and the source of the deformation-–the fault-slip at depth. While forward models allow us to predict deformation caused by fault-slip, substantial effort has gone into the development of inverse models that strive to quantify fault-slip, based on observed deformation and a priori forward deformation models. In practice, relatively little attention is given to the implications of the a priori forward models and sensitivity analyses of deformation model assumptions are rare (Masterlark, 2003). A suitable deformation model, which includes a self-consistent fault-slip distribution, is the key to any analysis of coseismic deformation, tsunami-genesis, postseismic deformation, or stress-coupling (Freed et al., 2006; Masterlark, 2003; Sobolev et al., 2007). The

reliability of SAE deformation interpretations is contingent on three fundamental elements: the quantity and quality of the deformation data, the suitability of the inverse scheme, and the validity of the deformation model, the latter of which is the focus of this study.

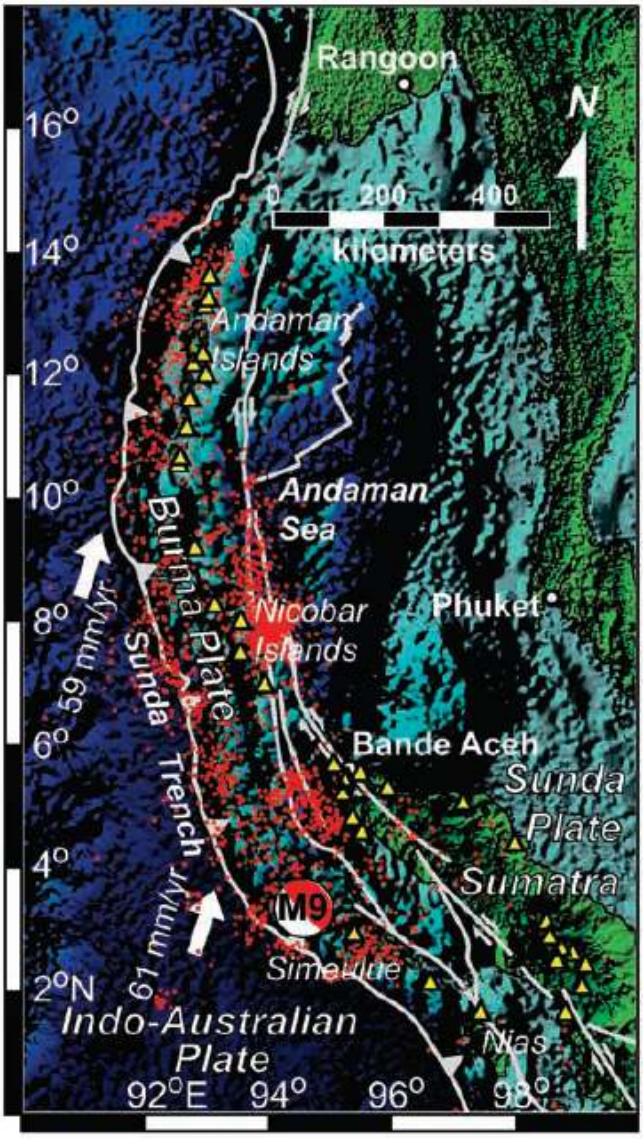

Figure 3.1. Seismotectonic setting. The Harvard CMT focal mechanism overlies the epicenter of the SAE. Aftershock epicenters (red dots) illuminate the surface projection of the rupture (http://neic.usgs.gov), which initiated on the southeast portion of the fault and propagated 1200 km northward. Yellow triangles are near-field GPS sites, summarized in Table 3.1. The tectonic configuration is modified from Bird (2003) and overlies a shaded relief image of global relief data (http://www.ngdc.noaa.gov).

The cold, down-going slab is the essence of a subduction zone and its relative stiffness significantly impacts deformation predictions for megathrust earthquakes (Masterlark, 2003). Deformation models for dislocations in homogeneous elastic half-spaces (HEHS) (e.g., Okada, 1992) are overwhelmingly implemented to describe, assess, and interpret observed deformation of the SAE (Han et al., 2006; Nalbant et al., 2005; Vigny et al., 2005). Alternatively, models that simulate

horizontally layered elastic half-spaces (LEHS) are implemented to simulate an assumed layered structure of the Earth (Chlieh et al., 2007; Subarya et al., 2006). Both of these models ignore the known presence, geometric complexity, and significance of the relatively stiff subducting slab.

FEMs permit us to simulate variable slip along fault surfaces embedded in a problem domain that accounts for the juxtaposition of the stiff, dipping subducting slab and relatively compliant overriding plate, as well as the material property variations of the forearc, volcanic arc, and backarc regions. Furthermore, FEMs are readily implemented in linear inverse analyses of observed deformation due to the fault-slip of an earthquake (Masterlark, 2003; Schmitt et al., 2007). In spite of these known capabilities, FEMs are rarely invoked for inverse analyses of static earthquake deformation. We provide methods to replace standard HEHS and LEHS models that are computationally efficient, but poorly represent the geologic complexity of the subduction zone, with computationally intensive FEMs that can readily provide geologically satisfying configurations for the SAE. The inability to reliably predict recent events triggered by the SAE fault-slip reflects the need to pursue better deformation models. The integration of geology into deformation modeling methods is a critical and necessary advancement toward more reliable predictions and early warning systems for earthquake stress-coupling (Masterlark, 2003) and tsunami genesis (McCloskey et al., 2008).

The remainder of this paper is organized into three sections. First, the main body introduces the FEM-based deformation modeling protocol and describes its implementation for the SAE. We present a fault-slip distribution for the SAE that is

calibrated to GPS data for a deformation model that honors the know structure of the subduction zone. We then present a discussion of the results and implications of the protocol-based modeling and how the predictions differ from those of standard deformation models. This discussion includes several possibilities for improving the model through reassessment, a concept that is central to protocol-based modeling. Finally, we present conclusions and recommendations.

DEFORMATION MODELING PROTOCOL

Inspired by the formal protocol that standardizes groundwater modeling analyses (Anderson and Woessner, 1992), we introduce a deformation modeling protocol to guide and test the model design and ensure the deformation model adequately represents the natural system (Fig. 3.2a). FEM-based techniques are embedded in the modeling protocol and allow us to estimate the fault-slip distribution and predict near-field deformation, while simultaneously honoring the known geologic complexity associated with the SAE. This protocol calls for reassessment at any stage, in which the model either fails to adequately represent the known problem domain constraints or effectively predict observations. This call for reassessment and ability to implement improvements in deformation model configurations via FEMs is a significant departure from standard HEHS-based analyses, for which the fault geometry and slip are the only permissible variations.

The design of the conceptual model is the foundation of the deformation modeling protocol and therefore a fundamental consideration for predicting earthquake deformation. Implications of the conceptual model propagate

throughout the modeling analysis and shape predictions and interpretations. Our conceptual model of the SAE relates near-field coseismic deformation to the fault-slip distribution as the mechanical response of a three-dimensional elastic/poroelastic problem domain to an embedded dislocation. The deformation is static and undrained, that is, the deformation that remains after dynamic wave propagation, but prior to postseismic fluid flow in the brittle crust and viscoelastic flow of the mantle. A representative cross-section of the subduction zone is

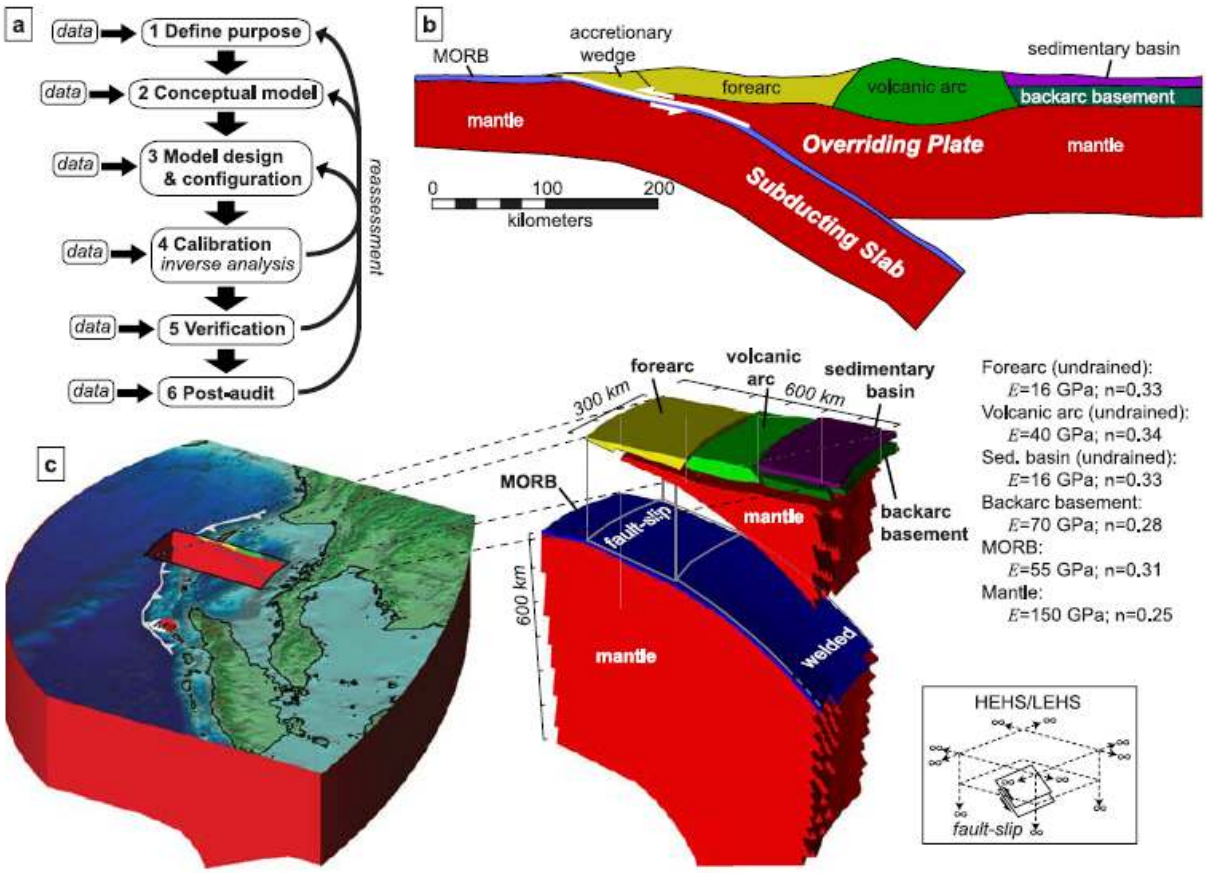

Figure 3.2. Protocol-based deformation model for the SAE. (a) Protocol. The protocol ensures that the modeling progression honors the available information and provides a mechanism for iterative reassessment. (b) Conceptual model. This design includes geologic constraints discussed in the text. (c) FEM design and configuration. The FEM comprises about 340,000 elements. The exploded view reveals the likeness of the FEM to the geologic structure of the conceptual model. Neither the HEHS nor the LEHS configuration (bottom right) accounts for the relatively stiff subducting slab and associated structures shown in the conceptual model.

constructed as an 800-km-long trench-normal slice through the Sumatra region (Fig. 3.2b). Seismicity data (Engdahl et al., 2007) constrain the geometry of the subducting slab. The fault-slip of the SAE occurs along the interface separating the subducting slab, consisting of lithospheric mantle capped by mid-oceanic ridge basalt, and the overriding forearc and upper mantle wedge (Kieckhefer et al., 1980; Kopp and Kukowski, 2003; Kopp et al., 2002). Geologic maps and cross-sections of Sumatra (Barber et al., 2005; Kopp and Kukowski, 2003; Kopp et al., 2002) guide the configuration of the volcanic arc and backarc basin of the overriding plate. This two-dimensional cross section is swept through the curving strike of the Sunda trench from northern Sumatra through the Andaman Islands to produce a three-dimensional model (Fig. 3.2c). A limitation of this configuration is the constant cross-section along the trench, which does not account for along-strike variations associated with the transition of island arc volcanism in Sumatra to the backarc spreading in the Andaman Basin (Fig. 3.1) (Curray, 2005). This additional complexity will be addressed in future modifications to the model configuration.

All FEMs in this study are constructed with Abaqus (http://www.simulia.com) and solve the elastic and poroelastic governing equations (Wang, 2000) over the three-dimensional problem domain. The free surface at the top of the problem domain represents the Earth's surface. The top of the simulated oceanic crust represents a flat seafloor having a reference elevation of zero. The free-surface along the toe of the thrust includes a transition from the seafloor to the top surface of the overriding continental plate, which has a simulated reference elevation of 4 km. More detailed relief significantly affects neither

deformation predictions nor fault-slip estimations (Masterlark, 2003). The lateral boundaries and base of the problem domain have zero displacement. We simulate fault-slip by imposing kinematic constraint equations (Masterlark, 2003) for 165 fault-patches along the curving rupture interface (Appendix). The converging plates are welded together along the non-slipping portions of the plate boundary. The initial conditions are equilibrium, therefore deformation, stress, and pore pressure predictions are incremental changes with respect to the state of the system prior to the fault-slip. Material properties are taken from compilations of elastic (Turcotte and Schubert, 1982) and poroelastic (Wang, 2000) rock properties. The FEM validation for using kinematic constraint equations to simulate elastic dislocations is described in the Appendix.

For a system of multiple displacement observations and a distribution of fault-slip patches along the rupture, the net displacement for a given GPS site is the superposition of contributions from each fault-patch. Green's functions for displacement are calculated by predicting displacement caused by unit slip over a given fault-patch while simultaneously welding the remaining fault-patches. We implement an algorithm that systematically generates the unit slip and welding configuration over the rupture, executes the model, and extracts the Green's functions for both thrust and strike-slip components for each fault-patch. We invert the resulting system of linear equations to estimate the distribution of fault-slip (Appendix). Results suggest that more than 20 meters of fault-slip occurred along the southern two-thirds of the rupture (Fig. 3.3a). This band of slip is generally deeper along the southern end of the rupture and becomes shallower to the north.

The thrust component dominates along the entire rupture. The right-lateral strike-slip component is minimal along the southern end and increases northward. This calibrated FEM, loaded by this fault-slip distribution, adequately predicts the observed GPS deformation (Fig. 3.3).

DISCUSSION

We modify the FEM to simulate an HEHS to test the sensitivity of deformation predictions to the distribution of material properties. Green's functions are calculated and assembled for this HEHS and a fault-slip distribution is estimated with the same inverse scheme. The general magnitude of the estimated fault-slip distribution for the HEHS is somewhat reduced compared to that of the heterogeneous FEM (Fig. 3.3b). The differences are most pronounced west of Northern Sumatra and GPS displacement sensitivities to the distribution of material

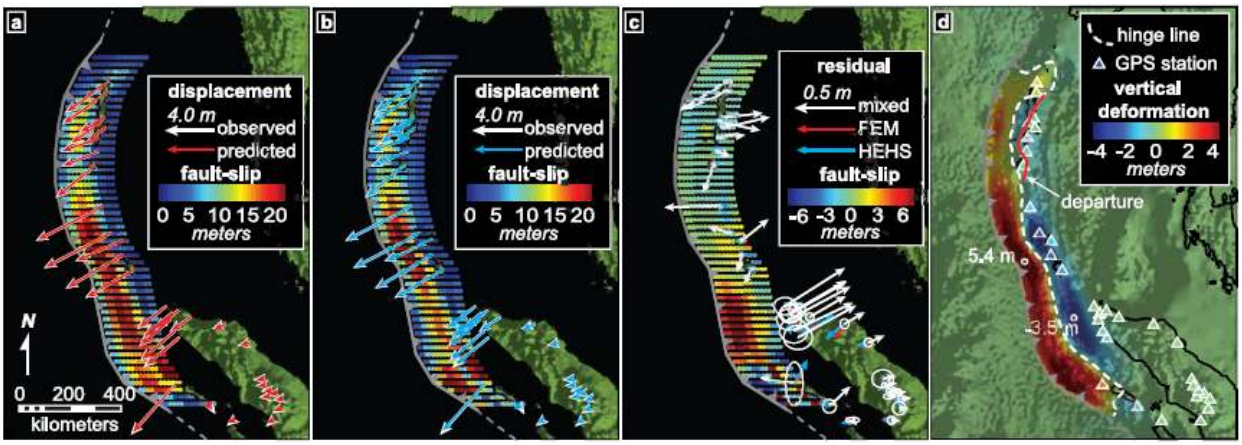

Figure 3.3. Calibration. (a) FEM. (b) HEHS. (c) Model-dependent prediction errors. The model-dependent sensitivity of displacement predictions is illustrated by loading the FEM with the difference between the estimated FEM and HEHS slip distributions. This sensitivity is significantly greater than GPS measurement uncertainties, shown as 1σ ellipses. The fault-slip distribution shown here is the difference between fault-slip distributions estimated for the FEM and HEHS models. (d) Coseismic vertical deformation, FEM. White circles correspond to locations of predicted vertical displacement extremes.

properties are significantly greater than GPS measurement uncertainties (Fig. 3.3c). In spite the differing estimated fault-slip distributions, both the FEM and HEHS models predict the GPS deformation equally well, as shown by the residual in Figure 3.3c and discussed in the Appendix. Although both models can predict the observed coseismic deformation data, forward model predictions for tsunami genesis and stress-coupling processes that are driven by the differing estimated fault-slip distribution may vary significantly, due to the magnitude and spatial extent of the fault-slip differences (Masterlark, 2003; McCloskey et al., 2008; Sobolev et al., 2007). Thus, the validity of a given SAE deformation model configuration will influence the associated interpretations of forward model predictions.

The verification step is an assessment of the model's predictive reliability. In this step, we test if the model successfully predicts data that are independent of the calibration process. Coral measurements and optical remote sensing observations characterize the vertical deformation pattern of the SAE along a sinuous, trench-parallel trajectory (Meltzner et al., 2006). Vertical deformation predictions from the calibrated FEM generally agree with these data (Fig. 3.3d). The minor departure of our predicted axis of zero vertical deformation separating the near-field uplift and subsidence near the Andaman Islands may be a result of the constant trench-normal cross-section configuration of the FEM. Future work will investigate alternative model configurations that account for the along-strike variations in geometry and material properties.

The predicted vertical deformation substantially underestimates the seafloor uplift near the trench that is required for models of tsunami genesis (Geist et al.,

2007; Ioualalen et al., 2007). One way to resolve this problem is to increase the seafloor uplift by imposing a penalty function that favors shallow fault-slip in the inverse analysis (Menke, 1989). However, there is no obvious physical basis for this ad-hoc constraint that would be at odds with seismologic data (Ammon et al., 2005). Alternatively, we can approach this discrepancy by revising the conceptual model to include splay faults in the toe of the thrust (Kopp and Kukowski, 2003) or a partitioning of the forearc into a more refined distribution of stiff and compliant regions, such that the fit to the GPS data is optimized while simultaneously increasing the near-trench uplift. Both of these configurations are supported by geologic and geophysical data (Fisher et al., 2007; Kieckhefer et al., 1980; Kopp et al., 2002). This reassessment of the conceptual model design is another avenue toward future improvements of the model configuration.

The real power of FEM-based analyses lies in their ability to predict not only the coseismic deformation of the earthquake, but to simulate multiple postseismic deformation processes that are driven by fault-slip. We entered the protocol with the purpose of simulating the coseismic deformation of the SAE. Consequently, the FEM is calibrated and verified for the static coseismic deformation of the SAE and was not designed to simulate the ongoing postseismic deformation that is observed with GPS data (Chlieh et al., 2007). Because of this additional information, the protocol requires a reassessment of our fundamental purpose, which will address postseismic processes that are driven by the coseismic fault-slip. This reassessment is within the domain of the protocol and FEM capabilities and yet another direction for future improvements of SAE deformation models. The FEM-based protocol

treats deformation modeling as a dynamic process that is continuously subject to iterative improvements in an effort to better simulate the natural deformational system and ultimately provide reliable deformation predictions.

CONCLUSIONS

We demonstrate an approach, in which geologically satisfying FEMs are implemented in both forward and inverse models of coseismic deformation for the SAE. The FEM-based techniques, embedded in the modeling protocol, provide powerful tools to explore various aspects of coseismic fault-slip, while simultaneously honoring the rich geologic complexity associated with a subduction zone. The call for reassessment and the ability to explicitly modify deformation model configurations accordingly, is a fundamental advancement in assessments of earthquake deformation. Estimations of the fault-slip distribution and near-field deformation for the SAE, based on HEHS and LEHS model predictions, are significantly distorted, a result that propagates into interpretations of SAE deformation. The methods presented here can rectify these distortions and lead to more accurate interpretations and inferences in future modeling-based assessments of coseismic deformation, postseismic deformation, stress-coupling, and tsunami genesis.

REFERENCES

Ammon, C.J., Ji, C., Thio, H.K., Robinson. D., Ni, S., Hjorleifsdottir, V., Kanamori, H., Lay, T., Das, S., Helmberger, D., Ichinose, G., Polet, J., and Wald, D., 2005, Rupture process of the 2004 Sumatra-Andaman Earthquake: Science, v. 308, p. 1133–1139, doi: 10.1126/science.1112260.

Anderson, M. P., and Woessner, W.W., 1992, Applied Groundwater Modeling: Simulation of Flow and Advective Transport: San Diego, Academic Press, 381 p.

Aster, R., Borchers, B., and Thurber, C., 2005, Parameter Estimation and Inverse Problems: Elsevier Academic Press, 301 p.

Barber, A. J., Crow, M.J., and Milsom, J.S., 2005, Sumatra: Geology, Resources, and Tectonic Evolution: London, Geological Society, 290 p.

Bird, P., 2003, An updated digital model of plate boundaries: G-Cubed, v. 4, doi: 10.1029/2001GC000252.

Chlieh, M., Avouac, J.-P., Hjorleifsdottir, V., Song, T.-R.A., Ji, C., Sieh, K., Sladen, A., Hebert, H., Prawirodirdjo, L., Bock, Y., and Galetzka, J., 2007, Coseismic slip and afterslip of the great Mw 9.15 Sumatra-Andaman earthquake of 2004: Bulletin of the Seismological Society of America, v. 97, p. S152– S173, doi: 10.1785/0120050631.

Curray, J.R., 2005, Tectonics and history of the Andaman Sea Region: Journal of Asian Earth Sciences, v. 25, p. 187–232, doi: 10.1016/j.jseaes.2004.09.001.

Engdahl, E.R., Villaseñor, A., DeShon, H.R., and Thurber, C.H., 2007, Teleseismic relocation and assessment of seismicity (1918–2005) in the region of the 2004 Mw 9.0 Sumatra-Andaman and 2005 Mw 8.6 Nias Island great earthquakes: Bulletin of the Seismological Society of America, v. 97, p. S43–S61, doi: 10.1785/0120050614.

Fisher, D., Mosher, D., Austin Jr., J.A., Gulick. S.P.S., Masterlark, T., and Moran, K., 2007, Active deformation across the Sumatran forearc over the December 2004 Mw 9.2 rupture: Geology, v. 35, p. 99–102, doi: 10.1130/G22993A.1.

Freed, A.M., Bürgmann, R., Calais, E., Freymueller, J., and Hreinsdóttir, S., 2006, Implications of deformation following the 2002 Denali, Alaska, earthquake for postseismic relaxation processes and lithospheric rheology: Journal of Geophysical Research, v. 111, doi: 10.1029/2005JB003894.

Gahalaut, V.K., Nagarajan, B., Catherine, J.K., and Kumar, S., 2006, Constraints on 2004 Sumatra-Andaman earthquake rupture from GPS measurements in Andaman-Nicobar Islands: Earth and Planetary Science Letters, v. 242, p. 365-374, doi: 10.1016/j.epsl.2005.11.051.

Geist, E.L., Titov, V.V., Arcas, D., Pollitz, F.F., and Bilek, S.L., 2007, Implications of the 26 December 2004 Sumatra-Andaman earthquake of tsunami forecast and assessment models for great subduction-zone earthquakes: Bulletin of the

Seismological Society of America, v. 97, p. S249–S270, doi: 10.1785/0120050619.

Gubbins, D., 2004, Time Series Analysis and Inverse Theory for Geophysicists: Cambridge, Cambridge University Press, 225 p.

Han, S.-C., Shum, C.K., Bevis, M., Ji, C., and Kuo, C.-Y., 2006, Crustal dilatation observed by GRACE after the 2004 Sumatra-Andaman earthquake: Science, v. 313, p. 658–662, doi: 10.1126/science.1128661.

Ioualalen, M., Asavanant, J., Kaewbanjak, N., Grilli, S.T., Kirby, J.T., and Watts, P., 2007, Modeling the 26 December 2004 Indian Ocean tsunami: Case study of impact in Thailand: Journal of Geophysical Research, v. 112, doi: 10.1029/2006JC003850.

Kieckhefer, R.M., Shor Jr., G.G., Curray, J.R., Sugiarta, W., and Hehuwat, F., 1980, Seismic refraction studies of the Sunda trench and forearc basin: Journal of Geophysical Research, v. 85, p. 863– 889.

Kopp, H., and Kukowski, N., 2003, Backstop geometry and accretionary mechanics of the Sunda margin: Tectonics, v. 22, doi: 10.1029/2002TC001420.

Kopp, H., Klaeschen, D., Flueh, E.R., Bialas, J., and Reichert, C., 2002, Crustal structure of the Java margin from seismic wide-angle and multichannel reflection data: Journal of Geophysical Research, v. 107, doi: 10.1029/2000JB000095.

Masterlark, T., 2003, Finite element model predictions of static deformation from dislocation sources in a subduction zone: Sensitivities to homogeneous, isotropic, Poisson-solid, and half-space assumptions: Journal of Geophysical Research, v. 108, doi: 10.1029/2002JB002296.

McCloskey, J., Antonioli, A., Piatanesi, A., Sieh, K., Steacy, S., Nalbant, S., Cocco, M., Giunchi, C., Huang, J., and Dunlop, P., 2008, Tsunami threat in the Indian Ocean from a future megathrust earthquake west of Sumatra: Earth and Planetary Science Letters, v. 265, p. 61–81, doi: 10.1016/j.epsl.2007.09.034.

Meltzner, A.J., Sieh, K., Abrams, M., Agnew, D.C., Hudnut, K.W., Avouac, J.-P., and Natawidjaja, D.H., 2006, Uplift and subsidence associated with the great Aceh-Andaman earthquake of 2004: Journal of Geophysical Research, v. 111, doi: 10.1029/2005JB003891.

Menke, W., 1989, Geophysical Data Analysis: Discrete Inverse Theory: San Diego, Academic Press, 289 p.

Nalbant, S.S., Steacy, S., Sieh, K., Natawidjaja, D., and McCloskey, J., 2005, Earthquake risk on the Sunda trench: Nature, v. 435, p. 756–757, doi: 10.1038/nature435756a.

Okada, Y., 1992, Internal deformation due to shear and tensile faults in a half-space: Bulletin of the Seismological Society of America, v. 82, p. 1018–1040.

Schmitt, S.V., DeMets, C., Stock, J., Sánchez, O., Márquez-Azúa, B., and Reyes, G., 2007, A geodetic study of the 2003 January 22 Tecomán, Colima, Mexico earthquake: Geophysical Journal International, v. 169, p. 389–406, doi: 10.1111/j.1365-246X.2006.03322.x.

Smith Jr., A.T., 1974, Time-dependent strain accumulation and release at island arcs: Implications for the 1946 Nankido earthquake, Ph.D. Thesis, MIT, 292 pp.

Sobolev, S.V., Babeyko, A.Y., Wang, R., Hoechner, A., Galas, R., Rothacher, M., Sein, D.V., Schröter, J., Lauterjung, J., and Subarya, C., 2007, Tsunami early warning using GPS-Shield arrays: Journal of Geophysical Research, v. 112, doi: 10.1029/2006JB004640.

Stein, S., and Okal, E.A., 2005, Speed and size of the Sumatra earthquake: Nature, v. 434, p. 581–582.

Subarya, C., Chlieh, M., Prawirodirdjo, L., Avouac, J.-P., Bock, Y., Sieh, K., Meltzner, A.J., Natawidjaja, D.H., and McCaffrey, R., 2006, Plate-boundary deformation associated with the great Sumatra-Andaman earthquake: Nature, v. 440, p. 46–51, doi: 10.1038/nature04522.

Turcotte, D.L., and Schubert, G.J., 1982, Geodynamics: Applications of Continuum Physics to Geological Problems: New York, John Wiley and Sons, 450 p.

Vigny, C., Simons, W.J.F., Abu, S., Bamphenyu, R., Satirapod, C., Coosakul, N., Subarya, C., Socquet, A., Omar, K., Abidin, H.Z., Ambrosius, B.A.C., 2005, Insight into the 2004 Sumatra-Andaman earthquake from GPS measurements in Southeast Asia: Nature, v. 436, p. 201–206, doi: 10.1038/nature03937.

Wang, H.F., 2000, Theory of Linear Poroelasticity: With Applications to Geomechanics: Princeton, Princeton University Press, 287 p.

Wang, H.F., and Anderson, M.P., 1982, Introduction to Groundwater Modeling: Finite Difference and Finite Element Methods: San Diego, Academic Press, 237 p.

APPENDIX

1. VALIDATION

Model validation is a necessary and critical step in the modeling process (Anderson and Woessner, 1992). There are many ways to simulate slip along a fault. Because we are treating the fault-slip as an elastic dislocation, we test the validity of the FEM configuration to ensure it is a correct representation of an elastic dislocation. This validation allows us to isolate the sensitivities of predictions to the distribution of material properties, rather than some other artifact of the FEM configuration. To perform the validation, we construct a modified version of the FEM that has uniform material properties and a unit of pure fault-slip imposed over all fault patches. A profile of displacement predictions for the free surface is extracted from a trench-normal section that trends East-West and corresponds to about 10 degrees N Latitude. The predicted displacements agree with the corresponding predictions for a two-dimensional homogeneous elastic half-space (HEHS) (e.g., Okada, 1992) (Fig. 3.4). The differences are subtle and likely caused by a combination of the finite extent of the FEM problem domain, the along-strike curvature of the simulated

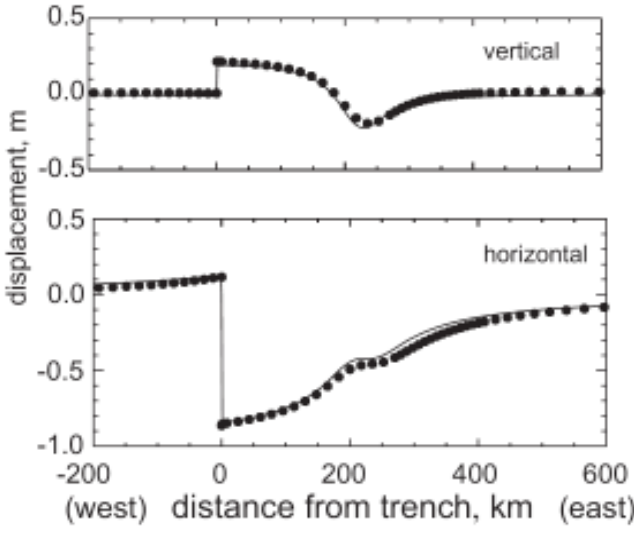

Figure 3.4. Validation. Vertical and horizontal predictions for deformation are calculated using an FEM (dots) and an HEHS (lines) (Okada, 1992). The simulated fault intersects the free surface and dips 12 degrees to the East over a length of 225 km. A unit of pure thrust is applied over the entire fault.

rupture, and the raised free surface of the overriding plate.

2. CALIBRATION

Quasi-static fault-slip can be simulated with an FEM as the dislocation of a node-pair, implemented via kinematic constraint equations (Masterlark, 2003; Smith, 1974). The curved surface of the rupture comprises an assembly of node-pairs along an internal boundary of the FEM problem domain. A vector of Green's Functions (GFs) is calculated by predicting the displacement of n GPS site positions caused by a unit dislocation for a given node-pair while simultaneously welding the remaining node-pairs. A matrix of GFs for the entire suite of m node-pairs is assembled by implementing an algorithm that systematically generates an FEM that has the unit dislocation and welding configuration over the rupture, executes the FEM, and extracts the predicted displacements caused by the dislocation of each node-pair. The forward solution for elastic deformation due to a distribution of dislocating node-pairs is:

$$\boldsymbol{G}\,\boldsymbol{s} = \boldsymbol{d} \tag{3.1}$$

where $\boldsymbol{G}$ is a matrix of GFs; s is a vector of dislocations; and $\boldsymbol{d}$ is a 1×n column vector of displacements. For both down-dip (dd) and strike-slip (ss) dislocations, $\boldsymbol{G}=(\boldsymbol{G}_{dd}, \boldsymbol{G}_{ss})$ and has dimensions of 2m×n. Similarly, the dislocation vector has dimensions 2m×1 and $\boldsymbol{s}=(\boldsymbol{s}_{dd}, \boldsymbol{s}_{ss})^{T}$. Each coefficient $\boldsymbol{G}_{ij}$ represents the contribution to the displacement of $\boldsymbol{d}_j$ due to unit dislocation of node-pair $\boldsymbol{s}_i$. Most importantly, this matrix of FEM-generated GFs is readily calculated for inverse analyses of deformation data for dislocations within a subduction zone (Masterlark, 2003).

Thus, FEMs permit us to simulate variable dislocations along fault surfaces embedded in a problem domain partitioned for the distribution of geologic material properties expected for the subduction zone.

We apply linear inverse methods to estimate the unknown slip distribution of the SAE, based on observed near-field GPS data (Table 3.1). We partition the curved rupture surface into a 25 (along-strike) × 7 (down-dip) grid of quadrilateral slip patches. Each patch comprises four node-pairs sharing slip characteristics. We then recast Eq. 3.1 into a forward model that when inverted, simultaneously 1) Estimates the slip distribution that minimizes misfit to GPS data, 2) Damps spurious solution oscillations, and 3) Accounts for the relative uncertainties of the GPS data. First, we pre-multiply Eq. 3.1 to account for the relative uncertainties of the data

$$\boldsymbol{WG}\,\boldsymbol{s} = \boldsymbol{Wd} = \boldsymbol{G_w}\,\boldsymbol{s} = \boldsymbol{d_w} \tag{3.2}$$

where $\boldsymbol{W}$ is a diagonal data weighting matrix constructed from reported GPS measurement uncertainties, $\boldsymbol{W_{ii}} = 1/\sigma_i$, (Table 3.1). Second, we reconfigure Eq. 3.2 using second-order Tikhonov regularization to damp the null space of the data kernel (Aster et al., 2005)

$$\left[\boldsymbol{G}_{\boldsymbol{W}}^{\mathrm{T}}\boldsymbol{G}_{\boldsymbol{W}} + \beta^2 \quad \boldsymbol{L}^{\mathrm{T}}\boldsymbol{L}\right]\boldsymbol{s} = \boldsymbol{G}_{\boldsymbol{W}}^{\mathrm{T}}\boldsymbol{d}_{\boldsymbol{W}} \qquad \text{and} \qquad \boldsymbol{L} = \begin{bmatrix} \boldsymbol{L}_{dd} & 0 \\ 0 & \boldsymbol{L}_{ss} \end{bmatrix} \tag{3.3}$$

where $\boldsymbol{L}$ is a 2m×2m matrix of coefficients for the finite difference approximation of the Laplacian operator. The boundaries of the rupture surface have Dirichlet (null) boundary conditions, which favor a smooth transition from slip to no-slip along the boundaries of the rupture (Wang and Anderson, 1982). The down-dip and strike-slip sub-matrices of $\boldsymbol{L}$ are independent of one another but share the boundary

condition specifications. The regularization parameter β controls the trade-off between minimizing misfit and satisfying the Laplacian smoothing. The least-squares solution to Eq. 3.3 is

$$\boldsymbol{s} = \left[\boldsymbol{G}_W^{\mathrm{T}}\boldsymbol{G}_W + \beta^2 \quad \boldsymbol{L}^{\mathrm{T}}\boldsymbol{L}\right]^{-1}\boldsymbol{G}_W^{\mathrm{T}}\boldsymbol{d}_W \tag{3.4}$$

We solve Eq. 3.4 by sweeping through beta parameter space to find optimal solutions for $\boldsymbol{s}$.

The least squares solution scheme simultaneously minimizes both prediction misfit and the roughness of the slip distribution for a given value of beta. Misfit is defined as the weighted prediction error, $\mathrm{e}^{\mathrm{T}}\boldsymbol{W}\,\mathrm{e}$, where e is the residual vector and the solution roughness is defined as $\boldsymbol{s}^{\mathrm{T}}\boldsymbol{L}^{\mathrm{T}}\boldsymbol{L}\boldsymbol{s}$. The value of beta controls the trade-off between misfit and roughness. As beta vanishes, the misfit is null but the fault-slip distribution is relatively rough. Conversely, as beta goes to infinity, the misfit becomes extreme but the fault-slip distribution is smooth. We construct an L-curve (Aster et al., 2005) to determine the

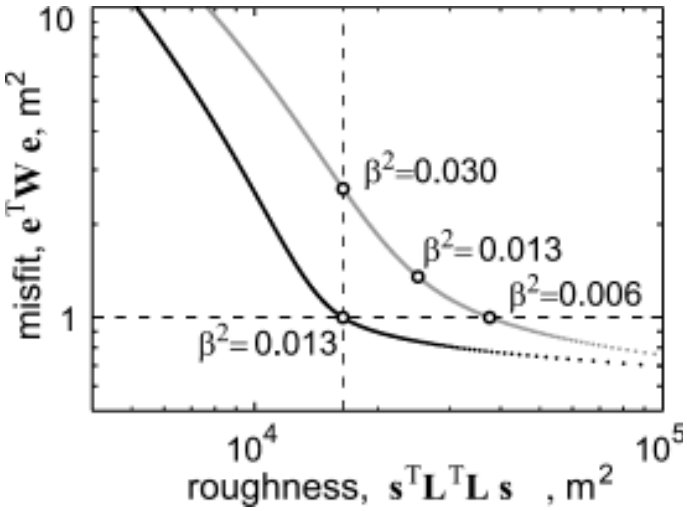

Figure 3.5. Calibration. L-curves (Aster et al., 2004) reveal the trade-off between misfit and solution roughness for the FEM (black dots) and HEHS model (gray dots). The weighted misfit for the FEM is unity for beta^2=0.013 and the preferred solution. The solutions for the FEM have slightly better misfit and smoothness characteristics compared to corresponding HEHS solutions. For purposes of comparison between the FEM and HEHS models, the preferred solution for both models is beta^2=0.013. Large circles highlight alternative solutions for corresponding misfit, roughness, or smoothing between FEM and HEHS models.

optimal fault-slip distribution, where the weighted misfit is unity (Gubbins, 2004) (Fig. 3.5). This is the preferred solution.

Table 3.1. Coseismic deformation data for 34 near-field GPS positions.

site	Lon	Lat	u_{east}	u_{north}	u_{up}	e_{east}	e_{north}	e_{up}	source
bm12	98.9449	2.64259	-0.0890	-0.0198	-0.0805	0.0666	0.0238	0.0733	a
d962	97.4465	1.68602	-0.0332	-0.0270	-0.0535	0.0649	0.0253	0.0558	a
D972	96.6245	2.17441	0.0100	-0.0246	-0.5710	0.0669	0.0649	0.0669	a
Jahe	98.5075	3.14524	-0.2031	-0.0218	0.0053	0.1079	0.0882	0.0899	a
k504	95.2435	5.43378	-2.1140	-1.7634	-0.1717	0.1057	0.0882	0.0597	a
K505	95.2716	5.48000	-2.0675	-1.7455	-0.0611	0.1034	0.0873	0.0807	a
K515	95.4873	5.56851	-1.6599	-1.3420	-0.0462	0.0830	0.0671	0.0637	a
LANG	97.9999	4.42753	-0.3681	-0.0989	-0.0119	0.0411	0.0426	0.0608	a
LHOK	97.1585	5.08665	-0.5779	-0.2190	0.0765	0.0434	0.0478	0.1054	a
MART	98.6823	2.52419	-0.1448	-0.0217	-0.1228	0.0414	0.0240	0.0869	a
NIND	98.7506	2.72953	-0.1312	-0.0065	-0.4546	0.0326	0.0230	0.0916	a
PAND	98.8188	1.67586	-0.0411	-0.0355	-0.0264	0.0418	0.0397	0.0277	a
PIDI	95.9333	5.33080	-1.3993	-0.9557	0.0354	0.0405	0.0388	0.0490	a
PISU	99.1472	2.44756	-0.0825	-0.0143	-0.0129	0.0277	0.0311	0.0617	a
SIPA	99.0890	2.10263	-0.1027	-0.0586	-0.1144	0.0662	0.0631	0.0699	a
TIGA	98.5622	2.91856	-0.1426	-0.0041	0.0452	0.0228	0.0236	0.0305	a
R171	95.3877	2.95996	-3.8209	-4.3221	2.0988	0.0859	0.2161	0.0458	a
R173	95.5183	4.60702	-2.8537	-2.3763	-0.6010	0.1427	0.1188	0.0420	a
R174	95.3654	4.84193	-2.7719	-2.4143	-0.5838	0.1386	0.1200	0.0841	a
R175	95.2030	5.24116	-2.4349	-2.0761	-0.2266	0.1217	0.1038	0.1211	a
R176	95.0572	5.71287	-2.1745	-1.7109	-0.1421	0.1087	0.0855	0.0908	a
ABAY	93.0270	13.27800	-3.9000	-2.7100	0.1900	0.0400	0.0100	0.0500	b
EAST	93.0470	13.63100	-3.6200	-2.5100	0.9600	0.0400	0.0200	0.0700	b
LONG	92.9320	12.37600	-1.9600	-1.1000	-0.4800	0.0200	0.100	0.0600	b
UGRH	92.7730	12.21600	-2.3900	-1.6600	-0.3600	0.0200	0.0100	0.0500	b
GOVI	92.9830	12.03600	-1.3600	-0.9500	-0.1800	0.0500	0.0200	0.0200	b
PBLR	92.7210	11.64900	-3.0700	-1.0300	-0.9600	0.0200	0.0100	0.0600	b
PASG	92.6760	11.17800	-2.9100	-1.1900	-0.7100	0.0200	0.0100	0.0500	b

HBAY	92.5690	10.69600	-3.2700	-2.6500	-0.2600	0.0100	0.0100	0.0200	b
CARN	92.8040	9.22500	-5.7600	-2.9500	-1.1100	0.0100	0.0100	0.0100	b
TERE	93.1240	8.30200	-5.8600	-3.0600	-2.8500	0.0200	0.0100	0.0400	b
KARD	93.5490	8.03600	-3.9700	-1.7200	-1.3500	0.0200	0.0100	0.0400	b
MERO	93.5410	7.51400	-4.9100	-2.8400	-2.1600	0.0200	0.0100	0.0500	b
CAMP	93.9340	7.00400	-4.1000	-2.3600	-1.6000	0.0200	0.0100	0.0300	b

Coseismic deformation of the 2004 M9 Sumatra-Andaman earthquake, measured for 34 near-field GPS positions. Displacements (u) and corresponding 1σ measurement uncertainties are given in meters. Data taken from sources; a = Subarya et al., 2006 and b = Gahalaut et al., 2006.

CHAPTER 4

POROELASTIC STRESS-TRIGGERING OF THE 2005 M8.7 NIAS EARTHQUAKE BY THE 2004 M9.2 SUMATRA-ANDAMAN EARTHQUAKE

Reprinted with permission from Elsevier and coauthors
Tim Masterlark, Ph.D., and Walter Mooney, Ph.D.

ABSTRACT

The M9.2 Sumatra-Andaman earthquake (SAE) occurred three months prior to the M8.7 Nias earthquake (NE). We propose that the NE was mechanically triggered by the SAE, and that poroelastic effects were a major component of this triggering. This study uses 3D finite element models (FEMs) of the Sumatra-Andaman subduction zone (SASZ) to predict the deformation, stress, and pore pressure fields of the SAE. The coseismic slip distribution for the SAE is calibrated to near-field GPS data using FEM-generated Green's Functions and linear inverse methods. The calibrated FEM is then used to predict the postseismic poroelastic contribution to stress-triggering along the rupture surface of the NE, which is adjacent to the southern margin of the SAE. The coseismic deformation of the SAE, combined with the rheologic configuration of the SASZ produces two transient fluid flow regimes having separate time constants. SAE coseismic pore pressures in the relatively shallow forearc and volcanic arc regions (within a few km depth)

dissipate within one month after the SAE. However, pore pressures in the oceanic crust of the down-going slab persist several months after the SAE. Predictions suggest that the SAE initially induced MPa-scale negative pore pressure near the hypocenter of the NE. This pore pressure slowly recovered (increased) during the three-month interval separating the SAE and NE due to lateral migration of pore fluids, driven by coseismic pressure gradients, within the subducting oceanic crust. Because pore pressure is a fundamental component of Coulomb stress, the MPa-scale increase in pore pressure significantly decreased stability of the NE fault during the three-month interval after the SAE and prior to rupture of the NE. A complete analysis of stress-triggering due to the SAE must include a poroelastic component. Failure to include poroelastic mechanics will lead to an incomplete model that cannot account for the time interval between the SAE and NE. Our transient poroelastic model explains both the spatial and temporal characteristics of triggering of the NE by the SAE.

INTRODUCTION

In northern Indonesia, the Indo-Australian plate obliquely subducts beneath the Burma microplate and Sunda plate. The complex tectonic setting transitions from oblique subduction off the west coast of Sumatra to almost complete right-lateral strike-slip motion near the Andaman and Nicobar Islands to the north (Fig. 4.1) (Bird, 2003). The 26 December 2004 Sumatra-Andaman earthquake (SAE) ruptured over 1200 km of the Indo-Australian and Burma plate boundary (Ammon et al., 2005; Bilek, 2007; Vigny et al., 2005). Three months later, the 28 March 2005 Nias earthquake (NE) ruptured

about 400 km of the same plate boundary immediately to the south of the SAE rupture (Ammon et al., 2005; Banerjee et al., 2007).

The southern boundary of the SAE rupture is thus a seismic barrier that divides slip on the megathrust into the northern Sumatra-Andaman and southern Nias segments (Fig. 4.1) (Ammon et al., 2005). The physical cause of this seismic

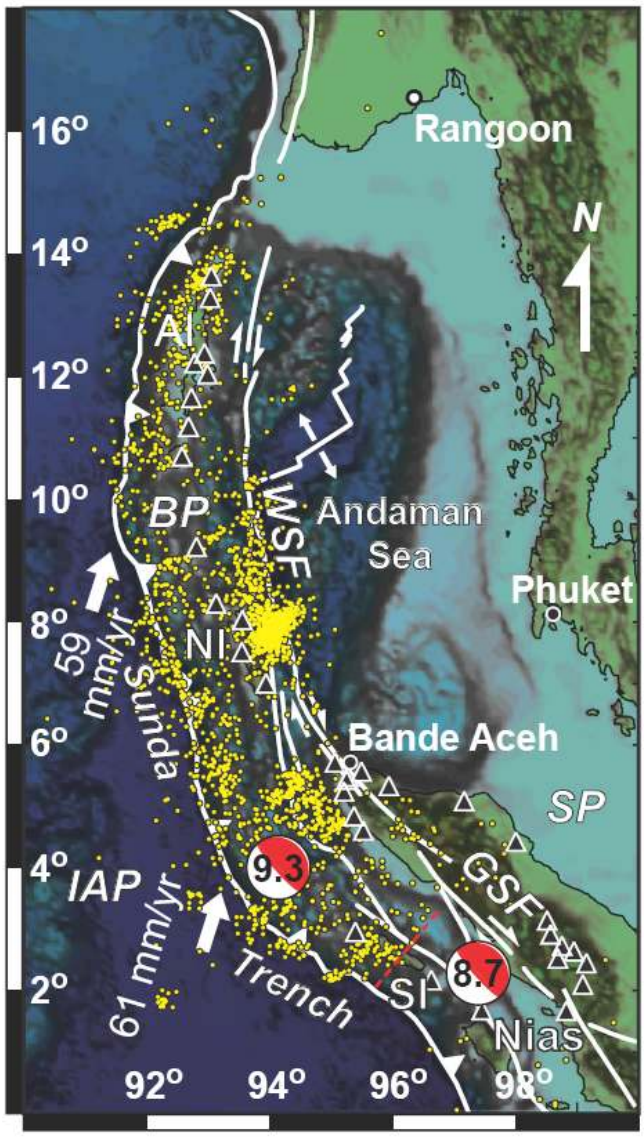

Figure 4.1. Seismotectonic setting of the SAE (adapted from Masterlark and Hughes (2008)). Harvard CMT Focal mechanisms are given for the 26 December 2004 (M9.2) and 28 March 2005 (M8.7) earthquakes. Aftershock epicenters (yellow dots), spanning 26 December 2004 through 28 March 2005, illuminate the surface projection of the M9.2 rupture (http://neic.usgs.gov). The rupture initiated on the southeast portion of the fault and propagated 1200 km northward. The sharply truncated aftershock distribution, shown with a NE-trending dashed line that bisects Simeulue Island, marks the boundary between rupture of the M9.2 and subsequent M8.7 events (seismic barrier). Black triangles are near-field GPS sites (Gahalaut et al., 2006; Subarya et al., 2006). The tectonic configuration is modified from Bird (2003) and overlies a shaded relief image of global relief data (http://www.ngdc.noaa.gov). Abbreviations are Andaman Islands (AI), Burma Plate (BP), Indo-Australian Plate (IAP), Nicobar Islands (NI), Simeulue Island (SI), Great Sumatran Fault (GSF), Sunda Plate (SP), and West Sumatra Fault (WSF).

barrier is likely due to a change in the seafloor morphology, associated with the northern extent of a series of prominent offshore islands that are the result of the uplift of the seafloor above the subducting oceanic ridge. The subduction of the extinct oceanic ridge may have caused a permanent kink in the subducting slab, which has been imaged by Pesicek et al. (2008). The seismic barrier also corresponds to a pronounced bend in the geometry of the oceanic trench at the toe of the megathrust (Fig. 4.1). Ridge subduction creates seismic barriers in numerous subduction zones worldwide (Gutscher et al., 1999; Ruff, 1996). The subduction of the Chile Rise at the southern terminus of the 1960 M_w = 9.5 megathrust earthquake is one example (Plafker and Savage, 1970). Seismic barriers may also correspond to changes in the coupling between the overriding plate and the subducting oceanic lithosphere at the megathrust due to the thinner sediment load above the subducting ridge. Seismic barriers thus correspond to a pronounced change in physical properties along the megathrust.

The coseismic and postseismic deformation of the SAE changed the stress regime of the Sumatra-Andaman subduction zone (SASZ). We propose that the M8.7 NE was triggered by the M9.2 SAE, based on the proximity of these two great earthquakes in both space and time. Previous stress-triggering analyses of the SAE predict that the SAE increased the Coulomb stress near the hypocenter of the NE (Gahalaut and Kalpna, 2005; McCloskey et al., 2005). However, neither of these analyses included a transient mechanism to account for the three-month interval separating the SAE and NE. Others suggest transient mechanisms, such as postseismic viscoelastic relaxation and afterslip, impose time-dependence on the

Coulomb stress, which thereby increases during the three-month interval between earthquakes and advanced the occurrence of the NE (Hsu et al., 2006; Mignan et al., 2006; Pollitz et al., 2006a). However, none of these previous analyses account for the pore pressure effects, which are known to significantly influence Coulomb stress calculations over time periods consistent with the separation of the SAE and NE events (Beeler et al., 2000; Masterlark, 2003; Masterlark and Wang, 2000; Masterlark and Wang, 2002). We construct poroelastic deformation models of the SAE to test the hypothesis that pore fluid pressure near the hypocenter of the NE continually increased during the three-month interval separating the SAE and NE. This increasing pore pressure translates to increasing Coulomb stress and thus predicts a systematic decrease in fault stability leading to the rupture of the NE.

METHODS

1. COULOMB STRESS

Stress-triggering is a mechanism for which a loading event, such as slip along a fault, changes the frictional stability of other faults in the near-field region. Coulomb stress calculations allow us to quantify the changes in tendency for frictional slip to occur along a locked, pre-existing fault. The change in Coulomb stress (σ_c) for a given fault is

$$\sigma_c = \sigma_s + f(\sigma_n + P) \tag{4.1}$$

where σ_s is shear stress parallel to a specified slip vector, σ_n is fault-normal stress (tension-positive), P is pore pressure, and f is the coefficient of friction (e.g., King et al., 1994; Masterlark and Wang, 2000). Positive values of the change in Coulomb

stress indicate an increased tendency for the fault to slip and negative values indicate increased stability. We assume that the state variables σ and *P* are incremental changes with respect to a reference state.

Fault-slip from an earthquake induces relatively instantaneous incremental changes in stress and pore pressure in the near-field region, while afterslip, poroelastic effects, viscoelastic relaxation, and interseismic strain accumulation drive transient changes in stress and pore pressure after an earthquake has occurred. Static (vis-à-vis quasi-static) stress-triggering analyses of the causal relationship between earthquakes are applicable for either short times (undrained conditions, negligible viscous relaxation) or long times (drained conditions, negligible deviatoric stresses in the viscous material) following a dislocation (Wang, 2000). Undrained or drained conditions imply either fluid-flux equals zero or pore pressure equals zero, respectively. Laboratory experiments on a variety of rocks indicate that the coefficient of friction is robust and lies between 0.65-0.85 (Byerlee, 1978).

Alternatively, changes in Coulomb stress are often calculated using the assumption that pore-pressure is proportional to the fault-normal stress rather than the mean-normal stress used in standard poroelastic theory (e.g., King et al., 1994; Stein, 1999). In this case, Eq. 4.1 is modified to

$$\sigma_c = \sigma_s + f'\sigma_n \tag{4.2}$$

where f' is an *apparent* coefficient of friction that is some unknown combination of material properties and transient fluid-flow conditions (Masterlark and Wang, 2000), such that f' is theoretically unbounded ($-\infty < f' < \infty$) (Beeler et al., 2000). The

assumption that pore-fluid pressure is proportional to fault-normal stress alone holds only if the fault zone is relatively compliant with respect to the surrounding materials (Cocco and Rice, 2002; Cocco and Rice, 2003). However, because Coulomb stress is often calculated for regions saturated with aftershocks along multiple faults (rather than a single fault), a problem domain including compliant fault zones no longer satisfies the homogeneous assumption required by standard analytical models for displacement due to an elastic dislocation (e.g., Okada, 1992). This problem can be extended to models that simulate distributions of material properties that do not include weak fault zones (Chlieh et al., 2007; Hsu et al., 2006; Masterlark and Hughes, 2008). Because of these contradictory assumptions, Eq. 4.2 leads to important prediction errors (Beeler et al., 2000; Masterlark, 2003; Masterlark and Wang, 2000).

2. Deformation Model

Deformation models provide the linkage between the observed surface deformation and the source of the deformation—the fault-slip at depth. While forward models allow us to predict deformation caused by fault-slip, inverse models estimate the distribution of fault-slip, based on observed deformation and pre-supposed deformation models. To delimit the geometry of the rupture surface, we can use geodetic or seismic data. In both cases, a model and some assumptions are required. For the SAE, the location of the rupture is constrained by seismicity (Fig. 4.1), seismogenic data (Ammon et al., 2005; Stein and Okal, 2005), and results from

previous modeling studies (Chlieh et al., 2007; Hughes and Masterlark, 2008; Masterlark and Hughes, 2008).

The 3D finite element model (FEM) presented in this study is designed to simulate coseismic and poroelastic postseismic deformation of the SAE, while simultaneously accounting for the known geologic structure of the subduction zone. We use the general-purpose FEM code Abaqus (http://www.simulia.com) to solve for displacement (u) and coupled displacement and pore-fluid pressure (u, P) over a 3D problem domain partitioned into elastic and poroelastic regions, respectively. The FEM is driven by a coseismic slip distribution calibrated to near-field GPS data. Rather than use a published slip distribution for the SAE, we calibrate the slip distribution via least-squares inverse methods that account for the distribution of material properties within the 3D problem domain of the FEM. Expressed in index notation, the governing equations for poroelastic materials are

$$G\nabla^2 u_i + \frac{G}{(1-2\nu)}\frac{\partial^2 u_k}{\partial x_i \partial x_k} = \alpha \frac{\partial P}{\partial x_i} - F_i \tag{4.3}$$

$$\alpha \frac{\partial \varepsilon_{kk}}{\partial t} + S_\varepsilon \frac{\partial P}{\partial t} = \frac{\kappa}{\mu_f}\nabla^2 P + Q \tag{4.4}$$

where G is the shear modulus, ν is Poisson's ratio (drained), α is the Biot-Willis coefficient, F is a body force per unit volume, $\varepsilon_{kk} = \Sigma \partial u_k / \partial x_k$ is the volumetric strain, S_ε is the constrained storage coefficient, κ is the permeability coefficient, and μ_f is the pore-fluid viscosity, and Q is a fluid source term defined as volume of fluid per unit bulk volume per unit time (Wang, 2000). The subscript i spans orthogonal direction components 1, 2, and 3 and the subscript k implies summation over these

three components. In this formulation, x_1, x_2, and x_3 are equivalent Cartesian coordinates x, y, and z (east, north, and vertical), respectively. Similarly, u_1, u_2, and u_3 are equivalent to u_x, u_y, and u_z, respectively. Viscoelastic behavior in the mantle is simulated by imposing an additional stress-dependent creep relationship. The total longitudinal equivalent strain is:

$$\varepsilon = \varepsilon_e + \varepsilon_f \quad \text{and} \quad \frac{d\varepsilon_f}{dt} = A\sigma_d^{\eta} \tag{4.5}$$

where ε_e is the elastic strain, ε_f is the strain due to viscous flow, A is a constant that can be augmented to account for temperature dependence, and σ_d is the deviatoric stress. The relationship is equivalent to a Maxwell material for $\eta = 1$ and A is half of the inverse of the linear viscosity (Turcotte and Schubert, 1982).

The governing equations for an elastic material are recovered from Eqs. 4.3, 4.4, and 4.5 by setting $P = 0$ and assuming steady-state conditions, with all time derivatives equal to zero. The governing equations for elastic materials are sufficient to describe limiting cases of drained (long time; $P = 0$) and undrained (short time; no fluid flow) static deformation, by substituting drained and undrained values of Poisson's ratios, respectively. However, a description of transient poroelastic deformation requires both Eqs. 4.3 and 4.4 (Wang, 2000).

3. FEM CONFIGURATION

Construction of the SAE FEM involves a series of steps. First, we design a trench-normal slice through the SASZ (Fig. 4.2). The fault-slip of the SAE occurs along the interface separating the subducting slab, consisting of depleted mantle

capped by mid-oceanic ridge basalt (MORB), and the overriding forearc (Kopp and Kukowski, 2003; Kopp et al., 2002) and enriched mantle wedge (Kieckhefer et al., 1980; Kopp et al., 2002; Kopp and Kukowski, 2003). Seismicity data (Engdahl et al., 2007) constrain the geometry of the subducting slab. The configurations of the volcanic arc and backarc basin regions are based on geologic maps and cross-sections of the SASZ (Barber et al., 2005).

Second, we sweep this two-dimensional cross section along the curving strike of the Sunda trench to produce a three-dimensional model (Fig. 4.2). This configuration implicitly assumes the geologic structure is constant along the trench. The tessellated problem domain comprises about 340,000 octahedral finite elements having trilinear interpolation basis functions and 1,000,000 degrees of freedom. The characteristic dimension for elements is a few kilometers near the fault and generally increases with distance from the fault. This tessellation is validated by Masterlark and Hughes (2008).

Third, we specify a distribution of rheologic properties over the partitioned problem domain (Fig. 4.2). The elastic and poroelastic properties are taken from compilations of laboratory experiments (Turcotte and Schubert, 1982; Wang, 2000). The elastic properties are in accord with seismic tomography and gravity data (Kieckhefer et al., 1980; Kopp et al., 2002; Kopp and Kukowski, 2003). This configuration is similar to that of Masterlark and Hughes (2008) and includes both lateral and vertical rheologic variations that correspond to the regional-scale geologic structure of a subduction zone. The viscoelastic rheology is specified for

the mantle only in a separate FEM used to predict long-term postseismic deformation discussed later.

Fourth, we specify boundary conditions and impose fault-slip. The far-field lateral boundaries and base of the problem domain are zero displacement. The top of the problem domain is a stress-free surface. The subducting slab and overriding

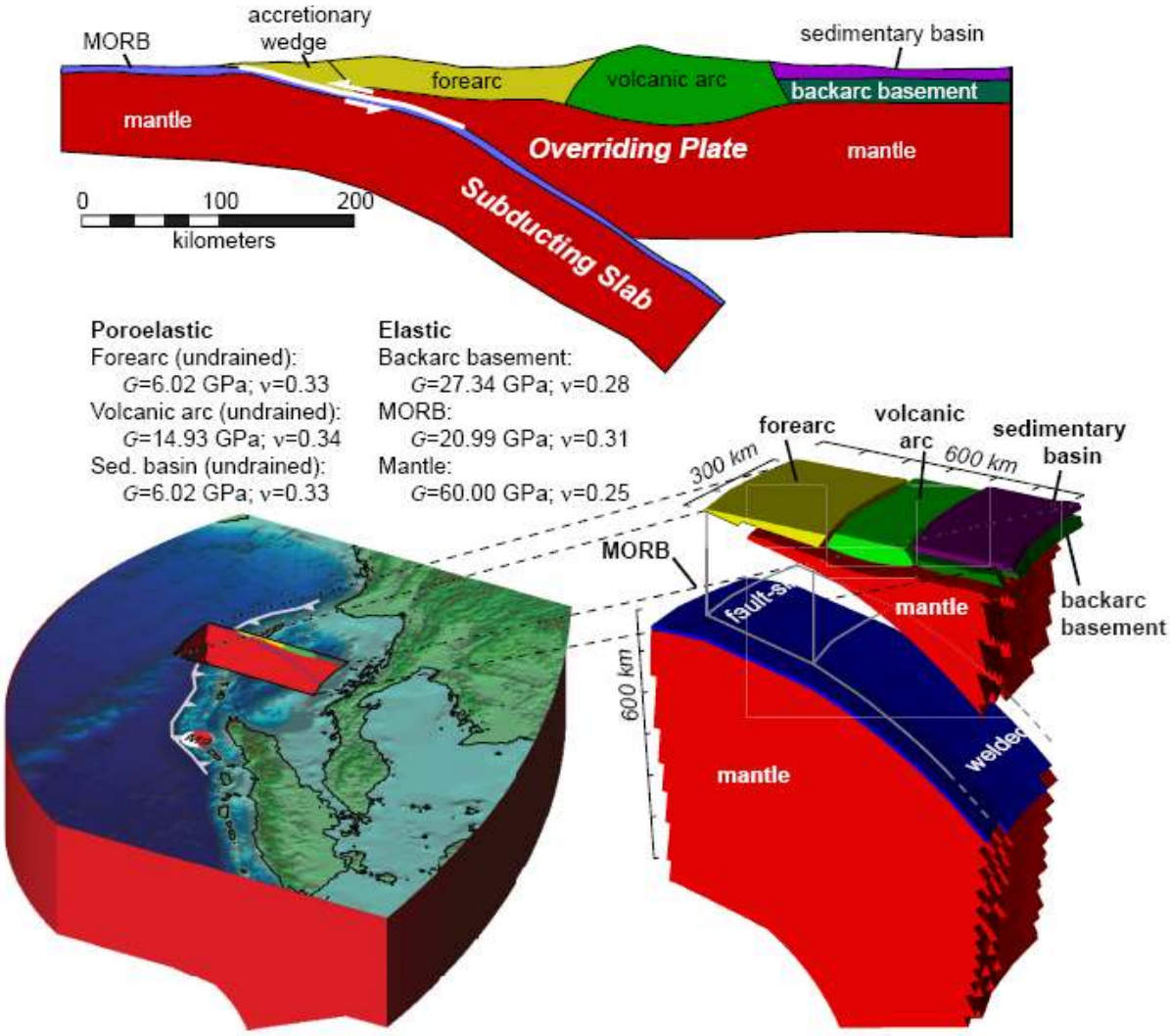

Figure 4.2. Conceptual model and FEM configuration (adapted from Masterlark and Hughes (2008)). (a) Conceptual model. This 2D profile illustrates the geologic structure of the subduction zone. (b) FEM design and configuration. The 3D FEM is constructed by sweeping the 2D profile along the curvature of the Sunda Trench. The FEM comprises about 340,000 elements. The top of the problem domain is a free-surface. Lateral and bottom boundaries are zero displacement. The exploded view reveals the likeness of the FEM to the conceptual model.

plate are welded together along the intersection of the fault and the trench. Quasi-static fault-slip can be simulated with an FEM as the dislocation of a node-pair, implemented via kinematic constraint equations (Masterlark, 2003; Masterlark and Hughes, 2008; Melosh and Raefsky, 1981; Smith, 1974). The curved surface of the rupture comprises an assembly of node-pairs along an internal boundary of the FEM problem domain. A vector of Green's Functions (GFs), for displacement due to slip along a fault, is calculated by predicting the displacement of GPS site positions caused by a unit dislocation for a given node-pair while simultaneously welding the remaining node-pairs. A matrix of GFs for the entire suite of *m* node-pairs is assembled by implementing an algorithm that systematically generates the unit dislocation and welding configurations over the rupture, executes the FEM, and extracts the predicted displacements caused by the dislocation of each node-pair.

A slip event induces relatively instantaneous incremental changes in stress and pore pressure and coseismic deformation is thus undrained. Therefore, the (undrained) coseismic deformation is calculated using the simplified elastic governing equations, having undrained values of Poisson's ratio substituted into the poroelastic portions of the problem domain. This is a useful result because m separate FEM calculations are required to assemble the matrix of GFs and the computation time for an elastic FEM is substantially lower than that of a coupled poroelastic FEM. The forward solution for elastic deformation due to a distribution of dislocating node-pairs is

$$\boldsymbol{G\,m = d} \tag{4.6}$$

where $\boldsymbol{G}$ is a matrix of GFs; $\boldsymbol{m}$ is a vector of dislocations; and $\boldsymbol{d}$ is a $1\times n$ column vector of three-component displacements and/or displacement derivatives of the GPS site positions that can be time-dependent. For both down-dip (*dd*) and strike-slip (*ss*) dislocations, $\boldsymbol{G} = (\boldsymbol{G}_{dd}\ \boldsymbol{G}_{ss})$ and has dimensions of $2m\times n$. Similarly, the dislocation vector has dimensions $2m$ and $\boldsymbol{m} = (\boldsymbol{m}_{dd}\ \boldsymbol{m}_{ss})^{T}$. Each coefficient $\boldsymbol{G}_{ij}$ represents the contribution to the displacement of $\boldsymbol{d}_j$ due to unit dislocation of node-pair $\boldsymbol{m}_i$. Most importantly, this matrix of FEM-generated GFs is readily calculated for inverse analyses of deformation data for dislocations embedded in an arbitrary domain (Masterlark, 2003; Masterlark and Hughes, 2008). Thus, FEMs permit us to simulate variable dislocations along fault surfaces embedded in a problem domain partitioned into the 3D rheologic configuration expected for the SASZ.

4. Inverse Methods

We apply linear inverse methods to calibrate the slip distribution of the SAE, based on observed near-field displacement data from 34 GPS sites in the near-field region. These data are compiled from previous studies (Gahalaut et al., 2006; Subarya et al., 2006) and span northern Sumatra and the Nicobar and Andaman Islands (Table 4.1). We limit our study to near-field deformation data because the relative data importance (Menke, 1989) of far-field GPS sites (more than a fault-width from the rupture) is insignificant compared to that of GPS sites within the surface projection of the rupture for a megathrust event (Hutton et al., 2001). We partition the curved rupture surface, indicated by the distribution of aftershocks (Fig. 4.1), into a 25 (along-strike) × 7 (down-dip) grid of quadrilateral slip patches.

Each patch comprises four node-pairs sharing slip characteristics. We then recast Eq. 4.6 into a forward model that when inverted, simultaneously 1) Estimates the slip distribution that minimizes misfit to GPS data, 2) Imposes positive thrust and right-lateral strike-slip components, 3) Damps spurious solution oscillations, and 4) Accounts for the relative uncertainties of the GPS data. First, we pre-multiply Eq. 4.6 to account for the relative uncertainties of the data

$$\boldsymbol{WG\,m = Wd = G_w\,m = d_w} \tag{4.7}$$

where $\boldsymbol{W}$ is a diagonal data weighting matrix constructed from reported GPS measurement uncertainties, $\boldsymbol{W}_{ii} = 1/\sigma_i$, (Table 4.1). Second, we reconfigure Eq. 4.7 using second-order Tikhonov regularization to damp the null space of the data kernel (Aster et al., 2005)

$$\left(\boldsymbol{G}_w^{\mathrm{T}}\boldsymbol{G}_w + \beta^2\boldsymbol{L}^{\mathrm{T}}\boldsymbol{L}\right)\boldsymbol{m} = \boldsymbol{G}_w^{\mathrm{T}}\boldsymbol{d}_w \quad \text{and} \quad \boldsymbol{L} = \begin{pmatrix} \boldsymbol{L}_{dd} & 0 \\ 0 & \boldsymbol{L}_{ss} \end{pmatrix} \tag{4.8}$$

where $\boldsymbol{L}$ is a $2m \times 2m$ matrix of coefficients for the finite difference approximation of the Laplacian operator for $\nabla^2\boldsymbol{m} = 0$ over the 2D rupture surface. The down-dip and strike-slip sub-matrices of $\boldsymbol{L}$ are independent of one another but share the boundary condition specifications; along-strike and down-dip boundaries are set to Dirichlet (null) boundary conditions and the up-dip boundary is set to Neumann specifications ($\partial\boldsymbol{m}/\partial x = 0$) (Fig. 4.3a) (Wang and Anderson, 1982). The regularization parameter β controls the tradeoff between minimizing misfit and satisfying the Laplacian operator. The least-squares solution to Eq. 4.8 is (Aster et al., 2004)

$$\boldsymbol{m} = (\boldsymbol{G}_w^{\mathrm{T}}\boldsymbol{G}_w + \beta^2\boldsymbol{L}^{\mathrm{T}}\boldsymbol{L})^{-1}\ \boldsymbol{G}_w^{\mathrm{T}}\ \boldsymbol{d}_w \tag{4.9}$$

Table 4.1. Near-field GPS data.

			Displacement, m			1σ, m		
site	Lon, °E	Lat, °N	east	north	up	east	north	up
Subarya et al., 2006								
bm12	98.9449	2.64259	-0.0890	-0.0198	-0.0805	0.0666	0.0238	0.0733
d962	97.4465	1.68602	-0.0332	-0.0270	-0.0535	0.0649	0.0253	0.0558
D972	96.6245	2.17441	0.0100	-0.0246	-0.5710	0.0669	0.0649	0.0669
jahe	98.5075	3.14524	-0.2031	-0.0218	0.0053	0.1079	0.0882	0.0899
k504	95.2435	5.43378	-2.1140	-1.7634	-0.1717	0.1057	0.0882	0.0597
K505	95.2716	5.48000	-2.0675	-1.7455	-0.0611	0.1034	0.0873	0.0807
K515	95.4873	5.56851	-1.6599	-1.3420	-0.0462	0.0830	0.0371	0.0637
LANG	97.9999	4.42753	-0.3681	-0.089	-0.0119	0.0411	0.0426	0.0608
LHOK	97.1585	5.08665	-0.5779	-0.2190	0.0765	0.0434	0.0478	0.1054
MART	98.6823	2.52419	-0.1448	-0.0127	-0.1228	0.0414	0.0240	0.0869
NIND	98.7506	2.72953	-0.1312	-0.0065	-0.4546	0.0326	0.0230	0.0916
PAND	98.8188	1.67586	-0.0411	-0.0355	-0.0264	0.0418	0.0397	0.0277
PIDI	95.9333	5.33080	-1.3993	-0.9557	0.0354	0.0405	0.0388	0.0490
PISU	99.1472	2.44756	-0.0825	-0.0143	-0.0129	0.0277	0.0311	0.0617
SIPA	99.0890	2.10263	-0.1027	-0.0586	-0.1144	0.0662	0.0631	0.0699
TIGA	98.5622	2.91856	-0.1426	-0.0041	0.0452	0.0228	0.0236	0.0305
R171	95.3877	2.95996	-3.8209	-4.3221	2.0988	0.0859	0.2161	0.0458
R173	95.5183	4.60702	-2.8537	-2.3763	-0.6010	0.1427	0.1188	0.0420
R174	95.3654	4.84193	-2.7719	-2.4143	-0.5838	0.1386	0.1200	0.0841
R175	95.2030	5.24116	-2.4349	-2.0761	-0.2266	0.1217	0.1038	0.1211
R176	95.0572	5.71287	-2.1745	-1.7109	-0.1421	0.1087	0.0855	0.0908
Gahalaut et al., 2006								
ABAY	93.0270	13.27800	-3.9000	-2.7100	0.4900	0.0400	0.0100	0.0500
EAST	93.0470	13.63100	-3.6200	-2.5100	0.9600	0.0400	0.0200	0.0700
LONG	92.9320	12.34600	-1.9600	-1.1000	-0.4800	0.0200	0.0100	0.0600
UGRH	92.7730	12.21600	-2.3900	-1.6600	-0.3600	0.0200	0.0100	0.0500
GOVI	92.9830	12.03600	-1.3600	-0.9500	-0.1800	0.0500	0.0200	0.0200
PBLR	92.7210	11.64900	-3.0700	-1.0300	-0.9600	0.0200	0.0100	0.0600
PASG	92.6760	11.17800	-2.9100	-1.1900	-0.7100	0.0200	0.0100	0.0500
HBAY	92.5690	10.69600	-3.2700	-2.6500	-0.2600	0.0100	0.0100	0.0200
CARN	92.8040	9.22500	-5.7600	-2.9500	-1.1100	0.0400	0.0100	0.1000
TERE	93.1240	8.30200	-5.8600	-3.0600	-2.8500	0.0200	0.0100	0.0400
KARD	93.5490	8.03600	-3.9700	-1.7200	-1.3500	0.0200	0.0100	0.0400
MERO	93.5410	7.51400	-4.9100	-2.8400	-2.1600	0.0200	0.0100	0.0500
CAMP	93.9340	7.00400	-4.1000	-2.3600	-1.6000	0.0200	0.0100	0.0300

We solve Eq. 4.9, subject to positivity constraints (Menke, 1989), while sweeping through β parameter space to find optimal solutions for ***m***. The positivity constraints require that solutions contain combinations of thrust and right-lateral

strike-slip. These positivity constraints are different from Masterlark and Hughes (2008) where solutions were allowed to contain both thrust and normal components. In the absence of these constraints, solutions for $\boldsymbol{m}$ will include more oscillatory distributions having both normal and left-lateral slip regions that are not compatible with the focal mechanism (Fig. 4.1), even though these unconstrained solutions fit the GPS data better than their constrained counterparts.

RESULTS

We wish to select a solution that gives a balance of misfit and smoothness. The generalized cross validation method (GCV) provides a means for selecting an optimal regularization parameter by minimizing the functional V(β)

$$V(\beta) = \frac{n \left\| \boldsymbol{G}_w \boldsymbol{m}_\beta - \boldsymbol{d}_w \right\|_2^2}{\text{Trace}\left[\boldsymbol{I} - \left(\boldsymbol{G}_w^T \boldsymbol{G}_w + \beta^2 \boldsymbol{L}^T \boldsymbol{L} \right)^{-1} \boldsymbol{G}^T \right]^2} \tag{4.10}$$

where $\boldsymbol{I}$ is a $2m \times 2m$ identity matrix and $\boldsymbol{m}_\beta$ is the solution of Eq. 4.9 for a given regularization parameter (Aster et al., 2004). GCV results suggest $\beta^2 = 0.006$ is statistically the best solution (Fig. 4.3b). This slip distribution is rather rough and includes an unrealistic slip maximum of ≥ 100 m along the northeast edge of the rupture. Other investigators report similar problems of GCV results producing rough solutions and having slip magnitudes that are much too high (Freymueller et al., 1994). Alternatively, we can use the trade-off curve for roughness versus misfit (Gubbins, 2004) and a priori fault-slip constraints to identify a slip distribution that simultaneously minimizes roughness and misfit and has a maximum slip magnitude of about 30 meters

(Fig. 4.3c) in accord with other studies, as discussed below. This is our preferred solution.

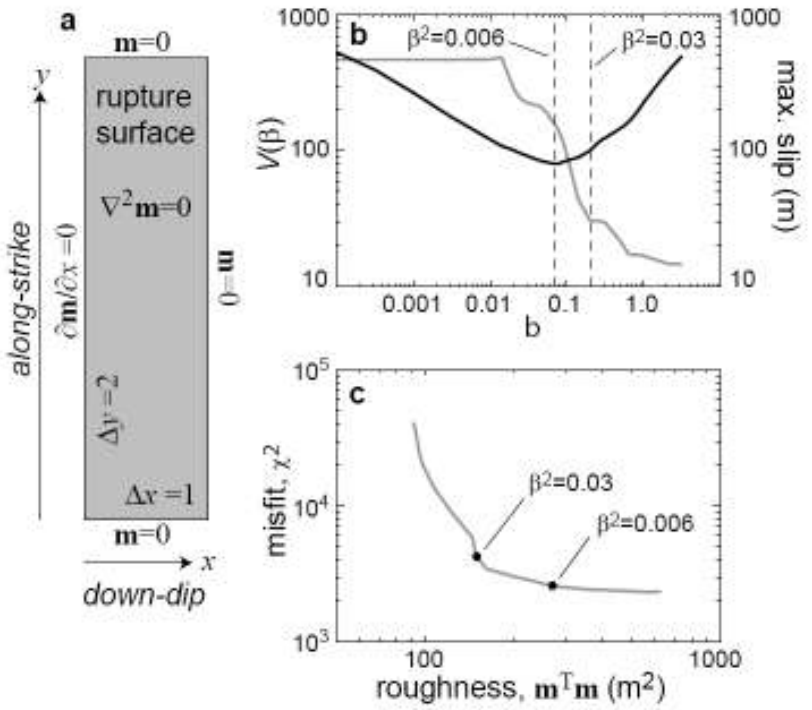

Figure 4.3. Inverse methods. (a) Smoothing. A Laplacian operator is applied via finite-difference methods to smooth the estimated slip distribution. (b) GCV and maximum slip versus β. The optimal solution (β^2=0.006), according to GCV, includes an unrealistic fault-slip maximum of more than 100 meters. (c) Tradeoff curve for roughness versus misfit. A value of β^2=0.03, our preferred solution, occurs at the knee of the curve. This solution produces a good balance of misfit and roughness, as well as a maximum fault-slip of about 30 meters.

Fault-slip is concentrated along the up-dip portion of the rupture that is west of northern Sumatra. A band of lower magnitude fault-slip occurs sub-parallel to the Sunda Trench and beneath the Nicobar and Andaman Islands (Fig. 4.4). This pattern is reasonably well resolved (Fig. 4.4b), based on the diagonal elements of the parameter resolution matrix, $\boldsymbol{R}_m$ (Aster et al., 2004)

$$\boldsymbol{R}_m = (\boldsymbol{G}_w^{\mathrm{T}}\mathbf{G}_w + \beta^2\boldsymbol{L}^{\mathrm{T}}\boldsymbol{L})^{-1}\ \boldsymbol{G}_w^{\mathrm{T}}\ \boldsymbol{G}_w \qquad (4.11)$$

The small patch of significant slip at the northern edge of the rupture (Fig. 4.4a) is probably a numerical artifact, reflecting some aspect of the FEM that fails to adequately represent some unknown complexity in that region of the SASZ. Resolving this issue is the subject of ongoing analyses and beyond the scope of this

study. Nonetheless, this misfit near the northern edge of the SAE rupture does not influence predictions for the southern portion of the SAE, the focus of this study. The pattern of shallow fault-slip, concentrated west of northern Sumatra, is consistent with seismological estimates (Ammon et al., 2005; Rhie et al., 2007) and tsunami-genesis results (Fujii and Satake, 2007; Grilli et al., 2007; Ioualalen et al., 2007). However, geodetic based analyses (Chlieh et al., 2007) place the majority of fault-slip near the Nicobar Islands. Our calibrated slip distribution (Fig. 4.4a) is applied to a 3D FEM to predict the transient postseismic poroelastic deformation. In this FEM, the accretionary wedge, forearc, volcanic arc, and backarc sedimentary basin are poroelastic materials (Fig. 4.2). The oceanic crust capping the subducting slab is also poroelastic to a depth of 50 km, the maximum limit of rupture depth (Hyndman, 2007). The top (free surface) and lateral boundaries of the poroelastic materials are no-flow boundaries.

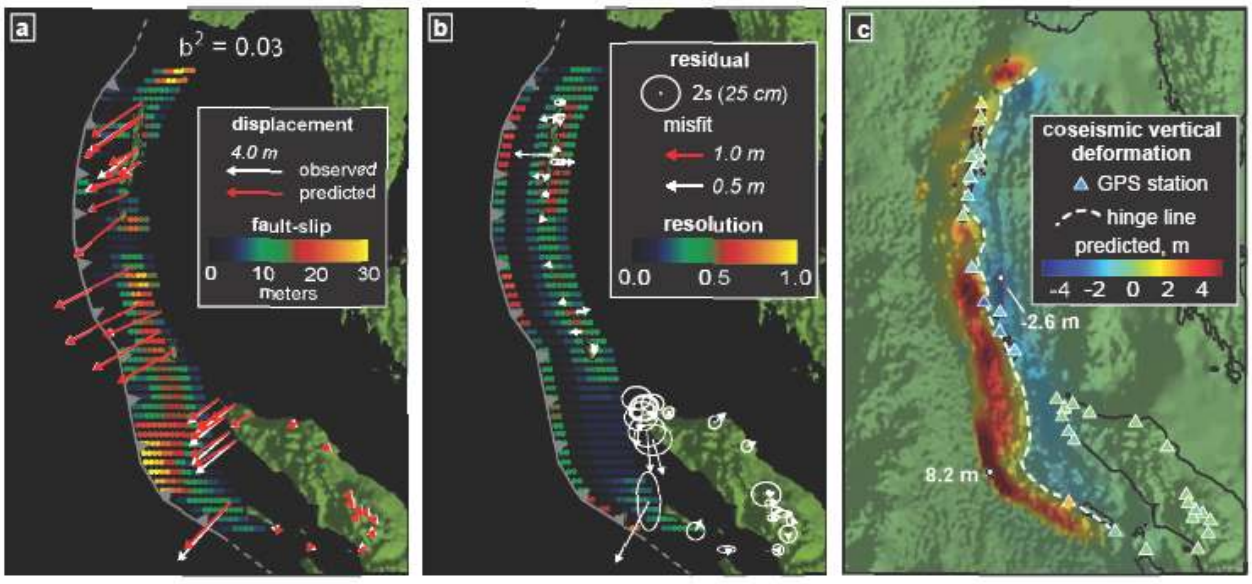

Figure 4.4. Predicted slip and deformation of the SAE (adapted from Masterlark and Hughes (2008)). (a) Estimated fault-slip distribution and deformation predictions. (b) Parameter resolution and prediction misfit. (c) Vertical deformation. The predicted hinge line delimits zero vertical deformation and agrees with field observations (Meltzner et al., 2006).

The permeability of the poroelastic materials is $\kappa = 10^{-16}$ m^2, an estimate for the bulk permeability of oceanic crust (Masterlark, 2003). The poroelastic properties of the oceanic crust are constrained by laboratory permeability experiments (Wang, 2000; Fisher, 1998) and seismological observations (Audet et al., 2009), and limited by the time interval between the two earthquakes (Fig. 4.5). Bulk permeability for the oceanic crust above 1×10^{-16} m^2 cannot account for the time delay between earthquakes due to rapid pore pressure re-equilibration, and bulk permeability below 1×10^{-17} m^2 is not geologically reasonable for cold, brittle subducting oceanic crust (Fisher, 1998; Christensen and Ramananantoandro, 1988). Additionally, the seismological observations of the Cascadian subduction zone indicate that the permeability contrast between the permeable oceanic crust and the overlying mantle wedge is more significant (1 to 4 orders of magnitude) than the actual bulk permeability assigned (Audet et al., 2009). We utilize an impermeable overlying plate on the time scale of the poroelastic model, which is geologically reasonable (Audet et al., 2009) due to the fact that the poroelastic effects occur within days to months. Audet and others (2009) determined the interface of the seismogenic zone between the subducting oceanic crust and overlying plate to have a permeability of 5×10^{-25} to 5×10^{-22} m^2 which is much lower than the permeability of the actual oceanic crust. Including this permeability instead of a no flow boundary would not significantly change our results.

Our model simulates the relatively instantaneous coseismic poroelastic deformation and subsequent transient poroelastic deformation over the 90-day time interval between the SAE and NE. The coseismic distributions of deformation,

stress, and pore pressure are initial conditions for the postseismic poroelastic deformation model. The uncertainties within these initial conditions rest on the assumptions of rheology, permeability, slip distribution, and boundary conditions of the FEM. We constrain these assumptions based on geological and seismological evidence for the SASZ (Barber et al., 2005; Kopp et al., 2002; Kopp and Kukowski, 2003; Pesicek et al., 2008). We ran multiple analyses of the FEM using varying permeability and rheology parameters and slip distributions. From these analyses, we deduce that the pore pressures range from 10^5 to 10^7. Furthermore, the sensitivity to the slip distribution was tested using an average slip of 15.25 meters for each fault patch. We found that the postseismic poroelastic results of the FEM were robust and did not change our conclusions. Following the coseismic time step, pore pressures range from -1.4 to 1.6 MPa in the deep forearc (about 10 km depth) and -2.7 to 4.1 MPa in the subducting oceanic crust near the seismic barrier (Table 4.2 and Fig. 4.6a). Additionally, the coseismic slip introduces significant pore pressure changes in the subducting oceanic crust

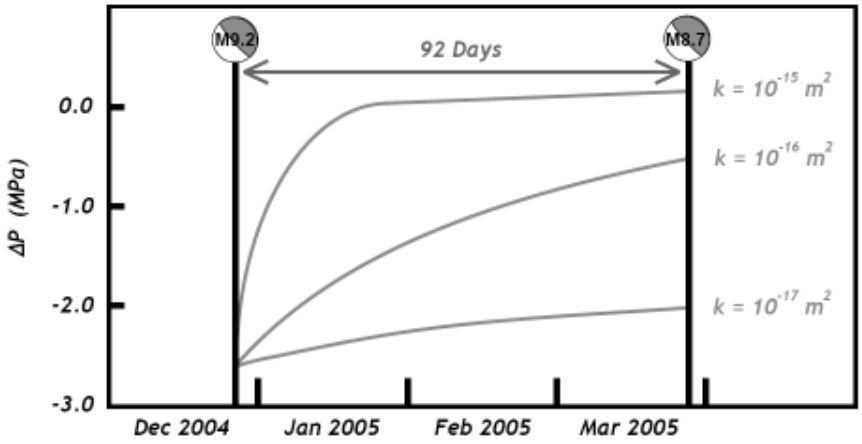

Figure 4.5. Poroelastic stress-triggering due to the SAE. The poroelastic model allows for pore pressure recovery following the SAE. Various bulk permeabilities were examined for the subducting oceanic crust. A bulk permeability above 1×10^{-16} m^2 cannot account for the 90 day time interval between earthquakes. A bulk permeability below 1×10^{-17} m^2 has not been shown to be geologically reasonable (Wang, 2000; Fisher, 1998; Christensen and Ramananantoandro, 1988).

Table 4.2. Pore pressure maxima and minima.

		Near Seismic Barrier, MPa		Whole Model, MPa	
Location	Time Step	Max	Min	Max	Min
Forearc (4°N/94°E)	Beginning	1.6	-1.4	4.1	-3.6
Forearc (4°N/94°E)	End	0.4	-0.5	0.7	-1.4
Oceanic Crust (2°N/97°E)	Beginning	4.1	-2.7	7.5	-4.4
Oceanic Crust (2°N/97°E)	End	0.7	-0.7	2.0	-1.3

south of the SAE rupture, along the rupture surface of the NE, but prior to the NE. At the conclusion of the model (two days before the NE), pore pressures range from -0.5 to 0.4 MPa in the deep forearc and from -0.7 to 0.7 MPa in the subducting oceanic crust near the seismic barrier (Fig. 4.6c). The predicted postseismic increase in pore pressure near the NE hypocenter, and thus Coulomb stress, is two orders of magnitude greater than the minimal threshold, 10 kPa (Toda et al., 1998), believed to trigger slip.

DISCUSSION

Although we focus on pore pressure changes near the NE hypocenter, the range of pore pressure in the subducting oceanic crust increases when considering the whole model (Table 4.2). The absolute changes in pore pressure far from the seismic barrier are 4.1 MPa and 0.7 MPa for the coseismic (initial conditions) and 90-day time step, respectively. Absolute changes in pore pressure near the seismic barrier are -2.7 and -0.7 MPa for corresponding time steps. That is, the pore pressure near the hypocentral location of the NE increased by 2.0 MPa during the 3-month interval separating the SAE and NE (Fig. 4.5). These predictions suggest that the coseismic pore pressure distribution leads to a more persistent flow regime near the seismic barrier.

The pore pressures in the shallow forearc and volcanic arc recover relatively quickly within about a month of the coseismic rupture (Fig. 4.6b). In contrast, the pore pressure recovery in the subducting oceanic crust takes several months, even though the specified permeability is constant for all poroelastic materials in the FEM. Furthermore, the pore pressure changes in the subducting oceanic crust north of Sumatra recover more quickly than the maxima and minima near the seismic barrier. Since the specified permeability and pore fluid boundary conditions are constant for all poroelastic materials in the FEM, this variation in recovery time is due to the down-dip variation in slip over the rupture surface combined with the

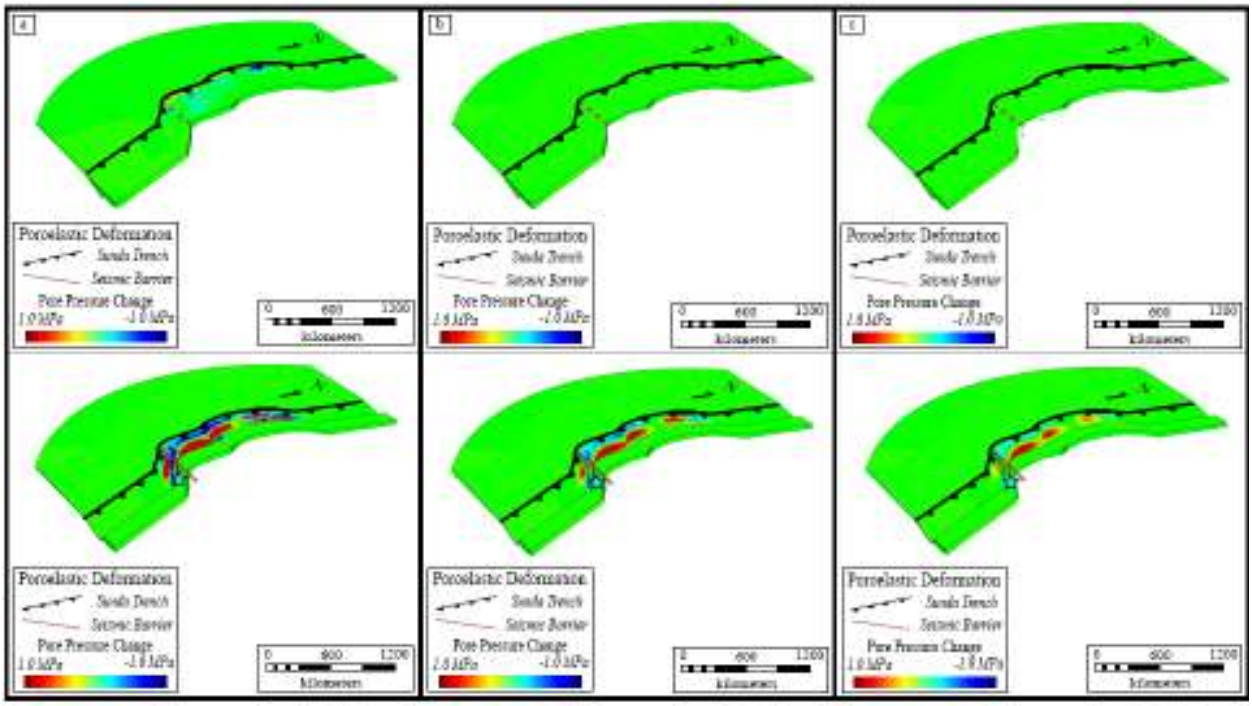

Figure 4.6. Pore pressure recovery following the SAE. (a) First time segment (coseismic poroelastic deformation). (b) Middle time segment (45 days after coseismic dynamic rupture). (c) Last time segment (two days before Nias earthquake). Red solid or dashed line represents location of the seismic barrier in the subducting oceanic crust. Teal star represents NE hypocentral location. Top row of images includes forearc poroelastic deformation. In the bottom row of images the forearc has been stripped away to view the subducting oceanic crust.

geometric configuration of the poroelastic oceanic crust near the down-dip limit of the rupture being "sandwiched" between relatively impermeable mantle of the underlying slab and overlying mantle wedge. That is, the geometric configuration of rheologic properties and boundary conditions can introduce multiple "apparent" deformation time constants even if the parameters that control the time dependence (e.g., permeability) are constant. This has implications for studies of postseismic deformation, for which it is customary to assign postseismic deformation mechanisms according to characteristic time constants of observed deformation epochs (Paul et al., 2007; Pollitz et al., 2006b).

The increase in pore pressure (2.0 MPa) southeast of the seismic barrier, and near the hypocentral location of the NE, translates to systematic increases in Coulomb stress (Eq. 4.1) and thus the systematic decrease in fault stability following the SAE. We envision triggering of the SAE and NE in both space and time as a two step (impulse and response) process. First, the oceanic crust juxtaposed to the seismic barrier experiences an increase in Coulomb stress (McCloskey et al., 2005) and decrease in pore pressure (Fig. 4.6a) due to the coseismic rupture of the SAE (the impulse). Second, as time progresses fluids flow and re-equilibrate in response to the coseismic pore pressure gradients in the region of decreased pore pressure near the hypocentral location of the NE (the response). Following the SAE, fluids migrate from regions of high pore pressure to regions of low pore pressure. In this flow regime, fluids migrate both up-dip and down-dip to the edge of the seismogenic zone, as well as laterally (along-strike) within the subducting oceanic crust. This lateral migration of fluids within the subducting oceanic crust occurs along the

rupture zone of the SAE, as well as through the seismic barrier to the south of the SAE rupture near the NE hypocenter. Thus, poroelastic effects may correspond to increasing changes in Coulomb stress due to slow re-equilibration and lateral migration of pore fluids within the subducting oceanic crust. Lateral migration of fluids demonstrated here has also been proposed to account for migration of slow slip events in subduction zones elsewhere (Melbourne et al., 2005).

The predicted increase in pore pressure (2.0 MPa) for the NE hypocentral region directly correlates to positive changes in Coulomb stress (Eq. 4.1) that are two orders of magnitude greater than corresponding Coulomb stress increases predicted for viscoelastic models of postseismic deformation (Pollitz et al., 2006a). Furthermore, the timing of postseismic poroelastic relaxation near the NE hypocenter is consistent with the three-month interval separating the SAE and NE. Therefore, the predicted coseismic distribution of pore pressure for the SAE and timing of postseismic poroelastic relaxation produce Coulomb stress changes of sufficient magnitude to account for both the spatial and temporal proximity of the SAE and NE.

The stress released by the coseismic fault-slip propagates into the region surrounding the fault. The response of the near-field region to this stress depends on the rheologic partitioning. There are three mechanisms (all of which have been demonstrated in laboratory and field measurements) that contribute to postseismic deformation--afterslip, viscoelastic relaxation, and poroelastic relaxation. Additionally, interseismic strain accumulation continues during all stages of the earthquake cycle, except during the relatively instantaneous coseismic slip.

Considering the sheer size of the SAE, contributions from all three postseismic deformation mechanisms are expected to be significant. Previous studies calibrate the afterslip and viscoelastic relaxation parameters to near-field GPS measurements (Chlieh et al., 2007; Paul et al., 2007).

Poroelastic deformation is not considered because the other two mechanisms dominate the measured near-field postseismic deformation. Comparatively speaking, the expected magnitude of viscoelastic deformation is expected to be five times greater than that of the poroelastic deformation for the SAE (Fig. 4.7). A similar dominance of viscoelastic (compared to poroelastic) postseismic deformation was predicted for other subduction zone earthquakes (Masterlark et al., 2001). Nonetheless, the predicted poroelastic deformation is expected to be a significant contributor to the observed GPS measurements, particularly for the vertical deformation of the Nicobar Islands and the islands west of northern Sumatra (Fig. 4.7). In contrast to the dominance of viscoelastic postseismic deformation, the poroelastic contribution to postseismic Coulomb stress changes near the NE hypocenter is much greater than that of the corresponding viscoelastic contribution. This suggests that postseismic poroelastic effects are important, particularly for earthquake stress-triggering analyses.

We propose treating the predicted poroelastic deformation as a correction to postseismic deformation data, as is customary for predicted interseismic strain accumulation. This addresses the bias inherent to interpretations that are based on a single mechanism and neglect the other contributions. For example, the rheologic (viscosity) structure proposed by Pollitz et al. (2006a) to account for postseismic

deformation of the SAE does not require any afterslip. Alternatively, the afterslip distribution proposed by Hashimoto et al. (2006) to account for this same deformation does not require any viscoelastic relaxation. Such studies based on a single postseismic deformation mechanism introduce unknown bias and suppress the reliability of interpretations and predictions. Compared to afterslip and

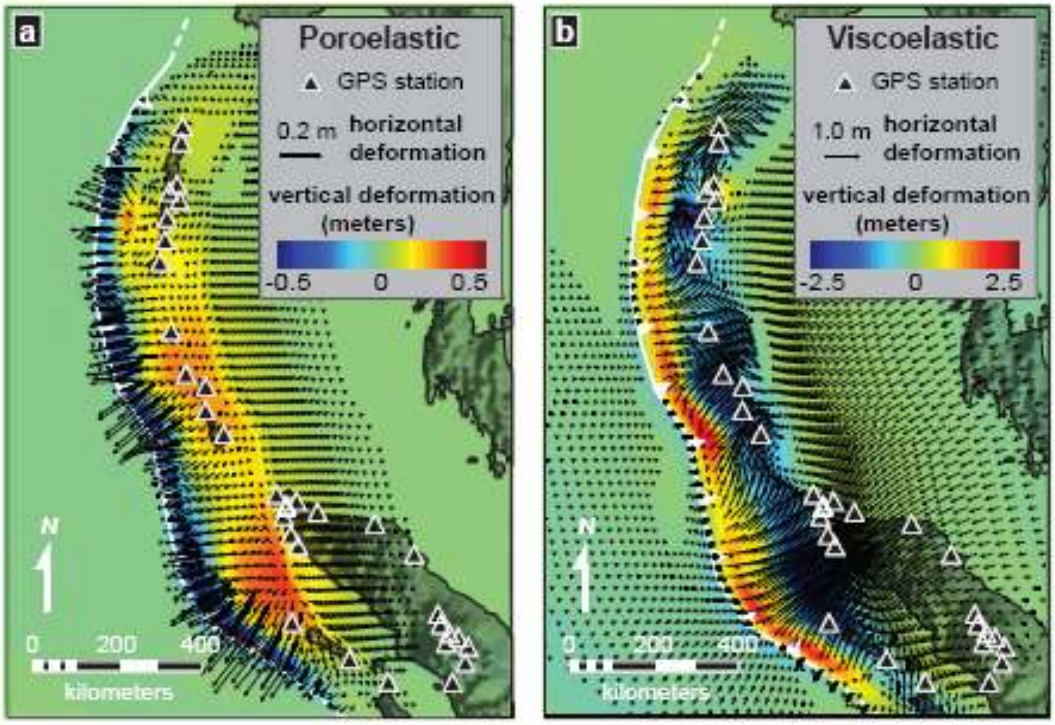

Figure 4.7. Predicted poroelastic and viscoelastic deformation of the SAE. The slip model of Masterlark and Hughes (2008) drives the FEM shown in Figure 2. Colors and arrows represent vertical and horizontal deformation, respectively, with respect to the coseismic deformation field. Arrows are not plotted for predicted horizontal displacements less than 1 cm. (a) Poroelastic deformation. Postseismic poroelastic deformation is complete several months after the SAE. Measurable poroelastic deformation is primarily limited to the surface projection of the rupture, due to the distribution of coseismic slip and geometric configuration of rheologic properties. The horizontal deformation is maximum (a few tens-of-centimeters) where the coseismic nodal plane intersects the land surface. Unfortunately, this region of predicted maximum horizontal poroelastic deformation is offshore and no GPS sites are available to verify the predictions. However, substantial poroelastic uplift is predicted for the Nicobar Islands. (b) Viscoelastic deformation. Viscoelastic relaxation is calculated for a period of 10 years following the SAE ($\mu = 10^{18}$ Pa•s). Magnitudes of viscoelastic deformation are about 5 times greater than those of poroelastic relaxation. However, the direction of displacements differs for the different deformation mechanisms.

viscoelastic relaxation, the poroelastic deformation will most certainly not explain a large portion of the observed postseismic deformation. In fact, the character of poroelastic deformation may be contrary to some displacement observations (e.g., Paul et al., 2007). If we then rule out poroelastic deformation altogether in favor of some other mechanism (say afterslip, which has many more adjustable parameters), we are assuming that either fluids are not present in the crust or that poroelastic behavior is insignificant. However, fluids are present in the crust (e.g., Nur and Walder, 1990, and references therein) and their presence and significance in an accretionary prism are clear (e.g., Moore et al., 2007). Furthermore, as demonstrated here, poroelastic contributions are significant for explaining the delayed triggering of the NE due to the SAE.

CONCLUSIONS

We present a quantitative analysis of poroelastic deformation of the SAE and stress-triggering of the NE. We estimate the slip distribution for the SAE from near-field GPS data using linear inverse methods and FEM-generated Green's Functions, which account for the distribution of material properties of the SASZ. The estimated slip distribution then drives a forward model that simulates poroelastic processes induced by the SAE. The poroelastic structure of the SASZ produces two flow regimes having two separate time constants. Pore pressure, and thus poroelastic deformation, decays rapidly (~1 month) in the shallow forearc and volcanic arc of the overriding plate. This relatively rapid recovery in pore pressure may help to explain the timing and location of near-field aftershock swarms (Fig. 4.1) (Piombo et

al., 2005). The timing for pore pressure recovery is more sluggish (several months) in the oceanic crust of the down-going slab due, in part, to the geometric configuration of the poroelastic oceanic crust being "sandwiched" between relatively impermeable mantle of the underlying slab and overlying mantle wedge (Audet et al., 2009). In particular, the pore pressure southeast of the seismic barrier and near the hypocenter of the NE slowly, but systematically, recovers during the three-month interval separating the SAE and NE. This suggests that transient pore pressure contributes significantly to the spatial and temporal proximity of these two events.

A complete explanation of stress-triggering initiated by the SAE must include poroelastic effects. It is well-known that a transient pore pressure pulse can trigger transient seismicity (Raleigh et al., 1976) and changes in pore pressure in this study and previous studies have been shown to contribute to changes in Coulomb stress at the same magnitude as normal and shear stresses (Eq. 4.1) (e.g., 2001 M7.6 Bhuj earthquake, 1995 M8 Jalisco, Mexico earthquake, and 1992 M7.3 Landers earthquakes) (Bosl and Nur, 2002; Gahalaut et al., 2008; Masterlark, 2003; Masterlark and Wang, 2000; Masterlark and Wang, 2002). By extension, if pore pressure is an important contributor to analyses of stress-triggering, then poroelastic deformation should not be neglected from postseismic deformation analyses, even if other postseismic deformation mechanisms dominate the deformation signal. The FEM-based techniques presented here allow for simulating the evolution of coseismic and postseismic deformation, stress, and pore pressure

due to megathrust earthquakes in subduction zones having complex geometric configurations of rheologic properties.

REFERENCES

Ammon, C.J., Ji, C., Thio, H.K., Robinson. D., Ni, S., Hjorleifsdottir, V., Kanamori, H., Lay, T., Das, S., Helmberger, D., Ichinose, G., Polet, J., and Wald, D., 2005, Rupture process of the 2004 Sumatra-Andaman Earthquake: Science, v. 308, p. 1133–1139, doi: 10.1126/science.1112260.

Aster, R., Borchers, B., and Thurber, C., 2005, Parameter Estimation and Inverse Problems: Elsevier Academic Press, 301 p.

Audet, P., Bostock, M.G., Christensen, N.I., and Peacock, S.M., 2009, Seismic evidence for overpressured subducted oceanic crust and megathrust fault sealing: Nature, v. 457, p. 76-78, doi: 10.1038/nature07650.

Banerjee, P., Pollitz, F., Nagarajan, B., and Bürgmann, R., 2007, Coseismic slip distributions of the 26 December 2004 Sumatra-Andaman and 28 March 2005 Nias earthquakes from GPS static offsets: Bulletin of the Seismological Society of America, v. 97, p. S86-S102, doi: 10.1785/0120050609.

Barber, A. J., Crow, M.J., and Milsom, J.S., 2005, Sumatra: Geology, Resources, and Tectonic Evolution: London, Geological Society, 290 p.

Beeler, N.M, Simpson, R.W., Hickman, S.H., and Lockner, D.A., 2000, Pore fluid pressure, apparent friction, and Coulomb failure: Journal of Geophysical Research, v.105, p. 25533-25542.

Bilek, S.L., 2007, Using earthquake source durations along the Sumatra-Andaman subduction system to examine fault-zone variations: Bulletin of the Seismological Society of America, v. 97, p. S62-S70, doi: 10.1785/0120050622.

Bird, P., 2003, An updated digital model of plate boundaries: G-Cubed, v. 4, doi: 10.1029/2001GC000252.

Bosl, W.J., and Nur, A., 2002, Aftershocks and pore fluid diffusion following the 1992 Landers earthquake: Journal of Geophysical Research, v. 107, doi: 10.1029/2001JB000155.

Byerlee, J., 1978, Friction of rocks: Pageoph, v. 116, p. 615-626.

Chlieh, M., Avouac, J.-P., Hjorleifsdottir, V., Song, T.-R.A., Ji, C., Sieh, K., Sladen, A., Hebert, H., Prawirodirdjo, L., Bock, Y., and Galetzka, J., 2007, Coseismic slip and afterslip of the great Mw 9.15 Sumatra-Andaman earthquake of 2004: Bulletin of the Seismological Society of America, v. 97, p. S152–S173, doi: 10.1785/0120050631.

Christensen, N.I., and Ramananantoandro, R., 1988, Permeability of the oceanic crust based on experimental studies of basalt permeability at elevated pressures: Tectonophysics, v. 149, p. 181-186.

Cocco, M., and Rice, J.R., 2002, Pore pressure and poroelasticity effects in Coulomb stress analysis of earthquake interactions: Journal of Geophysical Research, v. 107, doi: 10.1029/2000JB000138.

Cocco, M., and Rice, J.R., 2003, Correction to "Pore pressure and poroelasticity effects in Coulomb stress analysis of earthquake interactions": Journal of Geophysical Research, v. 108, doi: 10.1029/2002JB002319.

Engdahl, E.R., Villaseñor, A., DeShon, H.R., and Thurber, C.H., 2007, Teleseismic relocation and assessment of seismicity (1918–2005) in the region of the 2004 Mw 9.0 Sumatra-Andaman and 2005 Mw 8.6 Nias Island great earthquakes: Bulletin of the Seismological Society of America, v. 97, p. S43–S61, doi: 10.1785/0120050614.

Fisher, A.T., 1998, Permeability within basaltic oceanic crust: Reviews of Geophysics, v. 36, p. 143-182.

Freymueller, J., King, N.E., and Segall, P., 1994, The co-seismic slip distribution of the Landers earthquake: Bulletin of the Seismological Society of America, v. 84, p. 646-659.

Fujii, Y., and Satake, K., 2007, Tsunami source of the 2004 Sumatra-Andaman earthquake inferred from tide gauge and satellite data: Bulletin of the Seismological Society of America, v. 97, p. S192-S207, doi: 10.1785/0120050613.

Gahalaut, K., Gahalaut, V.K., and Kayal, J.R., 2008, Poroelastic relaxation and aftershocks of the 2001 Bhuj earthquake, India: Tectonophysics, v. 460, p. 76-82, doi: 10.1016/j.tecto.2008.07.004.

Gahalaut, V.K., and Kalpna, 2005, 28 March 2005 Sumatra earthquake: Expected, triggered or aftershock?: Current Science, v. 89, p. 452-454.

Gahalaut, V.K., Nagarajan, B., Catherine, J.K., and Kumar, S., 2006, Constraints on 2004 Sumatra-Andaman earthquake rupture from GPS measurements in

Andaman-Nicobar Islands: Earth and Planetary Science Letters, v. 242, p. 365-374, doi: 10.1016/j.epsl.2005.11.051.

Grilli M.ASCE, S.T., Ioualalen, M., Asavanant, J., Shi, F., Kirby M.ASCE, J.T., and Watts, P., 2007, Source constraints and model simulation of the December 26, 2004, Indian Ocean tsunami: Journal of Waterway, Port, Coastal, and Ocean Engineering, v. 133, p. 414-428, doi: 10.1061/(ASCE)0733-950X.

Gubbins, D., 2004, Time Series Analysis and Inverse Theory for Geophysicists: Cambridge, Cambridge University Press, 225 p.

Gutscher, M.-A., Malavieille, J., Lallemand, S., and Collot, J.-Y., 1999, Tectonic segmentation of the North Andean margin: Impact of the Carnegie Ridge collision: Earth and Planetary Science Letters, v. 168, p. 255-270.

Hashimoto, M., Choosakul, N., Hashizume, M., Takemoto, S., Takiguchi, H., Fukuda, Y., and Fujimori, K., 2006, Crustal deformations associated with the great Sumatra-Andaman earthquake deduced from continuous GPS observation: Earth Planets Space, v. 58, p. 127-139.

Hsu, Y.-J., Simons, M., Avouac, J.-P., Galetzka, J., Sieh, K., Chlieh, M., Natawidjaja, D., Prawirodirdjo, L., and Bock, Y., 2006, Frictional afterslip following the 2005 Nias-Simeulue earthquake, Sumatra: Science, v. 312, p. 1921-1926, doi: 10.1126/science.1126960.

Hughes, K.L.H., and Masterlark, T., 2008, Slip distribution for the 2004 Sumatra-Andaman earthquake constrained by both GPS data and tsunami run-up measurements: Bollettino di Geofisica: Teorica ed Applicata, v. 49, p. 165-169.

Hutton, W., DeMets, C., Sánchez, O., Suárez, G., and Stock, J., 2001, Slip kinematics and dynamics during and after the 1995 October 9 M_w = 8.0 Colima-Jalisco earthquake, Mexico, from GPS geodetic constraints: Geophysical Journal International, v. 146, p. 637-658.

Hyndman, R.D., 2007, The seismogenic zone of subduction thrust faults: What we know and what we don't know, *in* Dixon, T.H., and Moore, J.C., ed., The Seismogenic Zone of Subduction Thrust Faults, New York, Columbia University Press, p. 15-40.

Ioualalen, M., Asavanant, J., Kaewbanjak, N., Grilli, S.T., Kirby, J.T., and Watts, P., 2007, Modeling the 26 December 2004 Indian Ocean tsunami: Case study of impact in Thailand: Journal of Geophysical Research, v. 112, doi: 10.1029/2006JC003850.

Kieckhefer, R.M., Shor Jr., G.G., Curray, J.R., Sugiarta, W., and Hehuwat, F., 1980, Seismic refraction studies of the Sunda trench and forearc basin: Journal of Geophysical Research, v. 85, p. 863– 889.

King, G.C.P., Stein, R.S., and Lin, J., 1994, Static stress changes and the triggering of earthquakes: Bulletin of the Seismological Society of America, v. 84, p. 935-953.

Kopp, H., Klaeschen, D., Flueh, E.R., Bialas, J., and Reichert, C., 2002, Crustal structure of the Java margin from seismic wide-angle and multichannel reflection data: Journal of Geophysical Research, v. 107, doi: 10.1029/2000JB000095.

Kopp, H., and Kukowski, N., 2003, Backstop geometry and accretionary mechanics of the Sunda margin: Tectonics, v. 22, doi: 10.1029/2002TC001420.

Masterlark, T., 2003, Finite element model predictions of static deformation from dislocation sources in a subduction zone: Sensitivities to homogeneous, isotropic, Poisson-solid, and half-space assumptions: Journal of Geophysical Research, v. 108, doi: 10.1029/2002JB002296.

Masterlark, T., DeMets, C., Wang, H.F., Sánchez, O., and Stock, J., 2001, Homogeneous vs heterogeneous subduction zone models: Coseismic and postseismic deformation: Geophysical Research Letters, v. 28, p. 4047-4050.

Masterlark, T., and Hughes, K.L.H., 2008, Next generation of deformation models for the 2004 M9 Sumatra-Andaman earthquake: Geophysical Research Letters, v. 35, doi: 10.1029/2008GL035198.

Masterlark, T., and Wang, H., 2000, Poroelastic coupling between the 1992 Landers and Big Bear earthquakes: Geophysical Research Letters, v. 27, p. 3647-3650.

Masterlark, T., and Wang, H.F., 2002, Transient stress-coupling between the 1992 Landers and 1999 Hector Mine, California, earthquakes: Bulletin of the Seismological Society of America, v. 92, p. 1470-1486.

McCloskey, J., Nalbant, S.S., and Steacy, S., 2005, Earthquake risk from co-seismic stress: Nature, v. 434, p. 291.

Melbourne, T.I., Szeliga, W.M., Miller, M.M., and Santillan, V.M., 2005, Extent and duration of the 2003 Cascadia slow earthquake: Geophysical Research Letters, v. 32, doi: 10.1029/2004GL021790.

Melosh, H.J., and Raefsky, A., 1981, A simple and efficient method for introducing faults into finite element computations: Bulletin of the Seismological Society of America, v. 71, p. 1391-1400.

Meltzner, A.J., Sieh, K., Abrams, M., Agnew, D.C., Hudnut, K.W., Avouac, J.-P., and Natawidjaja, D.H., 2006, Uplift and subsidence associated with the great Aceh-Andaman earthquake of 2004: Journal of Geophysical Research, v. 111, doi: 10.1029/2005JB003891.

Menke, W., 1989, Geophysical Data Analysis: Discrete Inverse Theory: San Diego, Academic Press, 289 p.

Mignan, A., King, G., Bowman, D., Lacassin, R., and Dmowska, R., 2006, Seismic activity in the Sumatra-Java region prior to the December 26, 2004 (M_w=9.0-9.3) and March 28, 2005 (M_w=8.7) earthquakes: Earth and Planetary Science Letters, v. 244, p. 639-654, doi: 10.1016/j.epsl.2006.01.058.

Moore, G.F., Bangs, N.L., Taira, A., Kuramoto, S., Pangborn, E., and Tobin, H.J., 2007, Three-dimensional splay fault geometry and implications for tsunami generation: Science, v. 318, p. 1128-1131, doi: 10.1126/science.1147195.

Nur, A., and Walder, J., 1990, Time-dependent hydraulics of the Earth's crust, *in* National Research Council, ed., The Role of Fluids in Crustal Processes, Washington, D.C., National Academy Press, p. 113-127.

Okada, Y., 1992, Internal deformation due to shear and tensile faults in a half-space: Bulletin of the Seismological Society of America, v. 82, p. 1018–1040.

Paul, J., Lowry, A.R., Bilham, R., Sen, S., and Smalley Jr., R., 2007, Postseismic deformation of the Andaman Islands following the 26 December, 2004 great Sumatra-Andaman earthquake: Geophysical Research Letters, v. 34, doi: 10.1029/2007GL031024.

Pesicek, J.D., Thurber, C.H., Widiyantoro, S., Engdahl, E.R., and DeShon, H.R., 2008, Complex slab subduction beneath northern Sumatra: Geophysical Research Letters, v. 35, doi: 10.1029/2008GL035262.

Piombo, A., Martinelli, G., and Dragoni, M., 2005, Post-seismic fluid flow and Coulomb stress changes in a poroelastic medium: Geophysical Journal International, v. 162, p. 507-515, doi: 10.1111/j.1365-246X.2005.02673.x.

Plafker, G., and Savage, J.C., 1970, Mechanism of the Chilean earthquakes of May 21 and 22, 1960: Geological Society of America Bulletin, v. 81, p. 1001-1030.

Pollitz, F.F., Banerjee, P., Bürgmann, R., Hashimoto, M., and Choosakul, N., 2006a, Stress changes along the Sunda trench following the 26 December 2004 Sumatra-Andaman and 28 March 2005 Nias earthquakes: Geophysical Research Letters, v. 33, doi: 10.1029/2005GL024558.

Pollitz, F.F., Bürgmann, R., and Banerjee, P., 2006b, Post-seismic relaxation following the great 2004 Sumatra-Andaman earthquake on a compressible self-gravitating Earth: Geophysical Journal International, v. 167, p. 397-420, doi: 10.1111/j.1365-246X.2006.03018.x.

Raleigh, C.B., Healy, J.H., and Bredehoeft, J.D., 1976, An experiment in earthquake control at Rangely, Colorado: Science, v. 191, p. 1230-1237.

Rhie, J., Dreger, D., Bürgmann, R., and Romanowicz, B., 2007, Slip of the 2004 Sumatra-Andaman earthquake from joint inversion of long-period global seismic waveforms and GPS static offsets: Bulletin of the Seismological Society of America, v. 97, p. S115-S127, doi: 10.1785/0120050620.

Ruff, L.J., 1996, Large earthquakes in subduction zones: Segment interaction and recurrence times, *in* Bebout, G.E., Scholl, D.W., Kirby, S.H., and Platt, J.P., ed., Subduction: Top to Bottom, Washington, D.C., American Geophysical Union, p. 91-104.

Smith Jr., A.T., 1974, Time-dependent strain accumulation and release at island arcs: Implications for the 1946 Nankido earthquake, Ph.D. Thesis, MIT, 292 pp.

Stein, R.S., 1999, The role of stress transfer in earthquake occurrence: Nature, v. 402, p. 605-609.

Stein, S., and Okal, E.A., 2005, Speed and size of the Sumatra earthquake: Nature, v. 434, p. 581–582.

Subarya, C., Chlieh, M., Prawirodirdjo, L., Avouac, J.-P., Bock, Y., Sieh, K., Meltzner, A.J., Natawidjaja, D.H., and McCaffrey, R., 2006, Plate-boundary deformation associated with the great Sumatra-Andaman earthquake: Nature, v. 440, p. 46–51, doi: 10.1038/nature04522.

Toda, S., Stein, R.S., Reasenberg, P.A., Dieterich, J.H., and Yoshida, A., 1998, Stress transferred by the 1995 M_w = 6.9 Kobe, Japan, shock: Effect on aftershocks and future earthquake probabilities: Journal of Geophysical Research, v. 103, p. 24543-24565.

Turcotte, D.L., and Schubert, G.J., 1982, Geodynamics: Applications of Continuum Physics to Geological Problems: New York, John Wiley and Sons, 450 p.

Vigny, C., Simons, W.J.F., Abu, S., Bamphenyu, R., Satirapod, C., Coosakul, N., Subarya, C., Socquet, A., Omar, K., Abidin, H.Z., Ambrosius, B.A.C., 2005, Insight into the 2004 Sumatra-Andaman earthquake from GPS measurements in Southeast Asia: Nature, v. 436, p. 201–206, doi: 10.1038/nature03937.

Wang, H.F., 2000, Theory of Linear Poroelasticity: With Applications to Geomechanics: Princeton, Princeton University Press, 287 p.

Wang, H.F., and Anderson, M.P., 1982, Introduction to Groundwater Modeling: Finite Difference and Finite Element Methods: San Diego, Academic Press, 237 p.

CHAPTER 5

PORE FLUID MIGRATION AND THE TIMING OF THE 2005 M8.7 NIAS EARTHQUAKE

Reprinted with permission from Geological Society of America and coauthors Tim Masterlark, Ph.D., and Walter Mooney, Ph.D.

MEDIA PARAGRAPH

The 2004 M9 Sumatra Earthquake was one of the largest and deadliest earthquakes in history. This earthquake ruptured a 1200-km-long boundary separating the India and Eurasian Tectonic Plates. Three months later the 2005 M8.7 Nias Earthquake ruptured what was an adjacent and locked portion of the plate boundary. Numerical models that simulate tectonic plates suggest that stress from the Sumatra Earthquake initially weakened the adjacent plate boundary, but not enough to trigger the Nias Earthquake. However, during the three-months separating the two earthquakes, water in the pore spaces of the tectonic plates slowly migrated in response to the stress. This migration caused the water pressure to slowly increase and thus weaken the adjacent and locked portion—ultimately triggering the Nias Earthquake. These numerical models also suggest that without water in the pore spaces, the gradual movements of the tectonic plates would require seven years to accumulate sufficient stresses to trigger the Nias Earthquake.

This implies that water in the pore spaces advanced the timing of the Nias Earthquake by seven years. That is, without water in the pore spaces of rocks, we would be expecting the M8.7 Nias Earthquake later this year, rather than in 2005.

ABSTRACT

Two great earthquakes have occurred recently along the Sunda Trench, the 2004 M9.2 Sumatra-Andaman earthquake and the 2005 M8.7 Nias earthquake. These earthquakes ruptured over 1600 km of adjacent crust within 3 months of each other. We quantitatively present poroelastic deformation analyses suggesting that postseismic fluid flow and recovery induced by the Sumatra-Andaman earthquake advanced the timing of the Nias earthquake. Simple back-slip simulations indicate that the MPa–scale pore-pressure recovery is equivalent to 7 years of interseismic Coulomb stress accumulation near the Nias earthquake hypocenter, implying that pore-pressure recovery of the Sumatra-Andaman earthquake advanced the timing of the Nias earthquake by ~7 years. That is, in the absence of postseismic pore-pressure recovery, we predict that the Nias earthquake would have occurred in 2011 instead of 2005.

MAIN ARTICLE

The M9.2 Sumatra-Andaman earthquake and subsequent great tsunami of 26 December 2004 ruptured over 1200 km of crust, lasted ~8 min, and killed over 250,000 people in 12 countries surrounding the Indian Ocean (Ammon et al., 2005;

Bilek, 2007; Vigny et al., 2005). Three months later, on 28 March 2005, a M8.7 earthquake centered off the coast of Nias Island just west of northern Sumatra ruptured over 400 km of crust, killed over 1300 people, and caused a minor tsunami (Fig. 5.1) (Ammon et al., 2005; Banerjee et al., 2007). Here, we present poroelastic

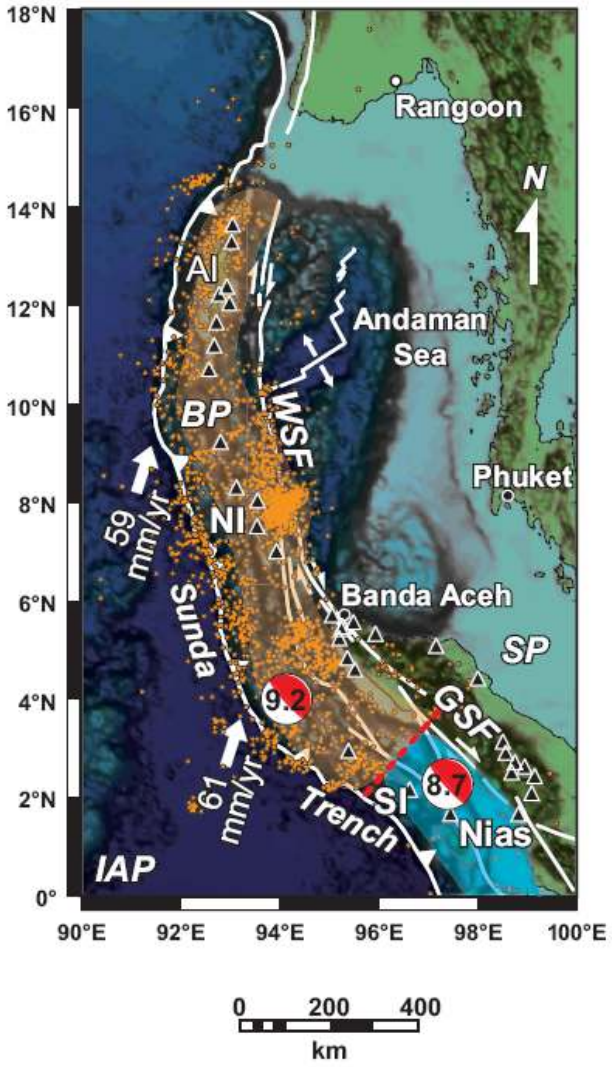

Figure 5.1. Seismotectonic setting of the Sumatra-Andaman subduction zone (adapted from Hughes et al., 2010). Harvard centroid moment tensor (CMT) focal mechanisms are given for the Sumatra-Andaman earthquake and Nias earthquake. Aftershock epicenters (orange dots), spanning 26 December 2004 through 28 March 2005 and transparent orange area, illuminate the surface projection of the Sumatra-Andaman earthquake rupture (http://neic.usgs.gov). The rupture initiated on the southeast portion of the fault and propagated ~1200 km northward. The blue transparent area represents the surface projection of the NE rupture (http://neic.usgs.gov). The sharply truncated aftershock distribution, shown with a northeast-trending dashed line (red) that bisects Simeulue Island, marks the boundary between rupture of the Sumatra-Andaman earthquake and subsequent Nias earthquake and represents the seismic barrier between the two earthquakes. Black triangles are near-field GPS sites (Gahalaut et al., 2006; Subarya et al., 2006). The tectonic configuration is modified from Bird (2003) and overlies a shaded relief image of global relief data (http://www.ngdc.noaa.gov). Abbreviations: AI-Andaman Islands, BP-Burma Plate, IAP-Indo-Australian Plate, NI-Nicobar Islands, SI-Simeulue Island, GSF-Great Sumatran Fault, SP-Sunda Plate, and WSF-West Sumatra Fault.

deformation analyses that suggest postseismic fluid flow and recovery induced by the Sumatra-Andaman earthquake advanced the timing of the later M8.7 Nias earthquake. We constructed finite-element models (FEMs) to simulate the co-seismic stress and pore (fluid) pressure fields of the Sumatra-Andaman earthquake, transient postseismic recovery of stress and pore pressure, and interseismic stress accumulation along the plate boundary (Hughes et al., 2010). FEMs are uniquely capable of simulating a subduction zone as a three-dimensional problem domain partitioned to represent poroelastic continental and oceanic crust and elastic mantle components.

The Sumatra-Andaman earthquake is still the largest earthquake for which coseismic deformation was recorded by global positioning system (GPS) data. We use the near-field GPS data, recorded for northern Sumatra and the Andaman and Nicobar Islands, to determine the slip distribution of the Sumatra-Andaman earthquake with FEM-generated Green's functions and linear inverse methods (Masterlark and Hughes, 2008; Hughes et al., 2010). It is the stress and pore-fluid pressure fields generated by this coseismic slip distribution that drive the postseismic poroelastic deformation as excess pore pressure recovers to equilibrium via Darcian flow. Changes in Coulomb stress—defined as $\Delta\sigma_c = \Delta\sigma_s + f(\Delta\sigma_n + \Delta P)$, where σ_c is Coulomb stress, σ_s is shear stress, f is friction, σ_n is normal stress, and P is pore pressure (Wang, 2000)—quantify the change in tendency for slip to occur along a fault. The Coulomb stress changes introduced by the Sumatra-Andaman earthquake, and thus the frictional stability of nearby faults, evolved in response to pore-pressure recovery.

The coseismic deformation due to the Sumatra-Andaman earthquake and the rheologic configuration of the three-dimensional FEM produce two transient flow regimes having two different time constants (Fig. 5.2). The first flow regime is shallow, within a few kilometers depth, and dissipates within 30 days of the Sumatra-Andaman earthquake. The second flow regime is deep, within the subducting oceanic crust of the downgoing slab, and it persists for several months after the Sumatra-Andaman earthquake (Fig. 5.2). The Sumatra-Andaman

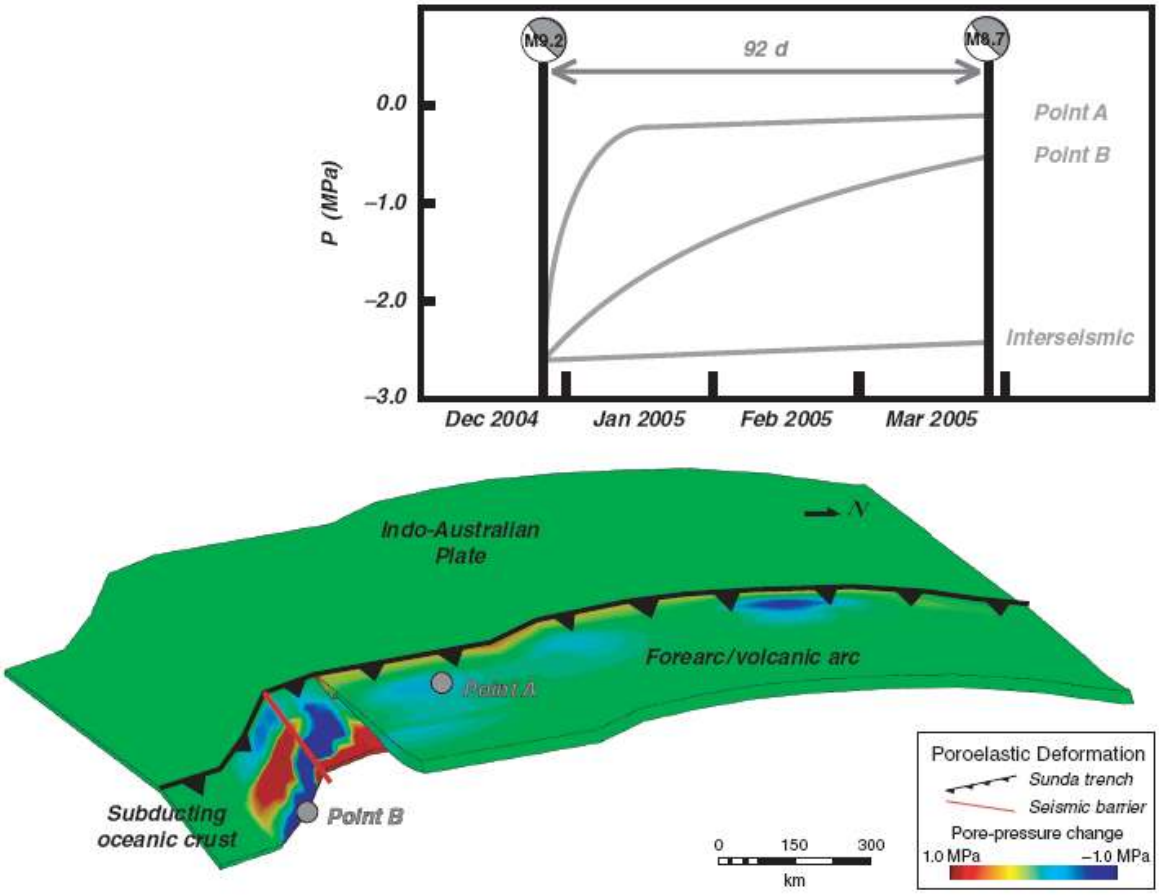

Figure 5.2. Graph shows change in pore pressure for point A (forearc), point B (near Nias earthquake hypocenter), and interseismic strain accumulation for the subduction zone. Map shows coseismic poroelastic deformation. Seismic barrier is red line between the Sumatra-Andaman earthquake (north) and Nias earthquake (south) ruptures. For point B, the upper forearc and volcanic arc have been cut away to view underlying subducting oceanic crust. For point A, the first few kilometers have been stripped off to see into the forearc.

earthquake initially induced a negative megapascal (MPa)–scale pore-pressure change near the Nias earthquake hypocenter, which then increased (recovered) during the 3 month time interval between the two earthquakes. This increase in pore pressure near the Nias earthquake hypocenter was due to pore fluids migrating both downdip and updip, as well as laterally along the strike of the slab within the oceanic crust due to coseismic pore-pressure gradients.

This 2.0 MPa pore-pressure recovery is two orders of magnitude greater than the Coulomb stress triggering threshold required for frictional slip, i.e., 10^4 Pa (Stein, 1999). Furthermore, these changes in Coulomb stress near the Nias earthquake hypocenter due to this pore-pressure recovery were significantly greater than changes attributed to either afterslip (McCloskey et al., 2005; Chlieh et al., 2007; Prawirodirdjo et al., 2010) or postseismic viscoelastic relaxation (Pollitz et al., 2006). Simple back-slip simulations (Savage, 1983) using the FEMs suggest that the 2.0 MPa pore-pressure recovery is equivalent to 7 years of interseismic accumulation of Coulomb stress (0.22 MPa) near the Nias earthquake hypocenter—a result that suggests pore-pressure recovery of the Sumatra-Andaman earthquake advanced the timing of the Nias earthquake by ~7 years. Therefore, instead of occurring in 2011, the Nias earthquake occurred in 2005 due to pore-pressure recovery. The results of this study indicate that the analysis of pore-pressure recovery is significant in addressing earthquake triggering at subduction zones worldwide.

REFERENCES

Ammon, C.J., Ji, C., Thio, H.K., Robinson, D., Ni, S., Hjorleifsdottir, V., Kanamori, H., Lay, T., Das, S., Helmberger, D., Ichinose, G., Polet, J., and Wald, D., 2005, Rupture process of the 2004 Sumatra-Andaman earthquake: Science, v. 308, p. 1133-1139, doi: 10.1126/science.1112260.

Banerjee, P., Pollitz, F., Nagarajan, B., and Bürgmann, R., 2007, Coseismic slip distributions of the 26 December 2004 Sumatra-Andaman and 28 March 2005 Nias earthquakes from GPS static offsets: Bulletin of the Seismological Society of America, v. 97, p. S86-S102, doi: 10.1785/0120050609.

Bilek, S.L., 2007, Using earthquake source durations along the Sumatra-Andaman subduction system to examine fault-zone variations: Bulletin of the Seismological Society of America, v. 97, p. S62-S70, doi: 10.1785/0120050622.

Bird, P., 2003, An updated digital model of plate boundaries: Geochemistry Geophysics Geosystems, v. 4, doi: 10.1029/2001GC000252.

Chlieh, M., Avouac, J.-P., Hjorleifsdottir, V., Song, T.-R.A., Ji, C., Sieh, K., Sladen, A., Hebert, H., Prawirodirdjo, L., Bock, Y., and Galetzka, J., 2007, Coseismic slip and afterslip of the great M_w 9.15 Sumatra-Andaman earthquake of 2004: Bulletin of the Seismological Society of America, v. 97, p. S152-S173, doi: 10.1785/0120050631.

Gahalaut, V.K., Nagarajan, B., Catherine, J.K., and Kumar, S., 2006, Constraints on 2004 Sumatra-Andaman earthquake rupture from GPS measurements in Andaman-Nicobar Islands: Earth and Planetary Science Letters, v. 242, p. 365-374, doi: 10.1016/j.epsl.2005.11.051.

Hughes, K.L.H., Masterlark, T., and Mooney, W.D., 2010, Poroelastic stress-triggering of the 2005 M8.7 Nias earthquake by the 2004 M9.2 Sumatra-Andaman earthquake: Earth and Planetary Science Letters, v. 293, p. 289-299, doi: 10.1016.j.epsl.2010.02.043.

Masterlark, T., and Hughes, K.L.H., 2008, Next generation of deformation models for the 2004 M9 Sumatra-Andaman earthquake: Geophysical Research Letters, v. 35, doi: 10.1029/2008GL035198.

McCloskey, J., Nalbant, S.S., and Steacy, S., 2005, Earthquake risk from co-seismic stress: Nature, v. 434, p. 291, doi: 10.1038/434291a.

Pollitz, F.F., Banerjee, P., Bürgmann, R., Hashimoto, M., and Choosakul, N., 2006, Stress changes along the Sunda trench following the 26 December 2004

Sumatra-Andaman and 28 March 2005 Nias earthquakes: Geophysical Research Letters, v. 33, doi: 10.1029/2005GL024558.

Prawirodirdjo, L., McCaffrey, R., Chadwell, C.D., Bock, Y., and Subarya, C., 2010, Geodetic observations of an earthquake cycle at the Sumatra subduction zone: Role of interseismic strain segmentation: Journal of Geophysical Research, v. 115, doi: 10.1029/2008JB006139.

Savage, J.C., 1983, A dislocation model of strain accumulation and release at a subduction zone: Journal of Geophysical Research, v. 88, p. 4984-4996.

Stein, R.S., 1999, The role of stress transfer in earthquake occurrence: Nature, v. 402, p. 605-609.

Subarya, C., Chlieh, M., Prawirodirdjo, L., Avouac, J.-P., Bock, Y., Sieh, K., Meltzner, A.J., Natawidjaja, D.H., and McCaffrey, R., 2006, Plate-boundary deformation associated with the great Sumatra-Andaman earthquake from GPS measurements in southeast Asia: Nature, v. 440, p. 46-51, doi: 10.1038/nature04522.

Vigny, C., Simons, W.J.F., Abu, S., Bamphenyu, R., Satirapod, C., Choosakul, N., Subarya, C., Socquet, A., Omar, K., Abidin, H.Z., and Ambrosius, B.A.C., 2005, Insight into the 2004 Sumatra-Andaman earthquake from GPS measurements in southeast Asia: Nature, v. 436, 201-206, doi: 10.1028/nature03937.

Wang, H.F., 2000, Theory of Linear Poroelasticity: With Applications to Geomechanics: Princeton University Press, Princeton, 287 p.

CHAPTER 6

SLIP DISTRIBUTION OF THE 2004 M9.2 SUMATRA-ANDAMAN EARTHQUAKE ESTIMATED FROM GPS DATA USING 3D FINITE ELEMENT MODELS AND LINEAR INVERSE METHODS

ABSTRACT

The spatial and temporal proximity of several large magnitude earthquakes (> M7.5) along the Sumatra-Andaman subduction zone prompted our investigation of the coseismic slip distribution for the 26 December 2004 M9.2 Sumatra-Andaman earthquake (SAE). We designed three-dimensional finite element models (FEMs) to simulate the coseismic slip distribution and surface displacement due to the SAE. Our FEM design incorporates four fundamental aspects of the Sumatra-Andaman subduction zone; the rigid subducting slab (Indo-Australian plate), the volcanic island arc (Sumatra), the backarc spreading center (Andaman Sea), and the weak forearc wedge (Nicobar and Andaman Islands). Including all of these critical elements in the FEMs is an innovation of this study and has not been utilized previously to quantify a slip distribution for the SAE. The motivation for designing a 3D FEM to simulate the coseismic slip distribution is that we can then use the same model to quantify poroelastic and viscoelastic deformation simultaneously, and thus FEMs are invaluable tools for analyzing coseismic and postseismic deformation. The improvement of this model design over previous FEMs is that our model accounts

for the backarc spreading center (Andaman Sea). The advancement of this model is that the results indicate a large amount of slip near the trench. This is the first model of coseismic slip estimated from geodetic data to simulate greater than 30 m of slip near the trench.

INTRODUCTION

The M9.2 Sumatra-Andaman earthquake (SAE) occurred on 26 December 2004 and generated a devastating tsunami (Vigny et al., 2005; Rastogi and Jaiswal, 2006; Bilek, 2007). Several large magnitude earthquakes have since occurred near the SAE rupture including the M8.7 Nias earthquake (NE) on 28 March 2005 (Mignan et al., 2006; Kreemer et al., 2006; Cattin et al., 2009), the M8.4 and M7.9 southern Sumatra earthquakes on 12 September 2007 (Lorito et al., 2008), the M7.8 northern Sumatra earthquake (NSE) on 6 April 2010 (Bilek and Engdahl, 2007), and the M7.5 Nicobar Islands earthquake (NIE) on 12 June 2010 (Fig. 6.1).

The Nias, northern Sumatra, and Nicobar Islands earthquakes all occurred near or within the rupture zone of the SAE. The spatial proximity and timing of these earthquakes suggests that these earthquakes are mechanically coupled. The stresses caused by the SAE drive the postseismic deformation processes; afterslip, poroelastic deformation, and viscoelastic deformation. Afterslip is the slip along the rupture surface after the coseismic static rupture has occurred, and is usually located down-dip from the coseismic rupture. The coseismic static rupture occurs minutes after the coseismic dynamic rupture which is the part of the rupture that causes the P- and S-waves. The coseismic static

rupture offset causes coseismic deformation which is deformation that remains following dynamic deformation of the mainshock.

Viscoelastic deformation occurs when stresses in the mantle relax and dissipate after an earthquake. The SAE caused MPa scale deviatoric stresses to build-up in the mantle. The surface and crust continued to deform in response to stresses relaxing via viscous flow in the mantle over the years following the coseismic displacement. Due to the magnitude of the SAE (M9.2), viscoelastic deformation started tens of months after the coseismic rupture and continues for about a decade afterwards. The

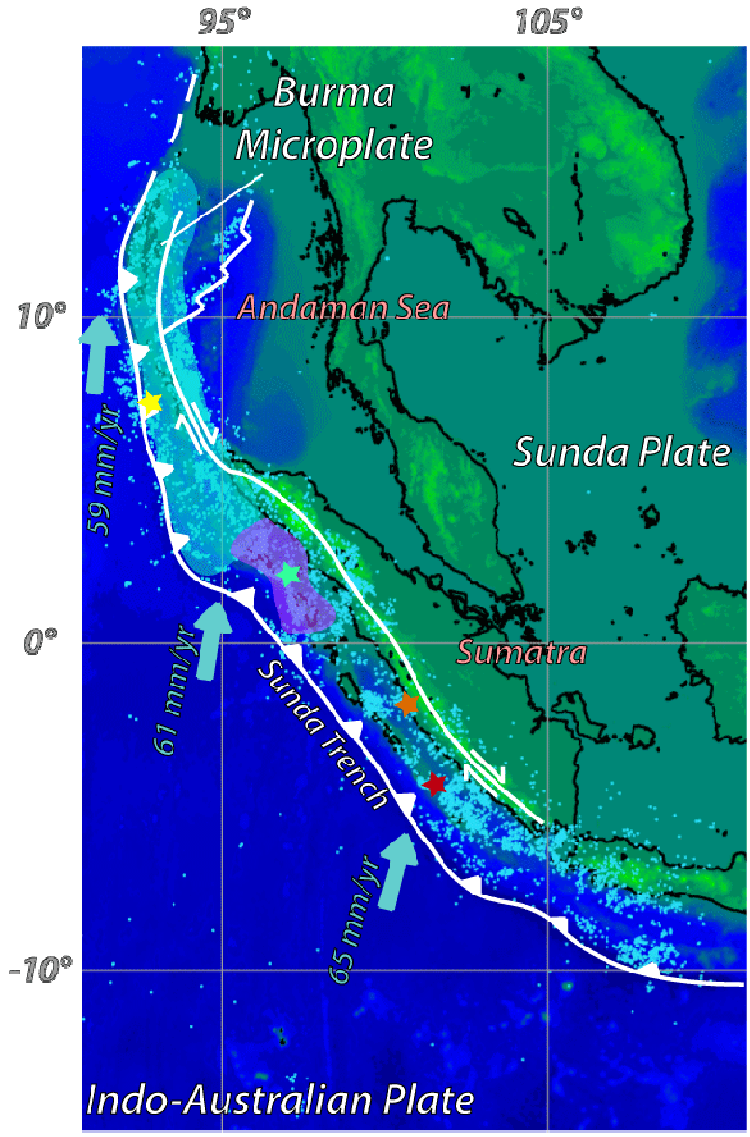

Figure 6.1. Tectonic setting of Sumatra-Andaman subduction zone (SASZ). Teal dots represent aftershocks of 2004 SAE. Teal and purple translucent areas are surface representations of SAE and NE rupture zones, respectively. Stars show the locations of the following earthquakes; yellow - NIE, teal - NSE, orange - 2007 M7.8, red - 2007 M8.4 (Vigny et al., 2005; Kreemer et al., 2006; Bilek, 2007; Bilek and Engdahl, 2007; Lorito et al., 2008; Cattin et al., 2009).

viscoelastic deformation component is a large constituent of postseismic deformation, and is predicted to be on the order of meters over the decade following the SAE.

Poroelastic deformation occurs when fluids in the crust migrate due to pore pressure gradients induced by the static rupture. Previous results indicate that poroelastic surface deformation due to the SAE is on the order of centimeters (Hughes et al., 2010; Hughes et al., 2011). These pore pressure gradients also cause triggering of later earthquakes on relatively short time scales (e.g., 2005 M8.7 Nias earthquake (Hughes et al., 2011)). Pore pressure re-equilibration occurs over relatively short time scales (tens of weeks to tens of months).

Previous researchers have attributed the NE to mainly afterslip (Kreemer et al., 2006; Hashimoto et al., 2006; Hsu et al.,
2006; Chlieh et al., 2007) because the GPS data can easily be fit by adjusting numerous parameters (underdetermined numerical problem), but this provides an ambiguous solution. Here we present a slip distribution generated by a three-dimensional finite element model (FEM) which is capable of solving elastic, viscoelastic, and poroelastic governing equations simultaneously while honoring the geologic complexity of a subduction zone via linear finite element methods (Masterlark et al., 2001; Masterlark, 2003; Masterlark and Hughes, 2008; Hughes et al., 2010). This slip distribution eliminates ambiguity in the solution due to fewer adjustable parameters by including a Laplacian smoothing matrix.

Here we provide a coseismic slip distribution derived from FEMs through linear inverse methods. We use a modeling protocol to design and implement our

FEMs. We incorporated many different types of data (e.g., tomography, cross-sections, gravity) to build FEMs which solve elastic governing equations using finite element methods. The simulated coseismic slip distribution is forward modeled to generate the predicted surface deformation and verified against observed seafloor deformation.

METHODS

Analytical solutions for deformation due to slip along a fault embedded in a homogeneous, elastic, half-space (HEHS) model are readily available (e.g. Okada, 1992). These models are commonly implemented in deformation models of subduction zone earthquakes. In spite of their widespread use, the inherent assumptions of HEHS models are not geologically satisfying. The HEHS assumptions maintain that the model domain must be homogeneous, elastic, topographically flat, and extend to infinity in all directions (Okada, 1992). A homogeneous model domain oversimplifies the natural system of a subduction zone because it does not account for the relatively rigid subducting slab which is the hallmark of a subduction zone. A topographically flat and infinitely large model domain is not a sufficient representation because it does not incorporate the actual topographically varying pre-earthquake GPS locations or other large local faults. However, the HEHS model has become the standard accepted model because it is an analytical solution that is computationally inexpensive and thus attractive for inverse methods that seek to estimate fault-slip based on geodetic data. The HEHS model is easy to conceptualize and removes design decisions which will be discussed later.

Some investigators applied alternatives (layered half-space or layered quarter-space models) to incorporate heterogeneity (e.g., Johnson and Segall, 2004; Hsu et al., 2006). These models still do not account for topography, near-field faults, and spatial heterogeneity, which are expected to be variable in a subduction zone. In addition, the HEHS model cannot solve for viscoelastic and poroelastic behavior that is known to occur in response to megathrust earthquakes. Both of these components are an important part of postseismic deformation and stress coupling and should not be neglected in simulations of postseismic deformation.

In order to quantify the coseismic slip distribution of the SAE we invoke the same modeling protocol as provided in Masterlark and Hughes (2008) to build our model. This protocol ensures that we develop a model which best represents the natural system by integrating available data, validation, and calibration.

1. Model Purpose

The purpose of our model is to simulate the SASZ as a deformational system that accurately predicts deformation and stress of the SAE while honoring the geologic and tectonic complexity of the SASZ. Our model can then be used in future analyses of coseismic and postseismic processes that are driven by the coseismic stress and deformation which is why this analysis is so critical. We determined that 3D FEMs would best accomplish this goal.

2. CONCEPTUAL MODEL

The fundamental component of a subduction zone is the cold, rigid subducting slab which is typically ignored in deformation models of coseismic slip. Therefore, characterizing the slab is a fundamental aspect of our subduction zone model. For the SASZ, the downgoing plate has been well imaged tomographically by the U.S. Geological Survey (2010) and Pesicek et al. (2008; 2010). We used these tomographic images to develop the geometry of our subducting slab in the conceptual model (Fig. 6.2). We used a commercially available software code known as AbaqusCAE to build our model domain (http://www.simulia.com). Abaqus is a general purpose finite element modeling environment that can simulate coseismic and postseismic deformation analyses. Abaqus-based FEMs have been successfully used for both forward and inverse analyses of coseismic geodetic data (Masterlark, 2003; Masterlark and Hughes, 2008; Hughes et al., 2010, Hughes et al., 2011). AbaqusCAE is a CAD-type interface that allows the user to generate three-dimensional objects in dimensionless space. These objects are then related through mathematical governing equations and are subject to initial and boundary conditions according to user input. The surface of our subducting plate was generated by using spline functions to estimate depth contours on the subducting plate. We created a loft cut through a brick shape using the spline functions as a guide. A loft cut is a cut through a three-dimensional object based on closed paths defined on sequential layers. The spline functions correlated to the eastern-most boundary of the subducting slab for 10 km increments. The western, northern and

southern boundaries were straight lines that were connected to the spline functions to create the closed paths.

The result of the loft cut was a curved surface according to the depth contours provided by the tomographic data (Pesicek et al., 2008; U.S. Geological Survey, 2010; Pesicek et al., 2010). The surface of the loft cut was projected down and west 6 km and then merged with the original part to generate the 3D representation of the oceanic crust. This final process was repeated down 35 km to generate the subducting slab.

a.

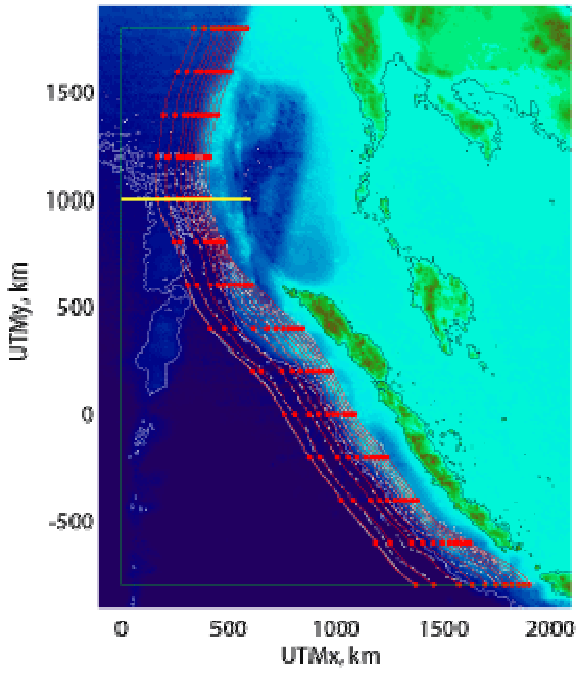

Figure 6.2. Conceptual model of subducting plate. a) Spline functions used to generate loft cut. Red circles are spline tie points, red lines are spline contours, and white dots are actual depth contours (U.S. Geological Survey, 2010). b) Shaded relief image of subducting plate geometry after loft cut. Black line represents Sunda trench, outlined area in red represents SAE rupture surface of the conceptual model, and yellow line represents cross-section location in Figure 6.6.

b.

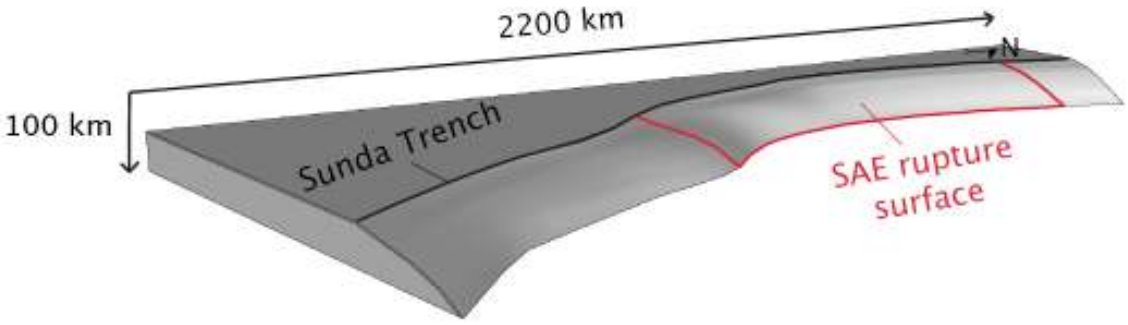

Published cross sections of the Sumatra, Andaman, and Nicobar Islands and velocity profiles of the Island of Sumatra were used to develop the upper plate (Fig. 6.3) (Kieckhefer et al., 1980; Kopp et al., 2001; Kopp et al., 2002; Conder et al., 2002; Kopp and Kukowski, 2003; Dasgupta et al., 2003; Barber et al., 2005). We cut the base of the overriding plate with the lofted surface of the subducting plate to create the two main pieces of the subduction zone and the seismogenic zone. The velocity profiles are used to constrain the rock property distribution in the upper plate. We designed the model to allow easy replacement of elastic elements with poroelastic and viscoelastic elements for future postseismic analyses, since changing the mesh of the model is not trivial. Thus, the model is partitioned such that the oceanic crust of the subducting plate will contain poroelastic elements based on the work of Audet et al. (2009) and the lower crust elements and all mantle elements will be viscoelastic in future analyses.

GRACE data (Mukhopadhyay, 1988; Chen et al., 2007; Chatterjee et al., 2007; Panet et al., 2007; Pesicek et al., 2008; Pesicek et al., 2010) are used to qualitatively verify picked V_p, V_s, and Poisson's ratio for each region of the model using data from Christensen (1996) and Contreras-Reyes et al. (2008) (Table 6.1). Densities were found using Brocher's equation for the Nafe-Drake curve

$$\rho = 1.6612V_p - 0.4721V_p^2 + 0.0671V_p^3 - 0.0043V_p^4 + 0.000106V_p^5 \qquad (6.1)$$

where V_p is in km/s and ρ is in g/cm^3 (Brocher, 2005). Lamé's first constant (λ) was determined in order to find Young's Modulus using Telford's equation

$$\lambda = \rho(V_p^2 - 2V_s^2) \qquad (6.2)$$

a.

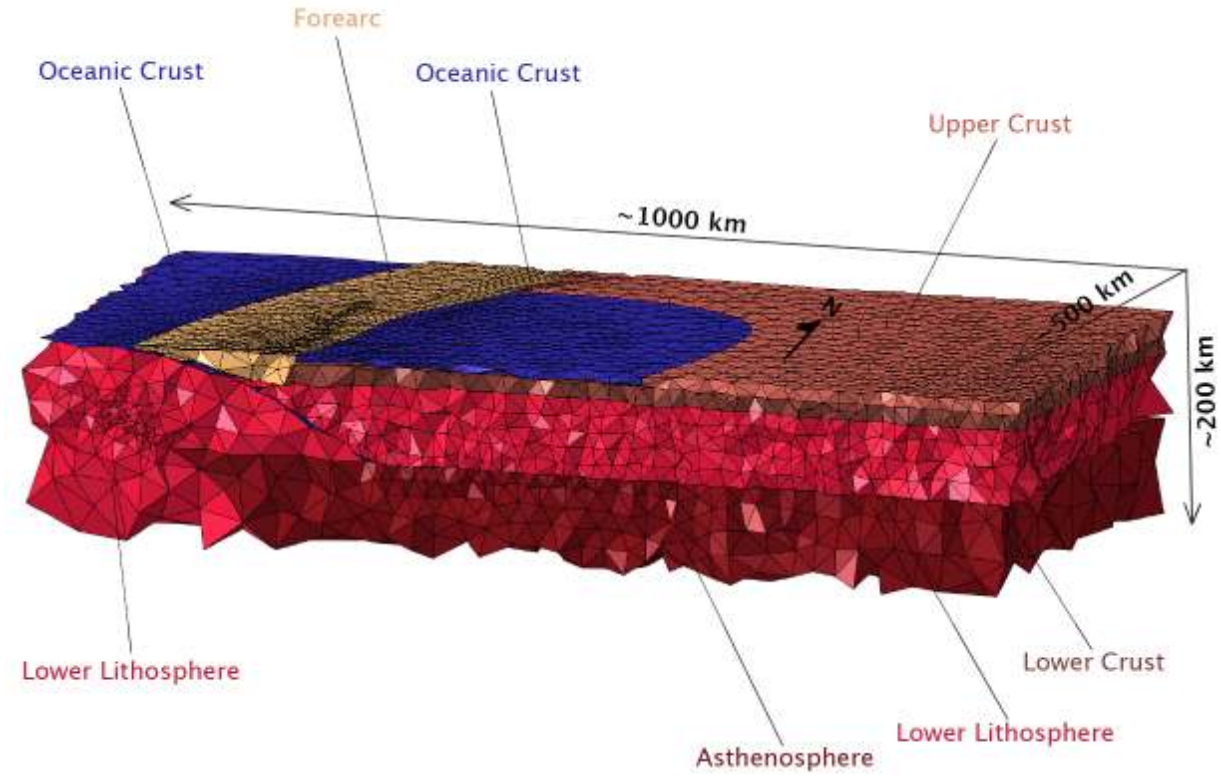

b.

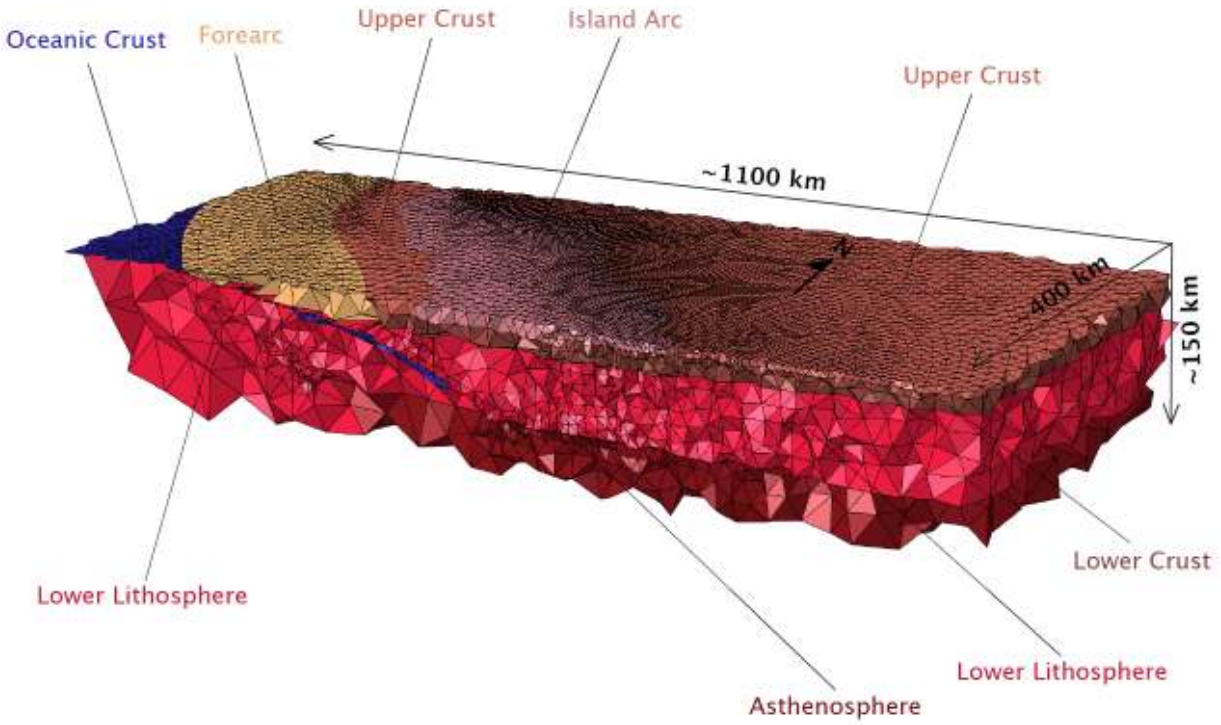

Figure 6.3. Cross-section profiles of SASZ 3D FEM. a) Cross-section of Andaman Islands. b) Cross-section of Sumatra.

where V_s is in km/s. Young's Modulus (E) was determined by the elastic constants relationship

$$E = \lambda \frac{(1+\upsilon)(1-2\upsilon)}{\upsilon} \tag{6.3}$$

where λ is Lamé's first constant, and υ is Poisson's ratio (Wang, 2000). We assigned each region in the model domain a Poisson's ratio and Young's Modulus calculated by the above equations from the velocity (V_p and V_s) of a representative rock type from the literature (Christensen, 1996; Contreras-Reyes, et al., 2008) (Table 6.1). Then, we used tomography and gravity data (Pesicek et al., 2008; Pesicek et al., 2010) to qualitatively verify the rheologic properties of the rocks at the subduction zone.

3. Model Design

Fault-slip is simulated as an elastic dislocation. Each slip patch is assigned to a slip node and a dummy node. The slip node moves with respect to the model domain and the kinematic constraint equation determines how the dummy node and corresponding slip patch moves—down-dip and north along strike for

Table 6.1. Rock properties and regional model placements (undrained conditions).

Rock Type	Model Placement	V_p (km/s)	V_s (km/s)	Poisson's Ratio	Young's Modulus (Pa)
[1]Basalt	Oceanic Crust	5.914	3.217	0.290	7.20×10^{10}
[1]Granite	Island Arc	6.246	3.669	0.237	9.20×10^{10}
[1]Felsic granulite	Lower Crust	6.545	3.657	0.268	1.00×10^{11}
[1]Metagreywacke	Upper Crust	5.829	3.406	0.241	7.71×10^{10}
[1]Dunite	Lower Lithosphere	8.399	4.783	0.260	1.98×10^{11}
[1]Pyroxenite	Asthenosphere	7.935	4.519	0.260	1.68×10^{11}
[2]Sediments	Forearc	1.700	0.500	0.480	5.17×10^{11}

[1]V_p, V_s, and Poisson's ratio data from Christensen (1996).
[2]V_p, V_s, and Poisson's ratio data from Contreras-Reyes et al. (2008).

subducting plate slip patches, up-dip and south along strike for overriding slip plate patches. The displacement of the surface is a linear function of slip on the fault. The kinematic constraint equations have the form

$$\vec{s} = \vec{u}_1 - \vec{u}_2 \qquad \text{and} \qquad \vec{s} = \vec{u}_3 \tag{6.4}$$

where $\vec{s}$ is slip, $\vec{u}_i$ is displacement, 1 is the node representing the overriding plate, 2 is the node representing the subducting plate, and 3 is the dummy node corresponding to the slip patch. The constraint generates the coseismic slip by specifying how each slip patch moves with respect to the corresponding dummy node in the local coordinate system which is determined by the strike and true dip of each individual slip patch.

The final conceptual model pieces are the initial and boundary conditions. The initial conditions of our model domain are equilibrium. This implies that there is no interseismic strain accumulation. For this study, we are analyzing static elastic displacement. Since we are interested in the coseismic displacement or the change in position before and after the earthquake, the assumption that the model is in equilibrium and returns to equilibrium after the coseismic load is satisfactory.

For the boundary conditions, all sides of the model domain have pinned boundary conditions except the top surface which is a free surface and the sliding surface which is displaced according to the slip distribution. The pinned boundary conditions set displacement and rotation of each surface to zero. The top surface (land surface) is free to move and rotate.

We designed and constructed our model in order to quantify the coseismic and postseismic deformation due to the SAE. The governing equations used to quantify displacement in a static elastic medium are expressed as

$$G\nabla^2 u + \frac{G}{1-2\upsilon}\left[\frac{\partial^2 u}{\partial x^2} + \frac{\partial^2 v}{\partial x \partial y} + \frac{\partial^2 w}{\partial x \partial z}\right] = -F_x$$

$$G\nabla^2 v + \frac{G}{1-2\upsilon}\left[\frac{\partial^2 u}{\partial y \partial x} + \frac{\partial^2 v}{\partial y^2} + \frac{\partial^2 w}{\partial y \partial z}\right] = -F_y \qquad (6.5)$$

$$G\nabla^2 w + \frac{G}{1-2\upsilon}\left[\frac{\partial^2 u}{\partial z \partial x} + \frac{\partial^2 v}{\partial z \partial y} + \frac{\partial^2 w}{\partial z^2}\right] = -F_z$$

where G is the shear modulus, u, v, and w are displacements in the u, v, and w directions, υ is the Poisson's ratio, x, y, and z are spatial components, and F_x, F_y, and F_z are body forces per bulk volume (Wang, 2000).

For elastic simulations, the boundary conditions of the FEM are u, v, w = zero over lateral boundaries and the base of the problem domain. The top surface is a stress free surface. The zero displacement boundaries are placed far enough away from the dislocation to minimize edge effects in the model (see SECTION 4. MODEL VALIDATION). The initial conditions of the FEM are equilibrium. The purpose of this model is to determine coseismic deformation. Thus, this model was only used to determine incremental displacement and changes in stress due to coseismic deformation, with respect to the assumed preseismic equilibrium conditions.

The seismogenic zone was partitioned into 318 slip patches (954 nodes, one node for each slip patch in the kinematic constraint equation (Eq. 6.4)) for the SAE

model domain. Due to the curvature of the seismogenic zone the slip patches are irregular in shape, but are about 20 km x 20 km and average 551.3 km^2 (Fig. 6.4).

The entire problem domain was tessellated into smaller quadratic tetrahedral elements in the near-field region (about 4 km^2), and the elements increased in size progressing towards the far-field and model boundaries (about 2500 km^2) (Fig. 6.5). The entire model domain consisted of 932,482 elements and 2,282,904 nodes. The governing equations were solved for each slip patch individually and each simulation took about 30 minutes on the Cray supercomputer (about 30 hours on a 64-bit quad hard-drive computer).

4. Model Validation

Validation is a fundamental step in the modeling process and provides assurances that a numerical model is working properly (Wang and Anderson, 1982).

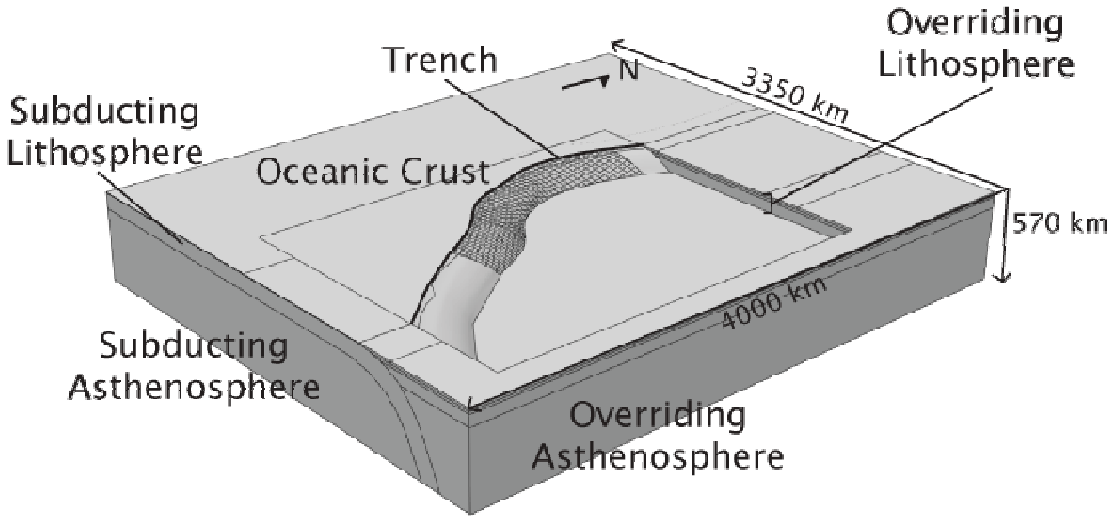

Figure 6.4. Slip patches used to model coseismic slip. These patches are partitioned on the top of the oceanic crust and the bottom of the overriding plate. Although irregular in shape, the patches match on either side of the plates due to using a loft cut on both pieces of the model. In the diagram, the overriding plate has been removed in order to see the slip patches on the subducting plate.

We validate the FEM configuration by comparing predictions to those from a corresponding analytical solution. We use the analytical solution for displacement due to an elastic dislocation over a rectangular plane embedded in a homogeneous elastic half-space (HEHS) (Okada, 1992). We then simplify the FEM configuration, by specifying a homogeneous distribution of material properties, to approximate that of the HEHS model. Although we can specify an assembly of rectangular fault patches that follow an arbitrarily complex path along the rupture as a function of

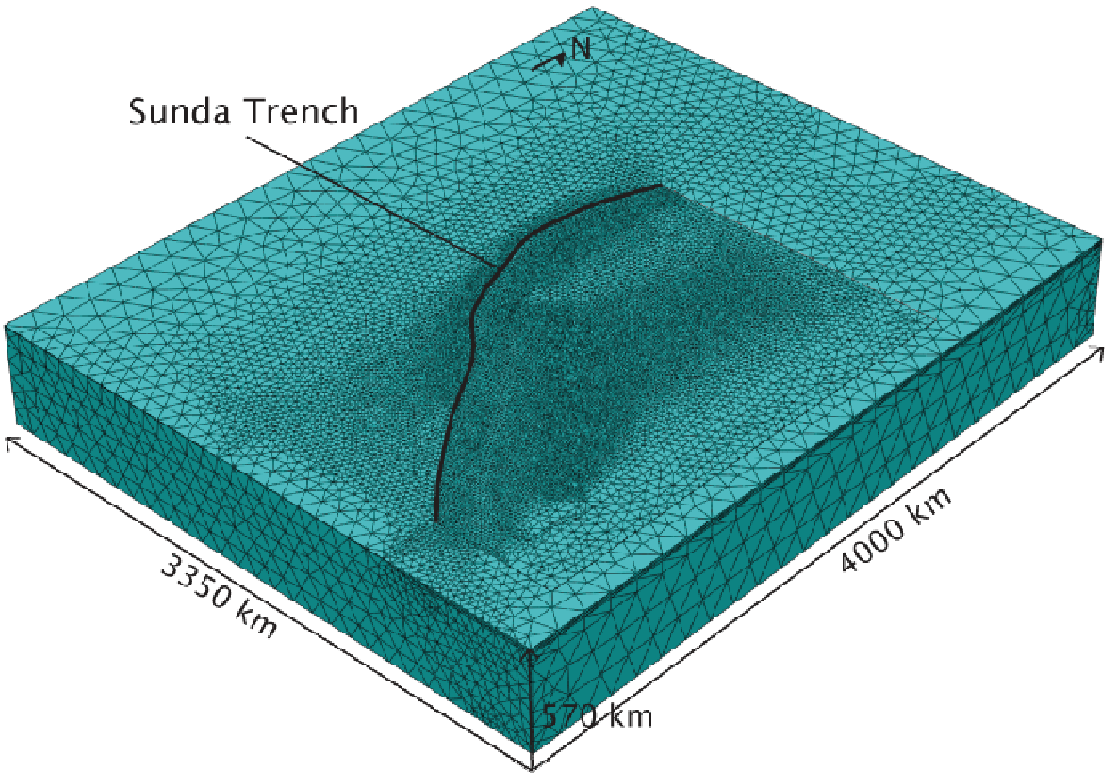

Figure 6.5. Diagram of problem domain mesh. We used quadratic tetrahedral elements due to the irregular geometry of the problem domain. The elements are small where the coseismic slip distribution occurs, and increase in size towards the edges of the model domain. The Sunda trench is designated by the thick black line for reference between the two plates of the model.

depth, the numerical analysis provided in Okada (1992) simply cannot simultaneously simulate the curvature of the rupture in the along-strike direction, which is substantial for the SAE.

For validation purposes, we construct a 2D model that simulates vertical and horizontal (eastward) deformation within a plane that is normal to the trench at approximately 1000 km UTM North, where the tangent of the trench has an azimuth of 0° (Fig. 6.2). Deformation in this 2D model is caused by unit thrust along a sequence of fault patches that follow the top surface of the subducting slab to a depth of 100 km (Fig. 6.6) using Okada (1992). We then simplify the FEM configuration, by specifying a homogeneous distribution of material properties, to approximate that of the half-space model. Finally, we impose unit slip (thrust only) along the entire rupture surface and extract the profile corresponding to that of the 2D model. This homogeneous FEM well predicts both corresponding vertical and horizontal displacements from Okada (1992) for the near-trench fault segments having depths of less than 20 km (Fig. 6.6). However, the ability of the FEM to predict displacements deteriorates for distances greater than about 50 km from the trench. This misfit is most likely due to the lateral curvature of the rupture simulated by the FEM, which violates the 2D assumption of the validation model. This problem is conceptualized as neighboring trench-normal sections intersecting the validation plane, and thus adversely contributing to the predicted deformation.

We also predict corresponding displacements from an FEM having heterogeneous material properties. Comparison against corresponding homogeneous FEM predictions gives insight into how the distribution of material

properties influences deformation predictions. Deformation predictions are discontinuous across the boundary between the forearc and crystalline rock, about 100 km east of the trench, in the overriding plate. This variation between homogeneous and heterogeneous FEM displacement predictions translates to variations in corresponding slip distributions and will influence predictions of coseismic and postseismic deformation and stress.

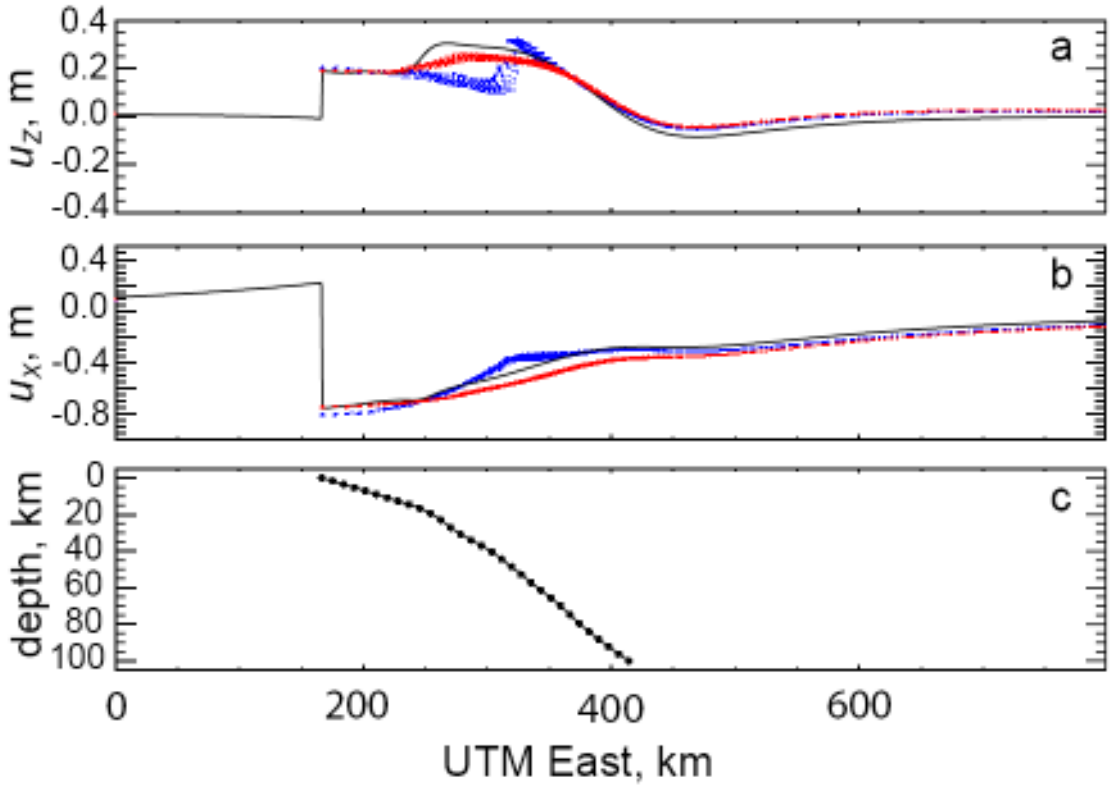

Figure 6.6. Validation. A) Vertical displacement. B) Horizontal (trench normal) displacement. Red and blue dots are homogeneous and heterogeneous FEM predictions, respectively for nodes within 10 km of the 2D validation domain. Homogeneous FEM predictions are excellent for deformation near the trench. Deviations over deeper fault segments are discussed in the text. The substantial offset (about 300 km UTM East) in displacements predicted with the heterogeneous FEM coincides with a change in elastic material properties. C) Fault segments. Black circles mark the edge of each fault segment. Homogeneous FEM predictions are excellent for deformation near the trench. Deviations over deeper fault segments are discussed in the text.

5. MODEL CALIBRATION

The slip for each patch is a calibration parameter. The slip distribution is the loading condition for coseismic deformation and stress. Calibration targets include published GPS measurements of near-field coseismic deformation (Gahalaut et al., 2006; Subarya et al., 2006; Simons et al., 2007) and gravity data (Mukhopadhyay, 1988; Chatterjee et al., 2007; Panet et al., 2007; Pesicek et al., 2008; Pesicek et al., 2010). The near-field GPS data are located on and near the islands of Sumatra, Nias, Simeulue, Nicobar, and Andaman. The largest displacement recorded is 5.86 m and the typical uncertainty is about 1 cm.

The forward model for deformation in an elastic problem domain, due to a distribution of fault-slip is

$$\boldsymbol{G}\,\boldsymbol{s} = \boldsymbol{d} \qquad (6.6)$$

where $\boldsymbol{G}$ is a matrix of Green's Functions (GFs), $\boldsymbol{s}$ is a vector of fault-slip (calibration parameters), and $\boldsymbol{d}$ is the data vector (calibration targets). In a forward model, each $\boldsymbol{G_{ij}}$ coefficient is applied to the displacement $\boldsymbol{d_j}$ for unit slip on fault patch $\boldsymbol{s_i}$. Each column in $\boldsymbol{G}$ requires and independent computation of an FEM. The problem domain for our study has variable rock properties and an irregularly gridded fault surface, thus published slip distributions based on a homogeneous or layered half-space models will introduce prediction errors (Hsu et al., 2006; Rhie et al., 2007; Masterlark and Hughes, 2008).

Instead, we use linear inverse methods and FEM-based GFs to estimate the slip distribution based on the GPS displacement data of the calibration targets (102 data measurements−34 GPS stations recording in all three directions). GPS

displacements are weighted according to the corresponding error of each measurement using a weighting matrix ($\boldsymbol{W}$) which is a diagonal matrix whose off-diagonal terms are zero and the diagonal terms are defined as

$$\boldsymbol{W_{ij}} = 1./\boldsymbol{e_j} \tag{6.7}$$

where $\boldsymbol{e_j}$ is the reported measurement uncertainty for $\boldsymbol{d_j}$. The least-squares solution for the fault-slip distribution, $\boldsymbol{s}^{est}$, is

$$\boldsymbol{s}^{est} = (\boldsymbol{G}^T\boldsymbol{W}\boldsymbol{G})^{-1}\,\boldsymbol{G}^T\boldsymbol{W}\boldsymbol{d} \tag{6.8}$$

where $\boldsymbol{G}^T$ is the transpose of $\boldsymbol{G}$ and $(\,)^{-1}$ is the inverse matrix. The least-squares solution for our problem domain and data vector is non-unique since we only have 102 displacement measurements to solve for 318 slip patches. We regularize the problem by imposing smoothing constraints. More specifically, we assume Laplacian smoothing such that the slip distribution satisfies

$$\nabla^2 = 0 \tag{6.9}$$

where ∇ represents the Laplacian del-squared operator (Turcotte and Schubert, 1982). Simple finite difference approximation used in previous studies are inadequate for this study due to the irregular geometry of the slip patches (Masterlark and Hughes, 2008; Hughes et al., 2010). Therefore, we use finite element methods to create a Global Conductance Matrix (GCM) to satisfy Eq. 6.9 and to damp the underdetermined portion of the problem domain (Wang and Anderson, 1982) (Fig. 6.7). This is an innovative part of this project because finite element methods provide a convenient means to imposing smoothing constraints over a fault having an irregular geometry.

The GCM is constructed based on the average position and the connectivity of the nodes of the finite element grid. Each slip patch of the model is represented by a node of the finite element grid and is assemble into an FEM mesh with triangular elements. The elements do not need to be the same size or shape which is why this

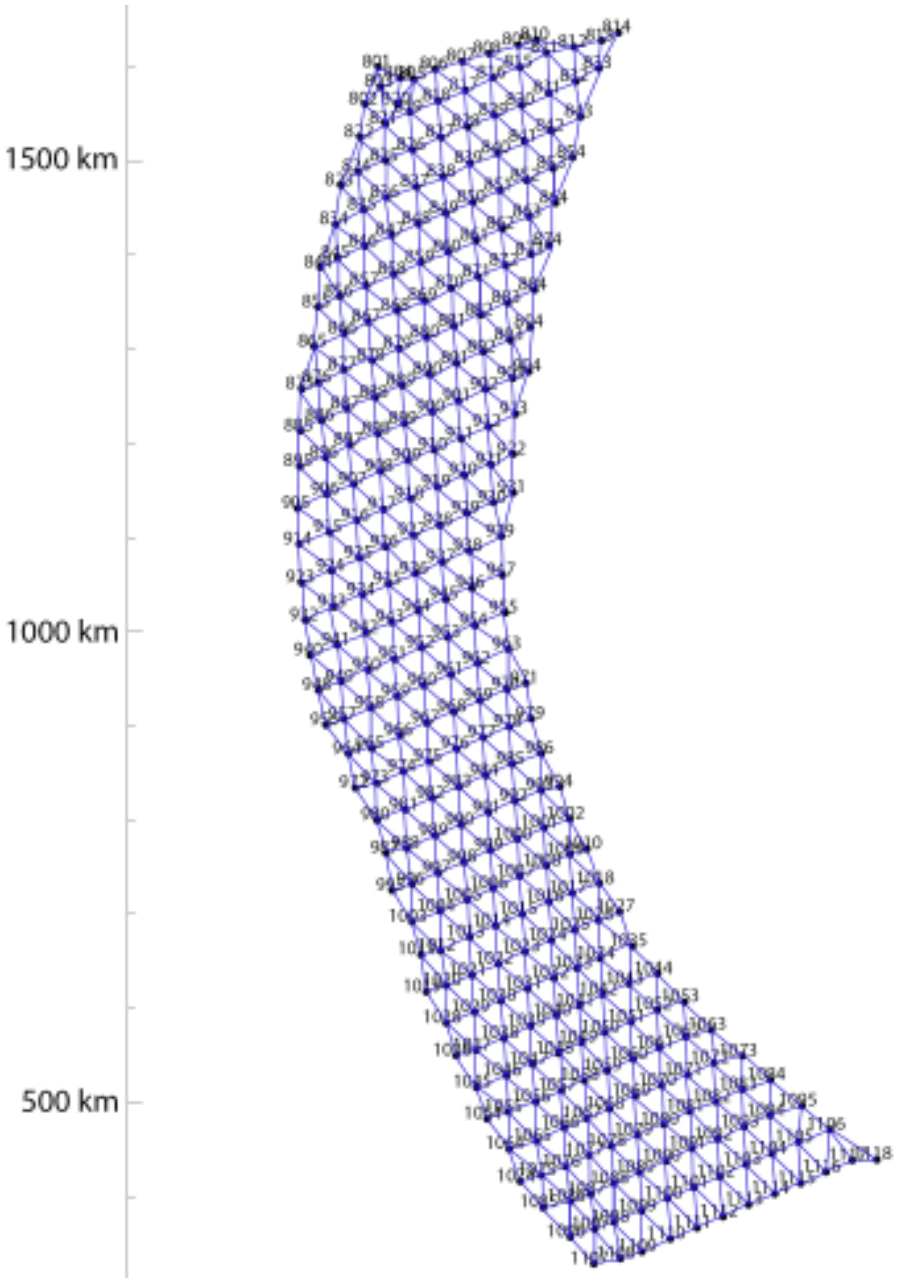

Figure 6.7. Finite element grid used to construct the GCM. Each numbered node represents a slip patch and the triangles are elements used to determine the connectivity between slip patches.

method is ideal for irregular geometries such as the fault surface of the SAE problem domain. The GCM is a symmetric matrix where the coefficients are summed according to the nodal indices of each element (Wang and Anderson, 1982). This matrix is constructed element by element instead of row by row like a Laplacian smoothing matrix (Menke, 1989) (Appendix).

We validate the GCM by running a simple fluid diffusion test model which satisfies Eq. 6.9 (s represents hydraulic head in this case) for previously specified boundary conditions. To test the coefficients of the GCM we set up a simple problem domain where the geometry of the fluid diffusion FEM is the same as that for the fault of the SAE problem domain (Fig. 6.7). The southern and northern boundaries are set at a constant head of 10 m and 2 m, respectively. The east and west boundaries were no flow boundaries simulating zero flux (Wang and Anderson, 1982; Anderson and Woessner, 1991).

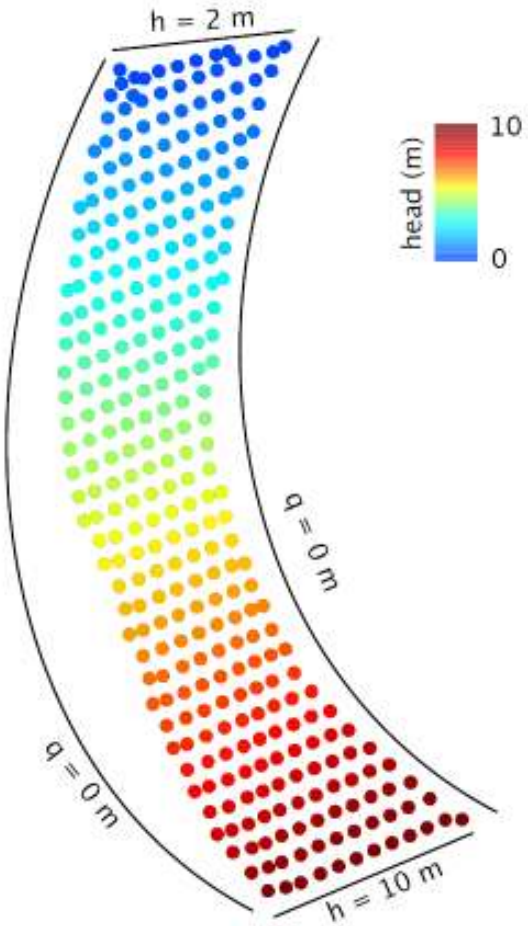

Figure 6.8. Diagram of fluid diffusion grid verification test. The southern and northern boundary nodes have known head values of 10 m and 2 m, respectively. The nodes in between have linearly decreasing values from 10 to 2 m south to north since the east and west boundaries are no flow boundaries.

For this case, the hydraulic heads calculated through the problem domain should decrease

linearly from 10 m to 2 m in approximately the northern direction (not exactly northern due to the geometry of the problem domain–the northern and southern boundaries are not exactly orthogonal to north and south, respectively) (Wang and Anderson, 1982). In Figure 6.8 we show that the result of the simple hydrogeological test shows a linearly decreasing measurement of head from 10 m to 2 m, and therefore the test validates the coefficients of the GCM.

The GCM is appended to the $\boldsymbol{G}$ matrix, and a vector of zeros to the $\boldsymbol{d}$ vector. A damping parameter β controls the trade-off between fitting the data and smoothing the fault-slip distribution

$$\begin{bmatrix} \boldsymbol{WG} \\ \beta\boldsymbol{C} \end{bmatrix} [\boldsymbol{s}] = \begin{bmatrix} \boldsymbol{Wd} \\ 0 \end{bmatrix} \tag{6.10}$$

where $\boldsymbol{C}$ represents the GCM.

The trade-off curve represents the trade-off between solution roughness and data misfit, and embodies the non-unique nature of inverse methods. The β-value chosen represented the most reasonable trade-off between complexity and error. Complexity (L) is measured by the sum of squares of the slip distribution

$$L = \boldsymbol{s}^{\mathrm{T}}\boldsymbol{s} \tag{6.11}$$

where $\boldsymbol{s}$ is the vector of the estimated slip distribution and $^{\mathrm{T}}$ is the transpose of the matrix or vector. L measures the roughness or oscillation of the solution since large differences represent rough solutions (Menke, 1989; Wang and Anderson, 1982). Error (E) is measured similarly and is defined as

$$E = \boldsymbol{e}^{\mathrm{T}}\boldsymbol{We} \qquad \text{where} \qquad \boldsymbol{e} = \boldsymbol{d} - \boldsymbol{d}^{\mathrm{pre}} \tag{6.12}$$

and where $\boldsymbol{d}^{pre}$ is a vector of the data predictions from the forward model $\boldsymbol{Gs}^{est} = \boldsymbol{d}^{pre}$ (Menke, 1989). The best β-value minimizes error while simultaneously smoothing the slip distribution generating a geologically reasonable solution. The trade-off curve is produced by sweeping through β-values and solving for the forward model. The "knee" (Gubbins, 2004) of the trade-off curve (Fig. 6.9) minimizes solution roughness (98301.9 m^2) and weighted error (6.261 m^2) at a corresponding β-value of $1.25e^{-2}$. The slip distribution generated by the forward model indicates a maximum of 42.5 m and a minimum of -14.7 m of dip-slip and a maximum of 26.1 m and a minimum of -32.7 m of strike-slip (Fig. 6.10).

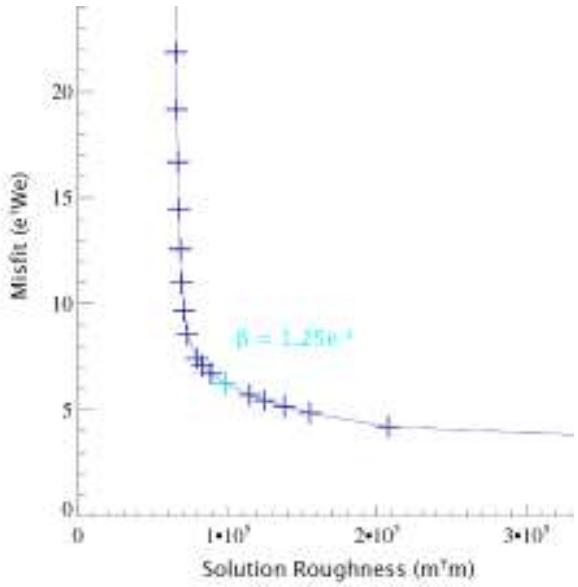

Figure 6.9. Trade-off curve for FEM slip distribution. The trade-off curve represents the trade-off between solution roughness and data prediction error due to the slip distribution. The corresponding β-value (teal cross) is the best smoothing parameter that balances the trade-off.

6. Model Verification

Our slip model is qualitatively compared to other geodetically derived and seismically derived slip distributions. Most geodetically estimated slip distributions show a similar magnitude of slip (> 30 m) to our model. However, most of the slip is concentrated in two main locations near the trench, whereas the slip distribution published by other investigators is concentrated more down-dip (Fig. 6.10)

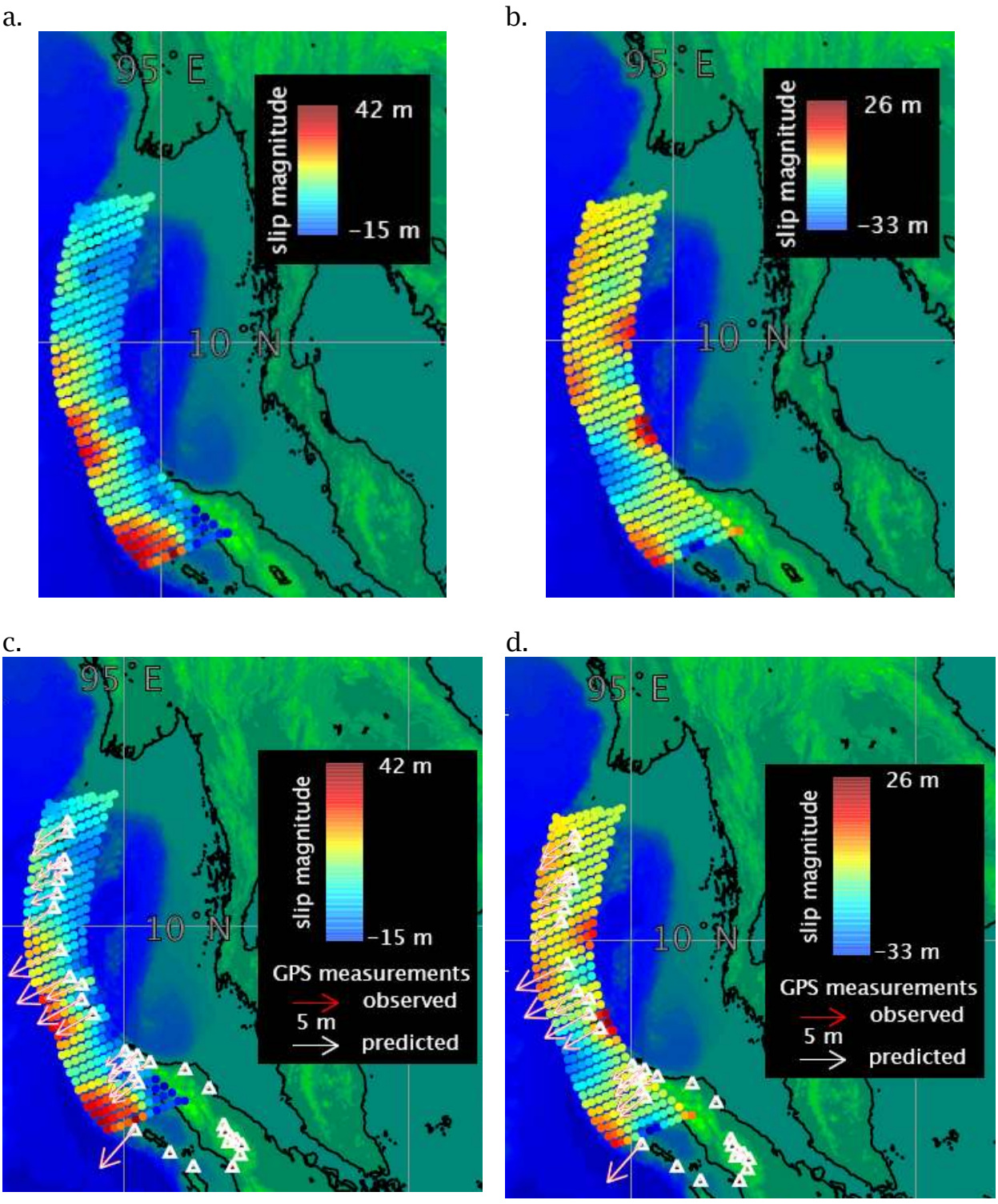

Figure 6.10. Slip distribution generated by finite element, linear inverse methods. Each dot represents a slip patch shown by diagram in Fig. 6.6. Colors represent total amount of slip. a) Distribution due to dip-slip motion. b) Distribution due to strike-slip motion. c) Dip-slip distribution, observed GPS arrows (red), predicted GPS arrows (white), and GPS station locations (white triangles). d) Strike-slip distribution, observed GPS arrows (red), predicted GPS arrows (white), and GPS station locations (white triangles) (Gahalaut et al., 2006; Subarya et al., 2006).

(Banerjee et al., 2005; Vigny et al., 2005; Catherine et al., 2005; Gahalaut et al., 2006, Hashimoto et al., 2006, Anu and Rajendran, 2006; Chlieh et al., 2007; Hoechner et al., 2008). Though our model does not predict the same slip distribution as other models based on geodetic data, our solution may represent a better geodetically derived solution due to the inclusion of the complex geology of the SASZ. Our model results are similar to seismically derived slip distributions and are required for accurate tsunami run-up measurement predictions. Seismically derived slip distributions show a maximum of about 30 m of slip and the majority of the slip occurs near the trench (Ammon et al., 2005; Lay et al., 2005; Sørensen et al., 2007). Once the coseismic displacement data were analyzed using inverse methods, then the slip distribution was applied to compute the forward FEM. The surface deformation has a maximum of 21 m of uplift and 8 m of subsidence with an average displacement of -0.027 m (Fig. 6.11). The maximum uplift occurs near the trench which is desired for accurate tsunami models (Fine et al., 2005; Song et al., 2005; Fujii and Satake, 2007; Geist et al., 2007; Grilli et al., 2007; Hanson et al., 2007; Piantanesi and Lorito, 2007). The large uplift near the trench is compared to the location of an observed 12 m fault scarp (Fig. 6.12). Scientists on board the 2005 SEATOS cruise built a photo-mosaic of a scarp in the accretionary wedge based on images taken by a remotely operated vehicle (ROV). This scarp is about 12 meters and is believed to be a direct result of the SAE coseismic rupture. The location of the scarp is offshore Sumatra (Fig. 6.12). Our maximum uplift agrees with the location of this fault scarp.

RESULTS

We quantified the slip distribution for both dip-slip and strike-slip motion. For the dip-slip distribution, our model generated a large thrust component near the trench (> 40 m) concentrated in two main areas off- shore northern Sumatra which decreases down-dip and to the north along strike (Fig. 6.9). For the strike-slip distribution, we quantified a large component of right-lateral motion to the north (> 15 m). This slip distribution is consistent with other studies which indicate large slip along a mega-splay in northern Sumatra, but is larger in magnitude (~10 m) (Hoechner et al., 2008; Lin et al., 2009).

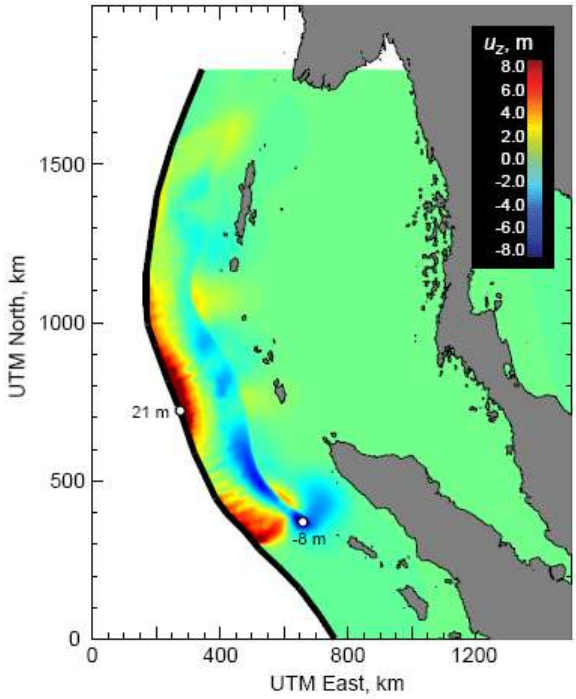

Figure 6.11. Map of uplift and subsidence predicted by our 3D FEM. Largest amount of uplift is 21 m and largest amount of subsidence is 8 m. Thick black line represents the location of the Sunda trench.

We forward modeled our slip distribution with the 3D FEM domain to generate the postseismic deformation due to the SAE. Using our slip distribution, the SAE caused a maximum of 8.1 m of uplift and a maximum of 20.1 m of subsidence (Fig. 6.11).

DISCUSSION

The most useful innovation of this study is the completion of a 3D FEM to generate a reliable and accurate dip-slip and strike-slip distribution for the SAE. This slip distribution is more reliable and accurate due to the model design, more specifically, this model better represents the geologic system of the SASZ than a HEHS or LEHS. After constructing the GCM (Appendix), we were able to quantify the slip distribution due to the SAE using FE methods from the GPS data. Use of the GCM does not require a regular geometry, and thus was a necessity for this project due to the irregular mesh and shape of the model partitions (e.g., subducting slab).

Our slip distribution is in agreement with other published slip distributions albeit about 20 percent larger in magnitude (Ammon et al., 2005; Lay et

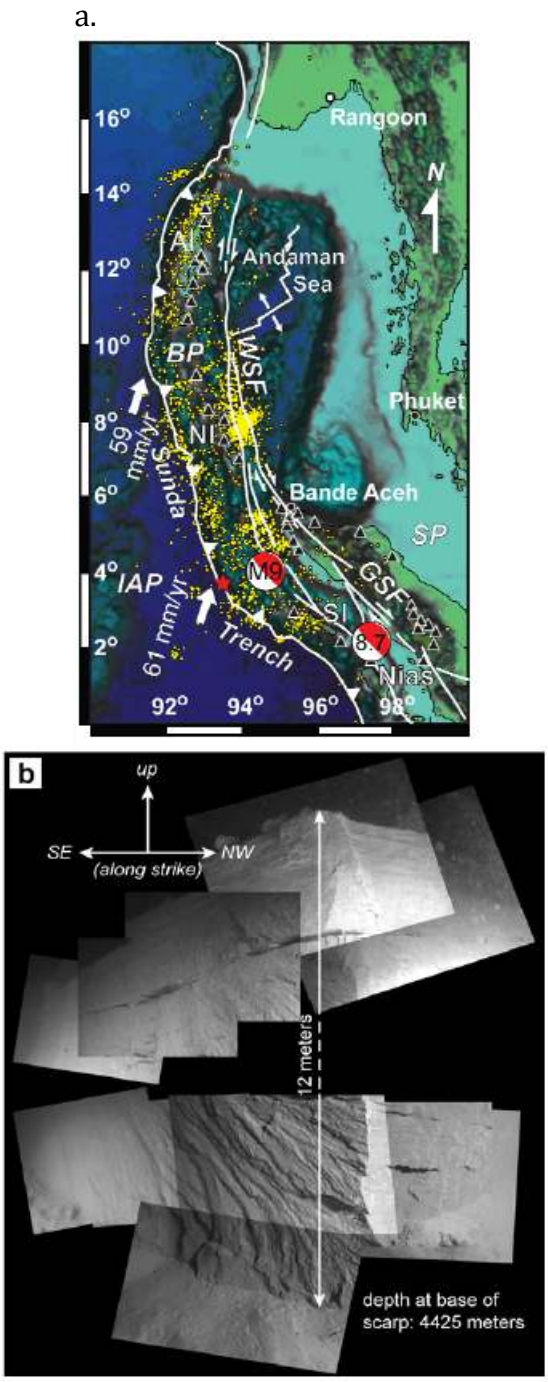

Figure 6.12. 12 m fault scarp from Sumatra–Andaman subduction zone. A) Location map of fault scarp, the red star represents where the photos were taken by ROV. B) Photo–mosaic of a fault scarp in the accretionary wedge (2005 SEATOS cruise).

al., 2005; Vigny et al., 2005; Hoechner et al., 2008; Masterlark and Hughes, 2008; Cattin et al., 2009; Lorito et al., 2010; Poisson et al., 2011). Other authors have determined that the maximum slip due to the SAE should be on the order of about 20 to 35 m quantified by analyzing the near-field and far-field GPS data (Vigny et al., 2005; Masterlark and Hughes, 2008, Hoechner et al., 2008; Lorito et al., 2010), 20 to 30 m using seismic data (Ammon et al., 2005; Lay et al., 2005; Cattin et al., 2009), and 20 to 35 m generated by tsunami run-up data (Lay et al., 2005; Hoechner et al., 2008; Lorito et al., 2010; Poisson et al., 2011).

The benefit of using FEMs is that FEMs are capable of analyzing coseismic and postseismic deformation (elastic, poroelastic, and viscoelastic mechanics) and Coulomb stress. Coulomb stress (σ_c) is the tendency for slip to occur along a fault and is defined as

$$\Delta\sigma_c = \Delta\sigma_s + f(\Delta\sigma_n + \Delta P) \tag{6.13}$$

where σ_s is shear stress, f is the coefficient of friction, σ_n is normal stress, and P is pore pressure (Wang, 2000). The components of Coulomb stress are found by calculating the change in shear and normal stress and the change in pore pressure near an earthquake. Therefore, we designed our model in order to later easily replace the elastic rock properties with poroelastic and viscoelastic rock properties where required to analyze the poroelastic and viscoelastic mechanics of the SAE. The quantification of the poroelastic and viscoelastic deformation due to the SAE will be published in a follow-up paper.

CONCLUSIONS

We designed 3D FEMs to quantify a coseismic slip distribution for the M9.2 Sumatra-Andaman earthquake. In order to create this model, we employed the use of tomographic, velocity profiles, and cross-sections to determine the geometry of the subducting slab and overriding plate (Kieckhefer et al., 1980; Kopp et al., 2001; Conder et al., 2002; Kopp et al., 2002; Kopp and Kukowski, 2003; Dasgupta et al., 2003; Barber et al., 2005; Pesicek et al., 2008, Pesicek et al., 2010; U.S. Geological Survey, 2010). Finite element methods and linear inverse methods were utilized to compute the slip distribution from GPS measurements (Menke, 1989; Wang, 2000; Subarya et al., 2006; Gahalaut et al., 2006).

Our slip distribution results show that the maximum dip-slip occurred within about 5 km depth and nucleated in two main locations (Fig. 6.10). The maximum strike-slip motion nucleated in three main locations one within about 5 km depth with the other two located at the down-dip extent of the rupture zone. The maximum dip-slip and strike-slip motion is greater than 40 m and 25 m, respectively. The slip distribution results are consistent with other studies of the SAE (Ammon et al., 2005; Lay et al., 2005; Vigny et al., 2005; Masterlark and Hughes, 2008; Hoechner et al., 2008; Cattin et al., 2009; Lorito et al., 2010; Poisson et al., 2011), but are about 10 m higher in magnitude.

We qualitatively verified the results of our geodetically derived slip distribution against published slip distributions. Tsunami run-up derived slip distributions rely on large (> 30 m) shallow slip near the trench (Fine et al., 2005; Song et al., 2005; Fujii and Satake, 2007; Geist et al., 2007; Grilli et al., 2007; Hanson

et al., 2007; Piantanesi and Lorito, 2007) which is what our model predicts. Additionally, seismically derived slip distributions indicate large slip near the trench (Ammon et al., 2005, Lay et al., 2005; Sørensen et al., 2007). Geodetically based slip distributions typically estimate the greatest amount of slip under the Nicobar Islands and down-dip compared to seismically derived and tsunami wave-height derived models (Banerjee et al., 2005; Vigny et al., 2005, Catherine et al., 2005; Anu and Rajendran, 2006; Hashimoto et al., 2006; Gahalaut et al., 2006; Chlieh et al., 2007; Hoechner et al., 2008). Our model is the first geodetically derived model to simulate a large amount of slip (> 35 m) and uplift (> 15 m) near the trench. Thus, it is imperative that geologic models incorporate the spatial complexity of varying mechanical properties where these properties may influence the results of the variables being quantified.

REFERENCES

Ammon, C.J., Ji, C., Thio, H.-K., Robinson, D., Ni, S., Hjorleifsdottir, V., Kanamori, H., Lay, T., Das, S., Helmberger, D., Ichinose, G., Polet, J., and Wald, D., 2005, Rupture process of the 2004 Sumatra-Andaman earthquake: Science, v. 308, p. 1133-1139, doi: 10.1126/science.1112260.

Anderson, M.P, and Woessner, W.W., 1991, Applied Groundwater Modeling: Simulation of Flow and Advective Transport: San Diego, Academic Press, 381 p.

Anu, R., and Rajendran, K., 2006, Co-seismic deformation along the Andaman-Nicobar arc based on GPS data and ground observations: Extended Abstract, XVIII Kerala Science Congress, p. 226-228.

Audet, P., Bostock, M.G., Christensen, N.I., and Peacock, S.M., 2009, Seismic evidence for overpressured subducted oceanic crust and megathrust fault sealing: Nature, v. 457, p. 76-78, doi: 10.1038/nature07650.

Banerjee, P., Pollitz, F.F., and Bürgmann, R., 2005, The size and duration of the Sumatra-Andaman earthquake from far-field static offsets: Science, v. 308, p. 1769-1772, doi: 10.1126/science.1113746.

Barber, A. J., Crow, M.J., and Milsom, J.S., 2005, Sumatra: Geology, Resources, and Tectonic Evolution: London, Geological Society, 290 p.

Bilek, S.L., 2007, Using earthquake source durations along the Sumatra-Andaman subduction system to examine fault-zone variations: Bulletin of the Seismological Society of America, v. 97, p. S62-S70, doi: 10.1785/0120050622.

Bilek, S.L., and Engdahl, E.R., 2007, Rupture characterization and aftershock relocations for the 1994 and 2006 tsunami earthquakes in the Java subduction zone: Geophysical Research Letters, v. 34, doi: 10.1029/2007/GL031357.

Brocher, T.M., 2005, Empirical relations between elastic wavespeeds and density in the earth's crust: Bulletin of the Seismological Society of America, v. 95, p. 2081-2092, doi: 10.1785/0120050077.

Catherine, J.K., Gahalaut, V.K., and Sahu, V.K., 2005, Constraints on rupture of the December 26, 2004, Sumatra earthquake from far-field GPS observations: Earth and Planetary Science Letters, v. 237, p. 673-679, doi: 10.1016/j.epsl.2005.07.012.

Cattin, R., Chamot-Rooke, N., Pubellier, M., Rabaute, A., Delescluse, M., Vigny, C., Fleitout, L., and Dubernet, P., 2009, Stress change and effective friction coefficient along the Sumatra-Andaman-Sagaing fault system after the 26 December 2004 (M_W = 9.2) and the 28 March 2005 (M_W = 8.7) earthquakes: G-Cubed, Geochemistry, Geophysics, Geosystems, v. 10, doi: 10.1029/2008GC002167.

Chatterjee, S., Bhattacharyya, R., and Majumdar, T.J., 2007, Generation and study of high-resolution satellite gravity over the Sumatran earthquake region: International Journal of Remote Sensing, v. 28, p. 2915-2925, doi: 10.1080/01431160601091829.

Chen, J.L., Wilson, C.R., Tapley, B.D., and Grand, S., 2007, GRACE detects coseismic and postseismic deformation from the Sumatra-Andaman earthquake: Geophysical Research Letters, v. 34, doi: 10.1029/2007GL030356.

Chlieh, M., Avouac, J.-P., Hjorleifsdottir, V., Song, T.-R.A., Ji, C., Sieh, K., Sladen, A., Hebert, H., Prawirodirdjo, L., Bock, Y., and Galetzka, J., 2007, Coseismic slip and afterslip of the great Mw 9.15 Sumatra-Andaman earthquake of 2004:

Bulletin of the Seismological Society of America, v. 97, p. S152–S173, doi: 10.1785/0120050631.

Christensen, N.I., 1996, Poisson's ratio and crustal seismology: Journal of Geophysical Research, v. 101, p. 3139-3156.

Conder, J.A., Wiens, D.A., and Morris, J., 2002, On the decompression melting structure at volcanic arcs and back-arc spreading centers: Geophysical Research Letters, v. 29, doi: 10.1029/2002GL015390.

Contreras-Reyes, E., Grevemeyer, I., Flueh, E.R., Scherwath, M., and Bialas, J., 2008, Effect of trench-outer rise bending-related faulting on seismic Poisson's ratio and mantle anisotropy: A case study offshore southern central Chile: Geophysical Journal International, v. 173, p. 142-156, doi: 10.1111/j.1365-246X.2008.03716.x.

Dasgupta, S., Mukhopadhyay, B., Bhattacharya, A., and Jana, T.K., 2003, The geometry of the Burmese-Andaman subducting lithosphere: Journal of Seismology, v. 7, p. 155-174.

Fine, I.V., Rabinovich, A.B., and Thomson, R.E., 2005, The dual source region for the 2004 Sumatra tsunami: Geophysical Research Letters, v. 32, doi: 10.1029/2005GL023521.

Fujii, Y., and Satake, K., 2007, Tsunami source of the 2004 Sumatra-Andaman earthquake inferred from tide gauge and satellite data: Bulletin of the Seismological Society of America, v. 97, p. S192-S207, doi: 10/1785/0120050613.

Gahalaut, V.K., Nagarajan, B., Catherine, J.K., and Kumar, S., 2006, Constraints on 2004 Sumatra-Andaman earthquake rupture from GPS measurements in Andaman-Nicobar Islands: Earth and Planetary Science Letters, v. 242, p. 365-374, doi: 10.1016/j.epsl.2005.11.051.

Geist, E.L., Titov, V.V., Arcas, D., Pollitz, F.F., and Bilek, S.L., 2007, Implications of the 26 December 2004 Sumatra-Andaman earthquake of tsunami forecast and assessment models for great subduction-zone earthquakes: Bulletin of the Seismological Society of America, v. 97, p. S249–S270, doi: 10.1785/0120050619.

Grilli M.ASCE, S.T., Ioualalen, M., Asavanant, J., Shi, F., Kirby M.ASCE, J.T., and Watts, P., 2007, Source constraints and model simulation of the December 26, 2004, Indian Ocean tsunami: Journal of Waterway, Port, Coastal, and Ocean Engineering, v. 133, p. 414-428, doi: 10.1061/(ASCE)0733-950X.

Gubbins, D., 2004, Time Series Analysis and Inverse Theory for Geophysicists: Cambridge, Cambridge University Press, 225 p.

Hanson, J.A., Reasoner, C.L., and Bowman, J.R., 2007, High-frequency tsunami signals of the great Indonesian earthquakes of 26 December 2004 and 28 March 2005: Bulletin of the Seismological Society of America, v. 97, p. S232-S248, doi: 10.1785/0120050607.

Hashimoto, M., Choosakul, N., Hashizume, M., Takemoto, S., Takiguchi, H., Fukuda, Y., and Fujimori, K., 2006, Crustal deformations associated with the great Sumatra-Andaman earthquake deduced from continuous GPS observation: Earth, Planets, Space, v. 58, p. 127-139.

Hoechner, A., Babeyko, A.Y., and Sobolev, S.V., 2008, Enhanced GPS inversion technique applied to the 2004 Sumatra earthquake and tsunami: Geophysical Research Letters, v. 35, doi: 10.1029/2007GL033133.

Hsu, Y.-J., Simons, M., Avouac, J.-P., Galetzka, J., Sieh, K., Chlieh, M., Natawidjaja, D., Prawirodirdjo, L., and Bock, Y., 2006, Frictional afterslip following the 2005 Nias-Simeulue earthquake, Sumatra: Science, v. 312, p. 1921-1926, doi: 10.1126/science.1126960.

Hughes, K.L.H., Masterlark, T., and Mooney, W.D., 2010, Poroelastic stress-triggering of the 2005 M8.7 Nias earthquake by the 2004 M9.2 Sumatra-Andaman earthquake: Earth and Planetary Science Letters, v. 293, p. 289-299, doi: 10.1016/j.epsl.2010.02.043.

Hughes, K.L.H., Masterlark, T., and Mooney, W.D., 2011, Pore-fluid migration and the timing of the 2005 M8.7 Nias earthquake, Lithosphere, v. 3, p. 170-172, doi: 10.1130/L109.1.

Johnson, K.M., and Segall, P., 2004, Viscoelastic earthquake cycle models with deep stress-driven creep along the San Andreas fault system: Journal of Geophysical Research, v. 109, doi: 10.1029/2004JB003096.

Kieckhefer, R.M., Shor, Jr., G.G., Curray, J.R., Sugiarta, W., and Hehuwat, F., 1980, Seismic refraction studies of the Sunda trench and forearc basin: Journal of Geophysical Research, v. 85, p. 863-889.

Kopp, H., and Kukowski, N., 2003, Backstop geometry and accretionary mechanics of the Sunda margin: Tectonics, v. 22, doi: 10.1029/2002TC001420.

Kopp, H., Flueh, E.R., Klaeschen, D., Bialas, J., and Reichert, C., 2001, Crustal structure of the central Sunda margin at the onset of oblique subduction: Geophysical Journal International, v. 147, p. 449-474.

Kopp, H., Klaeschen, D., Flueh, E.R., and Bialas, J., 2002, Crustal structure of the Java margin from seismic wide-angle and multichannel reflection data: Journal of Geophysical Research, v. 107, doi: 10.1029/2000JB000095.

Kreemer, C., Blewitt, G., and Maerten, F., 2006, Co- and postseismic deformation of the 28 March 2005 Nias M_w 8.7 earthquake from continuous GPS data: Geophysical Research Letters, v. 33, doi: 10.1029/2005GL025566.

Lay, T., Kanamori, H., Ammon, C.J., Nettles, M., Ward, S.N., Aster, R.C., Beck, S.L., Bilek, S.L., Brudzinski, M.R., Butler, R., DeShon, H.R., Ekström, G., Satake, K., and Sipkin, S., 2005, The great Sumatra-Andaman earthquake of 26 December 2004: Science, v. 308, p. 1127-1133, doi: 10.1126/science.1112250.

Lin, J.-Y., Le Pichon, X., Rangin, C., Sibuet, J.-C., and Maury, T., 2009, Spatial aftershock distribution of the 26 December 2004 great Sumatra-Andaman earthquake in the northern Sumatra area: G-Cubed, Geochemistry, Geophysics, Geosystems, v. 10, doi: 10.1029/2009GC002454.

Lorito, S., Piatanesi, A., Cannelli, V., Romano, F., and Melini, D., 2010, Kinematics and source zone properties of the 2004 Sumatra-Andaman earthquake and tsunami: Nonlinear joint inversion of tide gauge, satellite altimetry, and GPS data: Journal of Geophysical Research, v. 115, doi: 10.1029/2008JB005974.

Lorito, S., Romano, F., Piatanesi, A., and Boschi, E., 2008, Source process of the September 12, 2007, M_W 8.4 southern Sumatra earthquake from tsunami tide gauge record inversion: Geophysical Research Letters, v. 35, doi: 10.1029/2007GL032661.

Masterlark, T., 2003, Finite element model predictions of static deformation from dislocation sources in a subduction zone: Sensitivities to homogeneous, isotropic, Poisson-solid, and half-space assumptions: Journal of Geophysical Research, v. 108, doi: 10.1029/2002JB002296.

Masterlark, T., DeMets, C., Wang, H.F., Sánchez, O., and Stock, J., 2001, Homogeneous vs heterogeneous subduction zone models: Coseismic and postseismic deformation: Geophysical Research Letters, v. 28, p. 4047-4050.

Masterlark, T., and Hughes, K.L.H., 2008, Next generation of deformation models for the 2004 M9 Sumatra-Andaman earthquake: Geophysical Research Letters, v. 35, doi: 10.1029/2008GL035198.

Menke, W., 1989, Geophysical Data Analysis: Discrete Inverse Theory: San Diego, Academic Press, 289 p.

Mignan, A., King, G., Bowman, D., Lacassin, R., and Dmowska, R., 2006, Seismic activity in the Sumatra-Java region prior to the December 26, 2004 (M_w=9.0-

9.3) and March 28, 2005 (M_w=8.7) earthquakes: Earth and Planetary Science Letters, v. 244, p. 639-654, doi: 10.1016/j.epsl.2006.01.058.

Mukhopadhyay, M., 1988, Gravity anomalies and deep structure of the Andaman arc: Marine Geophysical Researches, v. 9, p. 197-210.

Okada, Y., 1992, Internal deformation due to shear and tensile faults in a half-space: Bulletin of the Seismological Society of America, v. 82, p. 1018–1040.

Panet, I., Mikhailov, V., Diament, M., Pollitz, F., King, G., de Viron, O., Holschneider, M., Biancale, R., and Lemoine, J.-M., 2007, Coseismic and post-seismic signatures of the Sumatra 2004 December and 2005 March earthquakes in GRACE satellite gravity: Geophysical Journal International, v. 171, p. 177-190, doi: 10.1111/j.1365-246X.2007.03525.x.

Pesicek, J.D., Thurber, C.H., Widiyantoro, S., Engdahl, E.R., and DeShon, H.R., 2008, Complex slab subduction beneath northern Sumatra: Geophysical Research Letters, v. 35, doi: 10.1029/2008GL035262.

Pesicek, J.D., Thurber, C.H., Widiyantoro, S., Zhang, H., DeShon, H.R., and Engdahl, E.R., 2010, Sharpening the tomographic image of the subducting slab below Sumatra, the Andaman Islands and Burma: Geophysical Journal International, v. 182, p. 433-453, doi: 10.1111/j.1365-246X.2010.04630.x.

Piatanesi, A., and Lorito, S., 2007, Rupture process of the 2004 Sumatra-Andaman earthquake from tsunami waveform inversion: Bulletin of the Seismological Society of America, v. 97, p. S223-S231, doi: 10.1785/0120050627.

Poisson, B., Oliveros, C., and Pedreros, R., 2011, Is there a best source model of the Sumatra 2004 earthquake for simulating the consecutive tsunami?: Geophysical Journal International, v. 185, p. 1365-1378, doi: 10.1111/j.1365-246X.2011.05009.x.

Rastogi, B.K., and Jaiswal, R.K., 2006, A catalog of tsunamis in the Indian Ocean: Science of Tsunami Hazards, v. 25, p. 128-143.

Rhie, J., Dreger, D., Bürgmann, R., and Romanowicz, B., 2007, Slip of the 2004 Sumatra-Andaman earthquake from joint inversion of long-period global seismic waveforms and GPS static offsets: Bulletin of the Seismological Society of America, v. 97, p. S115-S127, doi: 10.1785/0120050620.

Simons, W.J.F., Socquet, A., Vigny, C., Ambrosius, B.A.C., Abu, S.H., Promthong, C., Subarya, C., Sarsito, D.A., Matheussen, S., Morgan, P., and Spakman, W., 2007, A decade of GPS in southeast Asia: Resolving Sundaland motion and boundaries, Journal of Geophysical Research, v. 112, doi: 10.1029/2005JB003868.

Song, Y.T., Ji, C., Fu, L.-L., Zlotnicki, V., Shum, C.K., Yi, Y., and Hjorleifsdottir, V., 2005, The 26 December 2004 tsunami source estimated fom satellite radar altimetry and seismic waves: Geophysical Research Letters, v. 32, doi: 10.1029/2005GL023683.

Sørensen, M.B., Atakan, K., and Pulido, N., 2007, Simulated strong ground motions for the great M9.3 Sumatra-Andaman earthquake of 26 December 2004: Bulletin of the Seismological Society of America, v. 97, p. S139-S151, doi: 10.1785/0120050608.

Subarya, C., Chlieh, M., Prawirodirdjo, L., Avouac, J.-P., Bock, Y., Sieh, K., Meltzner, A.J., Natawidjaja, D.H., and McCaffrey, R., 2006, Plate-boundary deformation associated with the great Sumatra-Andaman earthquake: Nature, v. 440, p. 46–51, doi: 10.1038/nature04522.

Turcotte, D.L., and Schubert, G.J., 1982, Geodynamics: Applications of Continuum Physics to Geological Problems: New York, John Wiley and Sons, 450 p.

U.S. Geological Survey - Earthquake Hazards Program, 2010, Slab Models for Subduction Zones, http://earthquake.usgs.gov/research/data/slab/#models, date accessed 25 April 2010, date updated 5 November 2009.

Vigny, C., Simons, W.J.F., Abu, S., Bamphenyu, R., Satirapod, C., Choosakul, N., Subarya, C., Socquet, A., Omar, K., Abidin, H.Z., and Ambrosius, B.A.C., 2005, Insight into the 2004 Sumatra-Andaman earthquake from GPS measurements in southeast Asia, Nature, v. 436, p. 201-206.

Wang, H.F., 2000, Theory of Linear Poroelasticity: With Applications to Geomechanics: Princeton, Princeton University Press, 287 p.

Wang, H.F., and Anderson, M.P., 1982, Introduction to Groundwater Modeling: Finite Difference and Finite Element Methods: San Diego, Academic Press, 237 p.

APPENDIX

This is a table of the Global Conductance matrix (GCM) ($\boldsymbol{C}$) for the SAE. All non-zero terms are shown for each column in their entirety and only non-zero terms are presented. The GCM was constructed using finite element methods (Wang and Anderson, 1982) on the slip patches of the SAE (see SECTION 4. Model Calibration). All off-diagonal terms are negative, and the diagonal terms are the absolute value of the sum of all other terms on the row.

Table 6.2. Global Conductance Matrix (GCM) Values

	801	802	803	804	805	806	807	808
801	2.18074916	-0.43089511	-1.59009245	-0.15976160				
802	-0.43089511	3.00720575	-1.63258445					
803	-1.59009245	-1.63258445	4.99325155	-0.74481306				
804	-0.15976160		-0.74481306	2.32389118	-0.97630665			
805				-0.97630665	2.46121216	-0.53544469		
806					-0.53544469	1.73385171	-0.43348889	
807						-0.43348889	1.84877882	-0.37330658
808							-0.37330658	1.86765277
809								-0.26776579
815								-0.20983337
816							-0.23511295	-1.01674703
817						-0.22721762	-0.80687040	
818					-0.46288856	-0.53770051		
819					-0.25173467			
820			-0.89523236	-0.44300987	-0.23483759			
821		-0.78310480	-0.13052923					
822		-0.16062139						

	809	810	811	812	813	814	815	816
807								-0.23511295
808	-0.26776579						-0.20983337	-1.01674703
809	2.07534916	-0.67325867	-0.02625219				-1.10807252	
810	-0.67325867	2.93543373	-2.01777110	-0.24440396				
811	-0.02625219	-2.01777110	4.47900941	-1.10461283			-0.68810659	
812		-0.24440396	-1.10461283	2.63904935	-0.35809902			
813				-0.35809902	2.55918611	-1.15938172		
814					-1.15938172	1.45214796		
815	-1.10807252		-0.68810659				3.74865499	-0.85475660
816							-0.85475660	3.70211220
817								-0.79845205
829								-0.46860161
830							-0.46962766	-0.32844195
831			-0.37977144				-0.41825825	
832			-0.26249526	-0.51354393				
833				-0.41838961	-1.04170536	-0.29276624		

	817	818	819	820	821	822	823	824
802					-0.78310480	-0.16062139		
803				-0.89523236	-0.13052923			
804				-0.44300987				
805		-0.46288856	-0.25173467	-0.23483759				
806	-0.22721762	-0.53770051						
807	-0.80687040							
816	-0.79845205							
817	3.63597943	-0.91448130						
818	-0.91448130	3.59760405	-0.84024493					
819		-0.84024493	4.23682577	-1.81444671	-0.56256504			
820			-1.81444671	4.36466363	-0.97713709			
821			-0.56256504	-0.97713709	4.07634333	-0.84041371		
822					-0.84041371	3.09732556	-0.46451284	-1.13171789
823						-0.46451284	3.53903016	-2.28364558
824						-1.13171789	-2.28364558	4.86876871
825					-0.39323757	-0.50005974		-0.87567951
826			-0.44661203		-0.38935589			
827		-0.53121873	-0.32122239					
828	-0.51496893	-0.31107002						
829	-0.37398912							
834							-0.13379357	
835							-0.65707817	-0.20783794
836								-0.36988779

	825	826	827	828	829	830	831	832
811							-0.37977144	-0.26249526
812								-0.51354393
815						-0.46962766	-0.41825825	
816					-0.46860161	-0.32844195		
817				-0.51496893	-0.37398912			
818			-0.53121873	-0.31107002				
819		-0.44661203	-0.32122239					
821	-0.39323757	-0.38935589						
822	-0.50005974							
824	-0.87567951							
825	3.62978453	-1.01199765						
826	-1.01199765	3.65464254	-0.95661432					
827		-0.95661432	3.66363495	-1.03311108				
828			-1.03311108	3.68379875	-0.99586208			
829				-0.99586208	3.67434778	-1.03277603		
830					-1.03277603	3.67723022	-0.99383519	
831						-0.99383519	3.67783706	-1.03740253
832							-1.03740253	4.11031131
833								-1.41051347
836	-0.53232619							
837	-0.31648387	-0.52007966						
838		-0.32998298	-0.43715861					
839			-0.38430982	-0.51134591				
840				-0.31744073	-0.46463878			
841					-0.33848016	-0.51034712		
842						-0.34220227	-0.49321788	
843							-0.35535177	-0.88635611

	833	834	835	836	837	838	839	840
812	-0.41838961							
813	-1.04170536							
814	-0.29276624							
823		-0.13379357	-0.65707817					
824			-0.20783794	-0.36988779				
825				-0.53232619	-0.31648387			
826					-0.52007966	-0.32998298		
827						-0.43715861	-0.38430982	
828							-0.51134591	-0.31744073
829								-0.46463878
832	-1.41051347							
833	3.36640771							
834		2.47155363	-0.80485475					
835		-0.80485475	3.73039340	-1.20946713				
836			-1.20946713	3.73290657	-0.90556556			
837				-0.90556556	3.66945888	-1.07176049		
838					-1.07176049	3.68525995	-0.97104998	
839						-0.97104998	3.66919767	-1.03492643
840							-1.03492643	3.69453662
841								-1.02987736
843	-0.20303302							
844		-0.24362888						
845		-0.86685222						
846		-0.42242421	-0.47927157					
847			-0.37188384	-0.42430509				
848				-0.29135480	-0.54208843			
849					-0.31348087	-0.51327598		
850						-0.36203191	-0.45461386	
851							-0.31295167	-0.50972923
852								-0.33792409

	841	842	843	844	845	846	847	848
829	-0.33848016							
830	-0.51034712	-0.34220227						
831		-0.49321788	-0.35535177					
832			-0.88635611					
833			-0.20303302					
834				-0.24362888	-0.86685222	-0.42242421		
835						-0.47927157	-0.37188384	
836							-0.42430509	-0.29135480
837								-0.54208843
840	-1.02987736							
841	3.68752412	-1.02641153						
842	-1.02641153	3.64563408	-0.83588312					
843		-0.83588312	2.39813804					
844				2.85988145	-2.02409054			
845				-2.02409054	4.45480679	-0.94471502		
846					-0.94471502	3.65279217	-1.02207519	
847						-1.02207519	3.70985699	-1.08808344
848							-1.08808344	3.72331161
849								-1.02481773
852	-0.42200669							
853	-0.36040126	-0.32028498						
854		-0.62763430	-0.11751401					
855				-0.07208223				
856				-0.52007979	-0.25769959			
857					-0.36144941	-0.42850095		
858						-0.35580522	-0.44105899	
859							-0.36245044	-0.47055332
860								-0.30641388

	849	850	851	852	853	854	855	856
837	-0.31348087							
838	-0.51327598	-0.36203191						
839		-0.45461386	-0.31295167					
840			-0.50972923	-0.33792409				
841				-0.42200669	-0.36040126			
842					-0.32028498	-0.62763430		
843						-0.11751401		
844							-0.07208223	-0.52007979
845								-0.25769959
848	-1.02481773							
849	3.69200671	-1.02851889						
850	-1.02851889	3.68595427	-1.02890095					
851		-1.02890095	3.69982308	-1.04866020				
852			-1.04866020	3.67526975	-0.97795259			
853				-0.97795259	4.30062327	-1.78122869		
854					-1.78122869	2.76756754		
855							2.01529029	-1.29045478
856							-1.29045478	3.85183053
857								-1.06645788
860	-0.48907770							
861	-0.32283554	-0.46062852						
862		-0.35126014	-0.45394740					
863			-0.34563363	-0.47974929				
864				-0.40897690	-0.86075575	-0.24119054		
865							-0.19866242	
866							-0.45409086	-0.36712410
867								-0.35001440

	857	858	859	860	861	862	863	864
845	-0.36144941							
846	-0.42850095	-0.35580522						
847		-0.44105899	-0.36245044					
848			-0.47055332	-0.30641388				
849				-0.48907770	-0.32283554			
850					-0.46062852	-0.35126014		
851						-0.45394740	-0.34563363	
852							-0.47974929	-0.40897690
853								-0.86075575
854								-0.24119054
856	-1.06645788							
857	3.69676543	-0.99973374						
858	-0.99973374	3.67276403	-1.00776801					
859		-1.00776801	3.68793341	-1.04982668				
860			-1.04982668	3.68065870	-0.97418503			
861				-0.97418503	3.67386833	-1.04155543		
862					-1.04155543	3.68563964	-1.01267670	
863						-1.01267670	3.68468456	-0.96722076
864							-0.96722076	2.54616450
867	-0.52617871							
868	-0.31444473	-0.55363807						
869		-0.31476002	-0.46706924					
870			-0.33026572	-0.52083065				
871				-0.34032476	-0.51755181			
872					-0.35711201	-0.48060894		
873						-0.34559104	-0.29709957	
874							-0.58230461	-0.06802055

	865	866	867	868	869	870	871	872
855	-0.19866242	-0.45409086						
856		-0.36712410	-0.35001440					
857			-0.52617871	-0.31444473				
858				-0.55363807	-0.31476002			
859					-0.46706924	-0.33026572		
860						-0.52083065	-0.34032476	
861							-0.51755181	-0.35711201
862								-0.48060894
865	2.12275211	-0.78814032						
866	-0.78814032	3.67879076	-1.17511935					
867		-1.17511935	3.72379127	-0.93460539				
868			-0.93460539	3.65840435	-1.02549222			
869				-1.02549222	3.68076901	-1.00979437		
870					-1.00979437	3.67582728	-1.01328401	
871						-1.01328401	3.65550309	-0.96270880
872							-0.96270880	3.66178897
873								-1.03470736
875	-0.12513288							
876	-0.60973216							
877	-0.40108433	-0.55154739						
878		-0.34276873	-0.41960008					
879			-0.31827336	-0.50161469				
880				-0.32860926	-0.50587292			
881					-0.35778024	-0.45536572		
882						-0.34628681	-0.46187370	
883							-0.35976000	-0.45325806
884								-0.37339380

	873	874	875	876	877	878	879	880
862	-0.34559104							
863	-0.29709957	-0.58230461						
864		-0.06802055						
865			-0.12513288	-0.60973216	-0.40108433			
866					-0.55154739	-0.34276873		
867						-0.41960008	-0.31827336	
868							-0.50161469	-0.32860926
869								-0.50587292
872	-1.03470736							
873	4.43457395	-2.00064565						
874	-2.00064565	2.85794801						
875			2.76017548	-2.17010784				
876			-2.17010784	4.50381142	-1.02759976			
877				-1.02759976	3.68295755	-0.99433568		
878					-0.99433568	3.68279167	-1.03797946	
879						-1.03797946	3.69024621	-1.01256774
880							-1.01256774	3.66884216
881								-0.98711528
884	-0.75653033	-0.20697719						
885			-0.05435122					
886			-0.41058355	-0.30337245				
887				-0.39299922	-0.43215552			
888					-0.27623486	-0.53911425		
889						-0.34899347	-0.49564379	
890							-0.32416717	-0.51175532
891								-0.32292164

	881	882	883	884	885	886	887	888
869	-0.35778024							
870	-0.45536572	-0.34628681						
871		-0.46187370	-0.35976000					
872			-0.45325806	-0.37339380				
873				-0.75653033				
874				-0.20697719				
875					-0.05435122	-0.41058355		
876						-0.30337245	-0.39299922	
877							-0.43215552	-0.27623486
878								-0.53911425
880	-0.98711528							
881	3.67060390	-1.03140090						
882	-1.03140090	3.67382528	-0.99333920					
883		-0.99333920	3.64192943	-0.90690084				
884			-0.90690084	2.39862212				
885					2.03110490	-1.39072645		
886					-1.39072645	3.89392666	-1.04564565	
887						-1.04564565	3.68651295	-0.99343784
888							-0.99343784	3.67352260
889								-0.99137532
891	-0.49120303							
892	-0.34773874	-0.49302165						
893		-0.34790303	-0.33916404					
894			-0.58950729	-0.15481996				
895					-0.22431857			
896					-0.36170866	-0.36130263		
897						-0.38229593	-0.52073977	
898							-0.30153494	-0.54154503
899								-0.33181530

	889	890	891	892	893	894	895	896
878	-0.34899347							
879	-0.49564379	-0.32416717						
880		-0.51175532	-0.32292164					
881			-0.49120303	-0.34773874				
882				-0.49302165	-0.34790303			
883					-0.33916404	-0.58950729		
884						-0.15481996		
885							-0.22431857	-0.36170866
886								-0.36130263
888	-0.99137532							
889	3.66580921	-1.01339200						
890	-1.01339200	3.67678799	-1.01094091					
891		-1.01094091	3.67392481	-1.01327768				
892			-1.01327768	3.66813393	-0.99705082			
893				-0.99705082	3.89422985	-1.37974656		
894					-1.37974656	2.14231078		
895							1.88162582	-1.05659822
896							-1.05659822	3.72908046
897								-1.09385215
899	-0.47232689							
900	-0.34407774	-0.47854970						
901		-0.33798289	-0.46778603					
902			-0.36779552	-0.47334947				
903				-0.34369558	-0.30863633			
904					-0.52172907	-0.01823697		
905							-0.16324663	
906							-0.43746240	-0.48417508
907								-0.37144371

	897	898	899	900	901	902	903	904
886	-0.38229593							
887	-0.52073977	-0.30153494						
888		-0.54154503	-0.33181530					
889			-0.47232689	-0.34407774				
890				-0.47854970	-0.33798289			
891					-0.46778603	-0.36779552		
892						-0.47334947	-0.34369558	
893							-0.30863633	-0.52172907
894								-0.01823697
896	-1.09385215							
897	3.70201769	-0.98441332						
898	-0.98441332	3.69218597	-1.05261017					
899		-1.05261017	3.68596415	-0.99071071				
900			-0.99071071	3.68258199	-1.05438494			
901				-1.05438494	3.68834291	-1.00527110		
902					-1.00527110	3.65566463	-0.97953374	
903						-0.97953374	4.57997680	-2.26253504
904							-2.26253504	2.96972979
907	-0.38659760							
908	-0.33411891	-0.51440582						
909		-0.29767668	-0.51113646					
910			-0.32736461	-0.47097175				
911				-0.34388714	-0.47452443			
912					-0.34839352	-0.47354518		
913						-0.35616963	-0.68557611	-0.16722871

	905	906	907	908	909	910	911	912
895	-0.16324663	-0.43746240						
896		-0.48417508	-0.37144371					
897			-0.38659760	-0.33411891				
898				-0.51440582	-0.29767668			
899					-0.51113646	-0.32736461		
900						-0.47097175	-0.34388714	
901							-0.47452443	-0.34839352
902								-0.47354518
905	1.74452972	-0.90100683						
906	-0.90100683	3.63922450	-1.01524975					
907		-1.01524975	3.68389098	-1.02393346				
908			-1.02393346	3.69153670	-1.03299260			
909				-1.03299260	3.71168300	-1.06768467		
910					-1.06768467	3.70320626	-1.02008082	
911						-1.02008082	3.67827192	-1.00816633
912							-1.00816633	3.65692718
913								-0.97007073
914	-0.31247506							
915	-0.36780121	-0.49255124						
916		-0.30877919	-0.54036608					
917			-0.34630038	-0.46604860				
918				-0.32003731	-0.46504029			
919					-0.33715229	-0.48830313		
920						-0.32880127	-0.51007848	
921							-0.32153471	-0.38551168
922								-0.47123974

	913	914	915	916	917	918	919	920
902	-0.35616963							
903	-0.68557611							
904	-0.16722871							
905		-0.31247506	-0.36780121					
906			-0.49255124	-0.30877919				
907				-0.54036608	-0.34630038			
908					-0.46604860	-0.32003731		
909						-0.46504029	-0.33715229	
910							-0.48830313	-0.32880127
911								-0.51007848
912	-0.97007073							
913	2.33323586							
914		1.78225011	-0.87558518					
915		-0.87558518	3.62085401	-1.00208750				
916			-1.00208750	3.68065336	-1.02110747			
917				-1.02110747	3.68726845	-1.03185353		
918					-1.03185353	3.69695875	-1.03796507	
919						-1.03796507	3.68317647	-1.01171508
920							-1.01171508	3.69571234
921								-1.05648545
922	-0.15419067							
923		-0.26926167						
924		-0.32492821	-0.51630361					
925			-0.36652528	-0.47655671				
926				-0.33175640	-0.49084292			
927					-0.33111555	-0.51001021		
928						-0.33205235	-0.43972789	
929							-0.36831301	-0.46541649
930								-0.32321556

	921	922	923	924	925	926	927	928
911	-0.32153471							
912	-0.38551168	-0.47123974						
913		-0.15419067						
914			-0.26926167	-0.32492821				
915				-0.51630361	-0.36652528			
916					-0.47655671	-0.33175640		
917						-0.49084292	-0.33111555	
918							-0.51001021	-0.33205235
919								-0.43972789
920	-1.05648545							
921	3.82285856	-1.26376886						
922	-1.26376886	2.00025376						
923			1.78046741	-0.89223822				
924			-0.89223822	3.60541577	-0.92303988			
925				-0.92303988	3.66641224	-1.07204385		
926					-1.07204385	3.68998237	-0.98270993	
927						-0.98270993	3.69472280	-1.08060918
928							-1.08060918	3.69549490
929								-0.99314260
930	-0.34772680							
931	-0.44783104	-0.11105449						
932			-0.26686147					
933			-0.35210605	-0.58208872				
934				-0.36681714	-0.50212942			
935					-0.32611709	-0.48138602		
936						-0.33124325	-0.46359883	
937							-0.32667911	-0.48870194
938								-0.36126093

	929	930	931	932	933	934	935	936
919	-0.36831301							
920	-0.46541649	-0.32321556						
921		-0.34772680	-0.44783104					
922			-0.11105449					
923				-0.26686147	-0.35210605			
924					-0.58208872	-0.36681714		
925						-0.50212942	-0.32611709	
926							-0.48138602	-0.33124325
927								-0.46359883
928	-0.99314260							
929	3.70584186	-1.07323383						
930	-1.07323383	4.16792307	-1.64553657					
931		-1.64553657	2.31840800					
932				1.79342573	-0.92647144			
933				-0.92647144	3.61068084	-0.90615432		
934					-0.90615432	3.66428525	-1.07657772	
935						-1.07657772	3.72263149	-1.05669194
936							-1.05669194	3.70119426
937								-1.02960427
938	-0.53486695							
939	-0.27086898	-0.77821031	-0.11398590					
940				-0.30600972				
941				-0.29408309	-0.51583090			
942					-0.32802941	-0.49151672		
943						-0.32108995	-0.45679675	
944							-0.32506196	-0.48366655
945								-0.33638941

	937	938	939	940	941	942	943	944
927	-0.32667911							
928	-0.48870194	-0.36126093						
929		-0.53486695	-0.27086898					
930			-0.77821031					
931			-0.11398590					
932				-0.30600972	-0.29408309			
933					-0.51583090	-0.32802941		
934						-0.49151672	-0.32108995	
935							-0.45679675	-0.32506196
936	-1.02960427							-0.48366655
937	3.68332279	-1.01191002						
938	-1.01191002	3.59879982	-0.76496237					
939		-0.76496237	2.20824878					
940				1.81145597	-1.03973050			
941				-1.03973050	3.67842922	-0.96230675		
942					-0.96230675	3.69184684	-1.08870626	
943						-1.08870626	3.71853477	-1.03613606
944							-1.03613606	3.68221374
945	-0.48847254							-0.99863715
946	-0.33795491	-0.54086840						
947		-0.38493115	-0.28022122					
948				-0.27615815				
949				-0.18955759	-0.54718546			
950					-0.31929251	-0.49849393		
951						-0.32279378	-0.47702113	
952							-0.33878461	-0.50712794
953								-0.33158408

	945	946	947	948	949	950	951	952
936	-0.33638941							
937	-0.48847254	-0.33795491						
938		-0.54086840	-0.38493115					
939			-0.28022122					
940				-0.27615815	-0.18955759			
941					-0.54718546	-0.31929251		
942						-0.49849393	-0.32279378	
943							-0.47702113	-0.33878461
944	-0.99863715							-0.50712794
945	3.68285293	-1.04705994						
946	-1.04705994	3.63980075	-0.85066785					
947		-0.85066785	1.81349808					
948				2.03291389	-1.34038504			
949				-1.34038504	3.86386259	-1.02130776		
950					-1.02130776	3.69523354	-1.04764255	
951						-1.04764255	3.68848436	-1.00802621
952							-1.00802621	3.70203594
953	-0.46081486							-1.07361216
954	-0.35147904	-0.52923983						
955		-0.33400983	-0.29767786					
956				-0.21283298				
957				-0.20353772	-0.42960194			
958					-0.33582480	-0.46601702		
959						-0.34247977	-0.48547939	
960							-0.34752129	-0.46195991
961								-0.31252511

	953	954	955	956	957	958	959	960
944	-0.33158408							
945	-0.46081486	-0.35147904						
946		-0.52923983	-0.33400983					
947			-0.29767786					
948				-0.21283298	-0.20353772			
949					-0.42960194	-0.33582480		
950						-0.46601702	-0.34247977	
951							-0.48547939	-0.34752129
952	-1.07361216							-0.46195991
953	3.69654262	-1.00142106						
954	-1.00142106	3.62050692	-0.85786342					
955		-0.85786342	1.79756669					
956				2.06943064	-1.76564528			
957				-1.76564528	4.16452181	-1.04449451		
958					-1.04449451	3.71022933	-1.06915960	
959						-1.06915960	3.71376547	-1.04936164
960							-1.04936164	3.69628393
961	-0.48401382							-1.02656719
962	-0.34509664	-0.53266442						
963		-0.34783914	-0.30801557					
964				-0.09095238	-0.47571277			
965					-0.24552959	-0.39511149		
966						-0.39962191	-0.41870863	
967							-0.34857643	-0.48384505
968								-0.32702884

	961	962	963	964	965	966	967	968
952	-0.31252511							
953	-0.48401382	-0.34509664						
954		-0.53266442	-0.34783914					
955			-0.30801557					
956				-0.09095238				
957				-0.47571277	-0.24552959			
958					-0.39511149	-0.39962191		
959						-0.41870863	-0.34857643	
960	-1.02656719						-0.48384505	-0.32702884
961	3.68757201	-1.02615505						-0.48230421
962	-1.02615505	3.61560368	-0.82379765					
963		-0.82379765	1.96931079					
964				2.30848288	-1.38604138			
965				-1.38604138	3.85928525	-0.93484358		
966					-0.93484358	3.65558160	-1.03206140	
967						-1.03206140	3.68641087	-1.02550064
968	-0.48230421						-1.02550064	3.69125314
969	-0.35600663	-0.46926388						-1.03515503
970		-0.41862603	-0.31131129					
971			-0.17834712					
972				-0.29873057				
973				-0.05704578	-0.58249577			
974					-0.31526344	-0.54191243		
975						-0.32843365	-0.43817095	
976							-0.35825639	-0.48862797
977								-0.33263644

	969	970	971	972	973	974	975	976
961	-0.35600663							
962	-0.46926388	-0.41862603						
963		-0.31131129	-0.17834712					
964				-0.29873057	-0.05704578			
965					-0.58249577	-0.31526344		
966						-0.54191243	-0.32843365	
967							-0.43817095	-0.35825639
968	-1.03515503							-0.48862797
969	3.68496232	-1.01427763						
970	-1.01427763	4.10003057	-1.71257530					
971		-1.71257530	2.09458332					
972				1.96672099	-1.55845563			
973				-1.55845563	4.01641087	-1.00821294		
974					-1.00821294	3.70531012	-1.07335960	
975						-1.07335960	3.68804414	-0.97985354
976							-0.97985354	3.66643137
977	-0.48727510							-1.02923413
978	-0.32298405	-0.41977287						
979		-0.22346746	-0.20366090					
980				-0.10953480	-0.44212472			
981					-0.36807603	-0.43611878		
982						-0.33044292	-0.50026515	
983							-0.36796125	-0.45675141
984								-0.35370793

	977	978	979	980	981	982	983	984
968	-0.33263644							
969	-0.48727510	-0.32298405						
970		-0.41977287	-0.22346746					
971			-0.20366090					
972				-0.10953480				
973				-0.44212472	-0.36807603			
974					-0.43611878	-0.33044292		
975						-0.50026515	-0.36796125	
976	-1.02923413						-0.45675141	-0.35370793
977	3.70803153	-1.07366552						-0.44742685
978	-1.07366552	3.93284049	-1.41544492					
979		-1.41544492	2.13048294					
980				2.01384589	-0.98938618			
981				-0.98938618	3.66515242	-1.02173449		
982					-1.02173449	3.68525995	-1.02452949	
983						-1.02452949	3.67406524	-1.00787194
984	-0.44742685						-1.00787194	3.68186415
985	-0.33779349	-0.51658238						-1.03824181
986		-0.18439075	-0.28790967					
987				-0.33446172				
988				-0.13833848	-0.46917764			
989					-0.38065930	-0.46983398	-0.93454848	
990						-0.33845391	-0.45296476	
991							-0.36398639	-0.48827320
992								-0.34634242

	985	986	987	988	989	990	991	992
977	-0.33779349							
978	-0.51658238	-0.18439075						
979		-0.28790967						
980			-0.33446172	-0.13833848				
981				-0.46917764	-0.38065930			
982					-0.46983398	-0.33845391		
983						-0.45296476	-0.36398639	
984	-1.03824181						-0.48827320	-0.34634242
985	3.66190730	-0.94508931						-0.47956085
986	-0.94508931	1.94137986						
987			2.28393237	-1.62829163				
988			-1.62829163	4.02234051	-0.93454848			
989				-0.93454848	3.66790132	-1.06970083		
990					-1.06970083	3.67808138	-0.96884917	
991						-0.96884917	3.66366770	-1.03337620
992	-0.47956085						-1.03337620	3.69973262
993	-0.34463946	-0.42834997						-1.05322843
994		-0.09564016						
995			-0.20538870					
996			-0.11579033	-0.52691451				
997				-0.32506978	-0.48658102			
998					-0.32657770	-0.45901014		
999						-0.38910257	-0.45764789	
1000							-0.35153485	-0.44990811
1001								-0.33731661

	993	994	995	996	997	998	999	1000
985	-0.34463946							
986	-0.42834997	-0.09564016						
987			-0.20538870	-0.11579033				
988				-0.52691451	-0.32506978			
989					-0.48658102	-0.32657770		
990						-0.45901014	-0.38910257	
991							-0.45764789	-0.35153485
992	-1.05322843							-0.44990811
993	4.21726687	-1.83020393						
994	-1.83020393	2.25653386						
995			1.99009577	-1.62496983				
996			-1.62496983	4.07371872	-1.06616648			
997				-1.06616648	3.73161847	-1.08554405		
998					-1.08554405	3.70497603	-1.01285065	
999						-1.01285065	3.67387711	-1.02193741
1000							-1.02193741	3.68613804
1001	-0.47800957							-1.03357747
1002	-0.08283552	-0.33068978						
1003			-0.15973724	-0.36963558				
1004				-0.37024199	-0.43858254			
1005					-0.32967459	-0.45856395		
1006						-0.36242955	-0.43336959	
1007							-0.35896900	-0.48864076
1008								-0.34053944

	1001	1002	1003	1004	1005	1006	1007	1008
992	-0.33731661							
993	-0.47800957	-0.08283552						
994		-0.33068978						
995			-0.15973724					
996			-0.36963558	-0.37024199				
997				-0.43858254	-0.32967459			
998					-0.45856395	-0.36242955		
999						-0.43336959	-0.35896900	
1000	-1.03357747						-0.48864076	-0.34053944
1001	3.72992154	-1.11585869						-0.39527820
1002	-1.11585869	2.02766422						
1003			2.00926199	-1.00907539				
1004			-1.00907539	3.67520784	-1.02681231			
1005				-1.02681231	3.69802146	-1.05631363		
1006					-1.05631363	3.69063621	-1.01645822	
1007						-1.01645822	3.68132915	-1.02860998
1008	-0.39527820						-1.02860998	3.76409946
1009	-0.36988100	-0.33631131						-1.18758927
1010		-0.16196893						
1011			-0.32978810					
1012			-0.14102567	-0.43830486				
1013				-0.39219075	-0.46763945			
1014					-0.35901754	-0.45449588		
1015						-0.36756934	-0.44167690	
1016							-0.34697430	-0.46784320
1017								-0.34423938

	1009	1010	1011	1012	1013	1014	1015	1016
1001	-0.36988100							
1002	-0.33631131	-0.16196893						
1003			-0.32978810	-0.14102567				
1004				-0.43830486	-0.39219075			
1005					-0.46763945	-0.35901754		
1006						-0.45449588	-0.36756934	
1007							-0.44167690	-0.34697430
1008	-1.18758927							-0.46784320
1009	4.34593581	-1.91724962						
1010	-1.91724962	2.33727996						
1011			2.38127042	-1.75207153				
1012			-1.75207153	4.10136220	-0.89865225			
1013				-0.89865225	3.65197471	-1.06659980		
1014					-1.06659980	3.69339685	-1.01191580	
1015						-1.01191580	3.67025357	-1.01427227
1016							-1.01427227	3.78308214
1017	-0.40527633							-1.23654604
1018	-0.12962828	-0.25806142						
1019			-0.19763202					
1020			-0.10177877	-0.55802776				
1021				-0.31328013	-0.46760096			
1022					-0.35929151	-0.43356371		
1023						-0.36780412	-0.45901463	
1024							-0.37580463	-0.38095093
1025								-0.33649541

	1017	1018	1019	1020	1021	1022	1023	1024
1008	-0.34423938							
1009	-0.40527633	-0.12962828						
1010		-0.25806142						
1011			-0.19763202	-0.10177877				
1012				-0.55802776	-0.31328013			
1013					-0.46760096	-0.35929151		
1014						-0.43356371	-0.36780412	
1015							-0.45901463	-0.37580463
1016	-1.23654604							-0.38095093
1017	3.79902788	-1.05138748						
1018	-1.05138748	1.99488827						
1019			1.97950052	-1.62596935				
1020			-1.62596935	4.08655209	-1.07882864			
1021				-1.07882864	3.71664053	-1.03546907		
1022					-1.03546907	3.67590834	-1.00268562	
1023						-1.00268562	3.67976094	-1.04037218
1024							-1.04037218	3.78858584
1025	-0.39094012							-1.23229975
1026	-0.37063854	-0.34282322						
1027		-0.21298788						
1028			-0.15589915	-0.37217748				
1029				-0.34977009	-0.47558720			
1030					-0.34587452	-0.46757068		
1031						-0.37732774	-0.46873363	
1032							-0.34115077	-0.40784819
1033								-0.35131016

	1025	1026	1027	1028	1029	1030	1031	1032
1016	-0.33649541							
1017	-0.39094012	-0.37063854						
1018		-0.34282322	-0.21298788					
1019				-0.15589915				
1020				-0.37217748	-0.34977009			
1021					-0.47558720	-0.34587452		
1022						-0.46757068	-0.37732774	
1023							-0.46873363	-0.34115077
1024	-1.23229975							-0.40784819
1025	3.87296158	-1.21138593	0.00000000					
1026	-1.21138593	4.04911581	-1.47079281					
1027		-1.47079281	1.98654134					
1028				1.97196621	-0.96959848			
1029				-0.96959848	3.66257988	-1.02741970		
1030					-1.02741970	3.66726972	-0.98628256	
1031						-0.98628256	3.68002354	-1.05597779
1032							-1.05597779	3.80027370
1033	-0.34079607							-1.23865694
1034	-0.36104432	-0.49227009						
1035		-0.16120522	-0.30276066					
1036				-0.31880882				
1037				-0.15548228	-0.48405756			
1038					-0.35614684	-0.46945808		
1039						-0.37066418	-0.46040919	
1040							-0.33129264	-0.41288095
1041								-0.34375906

	1033	1034	1035	1036	1037	1038	1039	1040
1024	-0.35131016							
1025	-0.34079607	-0.36104432						
1026		-0.49227009	-0.16120522					
1027			-0.30276066					
1028				-0.31880882	-0.15548228			
1029					-0.48405756	-0.35614684		
1030						-0.46945808	-0.37066418	
1031							-0.46040919	-0.33129264
1032	-1.23865694							-0.41288095
1033	3.88485313	-1.22658336						
1034	-1.22658336	3.70672429	-0.78984599					
1035		-0.78984599	1.96899303					
1036				2.08857157	-1.64000515			
1037				-1.64000515	4.03976171	-0.96829145		
1038					-0.96829145	3.64808911	-0.99707009	
1039						-0.99707009	3.69702390	-1.08790876
1040							-1.08790876	3.81024063
1041	-0.34528964							-1.22954315
1042	-0.38221697	-0.43255854						
1043		-0.40442198	-0.48722709					
1044			-0.22795407					
1045				-0.12975759	-0.42971651			
1046					-0.36220875	-0.48535250		
1047						-0.37177014	-0.42650459	
1048							-0.35446708	-0.38327476
1049								-0.36534038

	1041	1042	1043	1044	1045	1046	1047	1048
1032	-0.34375906							
1033	-0.34528964	-0.38221697						
1034		-0.43255854	-0.40442198					
1035			-0.48722709	-0.22795407				
1036					-0.12975759			
1037					-0.42971651	-0.36220875		
1038						-0.48535250	-0.37177014	
1039							-0.42650459	-0.35446708
1040	-1.22954315							-0.38327476
1041	3.85139486	-1.17403750						
1042	-1.17403750	3.76207990	-1.04552592					
1043		-1.04552592	3.64706821	-0.90885312				
1044			-0.90885312	1.81258947				
1045					1.91062743	-0.84778953		
1046					-0.84778953	3.63278108	-1.04081078	
1047						-1.04081078	3.70753774	-1.06970456
1048							-1.06970456	3.78722141
1049	-0.36791706							-1.20427571
1050	-0.39084845	-0.37786114						
1051		-0.34987982	-0.43329162					
1052			-0.36774847	-0.52574596				
1053				-0.15003631				
1054					-0.32652328			
1055					-0.17684052	-0.56644190		
1056						-0.33017760	-0.45245152	
1057							-0.34629614	-0.40331181
1058								-0.37218748

	1049	1050	1051	1052	1053	1054	1055	1056
1040	-0.36534038							
1041	-0.36791706	-0.39084845						
1042		-0.37786114	-0.34987982					
1043			-0.43329162	-0.36774847				
1044				-0.52574596	-0.15003631			
1045						-0.32652328	-0.17684052	
1046							-0.56644190	-0.33017760
1047								-0.45245152
1048	-1.20427571							
1049	3.86953341	-1.23363069						
1050	-1.23363069	3.79587869	-1.05313844					
1051		-1.05313844	3.70208688	-1.04698507				
1052			-1.04698507	3.69512075	-1.01867754			
1053				-1.01867754	1.85299047			
1054						1.96949919	-1.48887667	
1055						-1.48887667	3.97392566	-1.02893715
1056							-1.02893715	3.70081696
1057								-1.06152656
1058	-0.33024545							
1059	-0.36812413	-0.37156746						
1060		-0.36883252	-0.43966730					
1061			-0.37912462	-0.43131969				
1062				-0.30464402	-0.56805577			
1063					-0.11622085			
1064						-0.15409924	-0.42301487	
1065							-0.28981454	-0.42739972
1066								-0.40032440

	1057	1058	1059	1060	1061	1062	1063	1064
1047	-0.34629614							
1048	-0.40331181	-0.37218748						
1049		-0.33024545	-0.36812413					
1050			-0.37156746	-0.36883252				
1051				-0.43966730	-0.37912462			
1052					-0.43131969	-0.30464402		
1053						-0.56805577	-0.11622085	
1054								-0.15409924
1055								-0.42301487
1056	-1.06152656							
1057	3.80639400	-1.24580463						
1058	-1.24580463	3.92147608	-1.28553645					
1059		-1.28553645	3.81166599	-1.02577629				
1060			-1.02577629	3.68866306	-1.04068008			
1061				-1.04068008	3.70138851	-1.05677125		
1062					-1.05677125	3.74981866	-1.10437442	
1063						-1.10437442	1.98164948	
1064								2.05504336
1065								-1.08017720
1066	-0.39980692							
1067	-0.34964795	-0.33990688						
1068		-0.34779519	-0.36028321					
1069			-0.40037845	-0.46402054				
1070				-0.34968634	-0.44849171			
1071					-0.34500117	-0.42764774		
1072						-0.28832546	-0.67875897	
1073							-0.08229525	
1074								-0.34703031
1075								-0.05072174

	1065	1066	1067	1068	1069	1070	1071	1072
1055	-0.28981454							
1056	-0.42739972	-0.40032440						
1057		-0.39980692	-0.34964795					
1058			-0.33990688	-0.34779519				
1059				-0.36028321	-0.40037845			
1060					-0.46402054	-0.34968634		
1061						-0.44849171	-0.34500117	
1062							-0.42764774	-0.28832546
1063								-0.67875897
1064	-1.08017720							
1065	3.70776310	-0.96386923						
1066	-0.96386923	3.78022098	-1.27262859					
1067		-1.27262859	3.92027748	-1.25717072				
1068			-1.25717072	3.80113430	-1.03598888			
1069				-1.03598888	3.71232719	-1.08235745		
1070					-1.08235745	3.72032580	-1.05436962	
1071						-1.05436962	3.70439547	-1.04107226
1072							-1.04107226	3.69600439
1073								-0.95388440
1075	-0.62160604							
1076	-0.32489637	-0.35490338						
1077		-0.38868845	-0.35257320					
1078			-0.34835014	-0.40606989				
1079				-0.39382641	-0.39088476			
1080					-0.33869712	-0.40004768		
1081						-0.38537300	-0.49244756	
1082							-0.34385711	-0.40604639
1083								-0.32791690

	1073	1074	1075	1076	1077	1078	1079	1080
1063	-0.08229525							
1064		-0.34703031	-0.05072174					
1065			-0.62160604	-0.32489637				
1066				-0.35490338	-0.38868845			
1067					-0.35257320	-0.34835014		
1068						-0.40606989	-0.39382641	
1069							-0.39088476	-0.33869712
1070								-0.40004768
1071								
1072	-0.95388440							
1073	1.83238664							
1074		1.90123477	-1.43967938					
1075		-1.43967938	4.06099280	-1.17432753				
1076			-1.17432753	3.85177308	-1.20220954			
1077				-1.20220954	3.89816579	-1.28247790		
1078					-1.28247790	3.81619705	-1.03751677	
1079						-1.03751677	3.71220993	-1.08256856
1080							-1.08256856	3.69851655
1081								-1.00380458
1082								
1083	-0.62570433							
1084	-0.17050267							
1085		-0.11452508	-0.58731213					
1086			-0.18734598	-0.47619681				
1087				-0.31923945	-0.29245408			
1088					-0.37976262	-0.39317519		
1089						-0.34860715	-0.44765497	
1090							-0.35975847	-0.45355953
1091								-0.41983908

	1081	1082	1083	1084	1085	1086	1087	1088
1070	-0.38537300							
1071	-0.49244756	-0.34385711						
1072		-0.40604639	-0.32791690					
1073			-0.62570433	-0.17050267				
1074					-0.11452508			
1075					-0.58731213	-0.18734598		
1076						-0.47619681	-0.31923945	
1077							-0.29245408	-0.37976262
1078								-0.39317519
1080	-1.00380458							
1081	3.70029751	-1.07534090						
1082	-1.07534090	3.69581006	-1.00683112					
1083		-1.00683112	3.63731896	-0.88073844				
1084			-0.88073844	1.80792564				
1085					1.85076933	-1.02690666		
1086					-1.02690666	3.96109361	-1.48998546	
1087						-1.48998546	4.04235496	-1.22165897
1088							-1.22165897	3.80536470
1089								-1.08462651
1091	-0.44502101							
1092	-0.29831045	-0.44475549						
1093		-0.41897904	-0.42811899					
1094			-0.36800918	-0.59815679				
1095				-0.15852774				
1096					-0.12202545	-0.49584218		
1097						-0.28481652	-0.37067917	
1098							-0.34833783	-0.35194474
1099								-0.37419667

	1089	1090	1091	1092	1093	1094	1095	1096
1078	-0.34860715							
1079	-0.44765497	-0.35975847						
1080		-0.45355953	-0.41983908					
1081			-0.44502101	-0.29831045				
1082				-0.44475549	-0.41897904			
1083					-0.42811899	-0.36800918		
1084						-0.59815679	-0.15852774	
1085								-0.12202545
1086								-0.49584218
1088	-1.08462651							
1089	3.69810997	-1.00478247						
1090	-1.00478247	3.66533009	-1.00832550					
1091		-1.00832550	3.73175635	-1.14670471				
1092			-1.14670471	3.72050772	-0.97860546			
1093				-0.97860546	3.66867170	-1.04546063		
1094					-1.04546063	3.61715733	-0.78582538	
1095						-0.78582538	1.75873620	
1096								1.89668617
1097								-1.10168524
1099	-0.40370121							
1100	-0.40873766	-0.44283601						
1101		-0.39606812	-0.38985060					
1102			-0.32201545	-0.44530045				
1103				-0.40683116	-0.43103613			
1104					-0.36647145	-0.41907455		
1105						-0.40063080	-0.56110158	
1106							-0.25328150	
1107								-0.17713330

	1097	1098	1099	1100	1101	1102	1103	1104
1086	-0.28481652							
1087	-0.37067917	-0.34833783						
1088		-0.35194474	-0.37419667					
1089			-0.40370121	-0.40873766				
1090				-0.44283601	-0.39606812			
1091					-0.38985060	-0.32201545		
1092						-0.44530045	-0.40683116	
1093							-0.43103613	-0.36647145
1094								-0.41907455
1096	-1.10168524							
1097	4.05040586	-1.58289356						
1098	-1.58289356	4.02016535	-1.04371030					
1099		-1.04371030	3.70873353	-1.07161543				
1100			-1.07161543	3.73711085	-1.09909362			
1101				-1.09909362	3.77476303	-1.15221480		
1102					-1.15221480	3.75246646	-1.04903874	
1103						-1.04903874	3.73765785	-1.12451606
1104							-1.12451606	3.75639863
1105								-1.08980382
1107	-0.50045594							
1108	-0.20987543	-0.42347340						
1109		-0.26980552	-0.39339789					
1110			-0.42211203	-0.38515368				
1111				-0.32967445	-0.40513098			
1112					-0.33240491	-0.39447188		
1113						-0.38942513	-0.38702846	
1114							-0.33920730	-0.40202781
1115								-0.35450495

	1105	1106	1107	1108	1109	1110	1111	1112
1094	-0.40063080							
1095	-0.56110158	-0.25328150						
1096			-0.17713330					
1097			-0.50045594	-0.20987543				
1098				-0.42347340	-0.26980552			
1099					-0.39339789	-0.42211203		
1100						-0.38515368	-0.32967445	
1101							-0.40513098	-0.33240491
1102								-0.39447188
1104	-1.08980382							
1105	3.64115628	-0.79669605						
1106	-0.79669605	2.71415371						
1107			1.22648232	-0.54889308				
1108			-0.54889308	1.93270318	-0.75046127			
1109				-0.75046127	1.90473460	-0.49106992		
1110					-0.49106992	1.87787054	-0.57953491	
1111						-0.57953491	1.89924056	-0.58490022
1112							-0.58490022	1.88221723
1113								-0.57044022
1115	-0.34692470							
1116	-0.44599933	-0.30218594						
1117		-1.01808315						
1118		-0.34390708						

	1113	1114	1115	1116	1117	1118
1102	-0.38942513					
1103	-0.38702846	-0.33920730				
1104		-0.40202781	-0.35450495			
1105			-0.34692470	-0.44599933		
1106				-0.30218594	-1.01808315	-0.34390708
1112	-0.57044022					
1113	1.92742131	-0.58052751				
1114	-0.58052751	1.91188924	-0.59012663			
1115		-0.59012663	1.89966575	-0.60810948		
1116			-0.60810948	1.92520999	-0.56891525	
1117				-0.56891525	2.86558168	-1.27858327
1118					-1.27858327	1.62249035

CHAPTER 7

PROJECT CONCLUSIONS

SUMMARY

This project examines the coseismic and postseismic deformation resulting from the 26 December 2004 M9.2 Sumatra-Andaman earthquake (SAE). I use 3D finite element models (FEMs) to quantify the poroelastic and viscoelastic deformation. The first FEM (Chapters 2-5) analyzes both poroelastic and viscoelastic effects of the SAE, but does not account for changes in geology or structure along strike. The second FEM (Chapter 6) simulates the coseismic slip distribution for the SAE and accounts for changes in geology and structure along strike.

The significance of this study lies in the ability to generate models for earthquake and tsunami prediction. Although models are simplifications of the natural earth system, the construction of models enables the modeler to understand with confidence which mechanical and geological processes and complexities are needed to simulate in order to predict future earthquakes. In addition, these models can further be used to help constrain which geologic processes and complexities are needed to constrain tsunami predictions.

The innovation of this work is the development of a fully 3D FEM for analysis of coseismic and postseismic deformation and the use of an irregular grid on which the slip distribution is smoothed and solved. The progression of this work has provided several iterations of the first FEM design and a new fully 3D FEM design which uses finite element methods instead of finite difference methods to smooth the slip distribution. This project is the first which analyzes poroelastic and viscoelastic deformation simultaneously while honoring the known and most prominent 3D geologic features of the Sumatra-Andaman subduction zone (SASZ). Previous studies have used layered half-space or quarter half-space models (Johnson and Segall, 2004; Hsu et al., 2006), but these models cannot account for the basic component of a subduction zone, the subducting slab, or solve for poroelastic deformation, viscoelastic deformation, and afterslip simultaneously.

Results and Discussion

The primary goal for this project was to analyze and quantify the coseismic and postseismic deformation of the SAE with the intention of determining whether the SAE affected the timing of the 28 March 2005 M8.7 Nias earthquake (NE). The secondary goal was to build a fully 3D FEM. An FEM can simulate the coseismic deformation of the SAE while simultaneously accounting for the complex geometry of the subducting slab and the distribution of rheologic properties according to tomography, GRACE, and geologic information. Future studies of the fully 3D FEM coseismic slip distribution will determine if investigators can predict the location

and timing of aftershocks including the M7.8 northern Sumatra earthquake (NSE) on 6 April 2010, and the M7.5 Nicobar Islands earthquake (NIE) on 12 June 2010.

I determined that the occurrence of the SAE affected the timing of the NE (Hughes et al., 2010; Hughes et al., 2011). I analyzed Coulomb stress (σ_c) which is the tendency for slip to occur along a fault and is defined as

$$\Delta\sigma_c = \Delta\sigma_s + f(\Delta\sigma_n + \Delta P) \quad (7.1)$$

where σ_s is shear stress, f is the coefficient of friction, σ_n is normal stress, and P is pore pressure (Wang, 2000). The components of Coulomb stress are found by calculating the change in shear and normal stress and the change in pore pressure near an earthquake. I determined that the MPa scale change in pore pressure was the main cause of the NE to occur 7 years before predicted occurrence based on interseismic strain accumulation (Hughes et al., 2010; Hughes et al., 2011).

The results of my fully 3D FEM indicate that the maximum dip-slip occurred within about 5 km depth and nucleated in two main locations. The maximum strike-slip motion nucleated in three main locations; one within about 5 km depth and the other two located at the down-dip extent of the rupture zone. The maximum dip-slip and strike-slip motion is greater than 40 m and 25 m, respectively. The magnitude of the slip distribution results are consistent with other geodetic studies of the SAE (Ammon et al., 2005; Lay et al., 2005; Vigny et al., 2005; Masterlark and Hughes, 2008; Hoechner et al., 2008; Cattin et al., 2009; Lorito et al., 2010; Poisson et al., 2011), but are about 10 m higher in magnitude. However, the location of the highest slip magnitude differs. The results of this study show that the highest slip occurs further offshore of Sumatra and near the trench, rather than deeper and

under the Nicobar Islands (Vigny et al., 2005; Masterlark and Hughes, 2008, Hoechner et al., 2008; Lorito et al., 2010). This slip distribution is qualitatively similar to the slip distributions generated by tsunami wave height and seismic data (Ammon et al., 2005; Lay et al., 2005; Hoechner et al., 2008; Cattin et al., 2009; Lorito et al., 2010; Poisson et al., 2011), and corresponds to the location of a 12 m fault scarp imaged by ROV on the 2005 SEATOS cruise.

The maximum uplift and subsidence predicted by the fully 3D FEM are 21 m and 8 m, respectively. The uplift and subsidence results and the location of the highest slip magnitude quantified by the fully 3D FEM indicate that the fundamental components of a subduction zone (rigid subducting slab and weak forearc) must be accounted for in the model in order to accurately predict uplift and subsidence due to the coseismic displacement of the 2004 M9.2 SAE.

CONCLUSIONS

There are two main innovations of this project, 1) creating a fully three-dimensional FEM which is capable of solving for poroelastic and viscoelastic deformation simultaneously and 2) using finite element models to quantify a slip distribution which generated a sustained pore pressure change that induced a second large magnitude earthquake. General Conclusions:

1) A formal modeling protocol is necessary to guide the decision making process of the deformation modeling analysis, which should clearly define the purpose, design, and analysis of geologic models of coseismic and postseismic deformation.

2) FEMs are capable of quantifying poroelastic and viscoelastic deformation while simultaneously honoring the 3D geologic complexity of a subduction zone.
3) Finite element methods are a powerful tool to quantify a numerical solution on an irregularly shaped geometry, namely the bending or breaking of a subducting slab.

Geologic Conclusions:

1) The pore pressure change induced by the Sumatra-Andaman earthquake is on the same scale as shear stress and normal stress, thus indicating that the change in pore pressure must be quantified and incorporated in Coulomb stress calculations.
2) The pore pressures in the forearc re-equilibrated quickly after the Sumatra-Andaman earthquake, but the pore pressures in the oceanic crust persisted and increased up to the point of the Nias earthquake rupture.
3) The fully 3D FEM had a larger magnitude slip distribution which was nucleated in two main areas within about 5 km depth than the single cross-section 3D FEM.
4) The fully 3D FEM had a greater displacement magnitude for vertical displacement than the single cross-section 3D FEM.
5) The 2004 M9.2 Sumatra-Andaman earthquake sped up the timing by 7 years of the 2005 M8.7 Nias earthquake compared to predictions based on interseismic strain accumulation. The NE was inevitable due to relative plate motions, but the SAE altered the timing.

REFERENCES

Ammon, C.J., Ji, c., Thio, H.-K., Robinson, D., Ni, S., Hjorleifsdottir, V., Kanamori, H., Lay, T., Das, S., Helmberger, D., Ichinose, G., Polet, J., and Wald, D., 2005, Rupture process of the 2004 Sumatra-Andaman earthquake: Science, v. 308, p. 1133-1139, doi: 10.1126/science.1112260.

Cattin, R., Chamot-Rooke, N., Pubellier, M., Rabaute, A., Delescluse, M., Vigny, C., Fleitout, L., and Dubernet, P., 2009, Stress change and effective friction coefficient along the Sumatra-Andaman-Sagaing fault system after the 26 December 2004 (M_W = 9.2) and the 28 March 2005 (M_W = 8.7) earthquakes: G-Cubed, Geochemistry, Geophysics, Geosystems, v. 10, doi: 10.1029/2008GC002167.

Hoechner, A., Babeyko, A.Y., and Sobolev, S.V., 2008, Enhanced GPS inversion technique applied to the 2004 Sumatra earthquake and tsunami: Geological Research Letters, v. 35, doi: 10.1029/2007GL033133.

Hsu, Y.-J., Simons, M., Avouac, J.-P., Galetzka, J., Sieh, K., Chlieh, M., Natawidjaja, D., Prawirodirdjo, L., and Bock, Y., 2006, Frictional afterslip following the 2005 Nias-Simeulue earthquake, Sumatra: Science, v. 312, p. 1921-1926, doi: 10.1126/science1126960.

Hughes, K.L.H., Masterlark, T., and Mooney, W.D., 2010, Poroelastic stress-triggering of the 2005 M8.7 Nias earthquake by the 2004 M9.2 Sumatra-Andaman earthquake: Earth and Planetary Science Letters, v. 293, p. 289-299, doi: 10.1016/j.epsl.2010.02.043.

Hughes, K.L.H., Masterlark, T., and Mooney, W.D., 2011, Pore-fluid migration and the timing of the 2005 M8.7 Nias earthquake, Lithosphere, v. 3, p. 170-172, doi: 10.1130/L109.1.

Johnson, K.M., and Segall, P., 2004, Viscoelastic earthquake cycle models with deep stress-driven creep along the San Andreas fault system: Journal of Geophysical Research, v. 109, doi: 10.1029/2004JB003096.

Lay, T., Kanamori, H., Ammon, C.J., Nettles, M., Ward, S.N., Aster, R.C., Beck, S.L., Bilek, S.L., Brudzinski, M.R., Butler, R., DeShon, H.R., Ekström, G., Satake, K., and Sipkin, S., 2005, The great Sumatra-Andaman earthquake of 26 December 2004: Science, v. 308, p. 1127-1133, doi: 10.1126/science.1112250.

Lorito, S., Piatanesi, A., Cannelli, V., Romano, F., and Melini, D., 2010, Kinematics and source zone properties of the 2004 Sumatra-Andaman earthquake and tsunami: Nonlinear joint inversion of tide gauge, satellite altimetry, and GPS data: Journal of Geophysical Research, v. 115, doi: 10.1029/2008JB005974.

Masterlark, T., and Hughes, K.L.H., 2008, Next generation of deformation models for the 2004 M9 Sumatra-Andaman earthquake: Geophysical Research Letters, v. 35, doi: 10.1029/2008GL035198.

Poisson, B., Oliveros, C., and Pedreros, R., 2011, Is there a best source model of the Sumatra 2004 earthquake for simulating the consecutive tsunami?: Geophysical Journal International, v. 185, p. 1365-1378, doi: 10.1111/j.1365-246X.2011.05009.x.

Vigny, C., Simons, W.J.F., Abu, S., Bamphenyu, R., Satirapod, C., Choosakul, N., Subarya, C., Socquet, A., Omar, K., Abidin, H.Z., and Ambrosius, B.A.C., 2005, Insight into the 2004 Sumatra-Andaman earthquake from GPS measurements in southeast Asia, Nature, v. 436, p. 201-206.

Wang, H.F., 2000, Theory of Linear Poroelasticity: With Applications to Geomechanics: Princeton, Princeton University Press, 287 p.

COMPLETE REFERENCE LIST

Ammon, C.J., Ji, C., Thio, H.K., Robinson. D., Ni, S., Hjorleifsdottir, V., Kanamori, H., Lay, T., Das, S., Helmberger, D., Ichinose, G., Polet, J., and Wald, D., 2005, Rupture process of the 2004 Sumatra-Andaman Earthquake: Science, v. 308, p. 1133–1139, doi: 10.1126/science.1112260.

Anderson, M.P., and Woessner, W.W., 1992, Applied Groundwater Modeling: Simulation of Flow and Advective Transport: San Diego, Academic Press, 381 p.

Anu, R., and Rajendran, K., 2006, Co-seismic deformation along the Andaman-Nicobar arc based on GPS data and ground observations: Extended Abstract, XVIII Kerala Science Congress, p. 226-228.

Aster, R., Borchers, B., and Thurber, C., 2005, Parameter Estimation and Inverse Problems: Elsevier Academic Press, 301 p.

Audet, P., Bostock, M.G., Christensen, N.I., and Peacock, S.M., 2009, Seismic evidence for overpressured subducted oceanic crust and megathrust fault sealing: Nature, v. 457, p. 76-78, doi: 10.1038/nature07650.

Banerjee, P., Pollitz, F.F., and Bürgmann, R., 2005, The size and duration of the Sumatra-Andaman earthquake from far-field static offsets: Science, v. 308, p. 1769-1772, doi: 10.1126/science.1113746.

Banerjee, P., Pollitz, F., Nagarajan, B., and Bürgmann, R., 2007, Coseismic slip distributions of the 26 December 2004 Sumatra-Andaman and 28 March 2005 Nias earthquakes from GPS static offsets: Bulletin of the Seismological Society of America, v. 97, p. S86-S102, doi: 10.1785/0120050609.

Barber, A. J., Crow, M.J., and Milsom, J.S., 2005, Sumatra: Geology, Resources, and Tectonic Evolution: London, Geological Society, 290 p.

Beeler, N.M, Simpson, R.W., Hickman, S.H., and Lockner, D.A., 2000, Pore fluid pressure, apparent friction, and Coulomb failure: Journal of Geophysical Research, v.105, p. 25533-25542.

Bilek, S.L., 2007, Using earthquake source durations along the Sumatra-Andaman subduction system to examine fault-zone variations: Bulletin of the

Seismological Society of America, v. 97, p. S62-S70, doi: 10.1785/0120050622.

Bilek, S.L., and Engdahl, E.R., 2007, Rupture characterization and aftershock relocations for the 1994 and 2006 tsunami earthquakes in the Java subduction zone: Geophysical Research Letters, v. 34, doi: 10.1029/2007/GL031357.

Bird, P., 2003, An updated digital model of plate boundaries: G-Cubed, v. 4, doi: 10.1029/2001GC000252.

Bosl, W.J., and Nur, A., 2002, Aftershocks and pore fluid diffusion following the 1992 Landers earthquake: Journal of Geophysical Research, v. 107, doi: 10.1029/2001JB000155.

Brocher, T.M., 2005, Empirical relations between elastic wavespeeds and density in the earth's crust: Bulletin of the Seismological Society of America, v. 95, p. 2081-2092, doi: 10.1785/0120050077.

Byerlee, J., 1978, Friction of rocks: Pageoph, v. 116, p. 615-626.

Catherine, J.K., Gahalaut, V.K., and Sahu, V.K., 2005, Constraints on rupture of the December 26, 2004, Sumatra earthquake from far-field GPS observations: Earth and Planetary Science Letters, v. 237, p. 673-679, doi: 10.1016/j.epsl.2005.07.012.

Cattin, R., Chamot-Rooke, N., Pubellier, M., Rabaute, A., Delescluse, M., Vigny, C., Fleitout, L., and Dubernet, P., 2009, Stress change and effective friction coefficient along the Sumatra-Andaman-Sagaing fault system after the 26 December 2004 (M_W = 9.2) and the 28 March 2005 (M_W = 8.7) earthquakes: G-Cubed, Geochemistry, Geophysics, Geosystems, v. 10, doi: 10.1029/2008GC002167.

Chatterjee, S., Bhattacharyya, R., and Majumdar, T.J., 2007, Generation and study of high-resolution satellite gravity over the Sumatran earthquake region: International Journal of Remote Sensing, v. 28, p. 2915-2925, doi: 10.1080/01431160601091829.

Chen, J.L., Wilson, C.R., Tapley, B.D., and Grand, S., 2007, GRACE detects coseismic and postseismic deformation from the Sumatra-Andaman earthquake: Geophysical Research Letters, v. 34, doi: 10.1029/2007GL030356.

Chlieh, M., Avouac, J.-P., Hjorleifsdottir, V., Song, T.-R.A., Ji, C., Sieh, K., Sladen, A., Hebert, H., Prawirodirdjo, L., Bock, Y., and Galetzka, J., 2007, Coseismic slip and afterslip of the great Mw 9.15 Sumatra-Andaman earthquake of 2004:

Bulletin of the Seismological Society of America, v. 97, p. S152–S173, doi: 10.1785/0120050631.

Christensen, N.I., 1996, Poisson's ratio and crustal seismology: Journal of Geophysical Research, v. 101, p. 3139-3156.

Christensen, N.I., and Ramananantoandro, R., 1988, Permeability of the oceanic crust based on experimental studies of basalt permeability at elevated pressures: Tectonophysics, v. 149, p. 181-186.

Cocco, M., and Rice, J.R., 2002, Pore pressure and poroelasticity effects in Coulomb stress analysis of earthquake interactions: Journal of Geophysical Research, v. 107, doi: 10.1029/2000JB000138.

Cocco, M., and Rice, J.R., 2003, Correction to "Pore pressure and poroelasticity effects in Coulomb stress analysis of earthquake interactions": Journal of Geophysical Research, v. 108, doi: 10.1029/2002JB002319.

Conder, J.A., Wiens, D.A., and Morris, J., 2002, On the decompression melting structure at volcanic arcs and back-arc spreading centers: Geophysical Research Letters, v. 29, doi: 10.1029/2002GL015390.

Contreras-Reyes, E., Grevemeyer, I., Flueh, E.R., Scherwath, M., and Bialas, J., 2008, Effect of trench-outer rise bending-related faulting on seismic Poisson's ratio and mantle anisotropy: A case study offshore southern central Chile: Geophysical Journal International, v. 173, p. 142-156, doi: 10.1111/j.1365-246X.2008.03716.x.

Curray, J.R., 2005, Tectonics and history of the Andaman Sea Region: Journal of Asian Earth Sciences, v. 25, p. 187–232, doi: 10.1016/j.jseaes.2004.09.001.

Dasgupta, S., Mukhopadhyay, M., Bhattacharya, A., and Jana, T.K., 2003, The geometry of the Burmese-Andaman subducting lithosphere: Journal of Seismology, v. 7, p. 155-174.

Delescluse, M., and Chamot-Rooke, N., 2007, Instantaneous deformation and kinematics of the India-Australia plate: Geophysical Journal International, v. 168, p. 818-842, doi: 10.1111/j.1365-246X.2006.03181.x.

Earnest, A., Rajendran, C.P., Rajendran, K., Anu, R., Arun, G.M., and Mohan, P.M., 2005, Near-field observations on the co-seismic deformation associated with the 26 December 2004 Andaman-Sumatra earthquake: Current Science, v. 89, p. 1237-1244.

Engdahl, E.R., Villaseñor, A., DeShon, H.R., and Thurber, C.H., 2007, Teleseismic relocation and assessment of seismicity (1918–2005) in the region of the

2004 Mw 9.0 Sumatra-Andaman and 2005 Mw 8.6 Nias Island great earthquakes: Bulletin of the Seismological Society of America, v. 97, p. S43–S61, doi: 10.1785/0120050614.

Fine, I.V., Rabinovich, A.B., and Thomson, R.E., 2005, The dual source region for the 2004 Sumatra tsunami: Geophysical Research Letters, v. 32, doi: 10.1029/2005GL023521.

Fisher, A.T., 1998, Permeability within basaltic oceanic crust: Reviews of Geophysics, v. 36, p. 143-182.

Fisher, D., Mosher, D., Austin Jr., J.A., Gulick. S.P.S., Masterlark, T., and Moran, K., 2007, Active deformation across the Sumatran forearc over the December 2004 Mw 9.2 rupture: Geology, v. 35, p. 99–102, doi: 10.1130/G22993A.1.

Freed, A.M., Bürgmann, R., Calais, E., Freymueller, J., and Hreinsdóttir, S., 2006, Implications of deformation following the 2002 Denali, Alaska, earthquake for postseismic relaxation processes and lithospheric rheology: Journal of Geophysical Research, v. 111, doi: 10.1029/2005JB003894.

Freed, A.M., and Lin, J., 2001, Delayed triggering of the 1999 Hector Mine earthquake by viscoelastic stress transfer: Nature, v. 411, p. 180-183.

Freymueller, J., King, N.E., and Segall, P., 1994, The co-seismic slip distribution of the Landers earthquake: Bulletin of the Seismological Society of America, v. 84, p. 646-659.

Fujii, Y., and Satake, K., 2007, Tsunami source of the 2004 Sumatra-Andaman earthquake inferred from tide gauge and satellite data: Bulletin of the Seismological Society of America, v. 97, p. S192-S207, doi: 10/1785/0120050613.

Gahalaut, V., and Gahalaut, K., 2007, Burma plate motion: Journal of Geophysical Research, v. 112, doi: 10.1029/2007JB004928.

Gahalaut, K., Gahalaut, V.K., and Kayal, J.R., 2008, Poroelastic relaxation and aftershocks of the 2001 Bhuj earthquake, India: Tectonophysics, v. 460, p. 76-82, doi: 10.1016/j.tecto.2008.07.004.

Gahalaut, V.K., and Kalpna, 2005, 28 March 2005 Sumatra earthquake: Expected, triggered or aftershock?: Current Science, v. 89, p. 452-454.

Gahalaut, V.K., Nagarajan, B., Catherine, J.K., and Kumar, S., 2006, Constraints on 2004 Sumatra-Andaman earthquake rupture from GPS measurements in Andaman-Nicobar Islands: Earth and Planetary Science Letters, v. 242, p. 365-374, doi: 10.1016/j.epsl.2005.11.051.

Geist, E.L., 2005, Tsunami simulation image: The Wave that Shook the World, NOVA, http://www.pbs.org/wgbh/nova/tsunami/.

Geist, E.L., Titov, V.V., Arcas, D., Pollitz, F.F., and Bilek, S.L., 2007, Implications of the 26 December 2004 Sumatra-Andaman earthquake of tsunami forecast and assessment models for great subduction-zone earthquakes: Bulletin of the Seismological Society of America, v. 97, p. S249–S270, doi: 10.1785/0120050619.

Grilli M.ASCE, S.T., Ioualalen, M., Asavanant, J., Shi, F., Kirby M.ASCE, J.T., and Watts, P., 2007, Source constraints and model simulation of the December 26, 2004, Indian Ocean tsunami: Journal of Waterway, Port, Coastal, and Ocean Engineering, v. 133, p. 414-428, doi: 10.1061/(ASCE)0733-950X.

Gubbins, D., 2004, Time Series Analysis and Inverse Theory for Geophysicists: Cambridge, Cambridge University Press, 225 p.

Gutscher, M.-A., Malavieille, J., Lallemand, S., and Collot, J.-Y., 1999, Tectonic segmentation of the North Andean margin: Impact of the Carnegie Ridge collision: Earth and Planetary Science Letters, v. 168, p. 255-270.

Hall, R., 2002, Cenozoic geological and plate tectonic evolution of SE Asia and the SW Pacific: Computer-based reconstructions, model and animations: Journal of Asian Sciences, v. 20, p. 353-431.

Han, S.-C., Ray, R.D., and Luthcke, S.B., 2007, Ocean tidal solutions in Antarctica from GRACE inter-satellite tracking data: Geophysical Research Letters, v. 34, doi: 10.1029/2007GL031540.

Han, S.-C., Shum, C.K., Bevis, M., Ji, C., and Kuo, C.-Y., 2006, Crustal dilatation observed by GRACE after the 2004 Sumatra-Andaman earthquake: Science, v. 313, p. 658–662, doi: 10.1126/science1128661.

Hanson, J.A., Reasoner, C.L., and Bowman, J.R., 2007, High-frequency tsunami signals of the great Indonesian earthquakes of 26 December 2004 and 28 March 2005: Bulletin of the Seismological Society of America, v. 97, p. S232-S248, doi: 10.1785/0120050607.

Hashimoto, M., Choosakul, N., Hashizume, M., Takemoto, S., Takiguchi, H., Fukuda, Y., and Fujimori, K., 2006, Crustal deformations associated with the great Sumatra-Andaman earthquake deduced from continuous GPS observation: Earth Planets Space, v. 58, p. 127-139.

Hébert, H., Sladen, A., and Schindelé, F., 2007, Numerical modeling of the great 2004 Indian Ocean tsunami: Focus on the Mascarene Islands: Bulletin of the

Seismological Society of America, v. 97, p. S208-S222, doi: 10.1785/0120050611.

Hoechner, A., Babeyko, A.Y., and Sobolev, S.V., 2008, Enhanced GPS inversion technique applied to the 2004 Sumatra earthquake and tsunami: Geological Research Letters, v. 35, doi: 10.1029/2007GL033133.

Hsu, Y.-J., Simons, M., Avouac, J.-P., Galetzka, J., Sieh, K., Chlieh, M., Natawidjaja, D., Prawirodirdjo, L., and Bock, Y., 2006, Frictional afterslip following the 2005 Nias-Simeulue earthquake, Sumatra: Science, v. 312, p. 1921-1926, doi: 10.1126/science1126960.

Hughes, K.L.H., and Masterlark, T., 2008, Slip distribution for the 2004 Sumatra-Andaman earthquake constrained by both GPS data and tsunami run-up measurements: Bollettino di Geofisica: Teorica ed Applicata, v. 49, p. 165-169.

Hughes, K.L.H., Masterlark, T., and Mooney, W.D., 2010, Poroelastic stress-triggering of the 2005 M8.7 Nias earthquake by the 2004 M9.2 Sumatra-Andaman earthquake: Earth and Planetary Science Letters, v. 293, p. 289-299, doi: 10.1016/j.epsl.2010.02.043.

Hughes, K.L.H., Masterlark, T., and Mooney, W.D., 2011, Pore-fluid migration and the timing of the 2005 M8.7 Nias earthquake, Lithosphere, v. 3, p. 170-172, doi: 10.1130/L109.1.

Hutchison, C.S., 1989, Geological Evolution of South-East Asia: Oxford, Oxford University Press, 368 p.

Hutton, W., DeMets, C., Sánchez, O., Suárez, G., and Stock, J., 2001, Slip kinematics and dynamics during and after the 1995 October 9 M_w = 8.0 Colima-Jalisco earthquake, Mexico, from GPS geodetic constraints: Geophysical Journal International, v. 146, p. 637-658.

Hyndman, R.D., 2007, The seismogenic zone of subduction thrust faults: What we know and what we don't know, *in* Dixon, T.H., and Moore, J.C., ed., The Seismogenic Zone of Subduction Thrust Faults, New York, Columbia University Press, p. 15-40.

Ioualalen, M., Asavanant, J., Kaewbanjak, N., Grilli, S.T., Kirby, J.T., and Watts, P., 2007, Modeling the 26 December 2004 Indian Ocean tsunami: Case study of impact in Thailand: Journal of Geophysical Research, v. 112, doi: 10.1029/2006JC003850.

Ishii, M., Shearer, P.M., Houston, H., and Vidale, J.E., 2007, Teleseismic *P* wave imaging of the 26 December 2004 Sumatra-Andaman and 28 March 2005

Sumatra earthquake ruptures using the Hi-net array: Journal of Geophysical Research, v. 112, doi: 10.1029/2006JB004700.

Jade, S., Ananda, M.B., Kumar, P.D., and Banerjee, S., 2005, Co-seismic and post-seismic displacements in Andaman and Nicobar Islands from GPS measurements: Current Science, v. 88, p. 1980-1984.

Johnson, K.M., and Segall, P., 2004, Viscoelastic earthquake cycle models with deep stress-driven creep along the San Andreas fault system: Journal of Geophysical Research, v. 109, doi: 10.1029/2004JB003096.

Kayanne, H., Ikeda, Y., Echigo, T., Shishikura, M., Kamataki, T., Satake, K., Malik, J.N., Basir, S.R., Chakrabortty, G.K., and Roy, A.K.G., 2007, Coseismic and postseismic creep in the Andaman Islands associated with the 2004 Sumatra-Andaman earthquake: Geophysical Research Letters, v. 34, doi: 10.1029/2006GL028200.

Kenner, S.J., and Segall, P., 2000, Postseismic deformation following the 1906 San Francisco earthquake: Journal of Geophysical Research, v. 105, p. 13195-13209.

Kieckhefer, R.M., Shor Jr., G.G., Curray, J.R., Sugiarta, W., and Hehuwat, F., 1980, Seismic refraction studies of the Sunda trench and forearc basin: Journal of Geophysical Research, v. 85, p. 863– 889.

King, G.C.P., Stein, R.S., and Lin, J., 1994, Static stress changes and the triggering of earthquakes: Bulletin of the Seismological Society of America, v. 84, p. 935-953.

Kopp, H., Flueh, E.R., Klaeschen, D., Bialas, J., and Reichert, C., 2001, Crustal structure of the central Sunda margin at the onset of oblique subduction: Geophysical Journal International, v. 147, p. 449-474.

Kopp, H., Klaeschen, D., Flueh, E.R., Bialas, J., and Reichert, C., 2002, Crustal structure of the Java margin from seismic wide-angle and multichannel reflection data: Journal of Geophysical Research, v. 107, doi: 10.1029/2000JB000095.

Kopp, H., and Kukowski, N., 2003, Backstop geometry and accretionary mechanics of the Sunda margin: Tectonics, v. 22, doi: 10.1029/2002TC001420.

Kreemer, C., Blewitt, G., and Maerten, F., 2006, Co- and postseismic deformation of the 28 March 2005 Nias M_w 8.7 earthquake from continuous GPS data: Geophysical Research Letters, v. 33, doi: 10.1029/2005GL025566.

Lay, T., Kanamori, H., Ammon, C.J., Nettles, M., Ward, S.N., Aster, R.C., Beck, S.L., Bilek, S.L., Brudzinski, M.R., Butler, R., DeShon, H.R., Ekström, G., Satake, K., and

Sipkin, S., 2005, The great Sumatra-Andaman earthquake of 26 December 2004: Science, v. 308, p. 1127-1133, doi: 10.1126/science.1112250.

Lin, J.-Y., Le Pichon, X., Rangin, C., Sibuet, J.-C., and Maury, T., 2009, Spatial aftershock distribution of the 26 December 2004 great Sumatra-Andaman earthquake in the northern Sumatra area: G-Cubed, Geochemistry, Geophysics, Geosystems, v. 10, doi: 10.1029/2009GC002454.

Lorito, S., Piatanesi, A., Cannelli, V., Romano, F., and Melini, D., 2010, Kinematics and source zone properties of the 2004 Sumatra-Andaman earthquake and tsunami: Nonlinear joint inversion of tide gauge, satellite altimetry, and GPS data: Journal of Geophysical Research, v. 115, doi: 10.1029/2008JB005974.

Lorito, S., Romano, F., Piatanesi, A., and Boschi, E., 2008, Source process of the September 12, 2007, M_W 8.4 southern Sumatra earthquake from tsunami tide gauge record inversion: Geophysical Research Letters, v. 35, doi: 10.1029/2007GL032661.

Lovholt, F., Bungum, H., Harbitz, C.B., Glimsdal, S., Lindholm, C.D., and Pedersen, G., 2006, Earthquake related tsunami hazard along the western coast of Thailand: Natural Hazards and Earth System Sciences, v. 6, p. 979-997.

Masterlark, T., 2003, Finite element model predictions of static deformation from dislocation sources in a subduction zone: Sensitivities to homogeneous, isotropic, Poisson-solid, and half-space assumptions: Journal of Geophysical Research, v. 108, doi: 10.1029/2002JB002296.

Masterlark, T., DeMets, C., Wang, H.F., Sánchez, O., and Stock, J., 2001, Homogeneous vs heterogeneous subduction zone models: Coseismic and postseismic deformation: Geophysical Research Letters, v. 28, p. 4047-4050.

Masterlark, T., and Hughes, K.L.H., 2008, Next generation of deformation models for the 2004 M9 Sumatra-Andaman earthquake: Geophysical Research Letters, v. 35, doi: 10.1029/2008GL035198.

Masterlark, T., and Wang, H., 2000, Poroelastic coupling between the 1992 Landers and Big Bear earthquakes: Geophysical Research Letters, v. 27, p. 3647-3650.

Masterlark, T., and Wang, H.F., 2002, Transient stress-coupling between the 1992 Landers and 1999 Hector Mine, California, earthquakes: Bulletin of the Seismological Society of America, v. 92, p. 1470-1486.

McCaffrey, R., Zwick, P.C., Bock, Y., Prawirodirdjo, L., Genrich, J.F., Stevens, C.W., Puntodewo, S.S.O., and Subarya, C., 2000, Strain partitioning during oblique plate convergence in northern Sumatra: Geodetic and seismologic

constraints and numerical modeling: Journal of Geophysical Research, v. 105, p. 28363-28376.

McCloskey, J., Antonioli, A., Piatanesi, A., Sieh, K., Steacy, S., Nalbant, S., Cocco, M., Giunchi, C., Huang, J., and Dunlop, P., 2008, Tsunami threat in the Indian Ocean from a future megathrust earthquake west of Sumatra: Earth and Planetary Science Letters, v. 265, p. 61–81, doi: 10.1016/j.epsl.2007.09.034.

McCloskey, J., Nalbant, S.S., and Steacy, S., 2005, Earthquake risk from co-seismic stress: Nature, v. 434, p. 291.

Melbourne, T.I., Szeliga, W.M., Miller, M.M., and Santillan, V.M., 2005, Extent and duration of the 2003 Cascadia slow earthquake: Geophysical Research Letters, v. 32, doi: 10.1029/2004GL021790.

Melosh, H.J., and Raefsky, A., 1981, A simple and efficient method for introducing faults into finite element computations: Bulletin of the Seismological Society of America, v. 71, p. 1391-1400.

Meltzner, A.J., Sieh, K., Abrams, M., Agnew, D.C., Hudnut, K.W., Avouac, J.-P., and Natawidjaja, D.H., 2006, Uplift and subsidence associated with the great Aceh-Andaman earthquake of 2004: Journal of Geophysical Research, v. 111, doi: 10.1029/2005JB003891.

Menke, W., 1989, Geophysical Data Analysis: Discrete Inverse Theory: San Diego, Academic Press, 289 p.

Mignan, A., King, G., Bowman, D., Lacassin, R., and Dmowska, R., 2006, Seismic activity in the Sumatra-Java region prior to the December 26, 2004 (M_w=9.0-9.3) and March 28, 2005 (M_w=8.7) earthquakes: Earth and Planetary Science Letters, v. 244, p. 639-654, doi: 10.1016/j.epsl.2006.01.058.

Moore, G.F., Bangs, N.L., Taira, A., Kuramoto, S., Pangborn, E., and Tobin, H.J., 2007, Three-dimensional splay fault geometry and implications for tsunami generation: Science, v. 318, p. 1128-1131, doi: 10.1126/science.1147195.

Moran, K., and Tappin, D., 2006, SEATOS 2005 Cruise Report: Sumatra Earthquake and Tsunami Offshore Survey (SEATOS): http://ocean.oce.uri.edu/seatos.

Mukhopadhyay, M., 1988, Gravity anomalies and deep structure of the Andaman arc: Marine Geophysical Researches, v. 9, p. 197-210.

Nalbant, S.S., Steacy, S., Sieh, K., Natawidjaja, D., and McCloskey, J., 2005, Earthquake risk on the Sunda trench: Nature, v. 435, p. 756–757, doi: 10.1028/nature435756a.

Natawidjaja, D.H., Sieh, K., Ward, S.N., Cheng, H., Edwards, R.L., Galetzka, J., and Suwargadi, W., 2004, Paleogeodetic records of seismic and aseismic subduction from central Sumatran microatolls, Indonesia: Journal of Geophysical Research, v. 109, doi: 10.1029/2003JB002398.

Nur, A., and Walder, J., 1990, Time-dependent hydraulics of the Earth's crust, *in* National Research Council, ed., The Role of Fluids in Crustal Processes, Washington, D.C., National Academy Press, p. 113-127.

Okada, Y., 1992, Internal deformation due to shear and tensile faults in a half-space: Bulletin of the Seismological Society of America, v. 82, p. 1018–1040.

Page, B.G.N., Bennett, J.D., Cameron, N.R., Bridge, D.McC., Jeffery, D.H., Keats, W., and Thaib, J., 1979, A review of the main structural and magmatic features of northern Sumatra: Journal of the Geological Society of London, v. 136, p. 569-579.

Pal, T., Chakraborty, P.P., Gupta, T.D., and Singh, C.D., 2003, Geodynamic evolution of the outer-arc--forearc belt in the Andaman Islands, the central part of the Burma-Java subduction complex: Geological Magazine, v. 140, p. 289-307.

Panet, I., Mikhailov, V., Diament, M., Pollitz, F., King, G., de Viron, O., Holschneider, M., Biancale, R., and Lemoine, J.-M., 2007, Coseismic and post-seismic signatures of the Sumatra 2004 December and 2005 March earthquakes in GRACE satellite gravity: Geophysical Journal International, v. 171, p. 177-190, doi: 10.1111/j.1365-246X.2007.03525.x.

Park, J., Song, T.-R.A., Tromp, J., Okal, E., Stein, S., Roult, G., Clevede, E., Laske, G., Kanamori, H., Davis, P., Berger, J., Braitenberg, C., Van Camp, M., Lei, X., Sun, H., Xu, H., and Rosat, S., 2005, Earth's free oscillations excited by the 26 December 2004 Sumatra-Andaman earthquake: Science, v. 308, p. 1139-1144, doi: 10.1126/science.1112305.

Parsons, T., 2002, Post-1906 stress recovery of the San Andreas fault system calculated from three-dimensional finite element analysis: Journal of Geophysical Research, v. 107, doi: 10.1029/2001JB001051.

Paul, J., Lowry, A.R., Bilham, R., Sen, S., and Smalley Jr., R., 2007, Postseismic deformation of the Andaman Islands following the 26 December, 2004 great Sumatra-Andaman earthquake: Geophysical Research Letters, v. 34, doi: 10.1029/2007GL031024.

Pesicek, J.D., Thurber, C.H., Widiyantoro, S., Engdahl, E.R., and DeShon, H.R., 2008, Complex slab subduction beneath northern Sumatra: Geophysical Research Letters, v. 35, doi: 10.1029/2008GL035262.

Pesicek, J.D., Thurber, C.H., Widiyantoro, S., Zhang, H., DeShon, H.R., and Engdahl, E.R., 2010, Sharpening the tomographic image of the subducting slab below Sumatra, the Andaman Islands and Burma: Geophysical Journal International, v. 182, p. 433-453, doi: 10.1111/j.1365-246X.2010.04630.x.

Piatanesi, A., and Lorito, S., 2007, Rupture process of the 2004 Sumatra-Andaman earthquake from tsunami waveform inversion: Bulletin of the Seismological Society of America, v. 97, p. S223-S231, doi: 10.1785/0120050627.

Piombo, A., Martinelli, G., and Dragoni, M., 2005, Post-seismic fluid flow and Coulomb stress changes in a poroelastic medium: Geophysical Journal International, v. 162, p. 507-515, doi: 10.1111/j.1365-246X.2005.02673.x.

Plafker, G., and Savage, J.C., 1970, Mechanism of the Chilean earthquakes of May 21 and 22, 1960: Geological Society of America Bulletin, v. 81, p. 1001-1030.

Poisson, B., Oliveros, C., and Pedreros, R., 2011, Is there a best source model of the Sumatra 2004 earthquake for simulating the consecutive tsunami?: Geophysical Journal International, v. 185, p. 1365-1378, doi: 10.1111/j.1365-246X.2011.05009.x.

Pollitz, F.F., Banerjee, P., Bürgmann, R., Hashimoto, M., and Choosakul, N., 2006, Stress changes along the Sunda trench following the 26 December 2004 Sumatra-Andaman and 28 March 2005 Nias earthquakes: Geophysical Research Letters, v. 33, doi: 10.1029/2005GL024558.

Pollitz, F.F., Bürgmann, R., and Banerjee, P., 2006, Post-seismic relaxation following the great 2004 Sumatra-Andaman earthquake on a compressible self-gravitating Earth: Geophysical Journal International, v. 167, p. 397-420, doi: 10.1111/j.1365-246X.2006.03018.x.

Prawirodirdjo, L., McCaffrey, R., Chadwell, C.D., Bock, Y., and Subarya, C., 2010, Geodetic observations of an earthquake cycle at the Sumatra subduction zone: Role of interseismic strain segmentation: Journal of Geophysical Research, v. 115, doi: 10.1029/2008JB006139.

Rajendran, C.P., Rajendran, K., Anu, R., Earnest, A., Machado, T., Mohan, P.M., and Freymueller, J., 2007, Crustal deformation and seismic history associated with the 2004 Indian Ocean earthquake: A perspective from the Andaman-Nicobar Islands: Bulletin of the Seismological Society of America, v. 97, p. S174-S191, doi: 10.1785/0120050630.

Raleigh, C.B., Healy, J.H., and Bredehoeft, J.D., 1976, An experiment in earthquake control at Rangely, Colorado: Science, v. 191, p. 1230-1237.

Rastogi, B.K., and Jaiswal, R.K., 2006, A catalog of tsunamis in the Indian Ocean: Science of Tsunami Hazards, v. 25, p. 128-143.

Rhie, J., Dreger, D., Bürgmann, R., and Romanowicz, B., 2007, Slip of the 2004 Sumatra-Andaman earthquake from joint inversion of long-period global seismic waveforms and GPS static offsets: Bulletin of the Seismological Society of America, v. 97, p. S115-S127, doi: 10.1785/0120050620.

Richards, S., Lister, G., and Kennett, B., 2007, A slab in depth: Three-dimensional geometry and evolution of the Indo-Australian plate: G-Cubed, v. 8, doi: 10.1029/2007GC001657.

Ruff, L.J., 1996, Large earthquakes in subduction zones: Segment interaction and recurrence times, *in* Bebout, G.E., Scholl, D.W., Kirby, S.H., and Platt, J.P., ed., Subduction: Top to Bottom, Washington, D.C., American Geophysical Union, p. 91-104.

Savage, J.C., 1983, A dislocation model of strain accumulation and release at a subduction zone: Journal of Geophysical Research, v. 88, p. 4984-4996.

Schmitt, S.V., DeMets, C., Stock, J., Sánchez, O., Márquez-Azúa, B., and Reyes, G., 2007, A geodetic study of the 2003 January 22 Tecomán, Colima, Mexico earthquake: Geophysical Journal International, v. 169, p. 389–406, doi: 10.1111/j.1365-246X.2006.03322.x.

Seno, T., and Hirata, K., 2007, Did the 2004 Sumatra-Andaman earthquake involve a component of tsunami earthquakes?: Bulletin of the Seismological Society of America, v. 97, p. S296-S306, doi: 10.1785/0120050615.

Simons, W.J.F., Socquet, A., Vigny, C., Ambrosius, B.A.C., Abu, S.H., Promthong, C., Subarya, C., Sarsito, D.A., Matheussen, S., Morgan, P., and Spakman, W., 2007, A decade of GPS in southeast Asia: Resolving Sundaland motion and boundaries, Journal of Geophysical Research, v. 112, doi: 10.1029/2005JB003868.

Smith Jr., A.T., 1974, Time-dependent strain accumulation and release at island arcs: Implications for the 1946 Nankido earthquake, Ph.D. Thesis, MIT, 292 pp.

Sobolev, S.V., Babeyko, A.Y., Wang, R., Hoechner, A., Galas, R., Rothacher, M., Sein, D.V., Schröter, J., Lauterjung, J., and Subarya, C., 2007, Tsunami early warning using GPS-Shield arrays: Journal of Geophysical Research, v. 112, doi: 10.1029/2006JB004640.

Song, Y.T., Ji, C., Fu, L.-L., Zlotnicki, V., Shum, C.K., Yi, Y., and Hjorleifsdottir, V., 2005, The 26 December 2004 tsunami source estimated fom satellite radar

altimetry and seismic waves: Geophysical Research Letters, v. 32, doi: 10.1029/2005GL023683.

Song, T.-R.A., and Simons, M., 2003, Large trench-parallel gravity variations predict seismogenic behavior in subduction zones: Science, v. 301, p. 630-633, doi: 10.1126/science.1085557.

Sørensen, M.B., Atakan, K., and Pulido, N., 2007, Simulated strong ground motions for the great M9.3 Sumatra-Andaman earthquake of 26 December 2004: Bulletin of the Seismological Society of America, v. 97, p. S139-S151, doi: 10.1785/0120050608.

Stein, R.S., 1999, The role of stress transfer in earthquake occurrence: Nature, v. 402, p. 605-609.

Stein, S., and Okal, E.A., 2005, Speed and size of the Sumatra earthquake: Nature, v. 434, p. 581–582.

Stein, S., and Okal, E.A., 2007, Ultralong period seismic study of the December 2004 Indian Ocean earthquake and implications for regional tectonics and the subduction process: Bulletin of the Seismological Society of America, v. 97, p. S279-S295, doi: 10.1785/0120050617.

Subarya, C., Chlieh, M., Prawirodirdjo, L., Avouac, J.-P., Bock, Y., Sieh, K., Meltzner, A.J., Natawidjaja, D.H., and McCaffrey, R., 2006, Plate-boundary deformation associated with the great Sumatra-Andaman earthquake: Nature, v. 440, p. 46–51, doi: 10.1038/nature04522.

Toda, S., Stein, R.S., Reasenberg, P.A., Dieterich, J.H., and Yoshida, A., 1998, Stress transferred by the 1995 M_w = 6.9 Kobe, Japan, shock: Effect on aftershocks and future earthquake probabilities: Journal of Geophysical Research, v. 103, p. 24543-24565.

Turcotte, D.L., and Schubert, G.J., 1982, Geodynamics: Applications of Continuum Physics to Geological Problems: New York, John Wiley and Sons, 450 p.

U.S. Geological Survey - Earthquake Hazards Program, 2010, Slab Models for Subduction Zones, http://earthquake.usgs.gov/research/data/slab/#models, date accessed 25 April 2010, date updated 5 November 2009.

Vigny, C., Simons, W.J.F., Abu, S., Bamphenyu, R., Satirapod, C., Coosakul, N., Subarya, C., Socquet, A., Omar, K., Abidin, H.Z., Ambrosius, B.A.C., 2005, Insight into the 2004 Sumatra-Andaman earthquake from GPS measurements in Southeast Asia: Nature, v. 436, p. 201–206, doi: 10.1038/nature03937.

Waltham, T., 2005, The Asian tsunami disaster, December 2004: Geology Today, v. 21, p. 22-26.

Wang, H.F., 2000, Theory of Linear Poroelasticity: With Applications to Geomechanics: Princeton, Princeton University Press, 287 p.

Wang, H.F., and Anderson, M.P., 1982, Introduction to Groundwater Modeling: Finite Difference and Finite Element Methods: San Diego, Academic Press, 237 p.

Wang, J., and Ye, Z.-R., 2006, Dynamic modeling for crustal deformation in the China: Comparisons between the theoretical prediction and the recent GPS data: Physics of the Earth and Planetary Interiors, v. 155, p. 201-207, doi: 10.1016/j.pepi.2005.11.003.

Weissel, J.K., 1981, Magnetic lineations in marginal basins of the western Pacific: Philosophical Transcriptions of the Royal Society of London, v. 300, p. 223-247.

Williams, C.A., and McCaffrey, R., 2001, Stress rates in the central Cascadia subduction zone inferred from an elastic plate model: Geophysical Research Letters, v. 28, p. 2125-2128.